Discrete element modeling of the impact of granular debris flows on rigid and flexible structures

Adel Albaba

UNIVERSITÉ GRENOBLE ALPES

THÈSE

Pour obtenir le grade de

DOCTEUR DE L'UNIVERSITÉ GRENOBLE ALPES

Spécialité : **Matériaux, Mécanique, Génie civil, Electrochimie**

Arrêté ministériel : 7 août 2006

Présentée par

Adel ALBABA

Thèse dirigée par **François NICOT** et
codirigée par **Stéphane LAMBERT et Bruno CHAREYRE**

préparée au sein du **Laboratoire IRSTEA Grenoble**
dans **l'École Doctorale IMEP2**

Modélisation par éléments discrets de l'impact des laves torrentielles granulaires sur des structures rigides et flexibles

Thèse soutenue publiquement le **14 Décembre 2015**,
devant le jury composé de :

M. Jean-Yves DELENNE
Directeur de recherche, INRA Montpellier, Président du jury, Rapporteur
M. Guido GOTTARDI
Full Professor, University of Bologna, Rapporteur
M. Ali LIMAM
Professeur, INSA Lyon, Examinateur
M. François NICOT
Directeur de Recherche, IRSTEA Grenoble, Directeur de thèse
M. Stéphane LAMBERT
Ingénieur de Recherches, IRSTEA Grenoble, Co-Directeur de thèse
M. Bruno CHAREYRE
Maître de conférence (HDR), 3SR INP Grenoble, Co-encadrement de thèse
M. Thierry FAUG
Maître de conférence (HDR), IRSTEA Grenoble, Membre invité

Discrete element modeling of the impact of granular debris flows on rigid and flexible structures

Adel ALBABA

Adel ALBABA
Irstea de Grenoble
Unité de Recherche Erosion Torrentielle Neige et Avalanches
Domaine Universitaire, BP 76
F38402 – Saint Martin d'Hères Cedex – France
adel.albaba@irstea.fr

Acknowledgement

At the end of this long journey, I would like to acknowledge the generous help and support I have received during the PhD. First, I would like to thank my thesis supervisor Prof. François Nicot for supervising and directing me during the different stages of the thesis. His commitment, passion for science and encouragement were inspirational to me. My sincere thanks go also to my co-supervisors Dr. Stéphane Lambert and Dr. Bruno Chareyre for their participation in all meetings and discussions and for their valuable contribution to the thesis development.

The thesis was funded by the People Programme (Marie Curie Actions) of the European Unions Seventh Framework Programme FP7 under the MUMOLADE ITN project (Multiscale Modelling of Landslides and Debris Flow) grant number 289911. I would like to thank the project leader Prof. Wei Wu and the project coordinator Dr. Faqiang Qian for the perfect organization of the different schools, workshops and meeting during the project. I am also grateful to the PhD and Postdoc fellows in the project for the collaborations and discussions.

I would also like to thank my colleagues in both laboratories IRSTEA and L3SR in Grenoble for their scientific collaboration and suggestions during the internal meetings and workshops. Special thanks for Raphael Murin my office mate for helping me with different aspects of numerical coding, François Kneib for helping me with YADE open source code and its different features, and Dr. Thierry Faug for his suggestions concerning the granular flow impact on rigid walls.

Many contributions from engineers and researchers working with the industry of natural hazard protection were greatly supportive. These include the ones from Nicollas Villard (GTS) whose presence in many committee meetings greatly highlighted the practical aspects of the numerical model of flexible barriers. Discussions with Dr. Corrina Wendler (GeoBrugg) during MuMoLaDe's meetings and workshops were of great help, thanks to her in-depth knowledge of flexible debris flow barriers.

Finally, I would like to thank my family and friends for their unlimited support during these years, especially my wife for standing beside me throughout the thesis. A lot of work I carried out was on weekends, nights, while on vacation, and other times inconvenient for her, so I am grateful for her patience and sacrifice.

Adel ALBABA

Abstract

Natural hazards such as debris flows are real threat to the urbanization of mountainous areas. Local communities and infrastructures can be exposed to large impact forces in extreme debris events. Mitigation of such threats requires, along other measures, the estimation of the impact of such flows on protection structures (rigid walls and flexible barriers). In this thesis, Discrete Element Method (DEM) is used to model the granular flow, the rigid walls and flexible barriers.

First, a dry granular flow made of non-spherical particles flowing in inclined plane is modeled using a visco-elastic contact law with Mohr-Coulomb failure criterion. Experimental data from the literature is used to calibrate and validate the model. The model is calibrated based on the shape of the particle, the flow thickness and the final shape of the deposit on the wall. Validation procedure is based on the impact on a rigid wall divided into six segments. The main contribution of total normal force applied on the wall is found to be due to the dynamic component. On the micro-scale, development of force chains is believed to cause heterogeneous distribution of normal force on each part of the wall, for multiple same-test conditions.

Next, a flexible barrier is modeled using cylindrical elements. The impact on the barrier is modeled using the same flow model used for wall-impact problem. The use of energy dissipators is found to be essential for minimizing the impact force on the barrier, and thus controlling the force applied on the lateral anchors.

By comparing a rigid wall and a flexible barrier for the same flow, we found that the rigid wall is exposed to higher impact force, due its high global stiffness compared with the flexible barrier. Next, different simulations are carried out to recommend design guidelines for the flexible barrier. It is found that using a mesh size as large as D_{90} of the

flow is acceptable in terms of mass retaining capacity. In addition, not fixing the bottom cable of flexible barriers might lead to the total loss of its retaining capacity in extreme events.

Keywords:
Discrete Element Method, Debris flows, Rigid Walls, Flexible Barriers, Protection Structures, Force Chains, Granular Flows

Résumé

Les risques naturels tels que les laves torrentielles constituent des menaces réelles pour les zones urbanisées de montagne. Les bâtiments et infrastructures peuvent être exposés à de grandes forces d'impact en cas d'évènement extrême. La réduction de cette menace, par des ouvrages de protection, impose de quantifier l'impact de ces écoulements sur les structures, qu'elles soient flexibles ou rigides.

Tout d'abord, un écoulement granulaire sec, composé de particules non-sphériques glissant sur un plan incliné, est modélisé en utilisant une loi de contact visco-élastique avec critère de rupture de Mohr-Coulomb. Des données expérimentales de la littérature ont été utilisé pour calibrer et valider le modèle. À cette fin, la forme de la particule, l'épaisseur de l'écoulement et la forme finale du dépôt sur le mur sont considerés. La validation est basée sur l'impact sur un mur rigide divisé en six segments. La principale contribution de la force totale normale appliquée sur le mur est due à la composante dynamiques. La distribution hétérogène de la force normale sur chaque partie du mur est due au développement des chaînes de force différent pour chaque arrangement des particules.

Ensuite, un filet est modélisé en utilisant des éléments cylindriques. L'impact sur le filet est modélisé en utilisant le même modèle d'écoulement que précédemment. Le rôle des dissipateurs d'énergie apparaît essentiel pour réduire la force d'impact sur le filet et limiter la force appliquée sur les points d'ancrage latéraux.

Pour la première fois, des simulations montrent que pour un même écoulement granulaire la force d'impact est plus élevée pour un obstacle rigide, avec une différence de 50% par rapport à un obstacle flexible. les simulations permettent de définir quelques recommandation pour le dimensionnement des filets. Il est constaté que l'utilisation

d'un maillage de filet plus petit que D_{90} de l'écoulement est acceptable en termes de capacité à retenir les matériaux en écoulement. En plus, si le câble en bas du filet n'est pas fixé, le filet pourrait perdre totalement sa capacité de retenue.

Mots clés:
Modélisation par éléments discrets, Laves torrentielles granulaires, Écoulement granulaire sur plan incliné, Mur rigide, Structure de protection, filet de protection, Lignes directrices pour le design des filets

Abbreviations

A_c	Reference surface area of a cylindrical element
b_o	Bottom opening of a flexible barrier
D_{50}	Value of the particle diameter at 50% in the cumulative distribution
DEM	Discrete Element Method
des_1	A flexible barrier where the lateral cables are connected to energy dissipators which are then connected to lateral anchors
des_2	A flexible barrier where the lateral cables are directly connected to the lateral anchors
DG	Design guidelines
D_{lc}	Diameter of lateral cables
D_{mc}	Diameter of main cables
D_n	Diameter of the net elements
D_r	Diameter of sliding rings
E	Elastic modulus
E_b	Bending modulus
E_c	Elastic modulus of the cylindrical element
ED	Energy Dissipator
E_{kin}	Total kinetic energy
E_n	Elastic modulus of the net
E_{rot}	Rotational kinetic energy
$fbEd$	Flexible barrier with energy dissipators

fbG	A flexible barrier positioned in a direction parallel to the gravity vector
fbN	A flexible barrier positioned in a direction normal to the channel base
$fbNo$	Flexible barrier without energy dissipators
F_a	Mean values of forces on the two anchors located at the extremities of a given main cable
F_d	Dynamic component of the total normal force
F_{dead}	Force applied by dead particles on a protection structure
F_{ED-els}	Elastic limit of the forces in the energy dissipators in which afterwards it starts deforming
FEM	Finite Element Method
F_g	Gravitational component of the total normal force
F_i	Resultant force applied on particle i
$\mathbf{F_{int}}$	Interaction force
F_{mov}	Force applied by moving particles on a protection structure
$\mathbf{F_n}$	Normal contact force
F_r	Froude number
F_{res}	Residual force at the end of the impact
$\mathbf{F_t}$	Tangential contact force
F_{tot_n}	Total normal force
F_{tot_t}	Total tangential force
G	Weight of the dead zone
$\mathbf{G}$	Gravity vector
g	Gravity acceleration
G_{tw}	Shear modulus for the twisting moment
H	Filling height of debris flows behind protection structures
h	Flow depth
h_{ch}	Channel height

h_{cl}	Flow centerline
H_{dead}	Height of the dead zone behind a protection structure
H_{fb}	Flexible barrier height
h_i	Distance between the centroid of segment i of the wall and the chute base
H_{mov}	Height of the moving particles that are interacting with a protection structure
$h_{particle}$	Particle height
H_w	Height of the rigid wall
I_b	Bending moment of inertia
I_i	Moment of inertia of particle i
I_{tw}	Polar moment of inertia
K	Empirical factor related to the lateral earth pressure coefficient
k_b	Bending stiffness
k_i	Stiffness of a spring connecting two particles
k_n	Normal stiffness of the contact
k_t	Tangential stiffness of the contact
k_{tw}	Twisting stiffness
L_c	Length of a cylindrical element
l_{ch}	Channel length
$\mathbf{M_b}$	Bending moment
m_{dz}	Dead zone mass at a given time
M_i	Resultant moment applied on particle i
m_i	Mass of particle i
MPM	Material Point Method
$\mathbf{M_t}$	Twisting moment
m_{tot}	Total mass of the granular flow
n_p	Number of particles in the simulation
n_v	Number of particles in a targeted volume
PIV	Particle image velocimetry

r	Radius of a particle
R_c	Radius of the cylindrical element
R_i	Radius of particle i
$rigW$	Rigid wall
$\mathbf{R_1}$	Base reaction
$\mathbf{R_2}$	Wall reaction
R_{1t}	Sum of tangential contact forces between particles and the chute base
R_{1n}	Sum of normal contact forces between particles and the chute base
R_{2t}	Sum of tangential contact forces between particles and the wall
R_{2n}	Sum of normal contact forces between particles and the wall
$SDEC$	Spherical Discrete Element Code
S_m	Mesh size of the net
SPH	Smoothed-Particle Hydrodynamics
S_{vir}	Virtual sphere of the cylindrical element
t_c	Collision duration
u_n	Normal displacement (overlapping distance between two particles)
u_t	Tangential displacement
$\overline{U}_x$	Average flowing velocity in the direction of the flow
$\overline{U}_z$	Average flowing velocity in the direction perpendicular to the flow
$\dot{u}(0)$	Relative velocity before the collision
$\dot{u}(t_c^0)$	Relative velocity after the collision
v	Impact speed
$\overline{v}$	Depth-averaged velocity of the flow
V_{max}	Velocity of the flow at the time of maximum total normal impact force on the wall, measured for particles lying in distances from 40 to 50 cm away from the wall

V_s	Volume of a single D_{50}-particle of the granular sample
V_t	Total volume of the granular sample
w_{ch}	Channel width
W_{fb}	Flexible barrier width
WP	Work Package
$YADE$	Yet Another Dynamic Engine
$\dot{\omega}_i$	Angular velocity of particle i
$\ddot{\omega}_i$	Angular acceleration of particle i
x_i	Position of particle i
$\dot{x}_i$	Rotational velocity of particle i
$\ddot{x}_i$	Rotational acceleration of particle i
γ_s	Specific weight of gravel particles
γ_n	Normal visco-elastic coefficient
γ_t	Specific weight of the granular sample
ε_n	Normal restitution coefficient
λ	Empirical factor related to the hydrodynamic pressure
Δt	Time step
α	Inclination angle of the base of a channel
p_{dyn}	Hydrodynamic pressure
p_{stat}	Hydrostatic pressure
ρ	Flow density
ϕ	Microscopic friction angle
$\theta_{F_{tot}}$	Orientation of the total force applied by the flow
θ_{fb}	Angle between the initial position of the flexible barrier and the gravity vector
θ_{rc}	Ring-cable friction angle
δ_1	Angle of friction between the base and the dead mass
δ_2	Angle of friction between the wall and the dead mass
δ_{rc}	Friction angle between the main cables and the sliding rings

δ_{ED}	Mean value of deformation of the two energy dissipators installed at the ends of a given main cable
δ_{ED-brk}	Maximum allowable deformation of the energy dissipators
$\mathbf{\Omega}_{12}^{b}$	Bending component of the relative rotation between two spheres
$\mathbf{\Omega}_{12}^{tw}$	Twisting component of the relative rotation between two spheres
σ_{n}^{el}	Elastic tensile limit
σ_{s}^{el}	Elastic shear limit

Contents

List of Figures

List of Tables

Chapter 1

General Introduction

Contents

1.1 Landslides and debris flows: a threat to urbanization

Geohazards such as land slides and debris flows present a serious threat to communities and infrastructures, especially in mountainous areas. Landslides are usually triggered by heavy rainfalls which cause slope instabilities. Such instabilities, under the effect of gravity, cause landslides either partially or fully saturated which lead to the development of debris flows. As they flow down slopes, debris flows grow in volume due to the entertainment of the bed and catch the large blocks and trees along their way.

Landslides cause millions of dollars in damage and thousands of deaths and injuries each year as well as loss of productive land (Hervás, 2003). They are present all over the world, especially in Europe, east Asia and the coastal parts of the Americas. In Europe, in particular, great efforts have been given over the decades to tackle this problem. However, until now, several European countries are still exposed to high hazard of landslides (Fig 1.1) which cause disasters resulting in casualties and injuries and also huge damage to urbanized areas.

In Sarno (Italy), in 1998, large number of mudflows took place in the area following a heavy long-lasting rainfalls which triggered 150 landslides in 10 hours. Their destructive nature was due to their high flowing velocities (up to 14 m/s) and their total volume (several hundreds m^3). The event caused 160 fatalities in the affected municipalities. The total cost of the damage was estimated to be around 35 million euros including destroyed houses and infrastructure (Hervás, 2003). Other examples include Stoze landslide and the Predelica torrent debris flow (2000, Slovenia), San Miguel Island landslides (1997, Portugal), Vagnharad landslide (1997, Sweden) and Ionian coast landslides and debris flows (2009, Italy).

In response to these catastrophic events, researchers have developed theories and carried out physical and numerical modeling of landslides and debris flows in order to analyze their behavior and predict their occurrence. In an effort to deepen the understanding of debris flows, the European project MuMoLaDe started in 2012 to study landslides and debris flows from both experimental and numerical aspects in addition to modeling and design of debris flow mitigation structures.

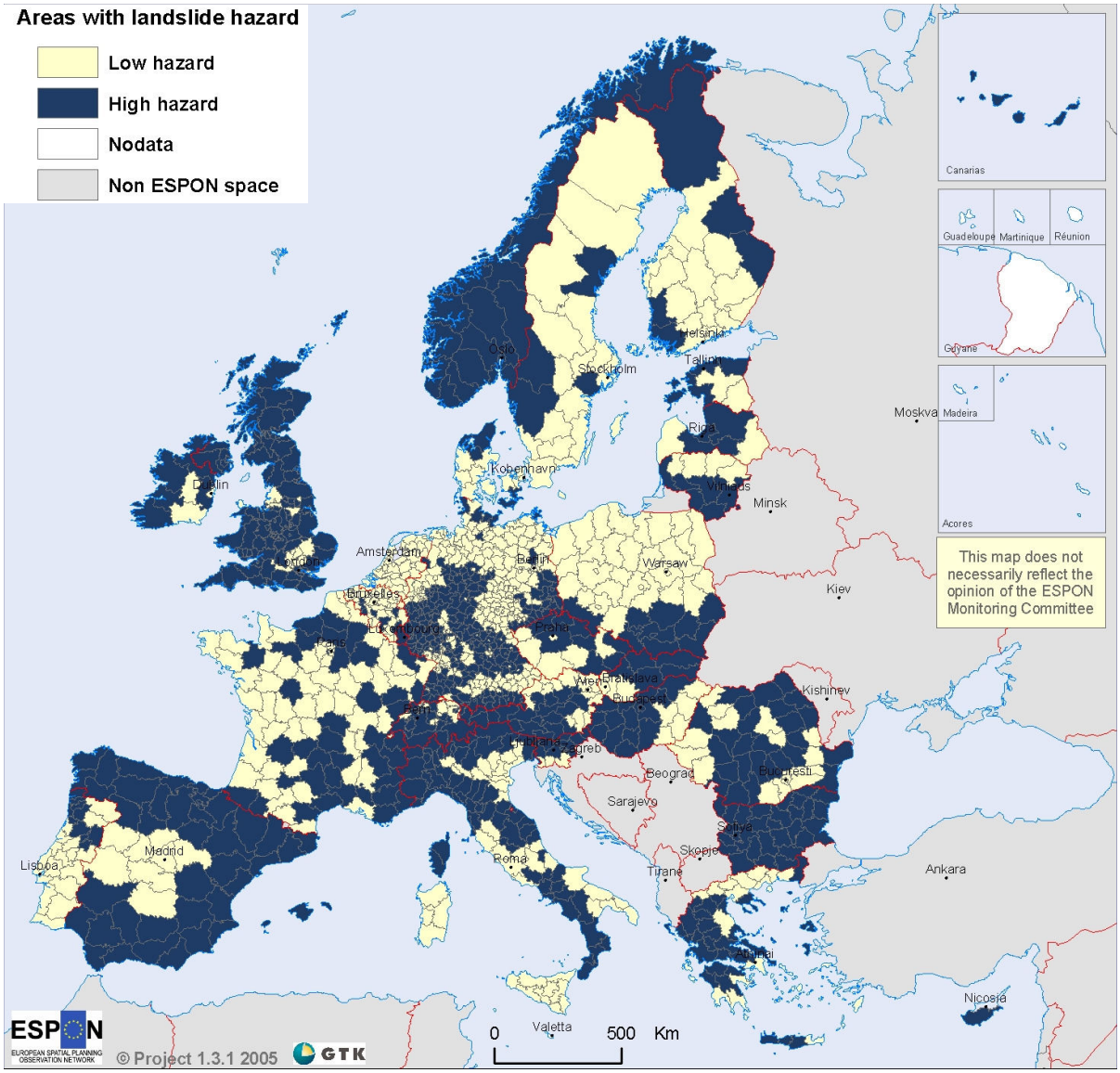

Figure 1.1: *Areas with landslide hazards, based on opinions of national experts of European Geological Surveys ((after ESPON, 2005), origin of data: EuroGeographics association for the administrative boundaries)*

1.2 Research framework (MuMoLaDe Project)

MuMoLaDe (Multiscale Modelling of Landslides and Debris Flows) is a European project within the framework of Marie Curie ITN (Initial Training Networks). It groups 13 full partners and 8 associated partners in a consortium including research institutes, universities, contractors, manufacturers and software developers. The overall aim of the project, in addition to the scientific outcome, is to provide high quality training for a group of young researchers. Such training will enable them to work in multidisciplinary research of natural hazards.

MuMoLaDe deals with the numerical and physical modeling of landslides and debris flows. 14 PhD students and 2 postdocs have been selected to study these phenomena. Their work covers the different stages of debris flow and landslides (Fig 1.2) by four work packages (WP):

- WP1: experimental testing to understand the material behavior (e.g. triaxial tests of soil samples)
- WP2: numerical (Finite element analysis) and physical modeling (centrifuge model tests) of slope stability failure to analyze the landslide initiation
- WP3: numerical (Finite Element and Discrete Element simulations) and physical modeling (rotating drum and inclined flume) of the evolution of debris flow in a channel
- WP4: the validation and design of structures protecting communities and infrastructure (numerical Discrete Element modeling)

The role of the this thesis, within the MuMoLaDe project, lies within work packages 3 and 4. This is because part of the work of this thesis deals with the evolution of channelized debris flow (WP3) while the other half deals with the impact and design of protection structures. This is achieved through the collaboration with other PhD students in the work package and also with other members of MuMoLaDe consortium.

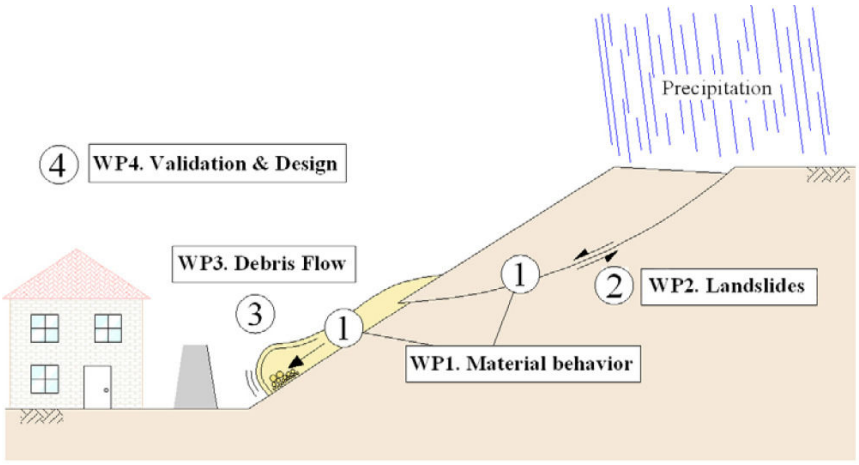

Figure 1.2: *The different stages of landslide and debris flow, divided into four work packages within MuMoLaDe project*

1.3 Thesis objectives

Debris flows can be classified, along other classifications, into two types: stony debris flows (coarse-grained debris flow) and muddy debris flows (fine-grained debris flow) (Takahashi, 2007). This thesis is concerned with the first type, in which stress is dominated by particle collision. This granular stony-type debris flow is approximated in the DEM model as a dry granular flow.

The thesis, based on numerical simulations using Discrete Element Method (DEM), has been divided into three stages. Each stage contributes to one year of the thesis three-years period. These stages are the following:

- Modeling of dry granular flow in inclined plane impacting a rigid wall. The objective of this part is to calibrate and validate a DEM model against experimental data of dry granular flow composed of gravel particles impacting a rigid wall. As a result, we will be able to account for debris-structure impact forces and estimate the micromechanical behavior of particles during the impact process.

- Modeling the different components of flexible barriers. The objective of this part is to be able to account for the behavior of different components of flexible barriers using DEM-based model. This is to investigate the behavior of flexible barriers when impacted by the dry granular flow model calibrated/validated in the first part.

- Parametric analysis, design guidelines and best practice. The objective of this part is provide recommendations for engineers concerning the best practice in designing flexible barriers, how to optimize retaining capacity and reduce the forces applied in the different components of flexible barriers.

1.4 Thesis structure

This Thesis is divided into five chapters: the first chapter has presented a general introduction of the thesis. In the second chapter, the state of the art concerning granular debris flows and protection structures is presented. Special attention is given to the physical and numerical modeling of granular flows in inclined planes. Moreover, the different numerical models proposed in the literature for modeling flexible barriers (for both rockfalls and debris flows) are presented. In addition, the Discrete Element Method (DEM) is presented showing its interaction calculating cycle and time step calculation.

In the third chapter, the modeling of a dry granular flow in inclined flume is presented. The experimental data used for model calibration and validation is detailed coupled with the effect of the shape of the particles on the results. Results concerning the impact force applied on a rigid wall are analyzed. Special attention is given to the evolution of the dead zone mass which controls the gravitational part of the total force on the wall. Afterwards, microstructural analysis are carried out to investigate the reason behind the presence of microstructural heterogeneities in the impact results. The effect of the size of the particles on the total normal force signal is also analyzed.

In the fourth chapter, the impact of granular flows on flexible barriers is investigated. First, the DEM-based model used to simulate the different components of flexible barriers is presented. Afterwards, the different components forming the flexible barriers are described along with their validation. Then, full scale simulations are carried out to present the model's prediction of the impact behavior and the importance of the presence of energy dissipators for flexible barriers. Results concerning total impact force, forces in the anchors and load transmission within the barrier are comparatively analyzed. Parametric analysis are carried out at the end demonstrating the effect of the inclination angle of the bed on the impact force applied on the barrier and the rate of dead zone formation.

In the fifth chapter, impact estimation models used by designers of debris flow protection structures are compared with the DEM model in terms of the impact force applied by the flow. Next, the difference is highlighted between rigid and flexible structures when impacted by the same granular flow. Afterwards, the dimensioning of flexible barriers is investigated in terms of the net mesh size and the bottom opening of the barrier. Next, the initial configuration of flexible barriers are investigated. Finally, conclusions and perspectives are globally drawn from the thesis outcomes.

Chapter 2

State of the art

Contents

2.1 Introduction

In this chapter, the previous works on granular flows and protection structures are presented. For granular flows, special attentions is given to numerical and physical modeling of granular flows in inclined planes. Then, experimental and numerical modeling of the impact of granular flows on rigid walls is highlighted. Afterwards, different numerical schemes proposed for modeling flexible barriers are presented, showing the difference between the two main schemes Finite Element Method (FEM) and DEM. Next, debris flow impact models used by engineers are briefly presented along with the guidelines for designing debris flow flexible barriers. Finally, the numerical method used in this thesis (DEM) is detailed with its time step calculation, contact detection, and the implemented open source code (YADE).

2.2 Debris flows

Debris flows have been classified as one of the most hazardous landslides due to their high flow velocity and impact forces, long runout distance and poor temporal predictability (Jakob and Oldrich, 2005). Scientists started studying the problem from a mechanical point of view in the late 1960's as, prior to this date, studies of granular flows were wholly empirical (Iverson and Denlinger, 1987). They define debris flows as a flow of sediment and water mixture resembling continuous fluid driven by gravity in which large saturated voids give their mobility (Takahashi, 2007). After being triggered, coarse debris accumulates at the front due to grain size segregation while the rare part of the debris is finer with richer water content. Lateral levees are then formed where the debris is found to deposit in alluvial fans (Hubert and Filipov, 1989; Iverson, 2003).

Researchers adopted different techniques for the physical modeling of this phenomena including rotating drums, centrifuge testing and inclined planes. On the numerical side, different approaches have been adopted including FEM, DEM, Material Point Method (MPM), Smoothed-particle hydrodynamics method (SPH) and other numerical schemes.

In the following sections, the previous work carried out for physical and numerical modeling of granular flows will be highlighted with special attention given to DEM modeling of granular flows, as it is the most relevant to this PhD thesis.

2.2.1 Physical modeling of granular flows

In the effort of reproducing granular flows behavior, various experiments have been conducted ranging from studies on geological debris flows to well characterized laboratorial granular flows down an inclined plane (Campbell et al., 1995; Azanza et al., 1999; Davies and McSaveney, 1999; Okura et al., 2000; Lemieux and Durian, 2000; Iverson et al., 2004; Friedmann et al., 2006; Goujon et al., 2007; Pudasaini et al., 2007; Valentino et al., 2008; Manzella and Labiouse, 2009). Several materials have been used varying from sand (Chu et al., 1995) to ping-pong balls (Keller et al., 1998).

Hutter et al. (1995) used spherical glass beads and different chute geometries (inclination angles of 30 , 40 and 50°) to carry out laboratory experiments of granular flows down rough curved beds in order to study the motion of landslides. Observations were taken for the length and flowing velocity of the created avalanches. They were then compared and found to agree with the simple equations proposed by Savage and Hutter (1991). Results were found to be insensitive to the numerical value of internal friction angle while they were critically sensitive to bed friction angle.

Others studied the initiation of motion of granular materials on inclined planes. For example, Pouliquen and Renaut (1996) investigated the critical angle in which granular materials on inclined rough surface would start flowing, by slowly inclining the bed. The internal friction angle was found to be greater near the surface than within the sample since the critical angle was found to increase by decreasing the height of the sample. This was connected to the dilatancy occurring for the material when it starts flowing. These results were found to be valid for both 2D cylinders and 3D glass beads.

Later on, Azanza et al. (1999) experimentally studied collisional flow of granular material down inclined planes. The aim of the study was to analyze the predictions and assumptions of kinetic theories that are used to describe such flows (Campbell, 1990).

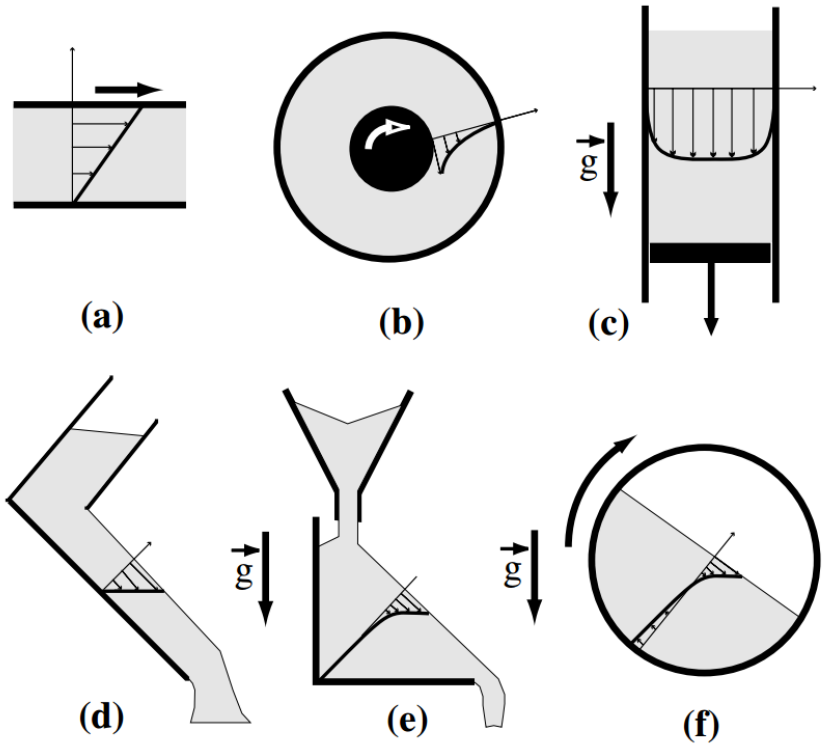

Figure 2.1: *The six investigated configurations of granular flows:* ***(a)*** *plane shear,* ***(b)*** *annular shear,* ***(c)*** *vertical-chute flows,* ***(d)*** *inclined plane,* ***(e)*** *heap flow,* ***(f)*** *rotating drum (after MiDi, 2004)*

Concerning dense granular flows, MiDi (2004) extensively investigated the behavior of dry grains undergoing continuous shear deformation, from both experimental and DEM modeling points of view. Different configurations were tested including annular shear cell, silos, inclined planes and rotating drums (Fig. 2.1). The aim was to get to coherent presentation of different quantities characterizing such flows, as flowing thresholds, kinematic profiles and effective friction. In this enormous work, the flow was found to start only after the driving force overcome threshold static value. Moreover, a wide diversity of velocity profiles was present. The shear is localized for confined flows and velocity decreases near the walls. For perfect plane shear, velocity profile remains linear. Bagnold or linear velocity profiles were present for free surface flows.

2.2.2 Numerical modeling of granular flows in inclined planes

Several researches have been carried out in order to model the flow of granular materials in inclined planes. On one hand, continuum treatment has often been adopted where flows characteristics are analyzed by the Eulerian forms of continuity and momentum equation (Hungr, 1995; Hutter et al., 1995; Gray et al., 1999; Azanza et al., 1999; Pudasaini and Hutter, 2003; Pitman et al., 2003; Pitman and Le, 2005; Pudasaini et al., 2005a; Pudasaini and Hutter, 2007; Moriguchi et al., 2009).

Savage and Hutter (1989) described the avalanching body in inclined planes as a finite mass of incompressible cohesionless granular continuum which is strongly affected by Coulomb-type yield both in the interior and at the base of the channel. A Lagrangian finite difference scheme was used for the numerical integration of the depth-averaged equations. They then verified the model by comparison with experimental data of granular flow in inclined (and then curved) chute (Hutter et al., 1995).

On the other hand, DEM is a powerful method in describing granular flows motion where the motion is modeled as an assembly of discrete particles obeying the basic laws of motion (Buchholtz and Pöschel, 1998; Teufelsbauer et al., 2009). They are advantageous when the granularity of the flowing material is concerned. The avalanche is approximated by a set of particles of simple geometrical forms (disks/cylinders, spheres). DEM is able to reproduce effects far beyond the reach of continuum models (Taboada and Estrada, 2009), such as inverse segregation (Calvetti et al., 2000) or grain breakage. In addition, the number of material parameters is rather small, making the numerical model easier to calibrate. Moreover, the spheres (in 3D) or disks (in 2D) can be combined to form more complex shapes of particles, and specific geometries can be generated (Pastor et al., 2014).

Silbert et al. (2001) carried out 2D and 3D simulations of mono-dispersed particles flowing in a steady-state condition where observations were taken regarding structure and rheology of the flow (Fig. 2.2). DEM was also used to simulate a rock avalanche event that took place in Italy, where comparison were made based on the position and shape of the avalanche in order to approximate the avalanche run-out (Calvetti et al., 2000).

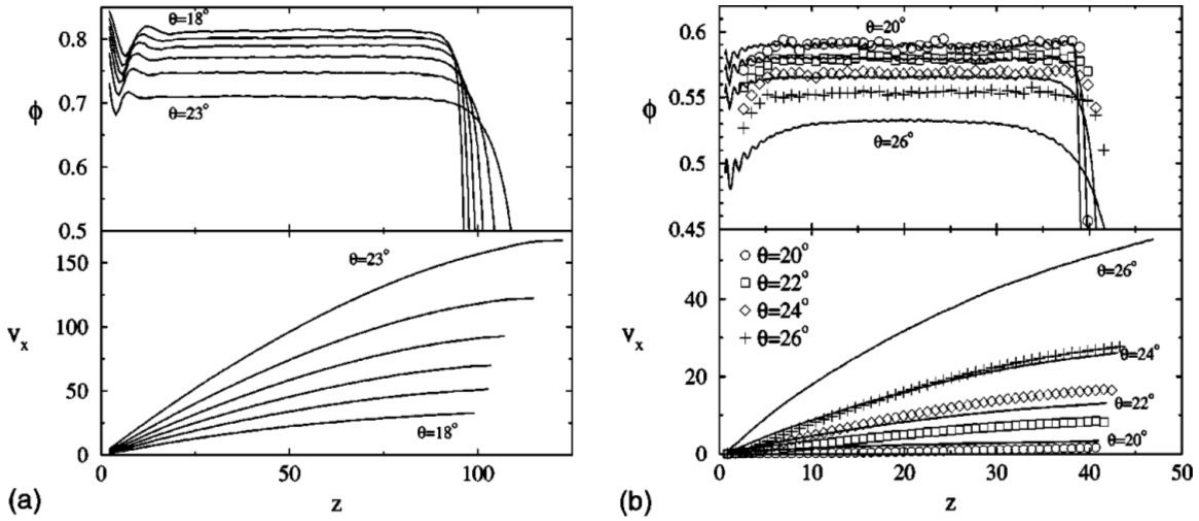

Figure 2.2: *Profiles of the solid fraction and the velocity in the direction of the flow, as a function of the distance from the channel base:* ***(a)*** *2D simulation,* ***(b)*** *3D simulation (after Silbert et al., 2001)*

2.3 Rigid walls for debris flow hazard mitigation

Check dams are one of the most common types of rigid walls for mitigating debris flows and controlling the sediment transport associated with their movement (Takahashi, 1991; Armanini et al., 1991; Jakob and Oldrich, 2005; Remaitre and Malet, 2010). They are usually constructed in series in the transportation zone of the debris in which they help in reducing slopes of channels and the flowing velocity subsequently. By doing so, they help in reducing the kinetic energy of debris flows and thus limit their hazard. In addition, they are effective in minimizing the entrainment along the stream, which in turn reduces the evolution of the mass of the debris along its path.

Although check dams are widely adopted in practice, their efficiency in stopping a debris event of an anticipated size maybe limited if dams have been previously filled up with sediment transport by several small-scale debris. This is anticipated in cases where frequent removal of the debris is not feasible due to economic and technical consideration. Thus, if check dams are adopted, there is a a need for further measures to be take in case the dams are filled.

In the following sections, previous physical models of granular flows impacting rigid walls are presented. Afterwards, the corresponding numerical models of the problem are discussed.

2.3.1 Physical modeling of granular flows impact on rigid walls

With the accumulative understanding of granular flows in experimental inclined chutes, researchers focused on analyzing the impacts of such flows on obstacles, for both fundamental and applied research purposes. Pudasaini and Kröner (2008) investigated shock waves propagation of rapid flowing dense granular flows. Such waves were propagating after the dry granular flow impacted a vertical wall at the end of a steep inclined chute. A regime change was observed in which the flow changed from being fast-thin supercritical flow to a thick stagnant heap with varying thicknesses. Results of measured shock position and the maximum velocity along the channel were compared and found to very well agree with theoretical predictions based on frictional granular flow equations.

The investigation of granular flows impact on obstacles also included the physics of flows overflowing obstacles. Faug et al. (2002) experimentally investigated the dead zone formation of glass beads behind an over-passed obstacle down an inclined rough chute. The dead zone (Fig 2.3) is the zone where dead particles deposit in quasi-static condition behind the wall (Caccamo et al., 2012). Observations were taken for the length of the dead zone behind the obstacle for different slope angles and obstacles height, and was correlated with the Froude number of the flow (F_r). Froude Number is a dimensionless parameter used to indicate the influence of gravity on fluid motion (Pudasaini and Domnik, 2009; Domnik and Pudasaini, 2012; Faug et al., 2012). It measures the ratio between the inertia force on a fluid element to the weight of that element, and is calculated as follows:

$$F_r = \frac{\overline{v}}{\sqrt{g\, h\, cos\alpha}} \tag{2.1}$$

where $\overline{v}$ is the depth-averaged velocity of the flow, g is the gravity acceleration, h is the flow depth and α is the inclination angle of the base.

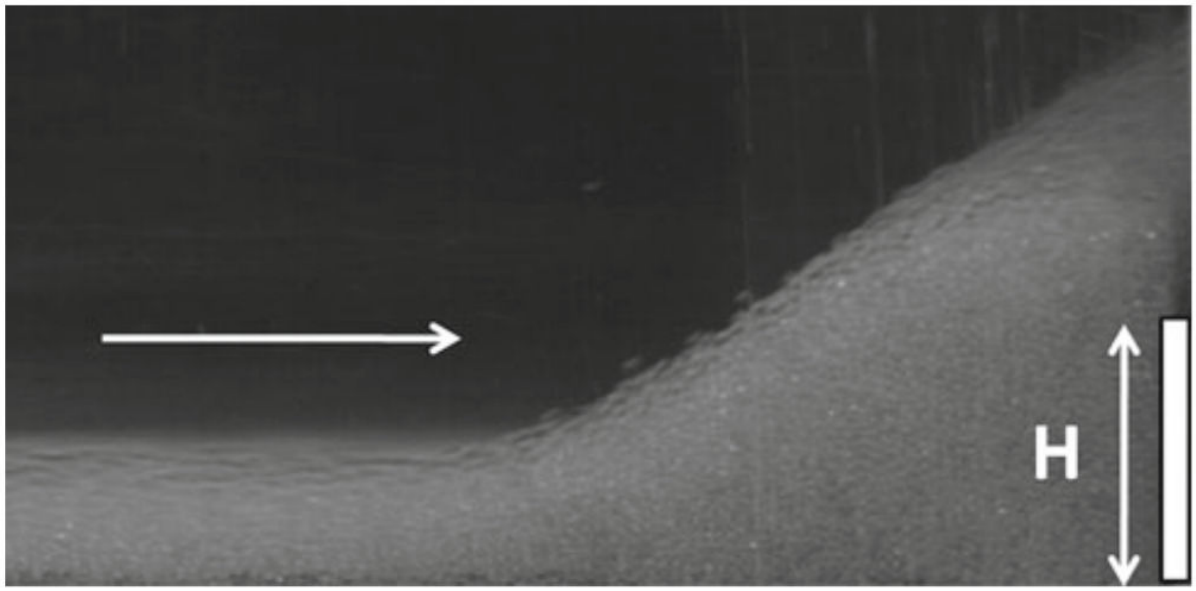

Figure 2.3: *A triangular dead zone is formed upstream of a rigid wall in which moving particles overflow it. The white horizontal arrow indicates the incoming flow direction which is made of glass beads (after Caccamo et al., 2012)*

The length of the dead zone was found to increase when increasing the obstacle height, especially for low values of the inclination angles. Low values of α reduce the overflowing of the obstacle and thus increase the dead zone length. The dead zone formation will be investigated in details in the following chapters, due to its importance in characterizing the flow and impact behavior of granular flows.

Faug et al. (2011) continued investigating the dry granular flows over-topping obstacles in inclined channels. First, the flow velocity and thickness were measured (in the absence of an obstacle) and dimensionlessly verified with MiDi (2004). Then, the impact force applied by dry granular flow (made of glass beads) on an overrun rigid wall was measured in the normal direction with time. The aim was to compare these results with a set of equations forming a hydrodynamic model, based on depth-averaged momentum conservation. The model takes into account the dead zone formation behind the wall and the inertial flow zone above it, and can thus predict the force applied on the wall with time (Faug et al., 2009; Chanut et al., 2010). The model's prediction of the normal force applied on the wall, with its different components, was found to reproduce well the experimental data.

The previous works using glass beads helped in giving an insight into the physics of dry granular flows and their impact on obstacles. However, others carried out experiments with real granular material (sand, gravel ..etc). Jiang and Towhata (2013) recently studied the impact behavior of dry granular flow against a rigid retaining wall using a poly-dispersed mixture of limestone gravel. Measurements of normal impact force versus time were recorded for different heights of the wall, i.e different segments forming the wall. In addition, observations of flow thickness and flow velocity were taken at the time where the total normal force on the wall reached its maximum value. These experimental data were selected for our model calibration and validation. This is because it considers elongated coarse-grained flow of angular particles rather than the simple spherical glass beads commonly used in literature. Such large-sized particles resemble a granular debris flow (coarse-grained debris) which is the aim of this thesis. In addition, the study provided detailed measurements of the time evolution of the normal impact force for different heights (different segments of the rigid wall). More details on this experiment will be given in Chapter 3.

2.3.2 Numerical modeling of granular flows impact on rigid walls

DEM has been an active method in recent years for studying the impact of granular flows on rigid walls. Faug et al. (2009) used 2D DEM simulation of spherical particles flowing in inclined channel and overflowing a rigid wall to verify their hydrodynamic model based on depth-averaged momentum conservation. In the DEM results, the normal force applied on the wall was characterized with high fluctuations due to the force chains developing in the dead zone behind the obstacle. These fluctuations are common feature of DEM modeling of impact forces. They are usually dealt with by averaging the data over small windows (Valentino et al., 2008).

Researchers also used non-spherical shape for modeling granular flows. Mollon et al. (2012) used non-spherical particles in DEM to numerically investigate the propagation of granular masses down a slope where energy evolution was studied along with run-out mechanism. The model was validated against experimental granular flow data. Due to the limited number of particles permitted by DEM for cost considerations, the model is

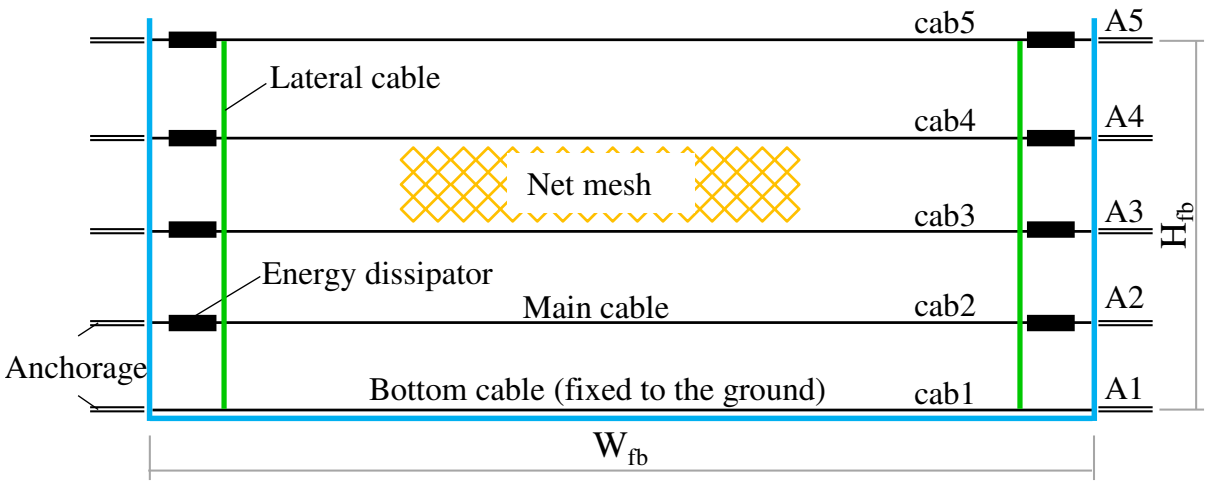

Figure 2.4: *Schematic representation of the different parts of flexible debris flow barriers*

suited for small to medium sized volumes. Continuum models cannot reproduce such small sized cases involving small number of blocks as the assumption of continuous kinematic field becomes too strong.

2.4 Flexible barriers for debris flows retention

Flexible barriers are ideal for stopping debris flows due to their high deformation capacity and their water permeability (Guasti et al., 2011). In addition, in comparison with rigid walls, they distribute the impact energy over longer impact duration and thus reduce the peak impact force (Boetticher et al., 2011). Furthermore, they are advantageous for their short construction times and ease of installation in hard-to-reach terrains. Flexible barriers for debris flows mitigation are mainly composed of net elements, sliding rings, main cables, lateral cables, energy dissipators and lateral anchors (Fig. 2.4), where a good design evaluates the forces in each component. One flexible net barrier system can retain up to 2000 m^3 of debris (Wendeler et al., 2008).

2.4.1 Flexible barriers: Rockfalls Vs. Debris flows

Flexible barriers for debris flows are similar in principle to the ones of rockfalls. However, their design is different due to the difference in their loading mechanism (Segalini et al., 2013). For rockfalls, an energy approach is adopted for the design assuming that the kinetic energy of the boulder is instantaneously transferred to the barrier which completely stops the boulder. In contrast, for debris flow flexible barriers, energy dissipation is rather gradual and thus the design approach can not be solely dependent on energy balance since the barrier loading rate can be heavily influenced by flow velocity, duration of impact .. etc. Moreover, rockfalls apply very high concentrated load at the impact point, while debris flow apply uniform load over the surface area of the barrier. As a result, different design approach better be adopted for debris flow flexible barriers as they are different in loading rate and induced stresses.

Another drawback of energy approach for debris flow flexible barriers design is that it is too conservative as it does not take into account the energy dissipated by collision due to the formation of dead zone behind the barrier (Segalini et al., 2013). In a recently published guidleinse (Volkwein, 2014), this approach has been unfavored for debris flow flexible barriers design.

Instead of energy approach, the force approach can be used for the design of debris flow protection barriers (Wendeler, 2008; Segalini et al., 2013; Volkwein, 2014). It is based on the determination of the impact force applied by the flow and consequently comparing them to the barrier resistance to impact forces. The impact force is assumed to have three components: static force (due to the weight of the material), dynamic force (due to kinetic energy of the flow) and a shear force on the top cable of the barrier (in case of overflowing). More details on load estimation models on protection structures, based on the force approach, will be presented in Section 2.5.1.

2.4.2 Numerical and physical modeling of flexible barriers

The use of numerical modeling of flexible barriers enabled a more innovative design of these barriers. This is because such simulations reduce the number of required physical prototype and can test loading conditions that sometimes can not be tested on-site due to some technical and economical challenges (Volkwein, 2005). In addition, numerical modeling of flexible barriers can analyze the loads in each component, and test innovative designs accordingly (e.g. Bertrand et al., 2012).

For the aim of modeling flexible barriers, two numerical methods have been mainly used: FEM (Cazzani et al., 2002; Castro-Fresno et al., 2008; Gentilini et al., 2012) and DEM (Nicot et al., 1999, 2001; Bertrand et al., 2008, 2012; Bourrier et al., 2015). Volkwein (2005) developed an FEM-based software named "FARO" to model highly flexible barriers (made of ring nets) against rockfall impact. The software was calibrated against quasi-static and dynamic laboratory and field experiments and validated against data of full scale testing (Grassl, 2002).

Gottardi and Govoni (2010) carried out full scale experiments of rockfall impact on flexible barriers with kinetic energies from 500 to 5,000 kJ. Such data formed an extensive database for the calibration of numerical models of rockfall flexible barriers. Detailed results were obtained concerning the boulder breaking time, evolution of the kinetic energy, the barrier deformation and the forces applied on the anchorage and post foundations. Gentilini et al. (2012) later on used these experimental data to calibrate and validate an FEM based numerical model of rockfall flexible barriers (Fig. 2.5). The falling boulder was simulated as a set of lumped masses using the commercial software ABAQUS. Connecting cables were modeled as elasto-plastic, behaving bi-linearly.

On the other hand, DEM as a more recent numerical method, was recently deployed for modeling flexible barriers. DEM is well adapted to describe the behavior of granular materials whereas FEM is mostly dedicated to modeling continuous media. Large displacements and failures between elements are easy to simulate and thus DEM is very well suited to model protection nets where important strains and failure may occur during a loading test.

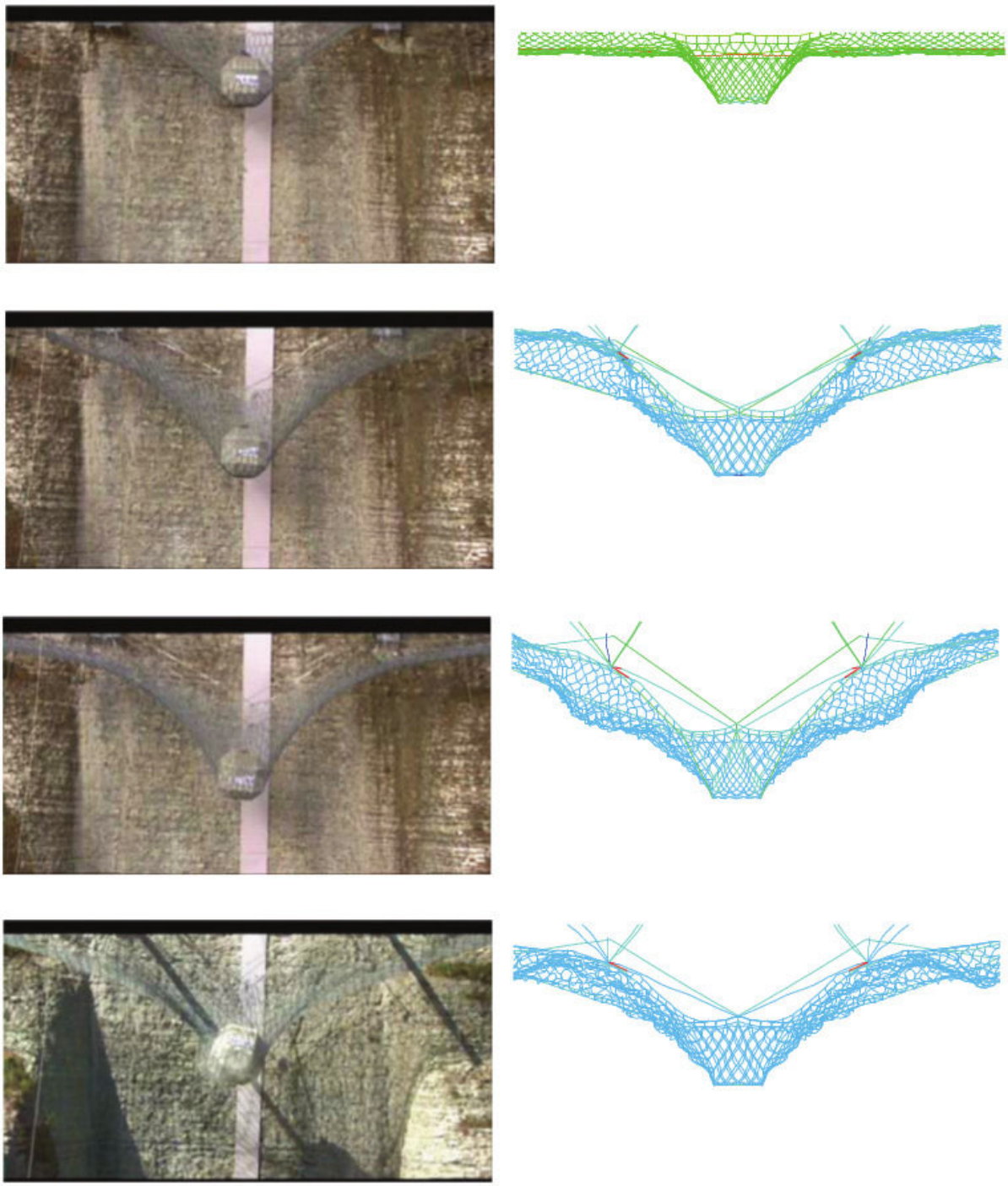

Figure 2.5: *Snapshots at different time of falling boulder intercepted by a flexible barrier: FEM Numerical simulation (right) compared with photograms (left) (after Gentilini et al., 2012)*

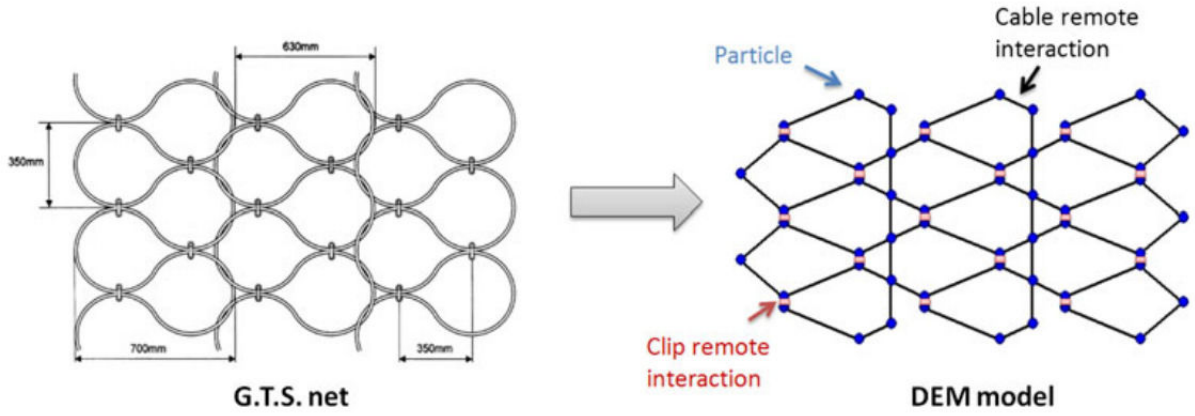

Figure 2.6: *DEM modeling of a net using remote interactions (after Bertrand et al., 2012)*

The first attempt to model rockfall fences using DEM was carried out by Mustoe and Huttelmaier (1993), who used rigid connecting bodies in DEM to approximate a rockfall fence made of truck tires. The fence was composed of a horizontal steel rod in which several hanging columnar attenuator masses composed of used tires where hanging on it.

Later, Hearn et al. (1995) and Nicot et al. (2001) used DEM to develop a model for highly flexible rockfall barriers where the approach was proved to be relevant in capturing the dynamics of the impact of a rockfall on flexible barriers made of ring nets. Afterwards, other types of nets were efficiently modeled in DEM, including for example hexagonal meshes (Bertrand et al., 2008; Thoeni et al., 2011).

An example of the recent DEM models of flexible barriers is the work of Bertrand et al. (2012), who modeled the net elements using remote interactions between nodes. These nodes are spherical particles placed at the intersection between the cable forming the net and the rigid clips. After detecting the contact, an elasto-plastic contact model is applied, for both loading and unloading phases. For the aim of calibrating the model, micro and meso scale experiments on single cables and punching tests of net meshes were carried out. The model was easy to calibrate as it only includes two parameters to fit: the stiffness and ultimate strength of the system. The model was then used to investigate the impact of a rigid boulder on a full-scale flexible barrier, using different loading conditions.

Although the aforementioned DEM models were successfully suitable for rockfall protection barriers, their suitability for modeling the impact against granular flows is questionable. Most DEM model for flexible barriers represent the intercepting components of the barrier with nodes which interacts remotely. Such type of interaction might lead to some particles of the flow to unrealistically go through the net. In addition, numerical roughness will be present between the different nodes. Thus, there is a need to use DEM as a powerful tool but in an innovative way in order to model debris flow flexible barriers.

In this thesis, DEM method is adopted as a numerical method, due to the numerous advantages mentioned in the previous sections concerning modeling the granular flow, rigid walls and flexible barriers. The method will be presented in Section 2.6 in addition to the open source code YADE. The numerical model of the impact of the granular flow on a rigid wall will be detailed in Chapter 3. The numerical model used for modeling the flexible barrier will be presented in details in Chapter 4.

2.5 Debris flow impact models for engineers and design guidelines

2.5.1 Debris flow impact models for engineering purpose

Although a complex phenomenon, the impact of debris flows on protection structures have been simplified for engineering purposes, which is mainly for the sake of designing these structures (Scheidl et al., 2013).

In general, practical impact models for engineers consider two types of impacting mechanisms. The first is the hydraulic mechanism which considers the impact to be caused by a bulk fluid-like flow (Hübl et al., 2009). On the other hand, the second considers the point-wise impact loading due to the coarse solid particle collision (Hu et al., 2011). In some guidelines (e.g. Volkwein, 2014), the hydraulic models has been adopted for design purposes which can be divided into hydrostatic and hydrodynamic models.

Hydrostatic models (e.g. Armanini, 1997) consider the horizontal pressure (with respect to the channel base) applied by the debris on the structure. The hydrostatic pressure p_{stat} applied by a debris flow is generally written as follows:

$$p_{stat} = KH\rho g \tag{2.2}$$

where K is an empirical factor, H is the filling height, ρ is the flow density and g is the gravity vector. Several studies suggested values for K ranging sometimes from 2.5-7.5 for vertical walls.

On the other hand, hydrodynamic models consider the peak force applied on structures as a factor of the kinetic energy per unit volume of the flow. The hydrodynamic pressure p_{dyn} is generally written as follows:

$$p_{dyn} = \lambda\rho v^2 \tag{2.3}$$

where v is the impact speed and λ is an empirical factor. Different values of λ have been considered in the literature depending on the type of the flow. The value of λ was taken as 2 for laminar and find grained material (Watanabe and Ikeya, 1981). Higher values of λ were taken for coarse grained debris flow, ranging from 3 - 5 (Zhang, 1993). In her PhD thesis, Wendeler (2008) recommended values of λ between 0.7 - 2 based on experimental and numerical modeling of debris flows impact on flexible barriers.

In Chapter 5, both the hydrodynamic and hydrostatic models will be tested against DEM impact results. Special attention will be given to the values of K and λ in both models highlighting the mechanics behind the difference observed for each.

2.5.2 Design guideliens of flexible debris flow mitigation barriers

Design guidelines of flexible debris flow mitigation barriers have generally focused on the impact models used to estimate debris flow impact, similar to the ones mentioned in the previous section. Lo (2000) provided detailed review of the methods suggested in the literature for estimating debris impact loads for engineering design. In addition, other recommended measures in the literature were also briefly reviewed, such as the improving retention capacity of flexible debris flow barriers.

Recently, Volkwein (2014) recommended guidelines for the design of debris flow flexible barriers. Load estimation equations of the hydrostatic and hydrodynamic pressures are presented along with values of the coefficients K and λ. The guidelines also present recommended values for parameters affecting the retaining capacity of the barriers. The mesh size of the net is recommended not to exceed D_{90} of the incoming debris flow. In addition, based on small-scale experiments (Wendeler and Volkwein, 2015), the bottom opening of the barrier should not exceed D_{90}. These recommendations will be compared with the DEM model in Chapter 5 of the thesis.

2.6 Discrete Element Method for modeling granular assemblies

Since granular materials are distinguishably discrete in nature, it is more adequate to model them using discrete models. The Discrete Element Method was first introduced by Cundall (1971) and then extended by Cundall and Strack (1979). DEM based simulations are efficient in reproducing the experimental behavior of granular materials. Moreover, they are advantageous in investigating the micro-scale phenomena, which are most often expensive or hard to characterize in experiments. Numerical simulations in DEM combine different concepts related to the discrete geometry of granular material, physical theories and numerical calculations. Forces are calculated at micro-scale at the point of interaction between two particles. From that scale, investigations on the relation between that scale and the macro-scale are possible leading to the developments of new theories and the optimization of industrial processes (e.g. particles flow in silos).

2.6.1 Calculation cycle in DEM

A finite difference scheme is used in DEM in which the position of the particles is calculated by integrating Newton's second law of motion over a time step Δt. The calculation cycle in DEM starts, after creating the geometry of the problem, by detecting the contact between the different bodies (Fig 2.7). Afterwards, the interaction force between each two bodies is calculated. This force is decomposed into a normal component acting in the direction of the normal vector and a tangential component acting in the contact plane. The contact law chosen is applied at the contact in which the two components are calculated according to the relative normal and tangential displacements and the

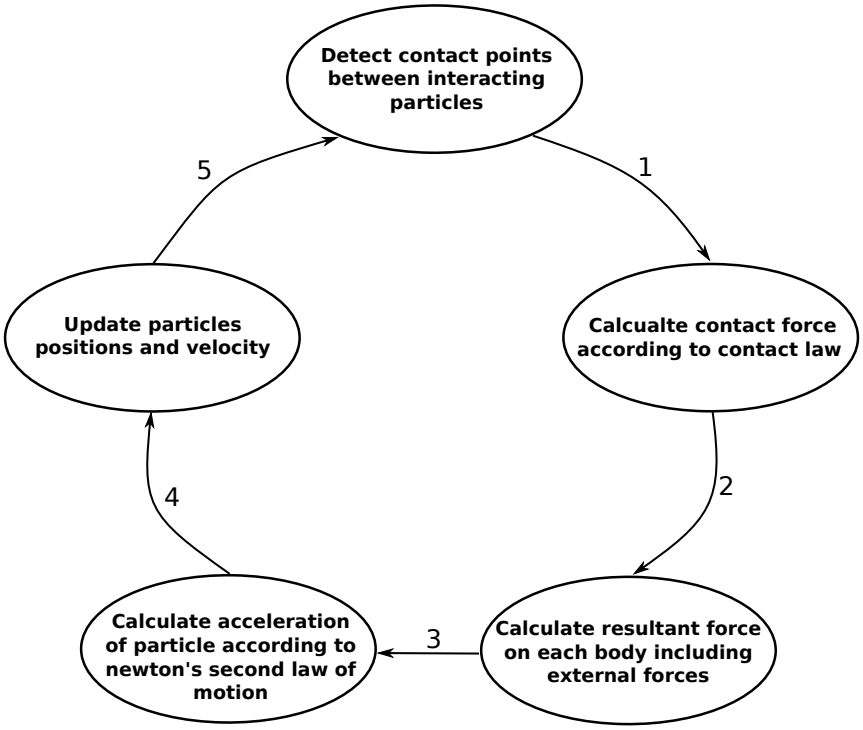

Figure 2.7: *Calculation cycle in DEM*

normal and tangential stiffnesses. Afterwards the acceleration of each body is calculated using Newton's second law of motion. The velocity and position of each particle is then calculated by integrating its acceleration. The position of each particle is then updated and contacts between bodies are detected and the cycle starts again.

The algorithms used in the calculation cycle can be illustrated in the following simple example:

For a rigid body with a position x_i and radius R_i, we can define its transnational motion by its velocity $\dot{x}_i$ and acceleration $\ddot{x}_i$. The rotational motion is defined by the angular velocity $\dot{\omega}_i$ and the angular acceleration $\ddot{\omega}_i$. $\ddot{x}_i$ is calculated from equation of transnational motion as:

$$F_i = m_i \, \ddot{x}_i \tag{2.4}$$

Where F_i is the resultant force applied on particle i and m_i is its mass.

Similarly, $\dot{\omega}_i$ is calculated from equation of angular motion as:

$$M_i = I_i \, \ddot{\omega}_i \tag{2.5}$$

Where M_i is the resultant moment applied on particle i and I_i is its moment of inertia ($I_i = \frac{2}{5} \, m_i \, R_i^2$).

Next, central finite difference scheme is adopted to integrate the transnational and angular acceleration over a time step Δt assuming that they are constant over the period $t - \frac{\Delta t}{2}$ and $t + \frac{\Delta t}{2}$. The velocities at $t = t + \frac{\Delta t}{2}$ are:

$$\dot{x}_{i,t+\frac{\Delta t}{2}} = \dot{x}_{i,t-\frac{\Delta t}{2}} + (F_{i,t}/m)\Delta t \tag{2.6}$$

$$\dot{\omega}_{i,t+\frac{\Delta t}{2}} = \dot{\omega}_{i,t-\frac{\Delta t}{2}} + (M_{i,t}/I)\Delta t \tag{2.7}$$

The new position of the particle is given by:

$$x_{i,t+\frac{\Delta t}{2}} = x_{i,t} + \dot{x}_{i,t+\frac{\Delta t}{2}} \Delta t \tag{2.8}$$

$$\omega_{i,t+\frac{\Delta t}{2}} = \omega_{i,t} + \dot{\omega}_{i,t+\frac{\Delta t}{2}} \Delta t \tag{2.9}$$

Afterwards, for the next cycle new values of $F_{i,t+\Delta t}$ and $M_{i,t+\Delta t}$ are used to get the new acceleration.

2.6.2 Critical time step in YADE

In order to insure the stability of the numerical simulation in DEM, the time step should be sufficiently small. Otherwise, particles will be excessively penetrated resulting in too large forces applied to spheres and the system will become unstable (exploding nodes). Thus, the choice of the value of the time step is very important in DEM.

In a general mass-spring system, the highest frequency occurs if two connected masses m_i and m_j are in opposite motion (Šmilauer et al., 2010). If the two particles have equal velocities (which is conservative) and they are connected by a spring with a stiffness k_i, a displacement Δx_i of particle i will be accompanied by a displacement $\Delta x_j = -\Delta x_i$ of particle j and that $\Delta F_i = -k_i(\Delta x_i - (-\Delta x_i)) = -2k_i \Delta x_i$. That results in apparent stiffness $k_i^* = 2k_i$, in which that maximum eigenfrequency of the whole system would be:

$$\omega_{\max} = \max_i \sqrt{K_i^* / m_i}. \tag{2.10}$$

The overall critical time step is then:

$$\Delta t_{cr} = \frac{2}{\omega_{\max}} = \min_i 2\sqrt{\frac{m_i}{k_i^{(*)}}} = \min_i 2\sqrt{\frac{m_i}{2k_i}} = \min_i \sqrt{2}\sqrt{\frac{m_i}{k_i}} \tag{2.11}$$

Equation 2.11 will be used in the simulations presented in this thesis to calculate the minimum stable time step.

2.6.3 YADE-DEM code

YADE (*Yet Another Dynamic Engine*) DEM code is used in the framework of this thesis (Šmilauer et al., 2010). It is a result of the development of the previously-existing code SDEC (*Spherical Discrete Element Code*) at the University of Grenoble. YADE is an extensible open-source framework for discrete numerical models, focused on Discrete Element Method. The computation parts are written in C++ using flexible object model, allowing independent implementation of new algorithms and interfaces. Python is used for rapid and concise scene construction, simulation control, postprocessing and debugging. YADE is becoming more widespread in the research community both nationally and internationally

Chapter 3

Dry granular flow impacting a rigid wall

Contents

3.1 Introduction

In this chapter the numerical model for simulating the granular flow is presented in details. First, the experimental data used for calibration and validation is described. Next, equations describing the contact law are presented along with defining their parameters. Afterwards, the model calibration is presented in details, which is mainly based on the shape of the particle, the flow thickness and the final shape of the deposit on the wall. After calibration, the model is validated against experimental data for impact tests of dry granular flows on a horizontally-divided rigid wall. Next, some michromechanical points are investigated: the development of force chains in the granular medium and the effect of particle size on the signal of the total normal force. Afterwards, the evolution of the total normal force with time is investigated by quantifying the part of the force that is due to the weight of the dead zone mass. Finally, main conclusions are drawn from the chapter. Some findings of this chapter were published in an article in Granular Matter journal, a copy of the article can be found in Appendix A.

3.2 Experimental Data

Jiang and Towhata (2013) recently studied the impact behavior of dry granular flow against a rigid retaining wall using poly-dispersed mixture of limestone gravel which has a measured angle of repose of 53°. The gravel flow mixture had particles ranging from 10 mm to 20 mm in grain size (Fig. 3.1). The samples were prepared with a specific weight of 13.5 kN/m^3 in a box with varying lengths (from 14 cm to 44 cm with a 5 cm step) and heights (from 5 cm to 20 cm with a 5 cm step) but with a 30 cm fixed width. The samples were released in a dam-break manner in which the gate was pulled instantaneously in accordance with other experiments in the literature (Pudasaini et al., 2005b; Wendeler and Volkwein, 2015).

The chute was rectangular in cross section with 219 cm length, 30 cm width and 35 cm height. Different inclination angles α were tested ranging from 30° to 45°. The friction angle between the gravel particles and the chute base, chute sides and the rigid wall were found to be 25°, 15° and 21° respectively. These friction angle values were obtained using the method of measurement previously followed by Mancarella and Hungr (2010). In this method, particles are packed in a cylinder that is placed on the board (the base, sides or the wall). Afterwards, the board is tilted up to a certain inclination angle where

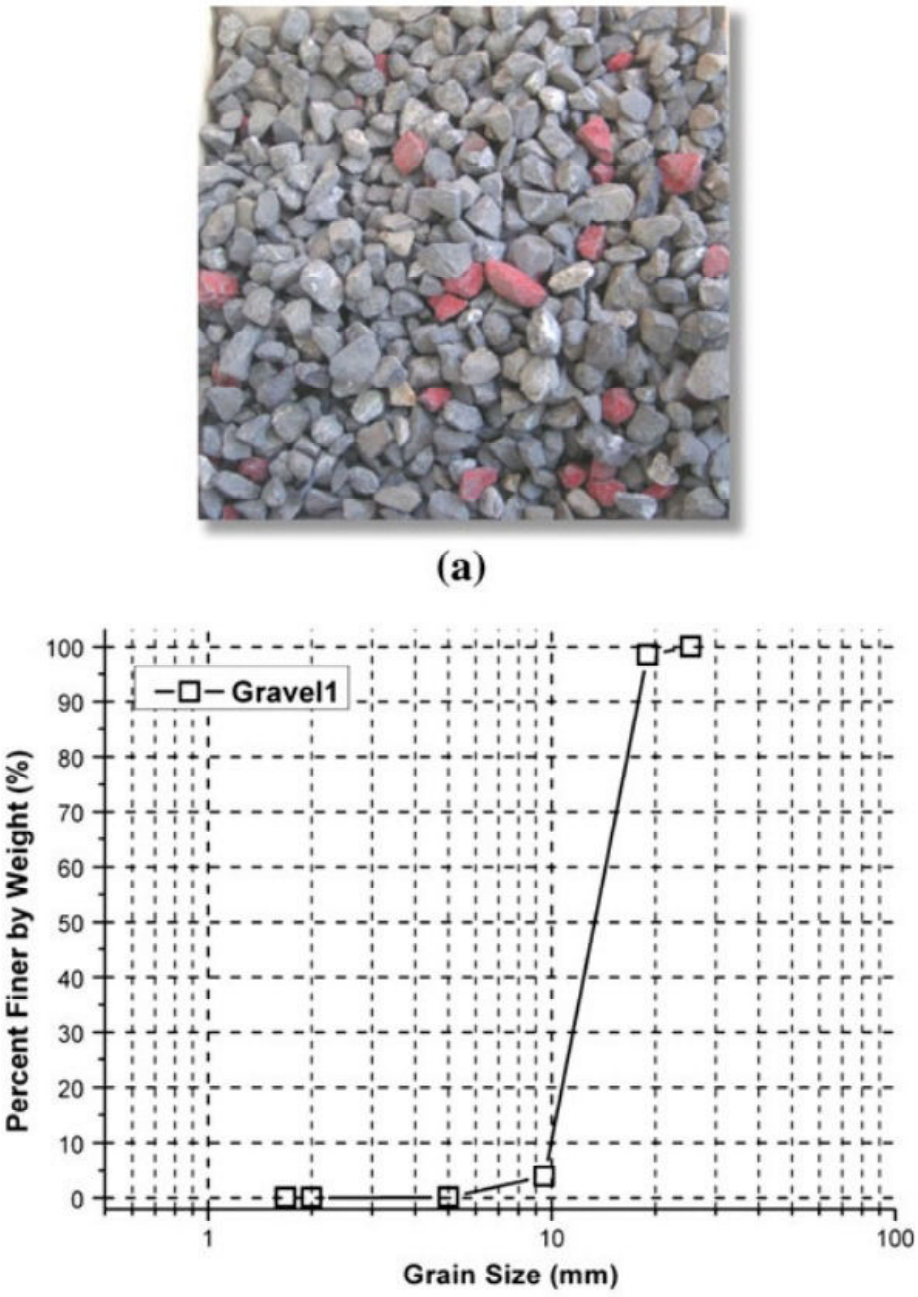

Figure 3.1: *(a) Shape of gravel particles, (b) Grain size distribution of the particles (after Jiang and Towhata, 2013)*

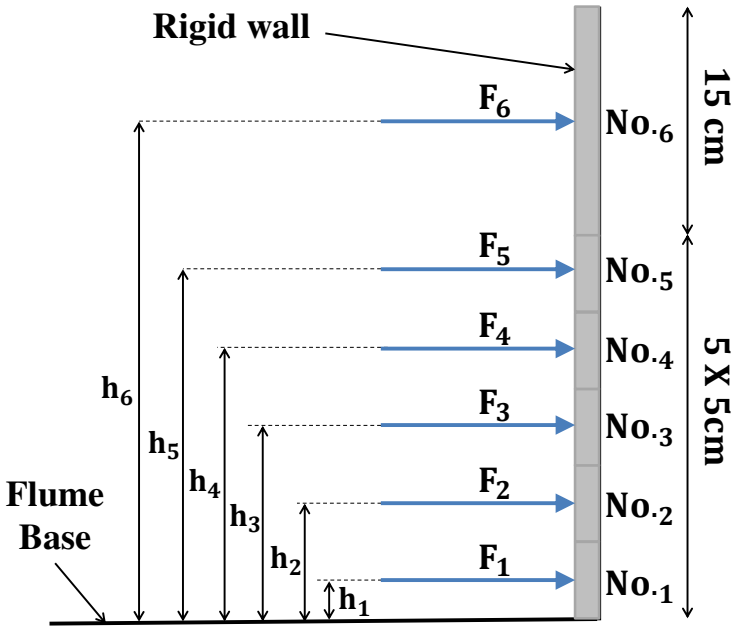

Figure 3.2: *Rigid wall division from the bottom to the top (adapted from Jiang and Towhata, 2013)*

the cylinder start sliding on it. The inclination angle where sliding starts taking place is considered the friction angle. The base of the chute was a planar surface without any fixation of particles. The chute ended with a rigid wall perpendicular to the chute base and divided into six horizontal segments, marked from 1 to 6 starting from the bottom (Fig. 3.2). Each segment had a height of 5 cm except the last one which was 15 cm high. Thus the total height of the wall was 40 cm.

Measurements of normal impact force versus time were recorded for different heights of the wall, i.e different segments forming the wall. In addition, observations of flow thickness and flow velocity were taken at the time where the total normal force on the wall reached its maximum value. These experimental data were selected for our model calibration and validation. This is because it considers elongated coarse-grained flow of angular particles rather than the simple spherical glass beads commonly used in literature. In addition, the study provided detailed measurements of the time evolution of the normal impact force for different heights (different segments of the rigid wall). Three different tests have been presented in the paper: Test L34-H15-α45°, Test L44-H15-α40° and Test L44-H20-α40°. A test marked by L44-H15-α40° represents a sample having 44 cm in length, 15 cm in height and 40° inclination angle.

3.3 Numerical Modeling

The experimental tests described in Section 3.2 were modeled in YADE using DEM. The contact law used, the shape and number of particles, methodology for quantifying the dead zone mass are detailed in the following sections.

3.3.1 Contact law

A visco-elastic contact law with Mohr-coulomb failure criterion (Fig. 3.3) has been adopted to model the dry granular flow. Such a model is commonly used in the literature for such problems (Silbert et al., 2001; da Cruz et al., 2005; Faug et al., 2009). This is because it allows for accounting for both friction (Mohr-coulomb) and collision (viscous damping) mechanisms of the contacts. The normal contact force $\mathbf{F_n}$ between two particles was defined as the sum of two components; an elastic one and a viscous one (representing the linear dashpot model). The viscous component of the normal force is a dissipative force that is proportional to the time derivative of the overlap between the two particles (Faug et al., 2009). The normal force at the contact is always repulsive, as particles are considered to be cohesionless. Thus, the normal force can be calculated as follows:

$$\mathbf{F_n} = (k_n u_n - \gamma_n \dot{u}_n)\mathbf{n} \tag{3.1}$$

where k_n is the normal stiffness parameter, u_n is the normal displacement (overlapping distance between two particles) and γ_n is the normal visco-elastic coefficient, which is related to the normal restitution coefficient ε_n in a binary collision (Campbell, 2002; Schwager and Pöschel, 2007).

The normal stiffness of the contact (k_n) was calculated as (Catalano et al., 2014):

$$k_n = \frac{2E_1 r_1 E_2 r_2}{E_1 r_1 + E_2 r_2} \tag{3.2}$$

where E_1 and E_2 are the elastic moduli of the first and second particles respectively (both taken as 10^8 Pa) and r_1 and r_2 are the radii of the first and second particles respectively.

For the tangential direction, the tangential contact force $\mathbf{F_t}$ is incrementally calculated as follows:

$$\Delta \mathbf{F_t} = k_t \, \Delta u_t \quad and \quad |F_t| \leqslant F_n \, tan\phi \tag{3.3}$$

where k_t is the tangential stiffness parameters, Δu_t is the incremental tangential displacement and ϕ is the friction angle. k_t was taken as $(2/7)k_n$ according to what was previously suggested by Silbert et al. (2001), although it has been shown in previous studies that it has very small influence (Campbell, 2002).

The restitution coefficient (ε) is generally defined as the ratio between relative velocities after and before the impact of two particles. Schwager and Pöschel (2007) solved the equation of motion with equation 3.1, with the initial condition u_n=0. The duration of the collision t_c was derived from equation 3.1 and found to be $t_c^0 = \pi/\omega$. Thus $\varepsilon_{n,t}$ (normal and tangential restitution coefficient) can be calculated as follows:

$$\varepsilon_{n,t} = \frac{\dot{u}(t_c^0)}{\dot{u}(0)} = e^{-\beta_{n,t}\pi/\omega_{n,t}} \tag{3.4}$$

where $\beta_{n,t}$ and $\omega_{n,t}$ are:

$$\beta_{n,t} = \frac{\gamma_{n,t}}{m_{eff}} \tag{3.5}$$

$$\omega_{n,t} = \sqrt{\left(\frac{2k_{n,t}}{m_{eff}}\right)^2 - \beta_{n,t}^2} \tag{3.6}$$

where $m_{eff} = (1/m_1 + 1/m_2)$, m_1 and m_2 are the masses of two interacting particles and $\dot{u}(t_c^0)$, $\dot{u}(0)$ are velocities after and before the collision respectively.

The value of $\varepsilon_{n,t}$ will be calibrated in Section 3.4.2 considering the flow thickness measurements.

3.3.2 Flowing particles: shape and number

In this section, the shape and number of particles generated in the numerical simulation are presented. The simple comparison of particles' shape between simple spheres and clumps was carried out in order to find out the most representative shape of the particles used in the experiment. Particles used in the experiment had sharp angles and elongated shapes (Fig. 3.1). To account for these irregularities in shape, two numerical granular samples of same volume and mass were comparatively studied: a sample made of

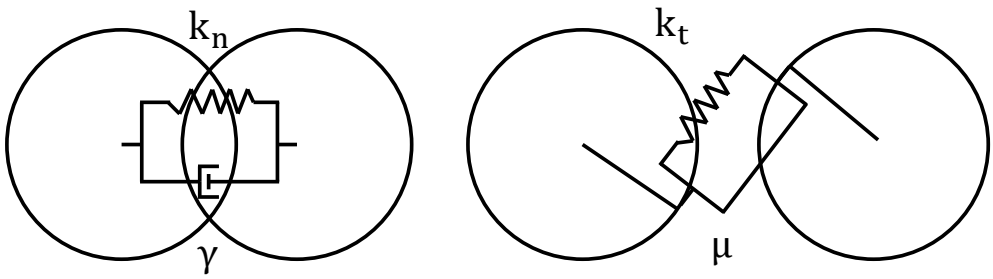

Figure 3.3: *Normal and tangential interaction forces of the contact law used in the model*

simple spheres and a second sample made of clumps (Fig. 3.4). The second sample is made of clumps where each clump consists of two identical spheres with radius $R^{'}$ and overlapping over a distance $R^{'}$ thus having an aspect ratio of 3/2. Since the two samples were generated with the same volume, the relationship between R and $R^{'}$ is:

$$\frac{4}{3}\pi R^3 = 2\frac{4}{3}\pi R'^3 - \frac{5}{12}\pi R'^3 \tag{3.7}$$

Thus, by arranging equation 3.7, we find that $R^{'} = \sqrt[3]{\frac{16}{27}}$ R. It is worth noting that, when using clumps, contact law equations 3.1 and 3.3 are applied at the contact between the members that form the clumps (deformation between spherical particles). Afterwards, contact forces are summed on clumps and then the rigid body equations of motion are applied to the clumps (Šmilauer et al., 2010).

Concerning the number of particles (n_p) in each simulation, samples were generated with a number of particles similar to that of the experiment (using the same particle size distribution and maintaining the same porosity). This number was calculated using the total weight of the sample and the weight of a single D_{50}-sphere as follows:

$$n_p = \frac{V_t \gamma_t}{V_s \gamma_s} \tag{3.8}$$

where V_t is the total volume of the sample, γ_t is the specific weight of the sample (13.5 kN/m^3), V_s is the volume of a single D_{50}-particle and γ_s is the specific weight of gravel particles (taken as 26.5 kN/m^3 for the limestone gravel considered). For instance, the number of particles (clumps) used to generate the sample used in test L44-H15-α40° was 5406 clumps. Since each clump is made of two overlapping spheres, thus, the number of spheres was 10812 spheres.

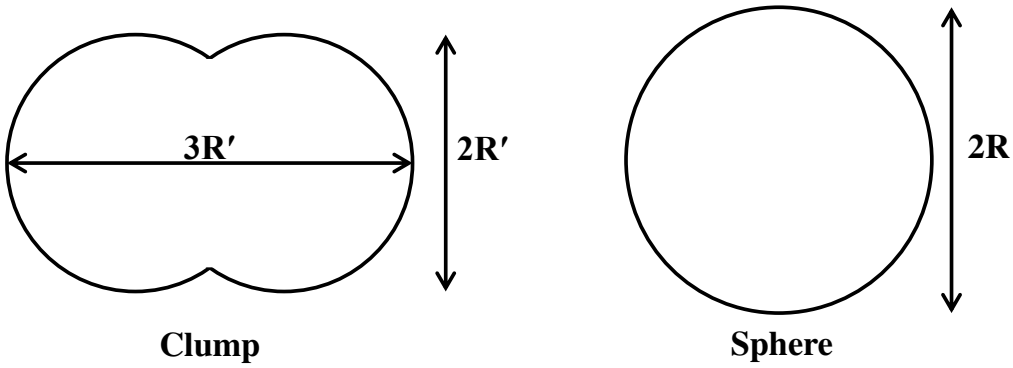

Figure 3.4: *Particle shapes tested in the simulation: a clump and a simple sphere*

3.3.3 Dead zone mass

In granular flows impacts against protection structures, a zone of particles trapped behind the structure in a quasi-static condition is formed. Such a zone is most often called a "dead zone" (Faug et al., 2002). In this section, the equations used to quantify the force applied to the wall by the mass of this zone are presented.

The total normal force applied on the wall has mainly two components: gravitational component and a dynamic one. The gravitational component (F_g) is due to the dead zone mass. On the other hand, the dynamic component (F_d) is due to the kinetic energy of the flow (Buchholtz and Pöschel, 1998). In order to calculate gravitational component of the total normal force, the dead zone mass needs to be identified. A criterion has been selected defining dead particles as the ones having a translational velocity component in the flow direction smaller than or equal to five percent of a fixed value of flow velocity. This fixed value is the velocity of the flow at the time of the maximum total impact force on the wall (V_{max}), measured for particles lying in distances from 40 to 50 cm away from the wall. Thus, a particle is considered dead if $V_{particle} \leq 5\% V_{max}$. In order to calculate the weight of the dead zone (G), we should consider the static equilibrium of this zone (Fig. 3.5). The base reaction $\mathbf{R_1}$ is the sum of interaction forces between dead particles and the base ($\mathbf{F_{int}}$):

$$\mathbf{R_1} = \sum_{i=1}^{n} \mathbf{F_{int}} \tag{3.9}$$

Similarly, the wall's reaction $\mathbf{R_2}$ is the sum of interaction forces between dead particles and the wall.

However, $\mathbf{R_1}$ and $\mathbf{R_2}$ can be related to each other as follows (see Fig. 3.5):

$$\mathbf{R_2} = \mathbf{R_1}\frac{sin(\alpha - \delta_1)}{cos(\alpha + \delta_2)} \tag{3.10}$$

where α is the chute inclination angle, δ_1 is the angle of friction between the base and the dead mass and δ_2 is the angle of friction between the wall and the dead mass.
The gravitational force (F_g) is equal to the normal component of the reaction on the wall:

$$F_g = \mathbf{R_2} \cdot \mathbf{n_2} \tag{3.11}$$

Finally, by considering the static equilibrium of dead zone mass and using equation 3.10 and 3.11, we find:

$$F_g = G\frac{sin(\alpha - \delta_1)}{cos(\alpha + \delta_2)}cos\delta_2 \tag{3.12}$$

The values of δ_1 and δ_2 are lower than or equal to the sliding condition values of friction angles mentioned in Section 3.2. δ_1 and δ_2 were calculated according to the following equations:

$$\tan^{-1}(\delta_1) = \frac{R_{1t}}{R_{1n}} \tag{3.13}$$

$$\tan^{-1}(\delta_2) = \frac{R_{2t}}{R_{2n}} \tag{3.14}$$

where R_{1t}, R_{1n} are the sum of tangential and normal contact forces with the chute base respectively, and R_{2t}, R_{2n} are the sum of tangential and normal contact forces with the wall respectively. Thus, using equation 3.12 with instantaneous values of δ_1 and δ_2, we can get the time evolution of the gravitational force (F_g) applied on the wall. Discussion of results of total normal force components (gravitational and dynamic) will presented in Section 3.7.

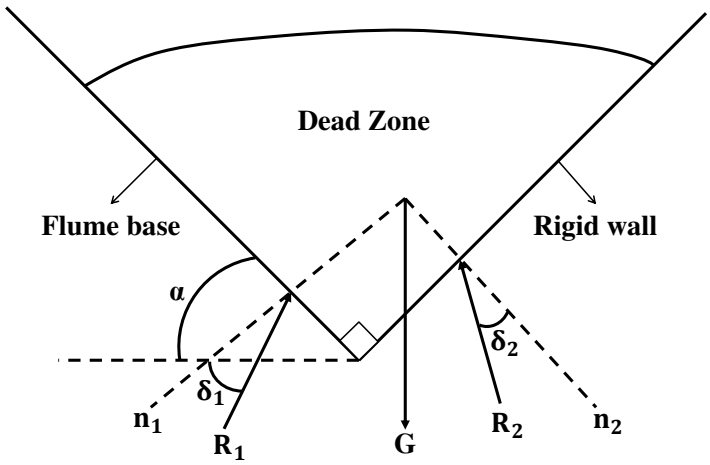

Figure 3.5: *Static equilibrium of the dead zone accumulated behind the wall*

3.4 Model Calibration

The calibration of the numerical model against experimental data is presented in this section. The aim of this calibration is to reach a suitable value of the normal restitution coefficient (ε_n) that leads to a closer behavior to the experimental flow. In addition, a representative numerical particle shape of the experimental gravel particles is needed for good calibration. Furthermore, model calibration is needed to avoid a very dilute flow which would overflow the obstacle, in contrast to the gravel flow interaction with the rigid wall obtained in the experimental data (Section 3.2).

The model calibration will be carried out considering the shape of the particles and the value of $\varepsilon_{n,t}$ based on the flow thickness measurements and the final shape of the deposit behind the wall. Due to the absence of lubricated contacts, the tangential viscous damping coefficient has been set to zero (i.e. ε_t = 1.0) as suggested by Ghaisas et al. (2004). Friction angles of chute base, side walls and rigid wall were taken similar to values provided by the experimental data (Section 3.2). The model has been calibrated and validated for test L34-H15-α45°, test L44-H15-α40° and test L44-H20-α40°. Results shown in this section are for test L44-H15-α40°.

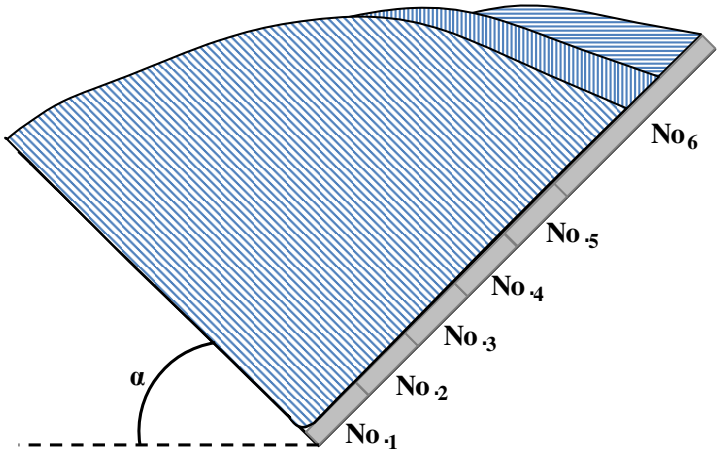

Figure 3.6: *Schematic representation of three different granular deposits (of same volume) showing the indirect relation between the final shape of the deposit and the residual force applied on the 6th segment of the wall*

3.4.1 Clumps vs. spherical particles

In this section, a comparative study was conducted between spherical and clumped shapes. This is to select the most representative shape of the angular particles of the experiment. The calibration of the shape of the particle in this section was carried out in parallel with the calibration of normal restitution coefficient (ε_n) mentioned in the following section.

For comparison between the two shapes, an indirect relation between the final force value on the top segment of the wall (F_6) and the shape of deposit has been adopted (Fig. 3.6). The final value of F_6 would change with the change in the length of deposit that vertically extend on the sixth segment of the wall. Thus, we compare the residual values of F_6 for each particle type (clump and sphere).

From Fig. 3.7, when compared to spheres, we see that using clumped particles gives a final force value that is closer to the experimental one ($F_{6exp} \approx 14$ N/meter-width of the wall), which might indicate a better final shape representation. This might be due to the natural rotational resistance delivered by the clumped shape and also the interlocking between particles which prevent them from rolling over the dead zone. To verify this, we compare the ratio of rotational energy to total kinetic energy (E_{rot}/E_{kin}) for both cases.

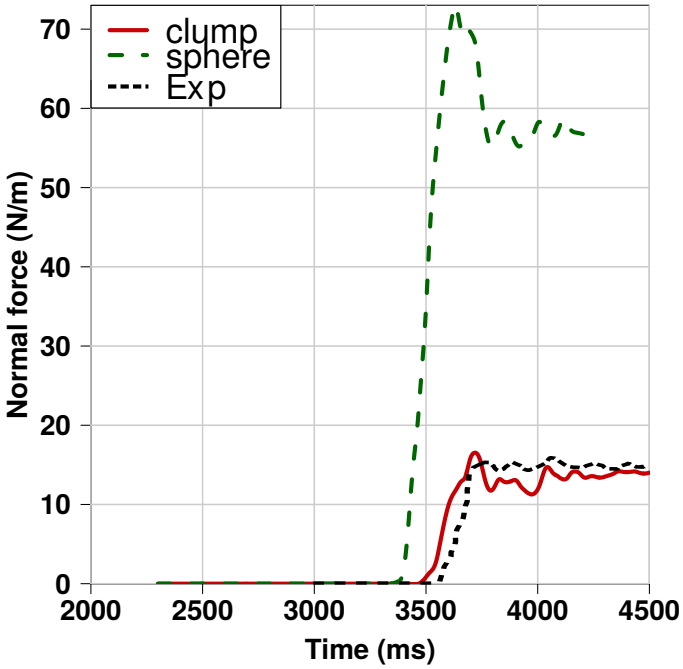

Figure 3.7: *Variation of normal force on part 6 of the wall with time for clumps and spheres (test L44-H15-α40°)*

From Fig. 3.8, a reduction of this ratio by 70% can be noticed once clumped particles are used. This way of reducing the ratio E_{rot}/E_{kin} by shape configuration is preferred to blocking the rotation of any axis as it does not violate the physical laws of motion. It is also preferred to adding an artificial rolling resistance to spherical particles (Zhou et al., 1999), since clumps resist rolling naturally by their shape. Thus, clumps are used henceforth as they proved to be advantageous over spherical shapes.

3.4.2 Flow thickness and deposit shape

In this section, the value of the normal restitution coefficient ε_n is calibrated against experimental data based on the flow thickness and granular deposit shape behind the wall.

The considered granular flow in the chute has two regimes along the flow thickness (Fig. 3.9); collisional and frictional regimes (Savage, 1984). The frictional regime is mainly controlled by the friction angle of the chute base which is clearly stated in the experimental data.

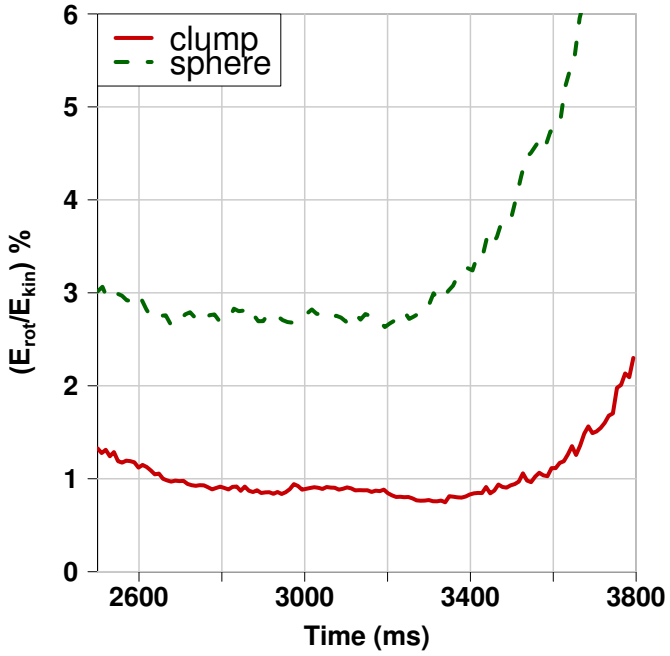

Figure 3.8: *Ratio of rotational energy to total kinetic energy for clumps and spheres (test L44-H15-α40°)*

On the other hand, ε_n values affect the collisional part of the flow regime where dissipation of energy is thought to be caused by particles collision. For this reason, different values of normal restitution coefficient (from 0.1 to 0.9, with 0.1 steps) were tested and compared with the experiment for the purpose of model calibration. For convenience, only curves of ε_n of 0.1, 0.3, 0.5, 0.7 and 0.9 are present in the following figures. The targeted part of the flow for calculating flow characteristics were particles within a distance ranging from 40 to 50 cm away from the wall, in order to be consistent with the experimental procedure.

As a first indicator, the flow centerlines of different simulations with different ε_n values are compared. The flow centerline is chosen as a reference for comparison because of the difficulty of identifying the flow surface, as the collisional regime of the flow is dispersive (snapshots of Fig. 3.9). The flow centerline (h_{cl}) was calculated as follows:

$$h_{cl} = \frac{\sum_{i=1}^{n} h_{particle}}{n_v} \tag{3.15}$$

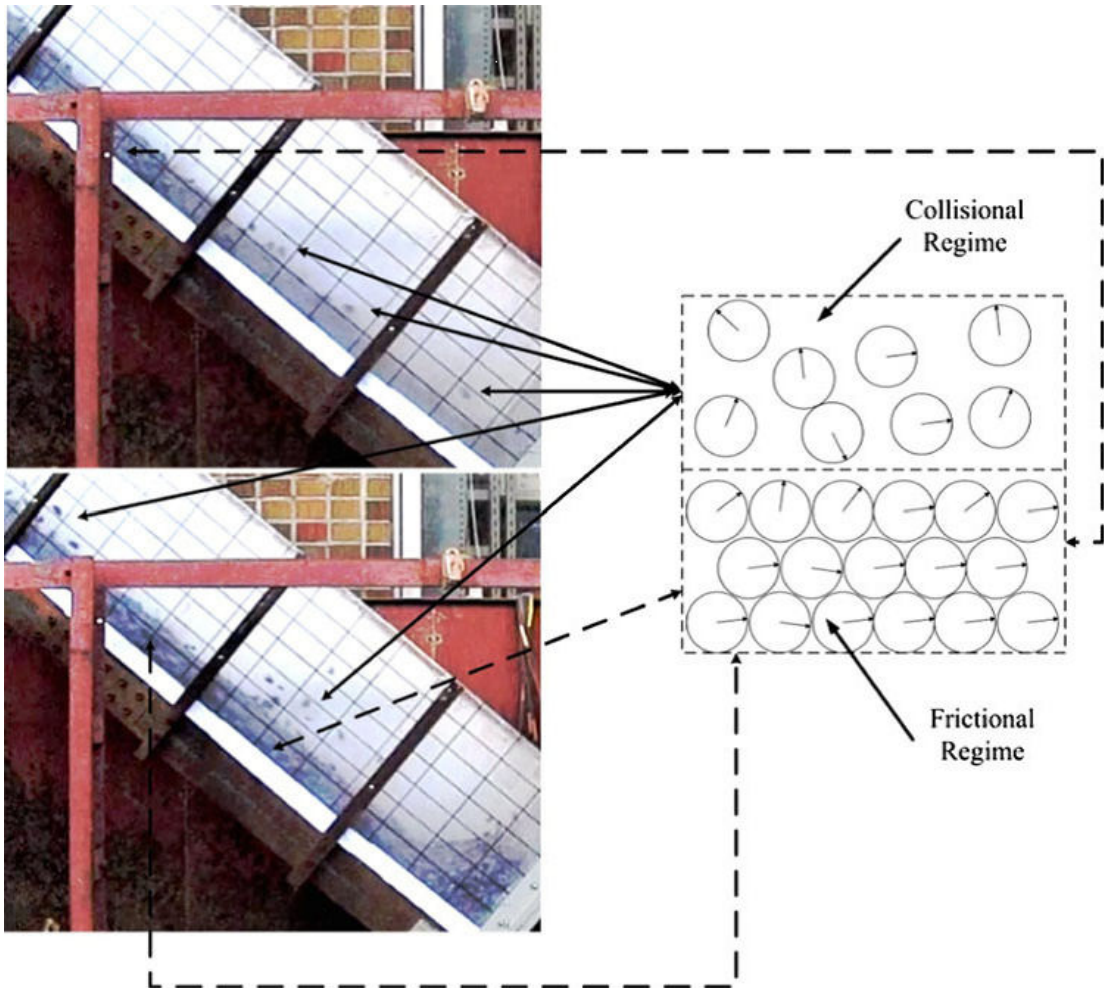

Figure 3.9: *Snapshots of the experiment showing frictional and collisional regimes of the flow, top: before the impact, bottom: after the impact (after Jiang and Towhata, 2013)*

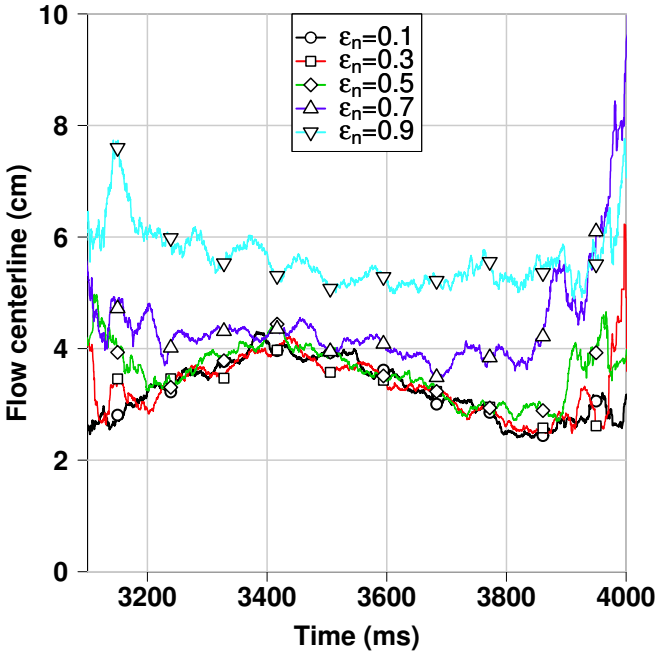

Figure 3.10: *Variation of average flow thickness (flow centerline) with time using different normal restitution coefficient values (test L44-H15-α40°)*

where $h_{particle}$ is the particle height (measured from its center in a perpendicular direction to the chute base) and n_v is the number of particles in the targeted volume.

Fig. 3.10 shows the evolution of flow centerline for different values of ε_n. The time range where the body of the flow was passing through the measuring window (window from 40 to 50 cm away from the wall) was from 3200 to 3800 ms. Comparison of different values of ε_n is mainly carried out within this time range in order to exclude the highly dispersive front and tail parts of the flow.

As shown in Fig. 3.10, values of ε_n higher than 0.5 lead to a very dilute flow with high flow centerline values. These dispersive flows overflow the wall in contradiction to the observed behavior of the experimental data where no wall overtopping took place. In contrast, denser flows are observed for values of ε_n lower than or equal to 0.5 in accordance with observations of Faug et al. (2009).

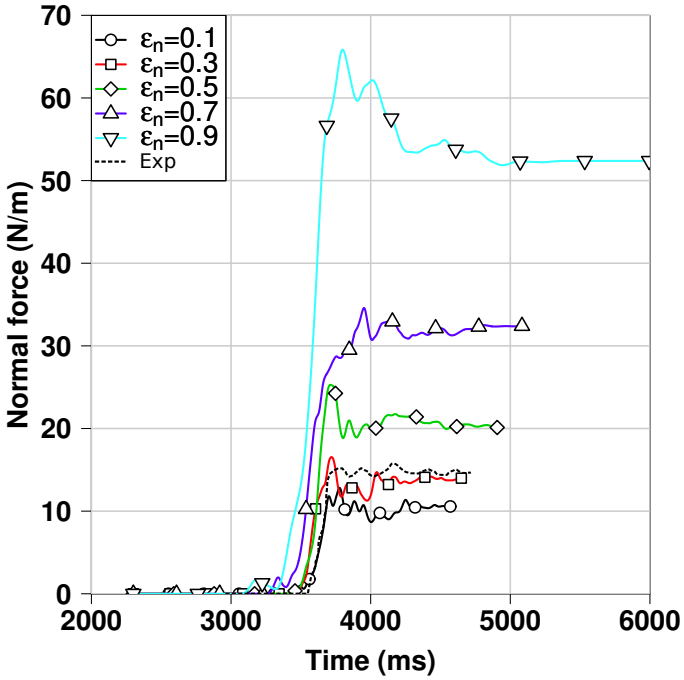

Figure 3.11: *Variation of normal force on the sixth segment of the wall with time using different normal restitution coefficient values (test L44-H15-α40°)*

Likewise, the final deposit shape needs to be verified for different ε_n values. We use again the indirect relation between the final shape and the residual force value F_6 illustrated earlier in Fig. 3.6. Different values of ε_n are tested and results of force variation on the top segment of the wall are recorded (Fig. 3.11). Values of ε_n between 0.2 and 0.4 were found to be the most suitable for the coarse-grained gravel flow that we have, as they give the closest values to the experiment in terms of residual force on the 6th segment of the wall ($F_{6exp} \approx 14$ N/m). As a result, a value of ε_n equal to 0.3 is chosen for our visco-elastic model. Next, we investigate the effect of ε_n values on the flow velocity. Little effect is noticed for the flow velocity values when changing ε_n (Fig. 3.12). The considered flow velocity values are the average velocities in the direction of the flow for particles that have positions (measured from their center) in the upper half of the flow, in order to see the variation of particles velocities in the collisional regime of the flow.

Now, the thickness of the flow for the chosen value of ε_n=0.3 needs to be compared with the experiment. In the experiment, the flow thickness was calculated at the flow surface excluding particles that are detached from the flow. On the numerical side, the same procedure is followed in order to be comparative. For this aim, we calculated the cumulative frequency of particles' heights in which thickness and velocity values were

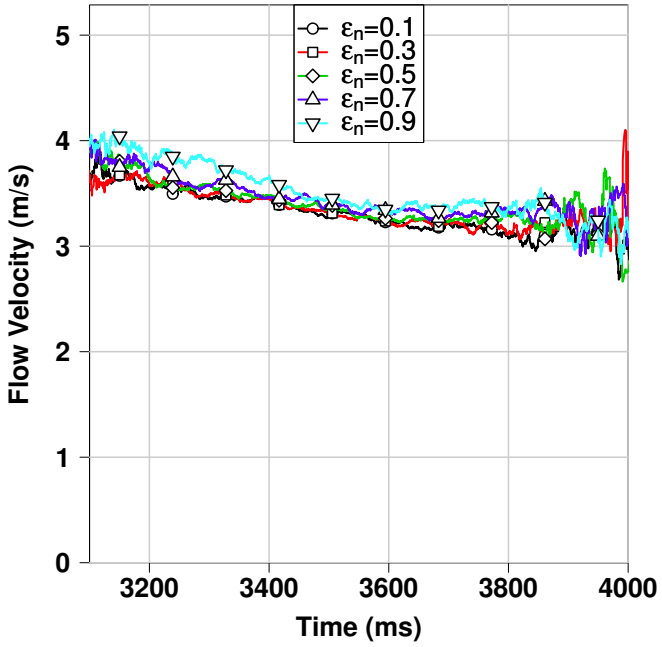

Figure 3.12: *Variation of average particles velocity with time, for particles in the upper half of the flow (test L44-H15-α40°)*

taken at 90% of total frequency of particle center (Fig. 3.13). A value of $D_{50}/2$ was added to 90% cumulative frequency of the flow thickness to account for the free surface of the flow. The calculated thickness in the model (Fig. 3.13) has a value of 3.9 cm which matches the experimental value of 3.9 cm taken at the time of maximum impact force on the wall. The flow velocity profile (Fig. 3.14) suggests a plug flow taking place, which might be due to the high inclination angle of the chute. In addition, comparing the arrival time between the model and the experiment (Fig. 3.17), we see good match between the two which suggests similar average flow velocities. Above all, features of dry granular flows have been observed by the model showing a dilute front followed by a denser part (Fig. 3.15).

3.5 Model Validation

In this section, the comparison with the experimental data is carried out for the aim of model validation. The validation is mainly concerned with the impact behavior of the granular flow on the rigid wall. This impact behavior comparison between the model and the experiment is carried out at both scales: the segment-scale (impact on each

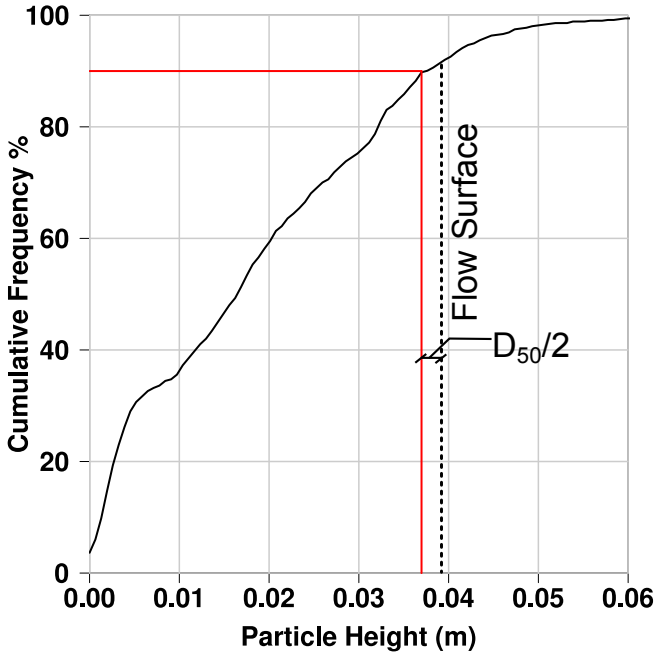

Figure 3.13: Cumulative frequency of particles height measured from the center (test L44-H15-α40°)

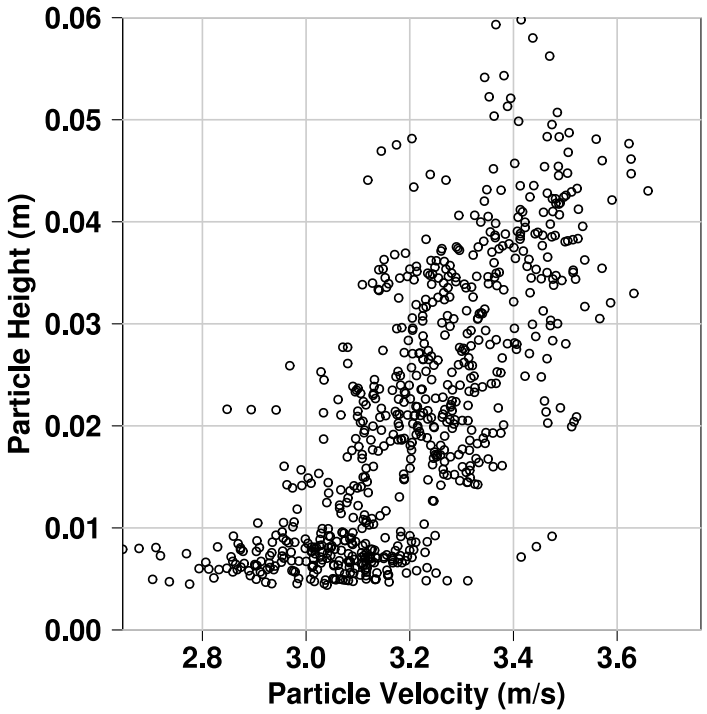

Figure 3.14: Variation of particles velocity with heights (test L44-H15-α40°)

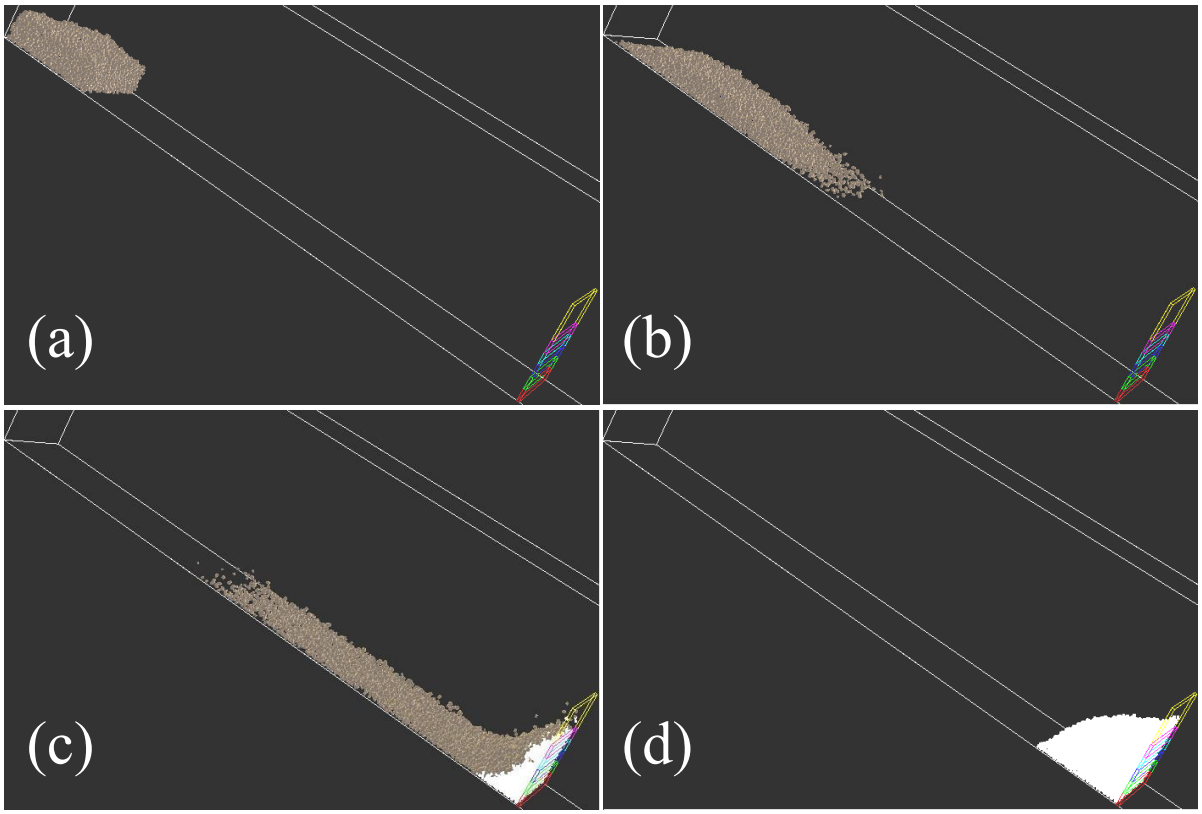

Figure 3.15: *Snapshots of the 3D view of the evolution of the calibrated flow through time (test L44-H15-α40°), along with the evolution of dead particles (colored in white): (a) at time = 2300 ms, (b) at time = 2793 ms, (c) at time = 3583, (d) at time = 4400 ms*

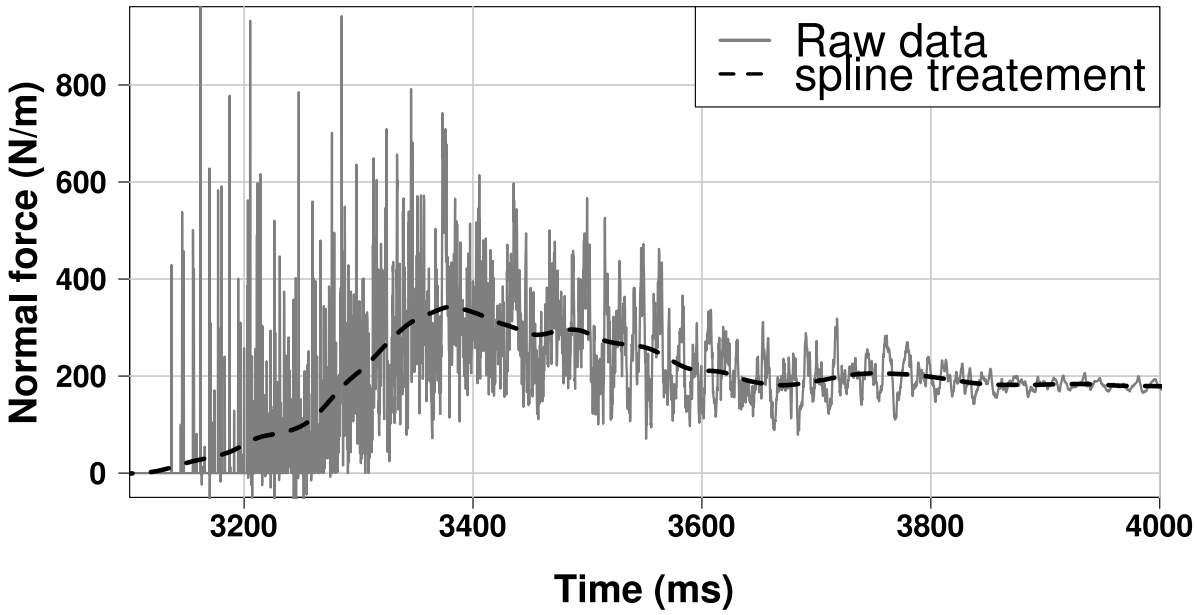

Figure 3.16: *Time evolution of the normal impact force on the bottom segment of the wall: raw data and spline-treated data*

part of the wall) and the wall-scale (total normal impact force on the wall). The rigid wall response against the granular flow impact is investigated in details, giving special attention to the normal force applied on each part of the rigid wall where curves of normal impact force vs. time were analyzed. Furthermore, total normal impact force and bending moment applied on the wall are compared.

3.5.1 Impact results data treatment

Due to the tendency of DEM results to show large fluctuation, a data treatment was needed in order to have results that are quantitatively comparable to the experimental data. Data treatment was carried out using smooth spline method where a smooth curve is fitted to a set of noisy data using spline function. The advantages of using splines are their computational speed and simplicity, as well as the clarity of controlling curvature directly (Chambers and Hastie, 1991). Fig. 3.16 shows an example of the raw data and its spline treatment. After treated with spline, the normal impact force results could be compared with the experimental data as will be shown in the following sections.

3.5.2 Normal impact force on each part of the wall

3.5.2.1 Test L34-H15-α45°

In this test (Fig. 3.17a), for the first element of the wall (F_1), the peak force was found to be 396 N/m which is fairly close to the experimental value (around 350 N/m). Moreover, the time of the peak force F_1 is relatively similar to the experiment with a value around 3676 ms but with a lower residual force in the model (145 N/m) compared with the experiment (175 N/m). Likewise, in contrast to F_1, the peak value of F_2 in the model (256 N/m) was lower than the experimental value (300 N/m). For F_3 and F_4, the model captured the peak time of forces fairly well (being 3883 and 3994 ms for F_3 and F_4 respectively) but with a lower peak value. The peak force and timing of the peak of F_5 and F_6 were fairly captured by the model along with their residual force values.

3.5.2.2 Test L44-H15-α40°

For this test, the peak impact force values were 341 and 232 N/m for F_1 and F_2 respectively (Fig. 3.17b). Compared to the experiment, similar values were observed but with a reversed order ($F_2 > F_1$). Such discrepancy of the force evolution will be discussed in details in Section 3.6.1. Concerning the rest of the wall, the model managed to capture the peak forces of F_3, F_4, F_5 and F_6 (with a small exception for F_3) with values of 154, 120, 66 and 15 N/m respectively along with peak times 3619, 3808, 3733 and 3761 ms respectively. Residual forces on these parts were found to be 112, 82, 40 and 12 N/m respectively which are close to the experimental observations.

3.5.2.3 Test L44-H20-α40°

With the use of higher volume of the sample, the trend of the impact force curves was better captured with the model along with the time lag between each force curve. For instance, F_1 peaks at 2523 ms with a value of 387 N/m (450 N/m in the experiment) which is followed by a peak of F_2 with 288 N/m (340 N/m in the experiment) at 2737 ms (Fig. 3.17c). Residual forces of F_1 and F_2 were found to be similar to the experiment with values of 227 and 226 N/m respectively. Very good agreement has also been observed for F_3, F_4, F_5 and F_6 in terms of peak forces (172, 172, 108 and 51 N/m) the time of the peak (2864, 3070, 2912 and 3043 ms) and residual force values (116, 134, 65 and 43 N/m).

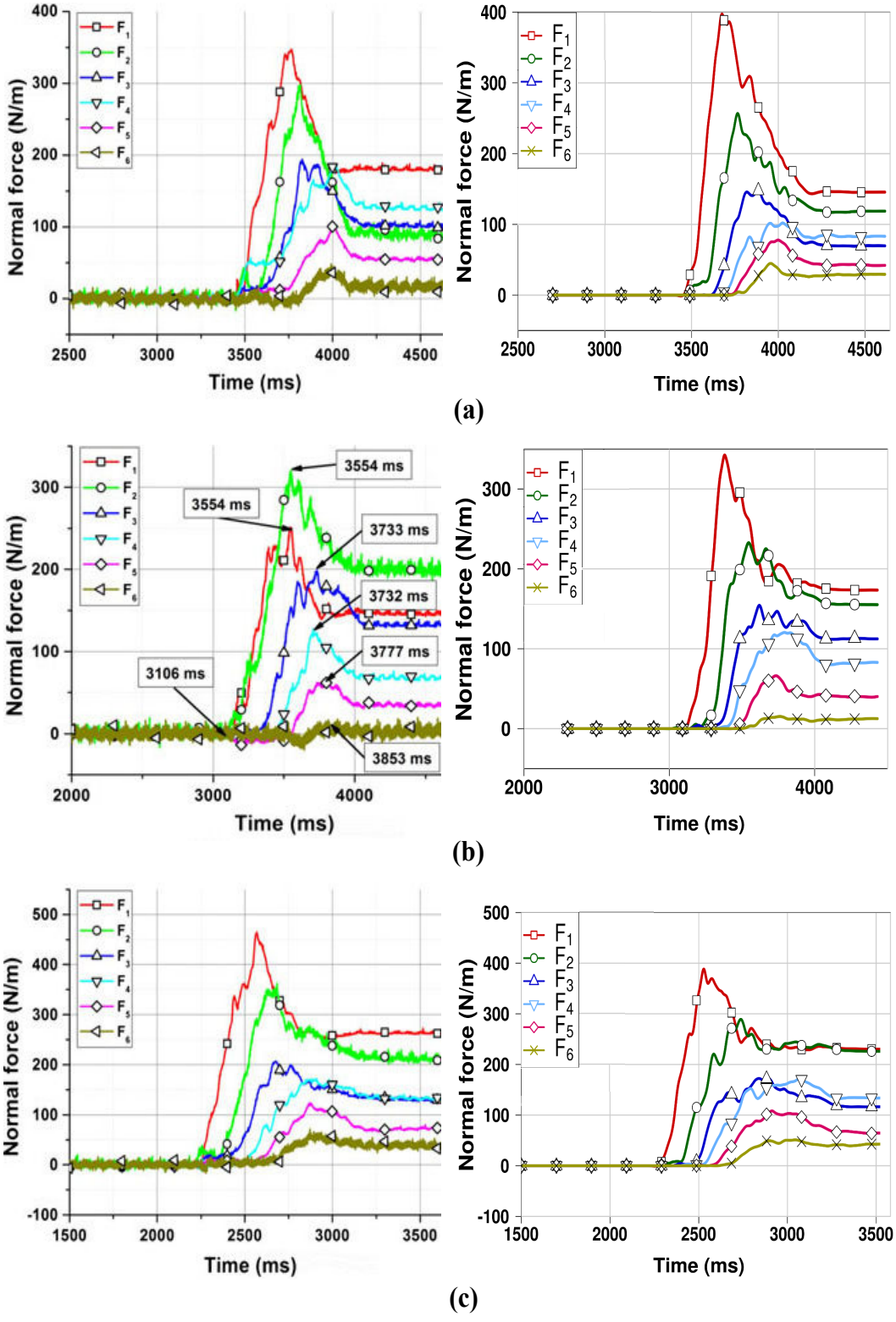

Figure 3.17: *Time history of normal force variation: experiment (after Jiang and Towhata, 2013) (left) and model (right): (a) test L34-H15-α45° (b) test L44-H15-α40° (c) test L44-H20-α40°*

3.5.3 Total normal force and bending moment

In this section, the total normal force F_{tot_n} and bending moments applied by the granular flow on the rigid wall are compared for both the model and the experiment for the purpose of model validation. They are calculated as follows:

$$F_{tot_n} = \sum_{i=1}^{6} F_i \tag{3.16}$$

$$M = \sum_{i=1}^{6} F_i h_i \tag{3.17}$$

where F_i is the normal force on each part of the wall and h_i is the distance between the centroid of the wall's parts and bottom of the retaining wall (Fig. 3.2). For the total normal force (Fig. 3.18), the model fairly agrees with the experiment in terms of the peak force (735 N/m), peak time (3733 ms) and residual force (576 N/m). The maximum total impact force was found to be around 1.25 times the hydrostatic force at the end of the test.

The bending moment results (Fig. 3.18) from the model also agrees with the experiment having a maximum bending moment of 80 N*m/m and peaking at the same time of the peak total normal force (3733 ms). Although out of the scope of this study, it is worth noting that the total tangential force (F_{tot_t}) on the wall was found to be negligible in accordance with Faug et al. (2009), whatever the slope inclination is. This might need further experimental studies with sensors measuring the variation of tangential force on the wall.

3.6 Micromechanical investigation of the normal force applied on the wall

The total normal force and bending moment applied on the wall were found agree with the experimental data. However, some differences between the the model and the experiment appear when comparing the force distribution on each part of the wall (Fig. 3.17b). Such differences suggest the presence of microstructural heterogeneities

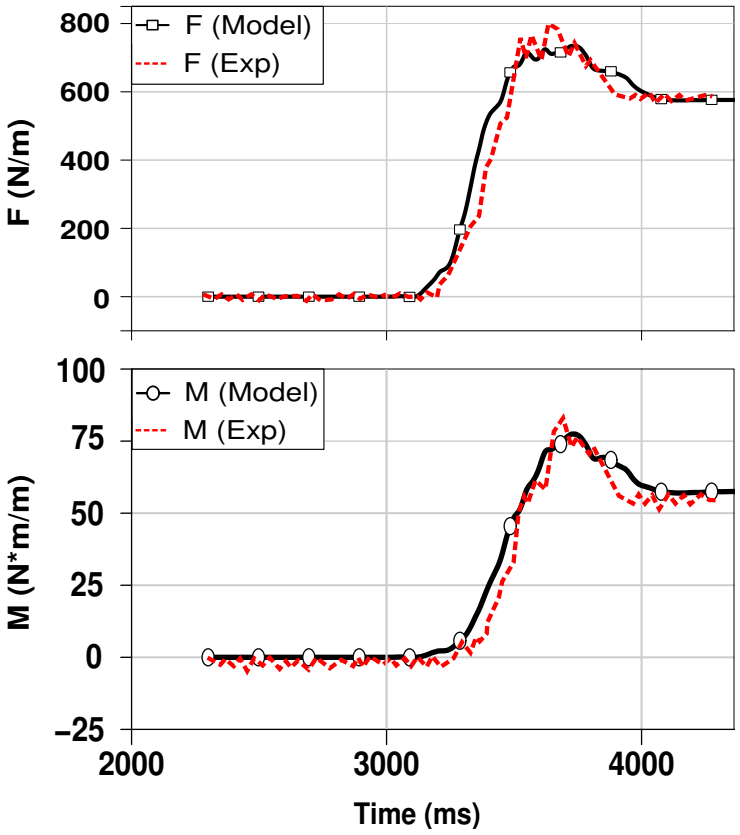

Figure 3.18: *Time history of total normal force and bending moment, test L44-H15-α40° : numerical model and experiment (data from Jiang and Towhata, 2013)*

(e.g. arching effects) in the granular deposit behind the wall (Handy, 1985). These microstructural heterogeneities are discussed in details in this section from two aspects: the possible presence of arching effect in the granular medium, and the effect of particle size on the fluctuation of the sign of the total normal force applied on the wall.

3.6.1 Arching effect within the granular medium

Results from Fig. 3.17 suggest a non-linear distribution of forces on different parts of the wall. In particular, the force at the toe of the wall is sometimes smaller than the one on the segment above. This indicates the possible presence of arching effects in the impacting and depositing stages of the flow. According to Jiang and Towhata (2013), this might be due to a formation of an arch-like protective layer on segment 1 of the wall resulting in a non-linear distribution of forces with depth. Such a layer is also thought to affect the residual force values. To some extent, non-linearity was observed to be present in the model, especially for residual forces of F_1-F_2 and F_3-F_4. This might be due to the force chain distribution behind the wall. Force chains are strongly depending on the particles position and orientation with respect to the wall (Azéma and Radjaï, 2012). The distribution of contact forces on the wall is expected to be different from one test to another, especially at the toe of the wall, even if conducted in the same initial conditions (same volume of the sample and inclination angle). Fig. 3.19 represents the variation of residual forces with the height of the wall for simulations performed for the same initial testing conditions; 44 cm length, 30 cm width and 15cm height and 40° inclination angle of 16 simulations in which only 5 are presented for convenience. However, each test has different initial spatial distribution of particles.

Differences between the 5 tests can be seen for the value of the residual force at each wall segment. These differences are found to increase with depth. For instance, the forces on the 6th segment of the wall (F_6) are very similar for the considered tests. Less agreement is seen for values of F_5 and beyond. The most significant difference can be seen in the segments number 1 and 2 (F_1 and F_2) at the bottom of the wall. For example, the difference between tests 4 and 5 for the value of F_2 is around 35%, although the shape of the granular deposits is the same at the end of the different simulations (Fig. 3.20). As a result, such discrepancy in residual force values can not be explained by a difference in granular shape deposit.

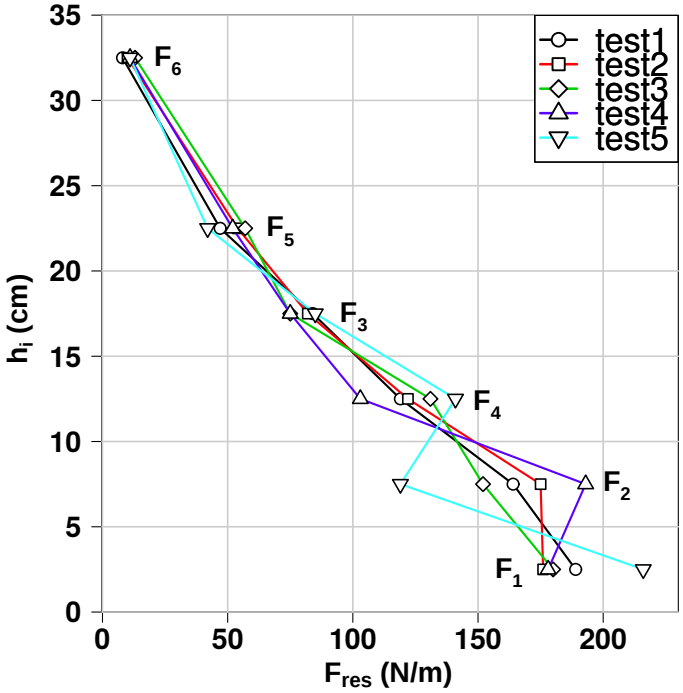

Figure 3.19: Variation of normal residual force with wall's height for 5 tests carried out under the same initial conditions (test L44-H15-α40°)

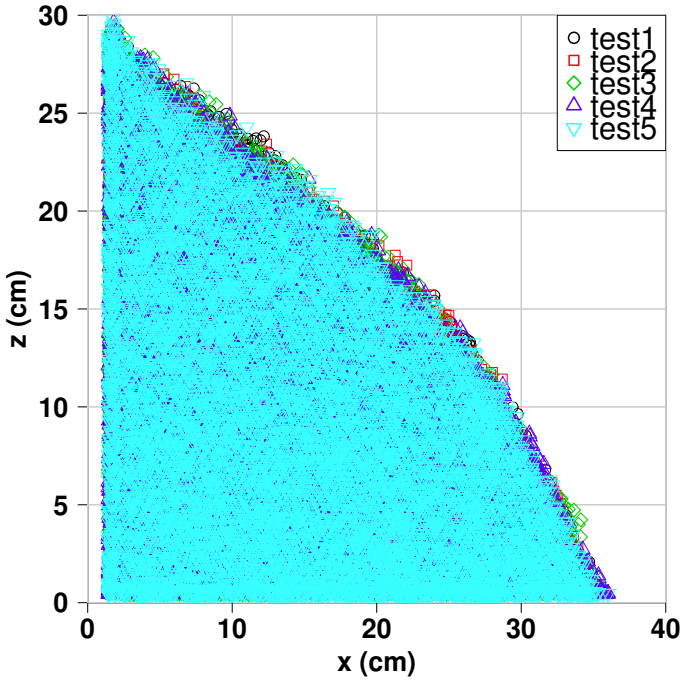

Figure 3.20: The final deposit shape for five tests that have the same initial conditions (test L44-H15-α40°)

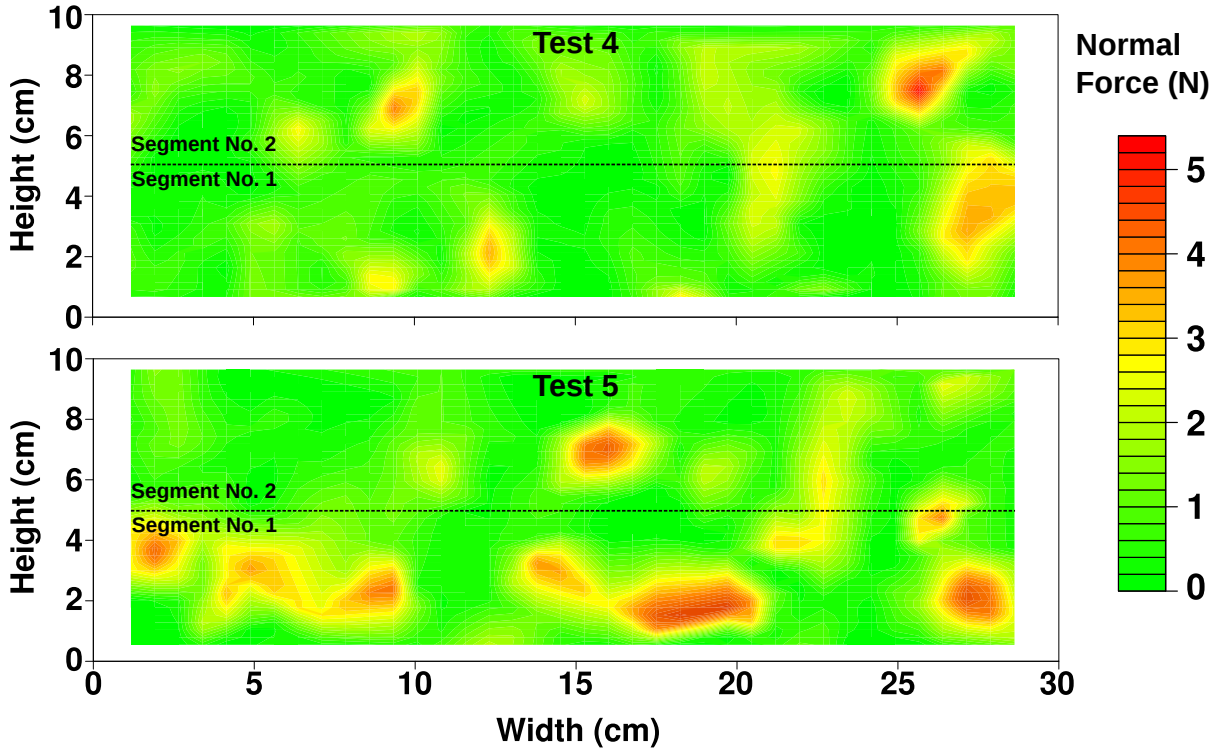

Figure 3.21: *Residual normal contact forces between segments 1 and 2 of the wall and particles deposited on them, top: test 4, bottom: test 5*

Since these differences between the 5 tests are the highest for segments 1 and 2 of the wall (i.e. F_1 and F_2), the spatial distribution of contact force values on these segments was investigated. Fig. 3.21 shows the distribution of contact forces for tests 4 and 5 over segments 1 and 2 of the wall. For test 4 (Fig. 3.21, top), there are two zones of high concentration of contact force in segment number 2 of the wall. Less force concentration is seen for segment number 1 of the wall. As a result, F_2 value is higher than F_1 in Figure 3.20 for test 4. In contrast, for test 5 (Fig. 3.21, bottom), several zones of high concentration of contact forces are present in segment number 1 of the wall. Much lower concentration of contact force is present for segment number 2. Consequently, F_1 value is much higher than that of F_2 in Figure 3.20 for test 5. Thus, it is more likely that the differences seen in Fig. 3.19 for the different tests are caused by microstructural heterogeneities, like for example arching effects.

However, it is important to investigate whether these differences affect the total normal force and bending moment applied on the wall, for the five different tests. For both, the total normal force (Fig. 3.22a) and bending moment (Fig. 3.22b), little difference is seen for the evolution of both quantities with time for the five different tests. Total normal impact force and bending moment values are similar in the impacting and depositing stages of the granular flow impact on the rigid wall. Thus, for engineering applications such as the design of rigid walls where the driving factor is the total normal force and bending moment applied on the wall, there might be no need to consider the differences seen on the segment-scale of the wall.

It is worth noting that it is numerically possible for the model (example: test 4 in Fig. 3.19) to capture what might be a strong arching in the experiment (Fig. 3.17b) in which we have $F_1 < F_2$. Nevertheless, quantifying the force chains in the 3D environment is out of the scope of this thesis. Above all, matching between numerical simulations and experiments should mainly concern the total normal force and bending moment on the wall rather than on each segment.

3.6.2 Effect of particle size on the total normal force signal

Several simulations have been conducted to study the effect of d_{50} of the granular flow on the fluctuations of the signal of the total normal force F_{tot_n} applied on the rigid wall by the flow. More specifically, several ratios of H_w/d_{50} were tested, where H_w is the height of the wall (40 cm), which was fixed for all of the simulations. All samples in

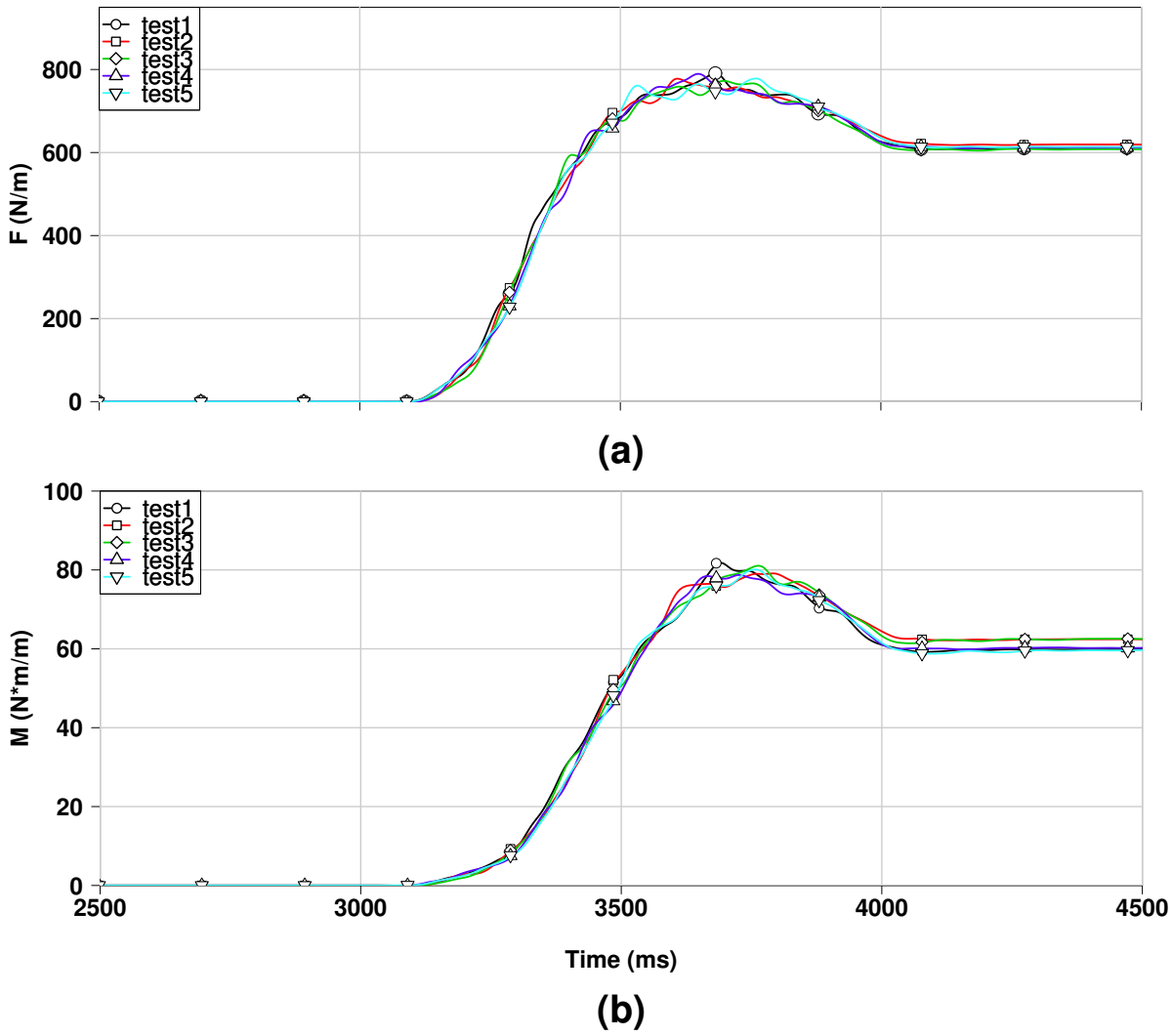

Figure 3.22: *Time history of the evolution of total normal force and bending moment (at the toe) for five tests that have the same initial conditions (test L44-H15-α40°): (a) Total normal force, (b) Total bending moment*

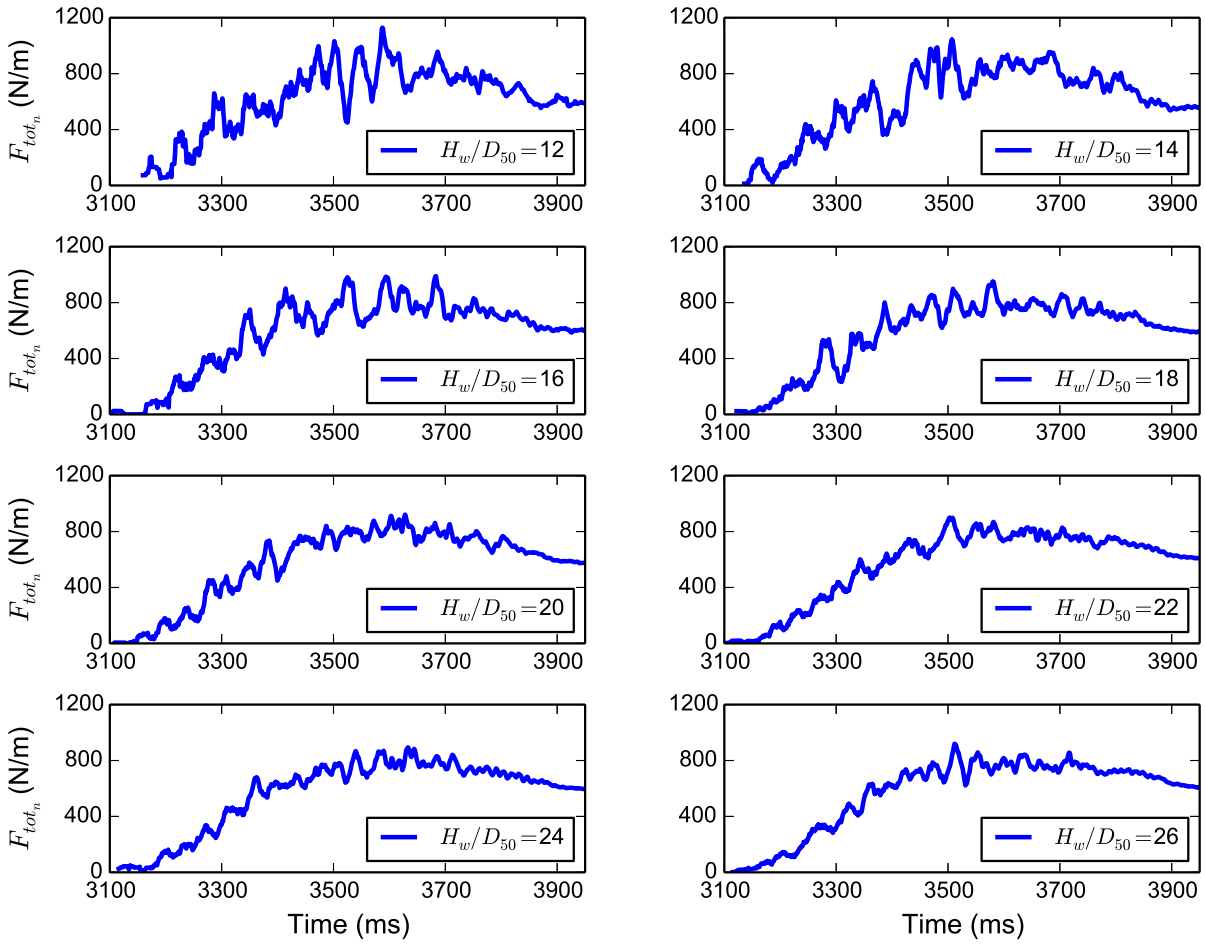

Figure 3.23: *Variation of the total normal force with time, for different ratios of* H_w/d_{50}

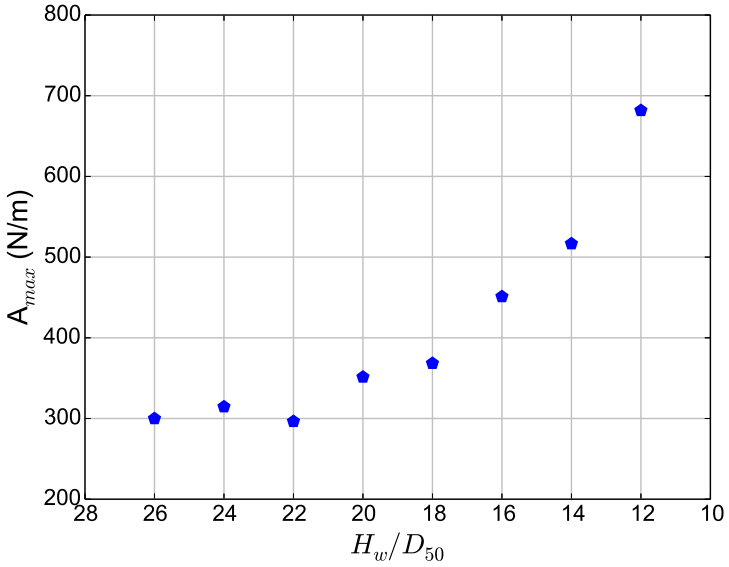

Figure 3.24: *Relationship between the amplitude of the total normal force and the ratio of H_w/d_{50}*

different simulations had the same weight and volume. Furthermore, the time step was the same for different simulations, which was calculated for the simulation with the lowest d_{50}, using equation 2.11. Testing geometrical conditions were the same as for test L44-H15-α40°. Data concerning F_{tot_n} was recorded at each time step of the different simulations. Figure 3.23 shows the evolution of F_{tot_n} with time for different ratios of H_w/d_{50}. When using big particles (small ratio of H_w/d_{50}), as the ones in H_w/d_{50} = 12, high fluctuations of F_{tot_n} value are observed. These fluctuations are the highest in the dynamic phase of the impact, around the maximum total normal force value (from t=3300 ms to t=3800 ms). On the other hand, with smaller particles (larger ratio of H_w/d_{50}), these fluctuations are found to be reduced (e.g. H_w/d_{50} = 26). As a result, a relation might exist between the amplitudes of the these fluctuations and the ratio of H_w/d_{50}.

To investigate this possible relation, the maximum amplitude of each signal A_{max} is extracted out of the force signal for each simulation (Fig. 3.24). The amplitude is calculated for the force signals in the period of time with the highest observed fluctuations; from t=3300 ms to t=3800 ms. The amplitude of F_{tot_n} is seen to increase when decreasing the ratio of H_w/d_{50}, i.e when increasing the size of d_{50} of the particles in the simulation. This relationship could be explained by the possible sudden buildup and vanishing of force chains behind the wall, in both impacting and depositing stages. If a two dimensional case is considered (for simplicity), the number of possible force chains to develop behind the wall could be related to the ratio H_w/d_{50}, assuming that

each particle in contact with the wall will develop one force chain. For the case of high fluctuations ($H_w/d_{50} = 12$), since d_{50} is large in comparison with the wall height, the number of force chains is small. As a result, sudden buildups and vanishes of number of force chains would strongly affect the total normal force applied to the wall. This would lead to high peaks (build up of force chains) followed by sharp drops of the signal of F_{tot_n}. On the other hand, for the case of low fluctuations (e.g. $H_w/d_{50} = 26$), d_{50} is small compared with the wall's height, thus higher number of force chains are expected to develop, however, each force chain value would be smaller than the case of $H_w/d_{50} = 12$. Thus, by having successive buildups and drops of force chains, little effect is noticed for F_{tot_n} signal. Such an argument needs to be investigated in details, by quantifying the force chains in 3D, which remains out of the scope of this thesis.

3.7 Evolution of total normal force components

The variation of total normal impact force with time is studied considering two components: gravitational and dynamic (Fig. 3.25). The calculation method has been presented earlier in Section 3.3.3.

Instantaneous values of δ_1 and δ_2 were calculated in the numerical simulation at each time step and then used in equation 3.12 to calculate the gravitational force. We can see that the final value of gravitational force (F_g) corresponds well to that of total normal force (F_{tot_n}) while the dynamic force (F_d) converges to zero agreeing with the absence of any movement of the particles.

We can also notice that at the beginning of the impact, small contribution of gravitational force is observed (Fig. 3.25). As time passes, more particles accumulate behind the wall and the gravitational force contribution becomes more significant. In addition, at the critical time where the total normal force reaches its maximum value, the dynamic component of the force is around 85% of the total while the gravitational one is only 15%. This indicates the importance of having a proper model for the flow with its flow thickness and velocity measurements.

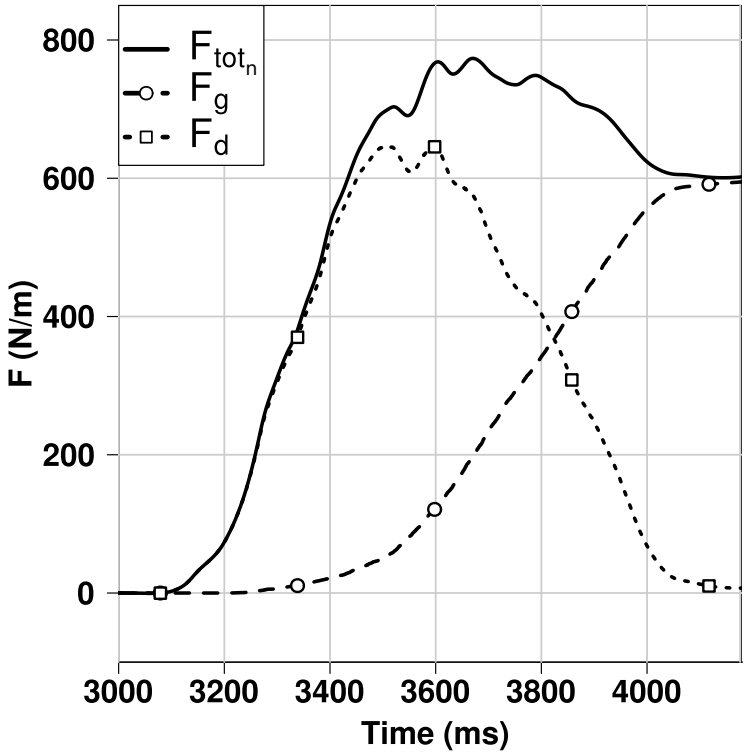

Figure 3.25: *Variation of total normal force components with time (test L44-H15-α40°)*

3.8 Conclusions

In this chapter, we presented the numerical model used to simulate the impact of dry granular flow against a rigid wall using clumped particles. With the use of experimental data of dry gravel flow, we calibrated our model considering the shape of the particle, the flow thickness and the final shape of the deposit on the wall. Concerning particle shape, the use of clumps was found to be beneficial in accounting for the shape effects caused by the sharp angles of coarse-grained particles. It was shown that the use of clumped particles is preferred over spherical ones in controlling rotational velocity which was reduced by 70 %. Indeed, the shape of the deposition behind the wall was improved by the clumped particles leading to a force distribution which is closer to the experimental values. Good agreement has been observed in terms of flow thickness and flow arrival times between the model and the experiment.

When compared with experimental data, the proposed model has shown capabilities of capturing the main features of normal impact force against a horizontally-divided rigid wall. These features are the peak force on each part of the wall, the time of the peak and the residual force at the end of the test. Moreover, total normal force and bending moment at the toe of the wall were closely captured by the model.

On the microscopic scale, microstructural heterogeneities (arching effect) were present in the experimental data and also, to some extent, in the numerical model. They were found to take place in the granular medium behind the rigid wall in both impacting and depositing stages. These heterogeneities were present even for samples with the same size and chute inclination angle, but different initial arrangement of particles. Such heterogeneities are unstable, and difficult to be precisely captured spatially and temporally.

The effect of particle size on the signal of the total normal force applied on the wall was investigated. An inverse relation was found to exist between the the fluctuation of the total normal force signal and the ratio between the height of the wall H_w and d_{50} of the flow (H_w/d_{50}). Such a relationship could be related to the successive buildup/drop of force chains behind the rigid wall.

In terms of total normal force components, it has been shown that accounting for the instant values of the ratio F_t/F_n for the interaction between the flow and both the wall and the base leads to better prediction of the accumulation process of the gravitational force on the wall. The dynamic component was found to contribute to 85% of the maximum total normal impact force on the wall, for high values of inclination angle. In the next chapter, the rigid wall will be replaced with a flexible barrier in which the impact behavior will be studied in details.

Chapter 4

Modeling the impact of granular flows against flexible barriers

Contents

4.1 Introduction

This chapter presents the simulation of flexible barriers impacted by granular flows. The granular flow simulated is the same flow model previously calibrated and validated in Chapter 3. The chapter starts with detailing the type of structure and flow to be considered. Afterwards, the numerical model and contact laws used for modeling flexible elements are presented. Three types of interaction are detailed; a sphere-sphere interaction, a sphere-cylinder interaction and a cylinder-cylinder interaction. Next, comparative simulations are carried out to compare two structures; one without energy dissipators (fbNo) and other one with energy dissipators (fbEd). Detailed results are presented concerning the evolution of flowing velocities, total force and dead zone mass with time. In addition, the internal forces and deformation within the structure are detailed. Next, parametric analyses are carried out in order to investigate the effect of some parameters on the impact behavior of the flow. These parameters are the inclination angle of the base and the inclination angle of the barrier with respect to the gravity vector. Finally, conclusions are drawn out of the discussed results.

4.2 Description of the flexible barrier and granular flow considered

In this section, the flexible barrier and granular flow considered in the numerical model are described. Flexible barriers (Fig. 4.1a) for hazard protection are generally composed of net elements, sliding rings, main cables, lateral cables, energy dissipators and lateral anchors (Nicot et al., 2001; Bertrand et al., 2012; Brighenti et al., 2013). All the flexible barrier components will be modeled using the cylinder model (Fig. 4.1b) that was primarily developed by Bourrier et al. (2013) for modeling plant roots' interaction with soil particles. General description of the considered flexible barrier components as well as the granular flow composition is detailed in the following sections. For convenience, the direction of the flow (i.e. parallel to the channel base) is referred to as x-direction, the transverse direction is called y-direction and the direction perpendicular to the channel base is called z-direction.

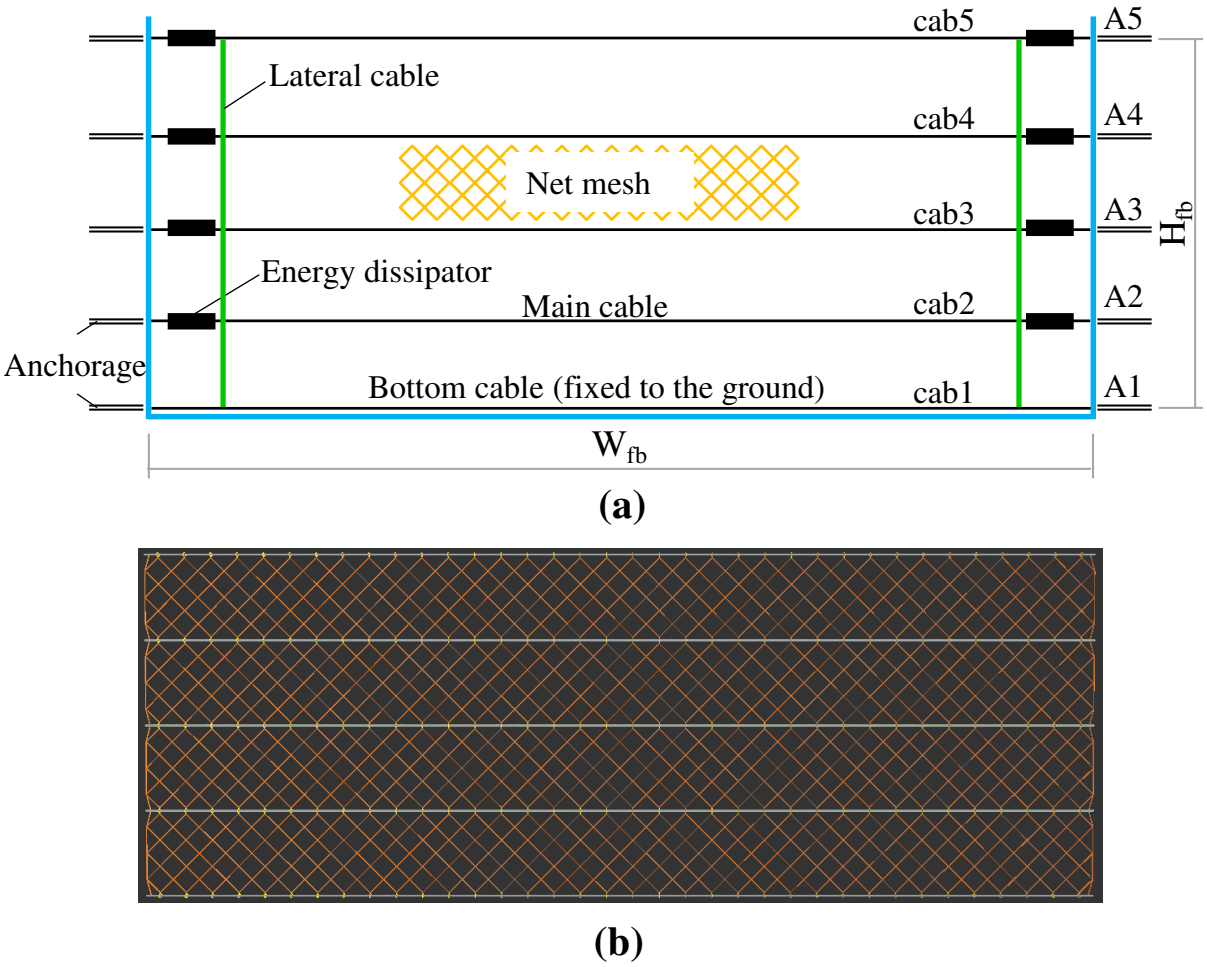

Figure 4.1: *Main components of flexible debris flow barriers* ***(a)*** *Schematic representation,* ***(b)*** *YADE model*

4.2.1 Net elements

Net elements in flexible barriers exist in many geometries which vary according to the purpose of the net element and manufacturing company. The net elements are the first to interact with external bodies of the flow and then transmit the forces into other components of the flexible barrier. They are usually tested using punching test. The punching test is aimed at representing the behavior of the net against a block punching through it, where the net is fixed to a metallic frame (Bertolo et al., 2009). Different punching bodies of different diameters were used in the past for testing square samples of nets (Bonati and Galimberti, 2004; Majoral et al., 2008; Agostini et al., 1988; Bertrand et al., 2012).

In this chapter, the net mesh considered in the numerical model was the same considered by Bonati and Galimberti (2004). The net is formed by 10 mm in diameter cable forming elementary mesh of 30 cm X 30 cm, which represents 45-degrees rotated squares (see net mesh in Figure 4.1). This type is considered because it is simple and easy to model in YADE using the cylindrical elements. Furthermore, in this thesis, no special industrial net configuration is considered in order to keep the design guidelines achieved rather general. Moreover, this simple net configuration with 45-degrees rotated squares allows for a diagonal load transmission which would limit the damage to the main cables. In addition, the cell size (300 mm) of the mesh is suitable for particles' mean diameter ($D_{50} = 450mm$) of the considered flow, which limits particles flowing through the net. The calibration of the net model against the experimental data of Bonati and Galimberti (2004) will be detailed in Section 4.4.1.

4.2.2 Sliding rings

Sliding rings are rigid elements that connect the net to the main cables and allow for the force transmission between them up to the lateral anchors. Moreover, they allow the net to slide on the main cables and add additional freedom for the structure to deform. Allowing for the sliding of these rings has not been addressed in details in the literature, except some few attempts (e.g. Volkwein, 2005). In the numerical model, these sliding rings are modeled as a square formed by four cylinders, each cylinder is 16 mm in diameter D_r (Fig. 4.2). Theses four cylinders could easily slide on the main cables with the presence of frictional force between the two interacting elements. From one of its corners, the ring is connected to the net using one cylinder element. Such approach of

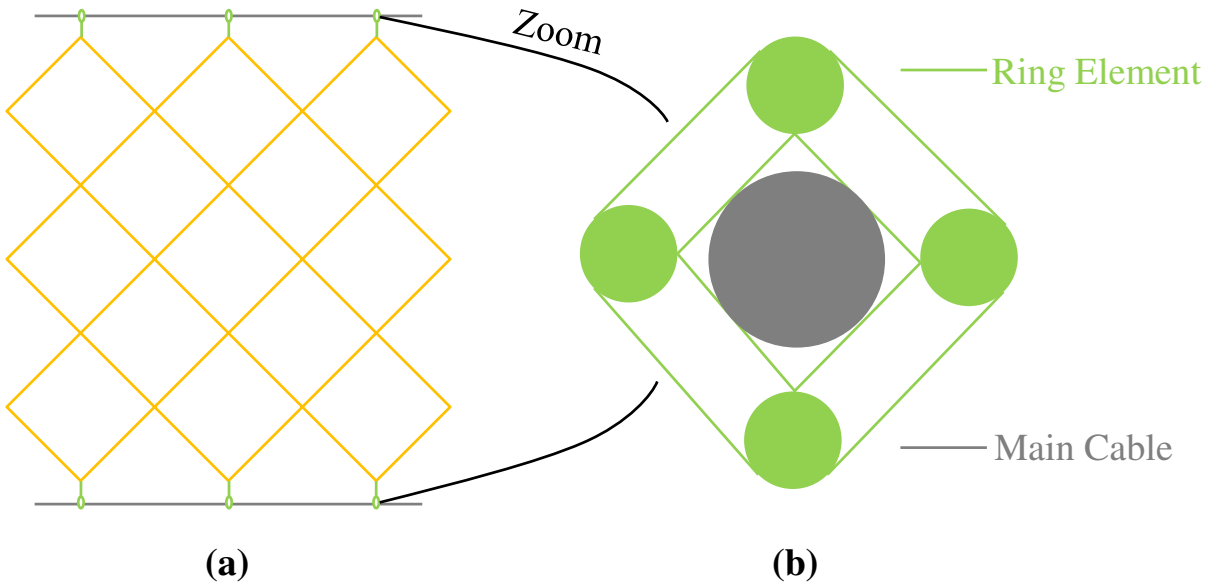

Figure 4.2: *A schematic representation of the sliding rings arrangement:* ***(a)*** *front view of the net, ring and main cables,* ***(b)*** *cross section of the ring*

representing the sliding rings is advantageous in being computationally inexpensive, especially that a full scale structure would require large number of rings. The choice of the value of friction between the rings and main cables along with more details on the ring model are presented in Section 4.4.2.

4.2.3 Main and lateral cables

Main cables are usually installed horizontally in the flexible barrier and are attached to the anchors on the two sides. The net elements are attached to the main cables via the rings. Main cables used in the simulation were of 32 mm in diameters (D_{mc} = 32 mm) with five cables being installed horizontally. The bottom cable was fixed to the bottom of the channel bed, in order to prevent flowing particles form escaping beneath the structure (Brighenti et al., 2013). If energy dissipators are in use, two of them are installed at the extremities of each main cable. Each main cable was modeled as a series of connected cylinders. The length of the cylinder should be small enough so that, on the scale of the structure, the cable could deform freely in a close representation of reality. However, as the cylinders get smaller in length, the number of cylinders required to form a long cable would be very large making the simulations computationally demanding. A cylinder length (center-to-center) of 70 mm has been chosen for the modeling of the main

cables. For example, a flexible barrier with a width of 15.20 m would need 217 cylinders to form each main cable. The lateral cables on the other hand connect the side points of the net and provide lateral confinement of the retained material. The diameter used for the lateral cable (D_{lc}) was 16 mm.

4.2.4 Energy dissipators

Energy dissipators are devices used to limit the forces transmitted to the lateral anchors by impacting bodies (rockfall, granular flow .. etc). Their working mechanism depends on their ability to deform, which provides the possibility of energy dissipation. They are usually installed at the extremities of the main cables in which they limit the force transmission from the main cables to the anchors, thus protecting the anchors from excessive loads. At the beginning of an impact (Fig. 4.3a), the external bodies impacting the structure would impose loads on the net. Afterwards, these loads will be transmitted to the main cables and then to the energy dissipator. The energy dissipators will deform elastically until reaching the elastic limit. Once reached, plastic strains will start taking place and energy dissipators will keep straining up to a failure length (Fig. 4.3b). Such length is not supposed to be reached during the impact as it would transmit high forces to the anchors which might cause the structure to fail. Energy dissipators exist in many mechanisms. Examples of these mechanisms include: elastic perfectly-plastic mechanism, buckling-friction mechanism and the brittle mechanism (Bertrand et al., 2012). Their elastic limit force can vary from 100 to 300 kN (Boutillier and Marzouk, 2010).

The energy dissipators in this thesis are modeled as elastic perfectly-plastic elements. At the beginning, the energy dissipators deform linearly elastic until reaching an elastic limit. Once reached, the dissipators start perfect plastic straining, which is limited by a maximum deformation of 2.5 m (Fig. 4.3c). If reached, the forces will be directly transferred to the anchors without limitation. Two energy dissipating devices were installed at the extremities of each main cable. Results showing the effects of using energy dissipators on the behavior of the flexible barrier will be presented in Section 4.5.

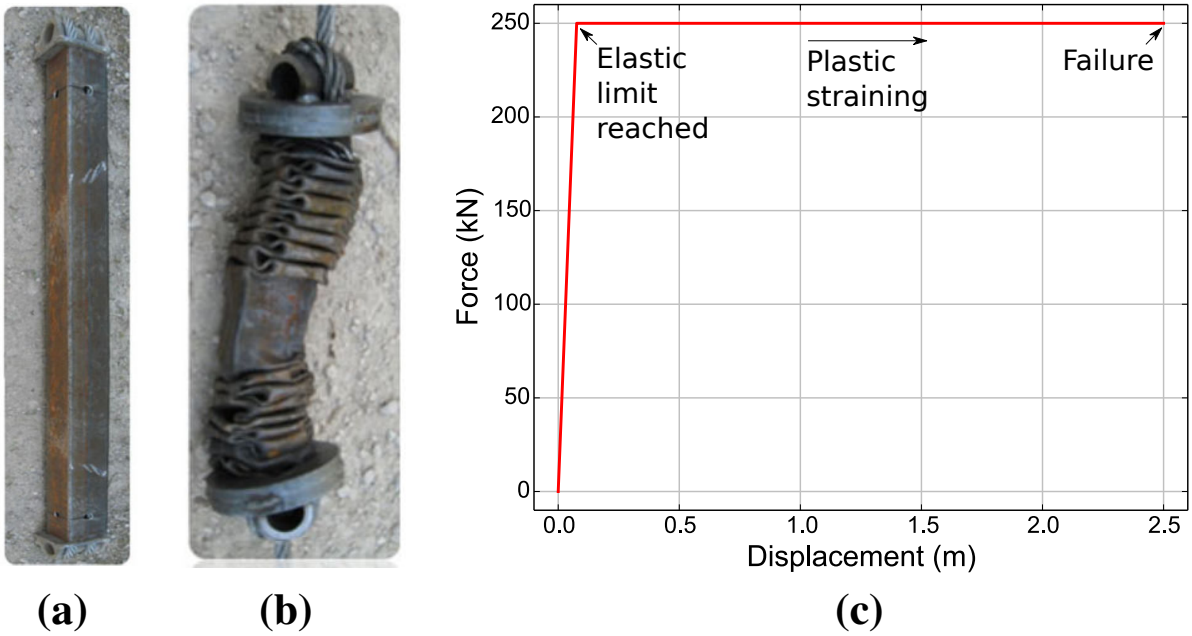

Figure 4.3: *Energy dissipators:* ***(a)*** *Before the impact,* ***(b)*** *At the end of the impact (after Bertrand et al., 2012),* ***(c)*** *The force:displacement response of the energy dissipators considered in our DEM model*

4.2.5 Granular flow description and scaling

The granular flow model in this chapter is the same as the one calibrated and validated in Chapter 3, but with a larger scale. The channel, which is rectangular in shape, has a width (w_{ch}) of 15.20 m, a length (l_{ch}) of 30 m , a height (h_{ch}) of 10 m and an inclination angle of (α) of 40°. At the end of the channel, a flexible barrier is installed in a vertical direction (parallel to gravity vector). The flexible barrier has a width (W_{fb}) of 15.20 m (same as the channel) and an initial height (H_{fb}) of 5.50 mm. The flow is composed of clumps that are formed by two identical spheres overlapping over a distance equal to their radius, with $D_{50} = 450$ mm and a total initial mass of 340 tons. The normal restitution coefficient $\varepsilon_n = 0.3$ and the tangential one is equal to zero. Although a larger scale is used, the flow is still in supercritical state. This is accounted for by the Froude number (F_r), which is a dimensionless parameter used to indicate the influence of gravity on fluid motion (Pudasaini and Domnik, 2009; Domnik and Pudasaini, 2012; Faug et al., 2012). It measures the ratio between of the inertia force on a fluid element to the weight of that element, and is calculated as follows:

$$F_r = \frac{\overline{v}}{\sqrt{g\, h\, cos\alpha}} \tag{4.1}$$

where $\overline{v}$ is the depth-averaged velocity of the flow, g is the gravity acceleration, h is the flow depth and α is the inclination angle of the base.

Three flow states could be identified using Froude number: a subcritical flow ($F_r < 1$) a critical flow ($F_r = 1$) and a supercritical flow ($F_r > 1$) (MiDi, 2004). Using equation 4.1, F_r values of the two flows (small scale of Chapter 3 and the large scale used here) have been calculated and found to be 6.15 and 3.28 respectively. Both values are larger than one indicating the presence of supercritical fast-flowing flows. As a result, the small scale flow calibrated and validated in Chapter 3 could be scaled up in this chapter and be used for the impact against full scale flexible barriers.

4.3 The cylinder model in YADE

In this section, the numerical model for flexible elements is presented. It is based on the general method of modeling deformable objects that was primarily developed by Bourrier et al. (2013) and later on extended by Effeindzourou et al. (2016) for modeling geotextiles and geomembranes. In this modeling method, every shape of flexible elements is represented using a cylinder as a basic element (Fig. 4.4). Cylinders in the model are rigid objects similar in principle to the spheres in DEM. They however deform at the contact area with other particles in which displacements and velocities are calculated. With such simplicity, any geometrical shape of flexible elements is easy to set up in the numerical model. In addition, the cylindrical element does not introduce any numerical roughness, in contrast to remote interaction models. This is because the cylinder geometrically corresponds to the Minkowski sum of a sphere and a segment (Effeindzourou et al., 2016). Furthermore, less effort is needed for contact detection due to the simplicity of the elements. Moreover, contact sliding is permitted to take place along the outer surface of cylinders, which has not been previously accounted for in the literature except some few attempts (e.g. Volkwein, 2005). Three types of possible interactions that could take place for flexible structures are presented in the following sections: sphere-sphere interaction, sphere-cylinder interaction and cylinder-cylinder interaction. Afterwards, the conditions for applying plastic deformation in the cylinders are presented.

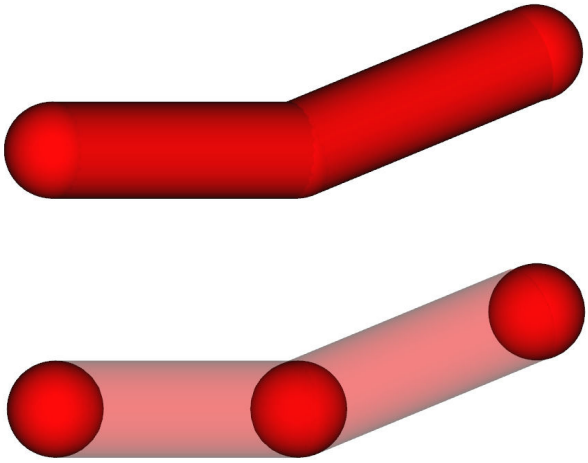

Figure 4.4: *A sample of two connected cylindrical elements with two nodes at the ends of each cylinder*

4.3.1 Sphere-sphere interaction

A sphere-sphere interaction for flexible elements is the internal interaction between the two adjacent nodes of a cylinder. The position and orientation of these two nodes define the deformation of the cylinder. Such deformation take place along the longitudinal axis of the cylinder and thus could be either normal (tensile and compressive), tangential, bending or twisting deformation. The contact law used for this interaction link the relative displacement and relative rotation at the contact point to the contact force **F** and bending moment **M** (Bourrier et al., 2013). The normal and tangential forces (F_n and F_t) are calculated as follows:

$$\mathbf{F_n} = k_n \mathbf{n}_n \tag{4.2}$$

$$d\mathbf{F_t} = k_t \dot{\mathbf{u}}_t \Delta t \tag{4.3}$$

where k_n and k_t are the elastic stiffness parameters of the normal and tangential force respectively, $\mathbf{n_n}$ is the normal displacement vector, $\dot{\mathbf{u}}_\mathbf{t}$ is the relative tangential velocity and Δt is the time step between two successive time steps.

Similarly, relative rotation of the two spheres is used to define the bending $\mathbf{M_b}$ and twisting moments $\mathbf{M_t}$. They are calculated as follows:

$$\mathbf{M_b} = k_b \mathbf{\Omega}_{12}^{b} \tag{4.4}$$

$$\mathbf{M_{tw}} = k_{tw} \mathbf{\Omega}_{12}^{tw} \tag{4.5}$$

where k_b and k_{tw} are bending and twisting stiffness parameters of the bending and twisting moments respectively and $\mathbf{\Omega}_{12}^{b}$ and $\mathbf{\Omega}_{12}^{tw}$ are the bending and twisting components of the relative rotation between the two spheres.

Bourrier et al. (2013) used the sphere-sphere interaction between two nodes (N_1 and N_2) of a cylinder to define the cylinder as a beam-like behaving object (Zienkiewicz and Taylor, 2005). Thus, by considering each cylinder as a beam with length L_c, stiffness parameters k_n, k_t, k_b, k_tw can be calculated as follows:

$$k_n = \frac{E_n A_c}{L_c} \tag{4.6}$$

$$k_t = \frac{12 E_b I_b}{L_c^3} \tag{4.7}$$

$$k_b = \frac{E_b I_b}{L_c} \tag{4.8}$$

$$k_{tw} = \frac{G_{tw} I_{tw}}{L_c} \tag{4.9}$$

where E_n is the elastic modulus (tensile or compressive), A_c is the reference surface area ($A_c = \pi R^2$, where R = min (R_1,R_2) in which R_1 and R_2 are the radii of the two cylinder nodes), L_c is the length of the cylinder (distance between the two nodes forming it), E_b is the bending modulus, I_b is the bending moment of inertia ($I_b = \pi R^4/8$), G_{tw} is the shear modulus for the twisting moment and I_{tw} is the polar moment of inertia ($I_{tw} = \pi R^4/4$)

4.3.2 Sphere-cylinder interaction

The sphere-cylinder interaction reflects an interaction between a body of the granular flow and a cylinder that forms part of a flexible barrier (e.g. net elements). In order to calculate the deformation at the contact between the sphere and the cylinder, a virtual sphere (S_{vir}), of same radius as the cylinder, is placed at the axis of the cylinder (Fig. 4.5).

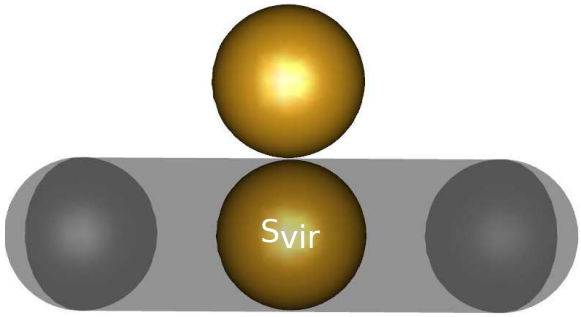

Figure 4.5: *A representation of the sphere-cylinder interaction showing the virtual sphere of a cylinder at the contact point*

When an external particle get in contact with the cylinder, the center of the virtual sphere is defined as the projection of the contact point along the segment connecting the cylinder's nodes. Displacements at the surface of the cylinder vary linearly between its two nodes. Forces and bending moments are distributed on the nodes of the cylinder after interpolating their share according to the transnational and rotational velocities of the virtual sphere. The normal and tangential contact forces between the sphere and the cylinder can be calculated using equations 4.2 and 4.3 in which:

$$k_n = \frac{2E_s r_s E_c r_c}{E_s r_s + E_c r_c} \tag{4.10}$$

where E_s and E_c are the elastic moduli of the sphere and cylinder respectively and r_s and r_c are the radii of the sphere and cylinder respectively. The tangential stiffness coefficient of the contact between the two is taken as $k_t = (2/7)k_n$.

4.3.3 Cylinder-cylinder interaction

In order to account for the interaction forces between some elements of the flexible barrier (e.g. rings and main cables), the cylinder-cylinder interaction is implemented in the model. For a set of two cylinders C_1 and C_2, two nodes exist on both sides of each one: $N_1^{C_1}$ and $N_2^{C_1}$ for the first cylinder and $N_1^{C_2}$ and $N_2^{C_2}$ for the second one (Fig. 4.6). The two cylinders could be represented by two segments A and B where A=$\|N_1^{C_1} N_2^{C_1}\|$ and B=$\|N_1^{C_2} N_2^{C_2}\|$. The parametric equations of segments A and B can be defined as (Effeindzourou et al., 2016):

$$A(m) = N_1^{C_1} + m\mathbf{a} \tag{4.11}$$

$$B(n) = N_1^{C_2} + n\mathbf{b} \tag{4.12}$$

where m and n are coefficients between 0 and 1 and **a** and **b** are the direction vector of segments A and B respectively.

At the contact point between the two cylinders, the minimum distance between the two could be represented by a vector **D** in which:

$$\mathbf{D_c} = A(m_c) - B(n_c) \tag{4.13}$$

If the two segments A and B are neither parallel nor intersecting, vector $\mathbf{D_c}$ is uniquely perpendicular to both of them. Thus the following set of equations are satisfied:

$$\begin{cases} \mathbf{D_c} = A(m_c) - B(n_c) \\ \mathbf{a} \cdot \mathbf{D_c} = 0 \\ \mathbf{b} \cdot \mathbf{D_c} = 0 \end{cases} \tag{4.14}$$

Solving equation 4.14 yields:

$$\begin{cases} \mathbf{m_c} = \frac{(\mathbf{a}\cdot\mathbf{b})(\mathbf{b}\cdot\mathbf{D_0}) - \|\mathbf{b}\|(\mathbf{a}\cdot\mathbf{D_0})}{\|\mathbf{a}\|\|\mathbf{b}\| - (\mathbf{a}\cdot\mathbf{b})^2} \\ \mathbf{n_c} = \frac{\|\mathbf{b}\|(\mathbf{b}\cdot\mathbf{D_0}) - (\mathbf{a}\cdot\mathbf{b})(\mathbf{a}\cdot\mathbf{D_0})}{\|\mathbf{a}\|\|\mathbf{b}\| - (\mathbf{a}\cdot\mathbf{b})^2} \end{cases} \tag{4.15}$$

where $\mathbf{D_0} = N_1^{C_1} - N_1^{C_2}$

After calculating the contact point's location on both cylinders, the normal and tangential contact forces between the two cylinders could be then calculated using equations 4.2, 4.3 in which:

$$k_n = \frac{2E_{c_1}r_{c_1}E_{c_2}r_{c_2}}{E_{c_1}r_{c_1} + E_{c_2}r_{c_2}} \tag{4.16}$$

where E_{c_1} and E_{c_2} are the elastic moduli of the first and second cylinder respectively and r_{c_1} and r_{c_2} are the radii of the first and second cylinder respectively. The tangential stiffness coefficient at the contact between the two is taken as $k_t = (2/7)k_n$.

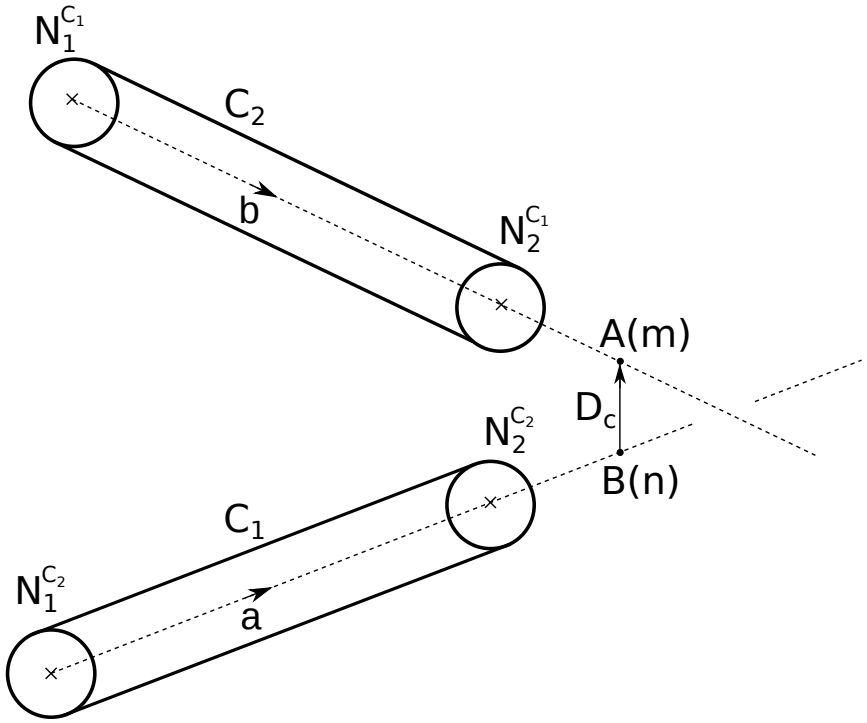

Figure 4.6: *The distance vector between two non-intersecting cylinders (adapted from Effeindzourou et al., 2016)*

4.3.4 Plastic deformation of the cylinders

The model has the capability to include an elastic limit. Once reached the cylinders will deform plastically. Such a limit is usually imposed when the failure of the structure is needed to be studied. However, in practice, the flexible barriers are supposed to sustain the loads without going through plastic deformation. The only elements that are usually allowed to deform permanently are the energy dissipators which are usually replaced by new ones at the end of impact events. Thus, in this thesis, elastic limit is only imposed on energy dissipators and not on the net or main cables. This elastic limit is introduced in the model by the following criteria:

$$\begin{aligned} \|\mathbf{F}_n\| &\leqslant \sigma_n^{el} A_c \\ \|\mathbf{F}_t\| &\leqslant F_n tan\phi + \sigma_s^{el} A_c \\ \|\mathbf{M}_b\| &\leqslant \frac{\sigma_s^{el} I_{tw}}{R} \\ \|\mathbf{M}_{tw}\| &\leqslant \frac{\sigma_n^{el} I_b}{R} \end{aligned} \tag{4.17}$$

where σ_n^{el} and σ_s^{el} are the elastic tensile and shear limits respectively, ϕ is the reference friction angle ($\phi = \min(\phi_1, \phi_2)$ in which ϕ_1 and ϕ_2 are the friction angles of the two cylinder nodes), I_b and I_{tw} are the reference polar and bending moments of inertia respectively ($I_b = \frac{\pi R^4}{4}$ and $I_{tw} = \frac{\pi R^4}{8}$) and R is the reference radius of the contact ($R = min(R_1, R_2)$). An elastic perfectly-plastic model has been adopted using this criteria to model the energy dissipators.

4.4 Model description and validation

In this section, the calibration procedure of the net elements against experimental data will be presented. Furthermore, the mechanical parameters of the sliding rings will be discussed with a special focus on the value of friction between the sliding rings and main cables.

4.4.1 Net element

The net elements in the model are calibrated using experimental date from Bonati and Galimberti (2004). They carried out two punching tests; the first using a cone 78 cm in height and 68 cm in diameter (Fig. 4.7a) and the second using a concrete round-shaped element 150 cm in diameter (Fig. 4.7b). The first test was the one considered for model calibration as it is easier to model in YADE. The net was composed of 10 mm in diameter cables forming elementary mesh of 30 cm X 30 cm, which represented 45-degrees rotated squares. The net panel (3 m X 3 m in size) was fixed to a metallic frame from the four sides and the punching elements were pulled out against the net panel through its center. Records were taken for the load-displacement behavior of the net panel. Results of the punching test are presented in Figure 4.8. A loose response is seen at the first phase of loading of the net (from displacement = 0 to displacement = 150 mm). Afterwards, a stiffer response is observed which is progressive until the failure point is reached at a normal force applied by the punching body on the net panel of 36.5 kN and a maximum vertical displacement of the net of 225 mm.

In order to calibrate the net mechanical parameters in the model, the same loading conditions are reproduced in the model along with the geometry of the net mesh (Fig. 4.9). In YADE, the net panel was 3 m X 3 m in size with the same mesh opening and diameter as the one in the experiment (300 mm and 10 mm respectively). The mesh panel was

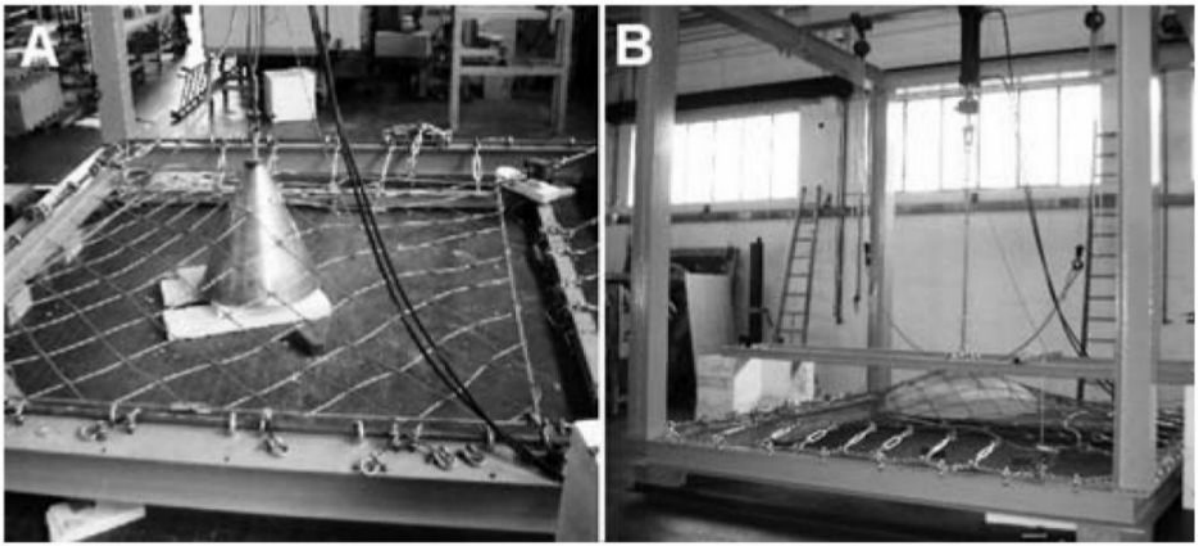

Figure 4.7: *Experimental punching test* ***(a)*** *cone punching element* ***(b)*** *rounded-concrete punching element (after Bonati and Galimberti, 2004)*

fixed to the boundaries, but the rotational displacement was permitted, similar to the conditions of the experiment. A spherical body with a diameter of 680 mm was vertically imposed to the net panel, punching through its center. Different values of the elastic modulus of the net (E_n) were tested until reaching a good calibration results (Fig. 4.8) using E_n = 4 GPa. In the full scale simulation, the same elastic modulus was used but with a diameter (D_n) increased to 16 mm to sustain the high loads of the granular flow (Section 4.5).

4.4.2 Sliding rings

Sliding rings in YADE are modeled using cylinders, by using the cylinder-cylinder interaction implemented in the model. In terms of stiffness, the rings are modeled with a twice higher stiffness than that of the net elements (E_r = 8 GPa). This is to ensure their rigidity and to prevent them from deforming. Besides, two diagonal remote interaction were added to each ring to prevent it from deforming. One parameter needs to be investigated here: the effect of the variation of friction angle value between the main cables and the sliding rings δ_{rc}. This is to verify whether or not changing such parameter will affect the obtained results in the numerical model. It is especially important as four points of contact exist between each ring and main cable.

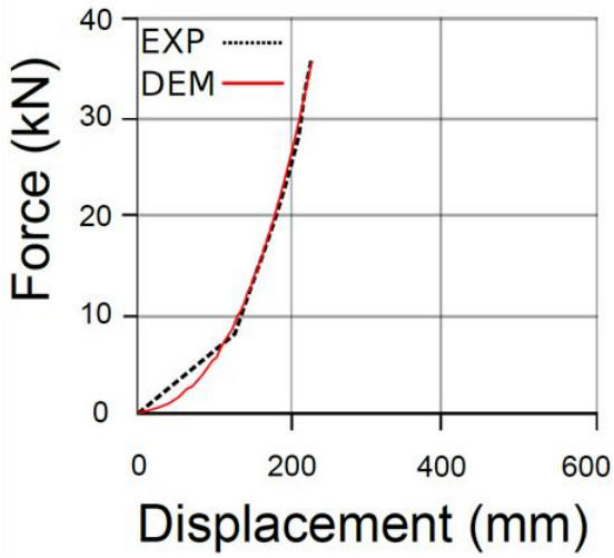

Figure 4.8: *Net punching results comparison between the experiment (data from Bonati and Galimberti, 2004) and the model*

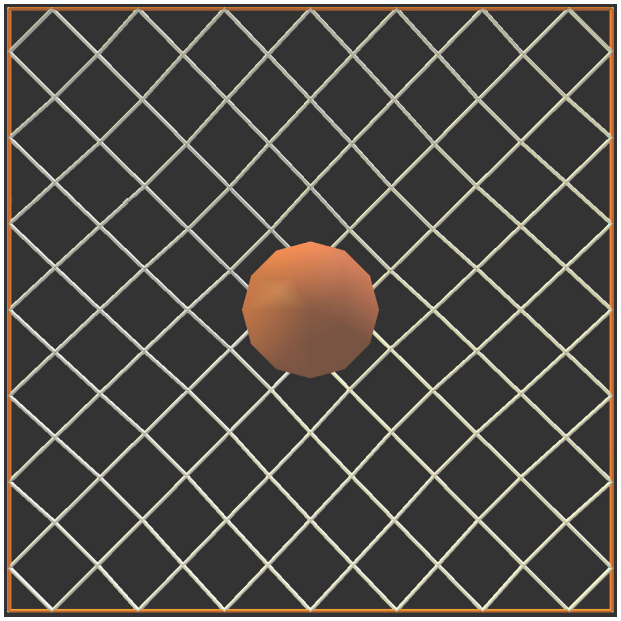

Figure 4.9: *The simulated net punching test in the numerical model with DEM*

To study the sensitivity of this parameter, full scale simulations need to be carried out on a flexible barrier with the same geometry and flowing material described in (Section 4.2). Comparisons are made based on the deformation of the structure, i.e. the elongation of the energy dissipators and maximum extension of main cables in the direction of the flow. Moreover, forces applied on the anchors are also compared. Three different values of friction angle have been tested: 4, 12 and 20°. All other parameters were kept the same through the three simulations. For convenience, the results shown are only for cables 3 and 4, as these cables were found to be the highest loaded ones.

First we compare the deformation of energy dissipators installed at the extremities of each main cable. The deformation of the energy dissipators has been recorded with time for each cable and the ratio of $\delta_{ED}/\delta_{ED-brk}$ has been plotted (Fig. 4.10). The values of δ_{ED} are the mean values of deformation of the two energy dissipators installed at the ends of each cable and δ_{ED-brk} is the maximum allowable deformation of the energy dissipators in which afterwards it would break (taken as 2.5 m for the case under consideration). For low values of friction angle ($\delta_{rc} = 4^{\circ}$), the deformation of the dissipators is found to start earlier than the other two cases. Moreover, higher deformations of energy dissipators of cables 3 and 4 are recorded (Fig. 4.10). These energy dissipators have final deformations that are 57% and 83% the value of δ_{ED-brk}. When increasing the friction angle ($\delta_{rc} = 12^{\circ}$ and 20°), lower deformations are recorded for energy dissipators (45% and 73% of δ_{ED-brk} for cables 3 and 4 respectively) which are very similar for the two cases.

Next, we compare the maximum extension of the main cables in the direction of the flow. It is defined as the maximum point reached by each main cable, in x-direction. When comparing maximum extension of cables in the direction of the flow, similar trends could be observed (Fig. 4.11). Low values of δ_{rc} result in higher extension of the cables 3 and 4, with extensions of 4.45 and 5.85 meters respectively. Furthermore, such extensions are relatively earlier for $\delta_{rc} = 4^{\circ}$ than for other values of δ_{rc}. In contrast, higher values of δ_{rc} result in lower maximum extension of cables 3 and 4. In addition, cables extension values for $\delta_{rc} = 12^{\circ}$ and $\delta_{rc} = 20^{\circ}$ are very similar. Final extensions of cables 3 and 4 are around 4.4 and 5.6 m respectively. The recorded extensions are found to be 0.1 seconds delayed on average, in comparison with the $\delta_{rc} = 4^{\circ}$ case. Overall, the difference between maximum extension of cables 3 and 4 for different values of δ_{rc} is rather limited (less than 5%).

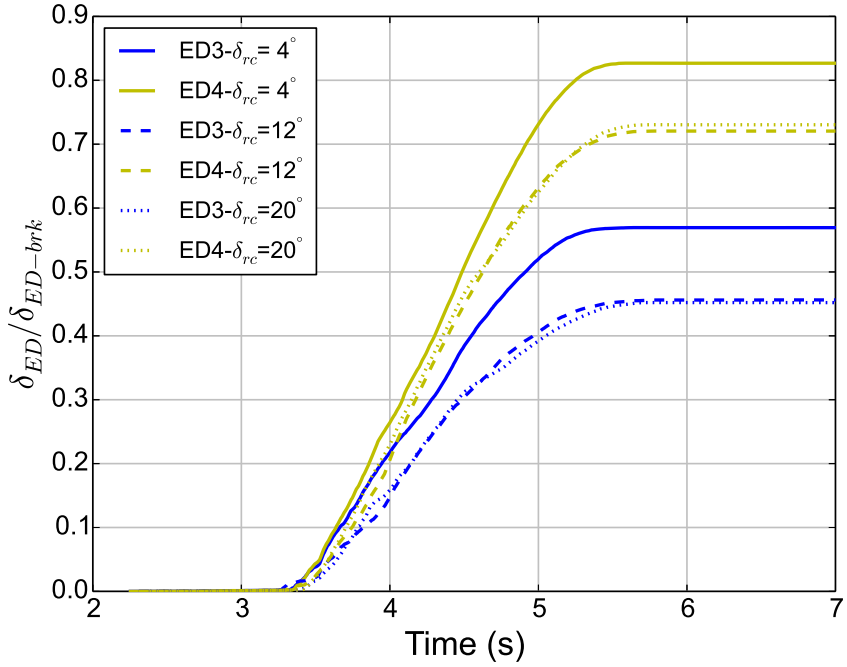

Figure 4.10: *The evolution with time of the average deformation of each two energy dissipators at the same cable, for different values of friction between the sliding rings and main cables*

Afterwards, we compare the force values on the anchors of cables 3 and 4, referred to as A3 and A4 respectively, for different values of δ_{rc}. Forces transmitted to the anchors have been recorded with time and the ratio of F_a / F_{ED-els} has been plotted (Fig. 4.12). F_a values are the mean values of forces on the two anchors located at the extremities of a given cable and F_{ED-els} is the elastic limit of the forces in the energy dissipators in which afterwards it starts deforming (taken as 250 kN for the case under consideration). For $\delta_{rc} = 4^\circ$, anchors are found to be loaded slightly earlier than the other two cases. After reaching the elastic limit of the force F_{ED-els}, they start plastic straining until the end of the avalanche event. Final values of residual force on the anchors are lower for low δ_{rc} values. However, the difference between residual force values of the anchors for the different δ_{rc} values is rather small (less than 5%).

The previous results could be analyzed by considering energy dissipation by friction. For low values of δ_{rc}, higher deformation of energy dissipators were recorded coupled with higher extensions of the main cables. This could be linked to the low frictional resistance against the tendency of the rings to slide on the main cable. As a result, the sliding rings do not dissipate much energy by friction and thus the energy dissipators

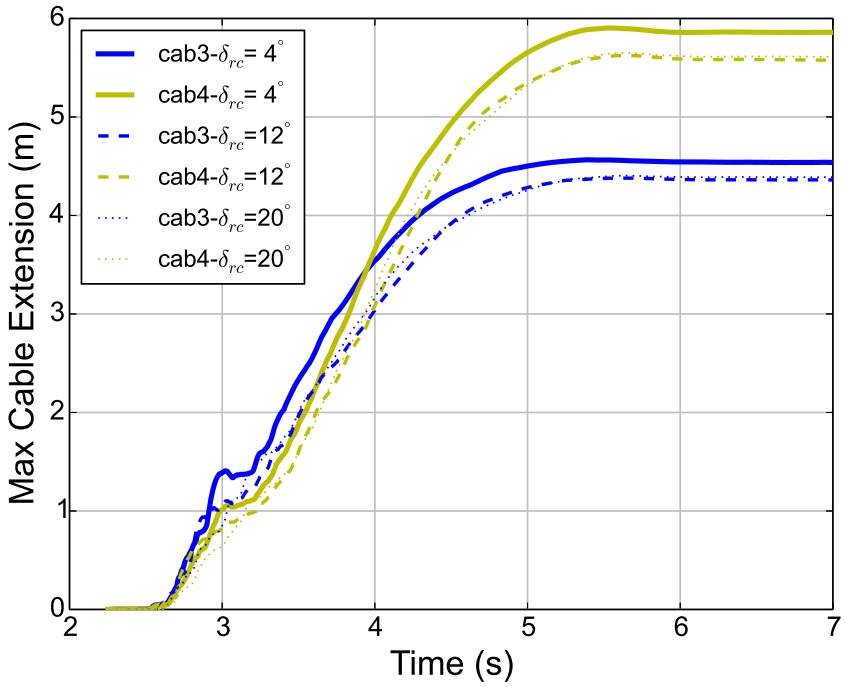

Figure 4.11: *The evolution with time of the maximum extension of main cables in the direction of the flow, for different values of friction between the sliding rings and main cables*

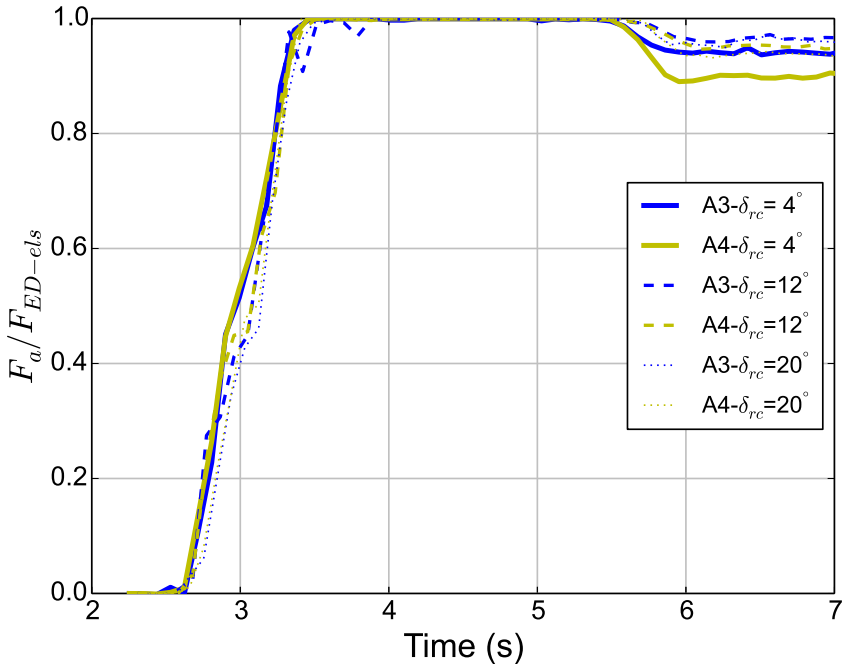

Figure 4.12: *The evolution with time of the average force on each two anchors at the same cable, for different values of friction between the sliding rings and main cables*

dissipate most of the energy. This results in higher deformations of energy dissipators which explains the high extension of main cables (global deformation of the structure). On the other hand, higher values of δ_{rc} might lead to higher frictional resistance to sliding. Such resistance might dissipate some of the kinetic energy of the flow which thus reduces the amount of energy that should be dissipated by the energy dissipators. This leads to lower deformations of energy dissipators which results in lower extensions of the structure in the direction of the flow. However, differences between the results for different values of δ_{rc} are found to be less than 5%.

To sum up, we can conclude that although some differences are seen on the deformation of the energy dissipators and barrier extension, such differences are rather small in values. Thus, overall, we can assume that the simulation results are not very sensitive to this parameter. However, high values of δ_{rc} could result in sliding rings being blocked from sliding due to the higher frictional resistance. Such blocked movement could result in high loads at the connection between the rings and the net which could lead to the failure of that point (rupture of cylinders that connect rings with net elements, see Figure 4.2). As a result, in order to avoid this possibility, a value of $\delta_{rc} = 5^{\circ}$ has been adopted for all the simulations of flexible barriers in this thesis.

4.5 Full scale simulations of granular flow impact on flexible barriers

In this section, full-scale simulations are conducted for the impact of granular flows against flexible barriers. The radii and mechanical parameters of the flexible barrier components are mentioned in table 4.1. Two cases are compared in the following sections; the case where no energy dissipators are used (fbNo) and a second case where energy dissipators are in use (fbEd). First, results concerning the evolution of flowing velocities (in x and z directions), total force applied on the structure and the evolution of the dead zone are compared. Next, comparison are carried out concerning the internal forces and deformation in the structure's components (main cables, energy dissipators and lateral anchors). Finally, the loads transmitted to the anchors are compared for the two cases.

Parameter	value
net diameter D_n (mm)	16
net elastic modulus E_n (GPa)	4
ring element diameter D_r (mm)	16
ring elastic modulus E_n (GPa)	8
ring-cable friction angle θ_{rc} (°)	5
main cable diameter D_{mc} (mm)	32
main cable elastic modulus E_{mc} (GPa)	4
lateral cable diameter D_{lc} (mm)	16
lateral cable elastic modulus E_{lc} (GPa)	4
energy dissipators elastic modulus E_{ED} (GPa)	4
elastic force limit of energy dissipators F_{ED-els} (kN)	250
maximum allowable deformation of energy dissipators δ_{ED-brk} (m)	2.5

Table 4.1: *Mechanical and geometrical properties of the flexible barrier elements*

4.5.1 Flowing velocity evolution with time

The evolution of the average velocity of the granular flow (in both x and z directions) with time were recorded for the two cases (fbNo and fbEd cases). This is to compare the break down with time of these flowing velocities between the two structures. The average flowing velocity in the direction of the flow ($\overline{U}_x$) and the direction perpendicular to the flow ($\overline{U}_z$) are the average velocities of all particles forming the flow in the directions parallel to the flow and perpendicular to the base respectively. $\overline{U}_x$ and $\overline{U}_z$ are calculated as follows:

$$\overline{U}_x = \frac{\sum_{i=1}^{n_p} U_x}{n_p} \tag{4.18}$$

$$\overline{U}_z = \frac{\sum_{i=1}^{n_p} U_z}{n_p} \tag{4.19}$$

where U_x and U_z are the particle's velocity components in the x and z directions respectively and n_p is the number of particles in the simulation.

The flowing velocity in the direction of the flow $\overline{U}_x$ reaches a maximum value of 8.85 m/s at t = 3 seconds (Fig. 4.13a). Afterwards, the value of $\overline{U}_x$ starts decelerating. For the case where no energy dissipators are used (fbNo), a sharp deceleration of flowing velocity is observed. The flowing velocity decelerates from its maximum value at t = 3 seconds to zero over a period of 2.2 seconds. For the case where energy dissipators are used (fbEd), a smoother break down of flowing velocity is observed. The flowing velocity gets broken down from its maximum value to zero over a period of 2.75 seconds. It worth noting that the moment when the two curves are thought to start splitting is the moment when the energy dissipators are activated (t = 3.4 seconds), as will be discussed in Section 4.5.5. At this moment, for fbEd case, the structure gets additional length from the energy dissipators which allows it to keep extending in the direction of the flow resulting in a delayed response with a longer period of flowing velocity break down.

For the z-component of flowing velocity $\overline{U}_z$ (Fig. 4.13b), it starts increasing at the moment where $\overline{U}_x$ reaches its maximum value (t = 3 seconds). This is because before that moment, all particles have their velocities in the direction of the flow with very small average velocity in the direction perpendicular to the base. At t = 3 seconds, part of the flow starts being diverted and particles start to have z-component of their flowing

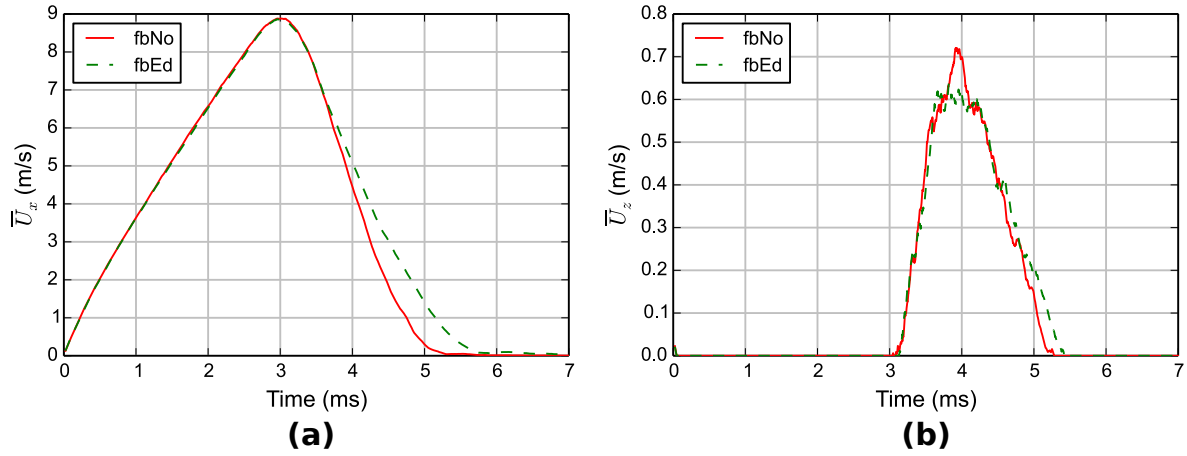

Figure 4.13: *The evolution with time of the average flow velocity component for two cases: a flexible barrier without energy dissipators (fbNo) and a flexible barrier with energy dissipators (fbEd):* ***(a)*** *in the direction of the flow,* ***(b)*** *perpendicular to the channel base*

velocity (movement in the x-z plane). The curves of fbNo and fbEd cases start splitting at the time where energy dissipators are activated (t = 3.4 seconds). However, the total period of the time for the evolution of $\overline{U}_z$ is rather short (2.25 seconds). Furthermore, the peak $\overline{U}_z$ is much smaller than that of $\overline{U}_x$. This implies that the main displacement of particles takes place along x-direction, while a only small fragment takes place in the z-direction.

4.5.2 Total force applied on the structure

The norm of the total force (F_{tot}), in both normal and tangential directions, applied by the granular flow particles on the different flexible barrier components is calculated. Such a force represents the sum of all interaction forces (normal and tangential) between flowing particles and cylindrical elements forming the flexible barrier. It is calculated as follows:

$$F_{tot} = \sqrt{\left(\sum_{i=1}^{n_{int}} F_{int,x}\right)^2 + \left(\sum_{i=1}^{n_{int}} F_{int,y}\right)^2 + \left(\sum_{i=1}^{n_{int}} F_{int,z}\right)^2} \tag{4.20}$$

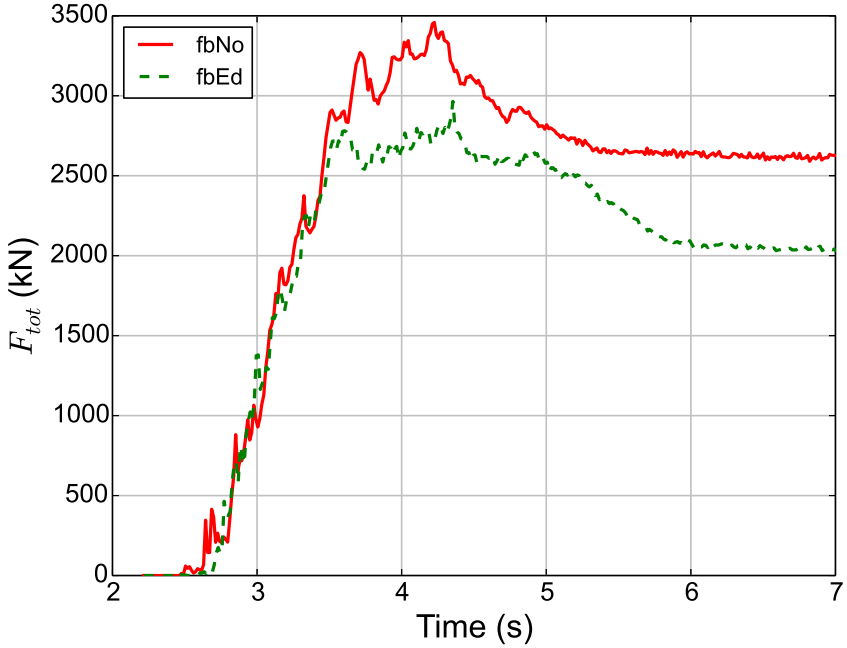

Figure 4.14: *The evolution with time of the total force applied on the barrier for two cases: a flexible barrier without energy dissipators (fbNo) and a flexible barrier with energy dissipators (fbEd)*

where n_{int} is the number of interactions between the flowing particles and cylindrical elements and $F_{int,x}$, $F_{int,y}$ and $F_{int,z}$ are the interaction force between a particle of the flow and a cylinder of the flexible barrier in x,y and z directions respectively.

Figure 4.14 shows the evolution of F_{tot} with time for both fbNo and fbEd cases. At the early stage of the impact, the two curves are very similar. Once energy dissipators are activated (t = 3.4 s), the two curves start splitting. From that moment, for fbNo case, the impact force on the structure keeps increasing progressively reaching a maximum value of 3450 kN at t = 4.22 seconds. Afterwards, the total force starts decreasing until it reaches a residual force value of 2600 kN at the end of the impact. For fbEd case, the peak value of F_{tot} is both delayed (takes place at t = 4.35 s) and minimized (2990 kN) by elongating the impact period, thanks to the activation of the energy dissipators. Such an elongation of the impact period prevents the high peaks of F_{tot} seen in fbNo case. Afterwards, the load progressively decrease until reaching a static value of 2040 kN at the end of the avalanche event. The final residual force value for fbEd is 22% smaller than that of fbNo although the initial avalanche mass is the same. This is mainly because as the structure in fbEd case progressively deform, part of the retained avalanche gets

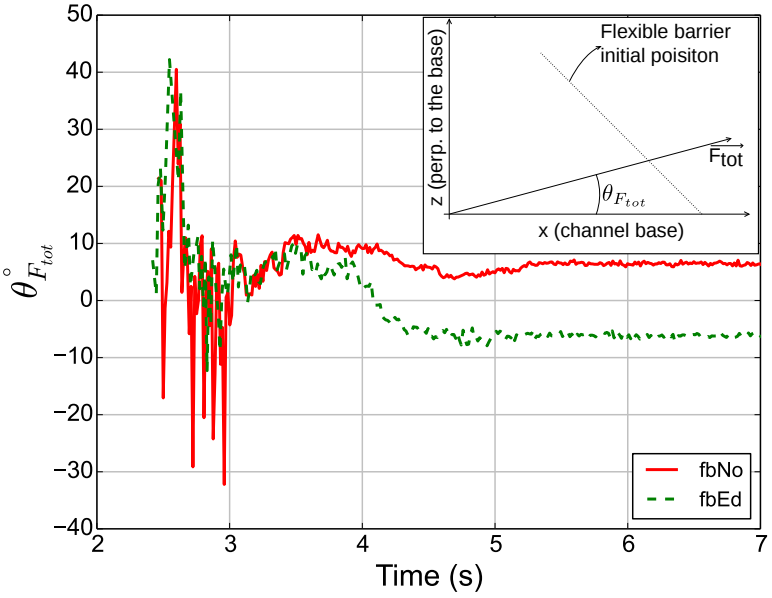

Figure 4.15: *The evolution with time of the direction of the total force vector with respect to the channel base for two cases: a flexible barrier without energy dissipators (fbNo) and a flexible barrier with energy dissipators (fbEd). Inset: schematic representation of the total force vector direction with respect to the initial position of the barrier and the channel bed*

into interaction with the downstream base of the channel. This leads to the situation where the weight of the retained avalanche is supported by both the barrier and the base, resulting in lower final values of F_{tot}. Another reason for the difference of final F_{tot} value is the loss of some of the material in fbEd case which overflows the barrier mainly from the sides, as will be discussed in Section 4.5.3.

The orientation of the total force vector with respect to the base of the channel (x-axis) has been recorded with time for both cases (Fig. 4.15). At the beginning of the impact, a highly fluctuating signal is recorded due to the low number of particles that are in contact with the structure. As more particles accumulate behind the structure and with the energy dissipators being activated (t > 3.4 seconds), a distinctive difference could be observed for the orientation of the total force ($\theta_{F_{tot}}$). In fbNo case, the total force applied by the flow has a positive sign with respect to the channel base. In contrast, for fbEd case, the total force orientation is negative with respect to the channel base. This is because of the additional deformation of the structure due to the elongation of the energy dissipators, which leads to negative component of F_{tot} in the z-direction.

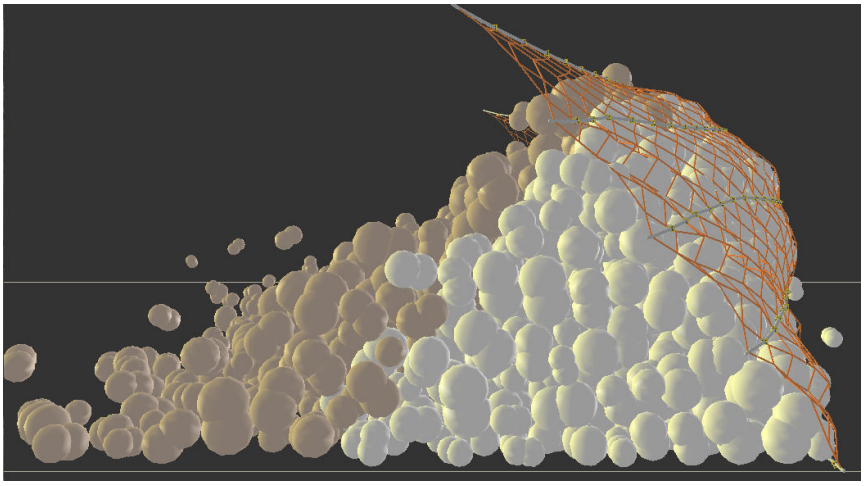

Figure 4.16: *A side view snapshot of the the flowing material impacting the barrier showing dead zone (in white) and moving particles (in grey) overflowing it*

4.5.3 Evolution of the dead zone mass

The dead zone is the zone where dead particles deposit in quasi-static condition behind the barrier. Such a zone is usually trapped between the channel base and the barrier, and is impacted by the flowing part. Figure 4.16 shows a side view snapshot of the dead zone (particles colored in white) that deposited behind a fbNo case barrier, with the rest of the flow flowing over it.

The evolution of the dead zone mass (m_{dz}) has been recorded and the ratio of m_{dz}/m_{tot} has been compared for the two cases: fbNo and fbEd (Fig. 4.17), where m_{tot} is the total initial mass of the avalanche. The evolution of the dead zone in each case is divided into three stages. For fbNo case, the first stage starts with a small evolution of the dead zone mass from the moment of the impact until t = 4.15 seconds, which is the moment where the total force reaches its peak value (Fig. 4.14). Afterwards, the second stage starts when the total force starts steadily decreasing towards the residual value which means more dynamic particles keep dying (becoming quasi-static, i.e. part of the dead zone) until t = 5.3 seconds. Finally, the third stage is observed with a slower rate of dead zone evolution as the rest of the particles that were overflowing the previously-created dead zone slowly die (Fig. 4.16).

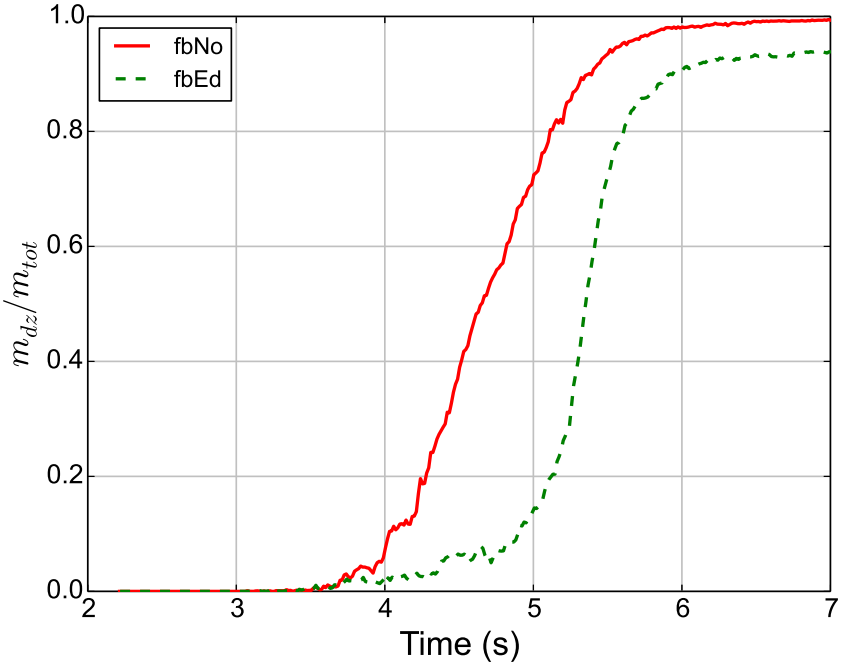

Figure 4.17: *The evolution with time of the dead zone mass for two cases: a flexible barrier without energy dissipators (fbNo) and a flexible barrier with energy dissipators (fbEd)*

Similar stages can be observed for fbEd case (Fig. 4.17): a slow accumulation of the dead zone, rapid accumulation and another slow one. However, the first stage of dead zone accumulation is much more delayed in comparison with fbNo case. This is because of the continuous deformation of the structure in the direction of the flow (thanks to the activation of the energy dissipators) which allows for further evolution of particles velocity. Next, at the end of the energy dissipators deformation, the structure stops its extension in the direction of the flow and thus a very fast rate of dead zone accumulation is observed, faster than that of fbNo case. At the end a gentler evolution of dead zone mass is observed again. However, the final value of the dead zone mass is not the same as the initial mass of the avalanche ($m_{dz}/m_{tot} < 1$). This is because some particles go through the net and keep descending down the channel (although very small part, less than 1%). The main loss is attributed to the part of the flow that overflow the barrier from the sides (and partially from the top) due to the existence of "escaping windows" on the sides of the barrier (Fig. 4.18). These windows are created by the extension of energy dissipators, resulting in an excessive displacement of the lateral supporting cables. The solution for closing these windows will be discussed in Chapter 5.

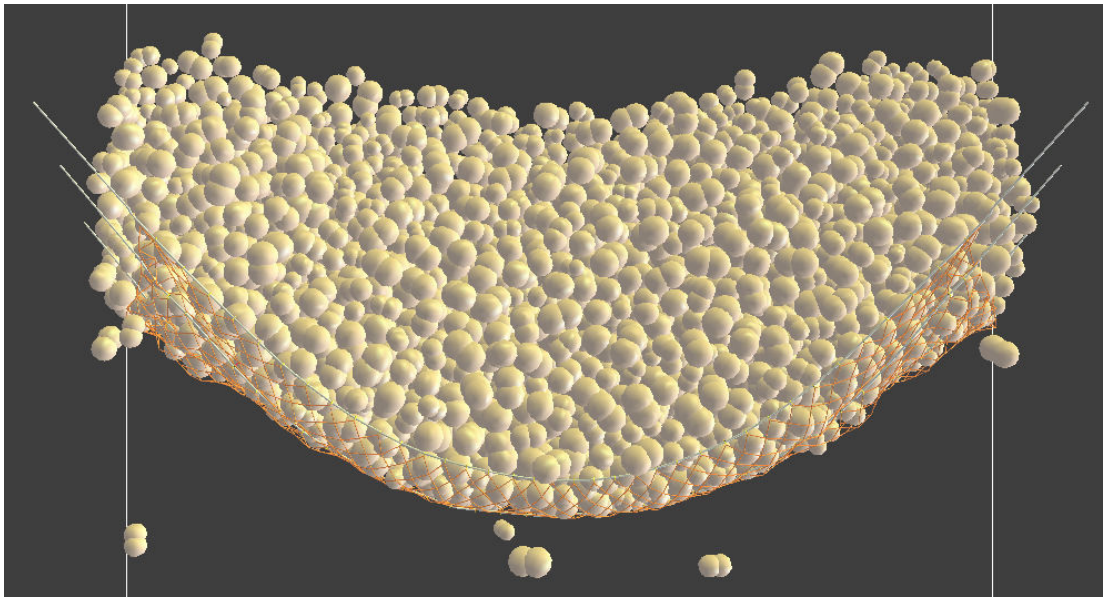

(a)

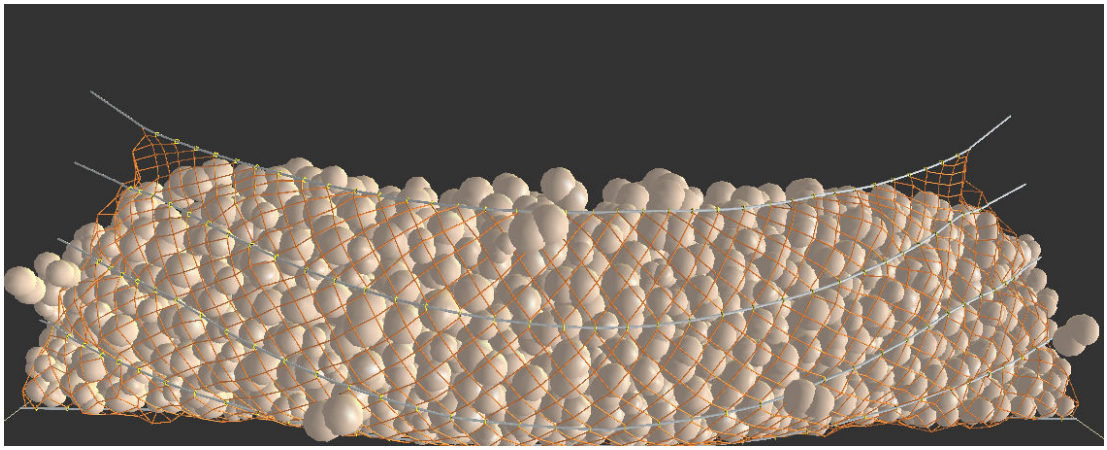

(b)

Figure 4.18: *Snapshots of the granular flow impact on the flexible barrier with energy dissipators (fbEd) showing the lateral escaping windows:* ***(a)*** *top view,* ***(b)*** *front view*

4.5.4 Internal forces in main cables

Forces in the cylinders are found to vary from one cylinder to the other along the same main cable, especially due to the presence of sliding rings. As a result, in order to compare the two cases (fbNo and fbEd), the average force developing in each main cable is calculated (Fig. 4.19). The force value in each cable is the average value of internal forces developing in all cylinders forming that cable. Cable 1 which is the bottom cable of the structure was fixed to the bed of channel so that no internal force was developing in it. Cable 2 starts being loaded earlier than the other cables as it is the closest to the impacting flow. For fbNo case, cables 3 and 4 are the highest ones loaded with a peak around 305 kN at t = 4.65 seconds and a residual force of 290 kN. Cable 5 is less loaded (peak force = 235 kN) but peaks at almost the same time as cables 3 and 4. The least loaded cable is cable 2 with almost no significant peak (residual force = 160 kN). The total duration of the impact for fbNo case is around 2.8 seconds.

For fbEd case, a lower peak is observed for cables 3 and 4, being 240 and 235 kN respectively, due to the activation of energy dissipators. In addition, the dynamic peak value for these two cables is delayed. The same observations can be seen for the internal force in cable 5, which has a peak force of 170 kN and a residual one of 145 kN. Similar to fbNo case, cable 2 is the least loaded with no significant peak force. The total duration of the impact for fbEd case is found to be 3.5 seconds. Such a longer response of the structure reduces the impact force applied on it and consequently reduces the peak internal force in the cables. Moreover, the total internal residual force of the cables in fbEd case is lower than that of fbNo case, due to the excessive deformation provided by the energy dissipators.

4.5.5 Deformation of the energy dissipators (ED) and maximum extension of the cables

Two energy dissipators are installed at the extremities of each main cable in order to limit the load transmitted to the anchors (Fig. 4.1). The deformation of the energy dissipators has been recorded with time for each cable and the ratio of $\delta_{ED}/\delta_{ED-brk}$ has been plotted (Fig. 4.20). It can be noted that all energy dissipators get activated at the same moment (t = 3.4 seconds), which is the moment the curves in figures 4.13 and 4.14 were found to split as discussed earlier. This takes place when the maximum elastic limit of the energy dissipators is reached, which is 250 kN for the case under consideration. However, the

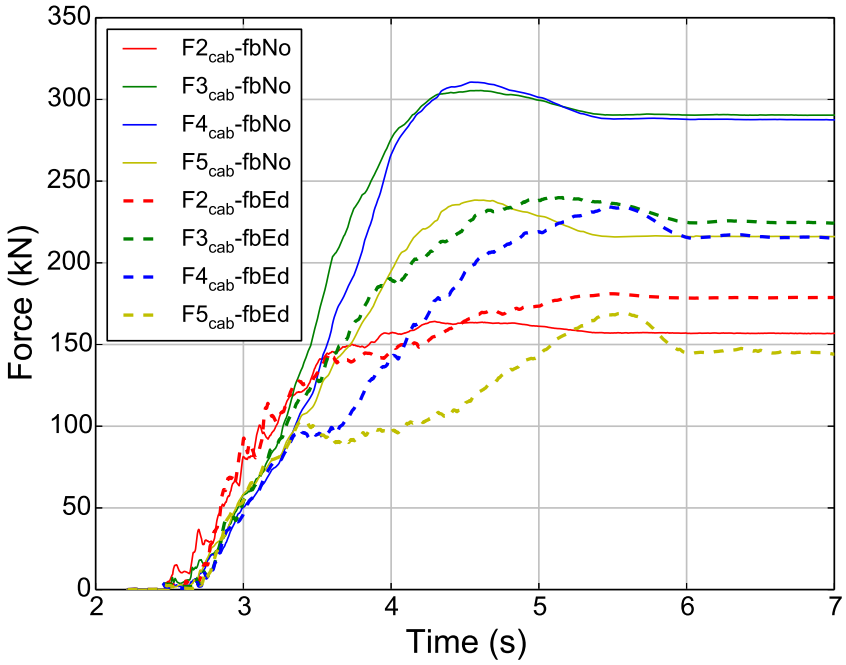

Figure 4.19: *The evolution with time of the internal forces in main cables for two cases: a flexible barrier without energy dissipators (fbNo) and a flexible barrier with energy dissipators (fbEd)*

deformation values are found to be different between the different cables. The highest deformation were found to take place for energy dissiaptors installed at cables 4 and 5, which are the upper cables of the structure. The additional length provided by the energy disspators to the structure results in a different final shape of the barrier between fbNo and fbEd cases. The maximum extension of the cables in the direction of the flow (Fig. 4.21) is larger in the case of fbEd. When comparing the maximum extension, a big difference is seen for cables 4 and 5 between fbNo and fbEd cases. This is consistent with the finding of Figure 4.20 and can be explained by the high deformations of energy dissipators of cables 4 and 5.

4.5.6 Forces in the anchors

Forces applied on the barrier are transmitted to the anchors through the main cables and energy dissipators (if any). It is important to control the amount of these forces in order to prevent the failure of some/all of the anchors. Forces transmitted to the anchors have been recorded with time for each cable and the ratio of F_a / F_{ED-els} has been plotted (Fig. 4.22). When no energy dissipators are used (fbNo), forces on the anchors

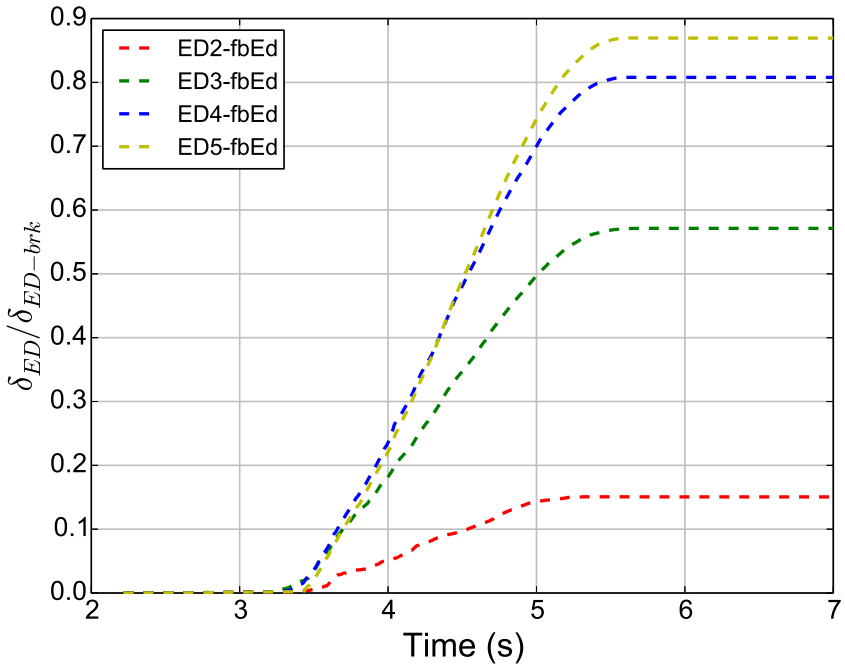

Figure 4.20: *The evolution with time of the average deformation of each two energy dissipators at the same cable, for a flexible barrier with energy dissipators (fbEd)*

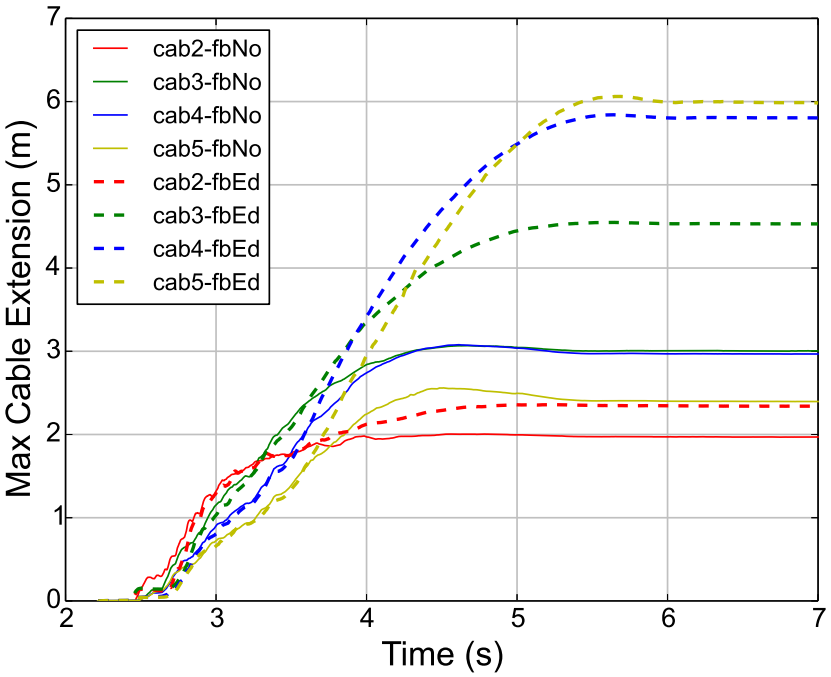

Figure 4.21: *The evolution with time of the maximum extension of main cables in the direction of the flow for two cases: a flexible barrier without energy dissipators (fbNo) and a flexible barrier with energy dissipators (fbEd)*

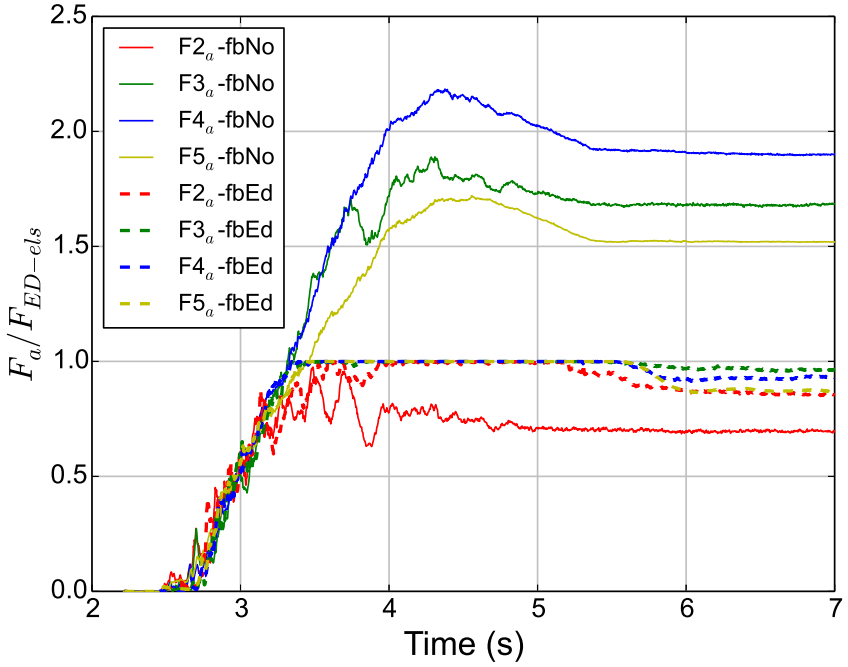

Figure 4.22: *The evolution with time of the average force on each two anchors at the same cable, for two cases: a flexible barrier without energy dissipators (fbNo) and a flexible barrier with energy dissipators (fbEd)*

are unevenly distributed, with a concentration of loads on the upper anchors. Anchors of the 4th cable peak with forces that are more than twice the value of F_{ED-els}. Residual forces on different anchors differ considerably from 0.7 F_{ED-els} to 1.8 F_{ED-els}. For fbEd case, loads on the anchors are almost evenly distributed, with no concentration of forces on specific anchors. This is due to load redistribution once a specific anchor reach the elastic limit value F_{ED-els}. The dynamic peak of the forces seen in fbNo case has been eliminated in fbEd case due to the activation of the energy dissipators. In addition, the final residual forces on the anchors are mainly the same for all anchors. It allows for having a unique design and less conservative for the anchors in the presence of energy dissipators.

4.5.7 Load transmition in the barrier

In this section, the tensile force developing in cylinders forming the net and main cables are compared for two cases: fbNo and fbEd. The comparison is made for the loads at the end of the impact event, showing the residual tensile force in each cylinder. Figure 4.23 shows y and z coordinates of the center of geometry of each cylinder in both barriers col-

ored according to the corresponding tensile force. The main cables in each barrier, which are cables 1 to 5 are shown from the bottom to the top. Cable 1 is fixed to the ground and does not sustain tensile forces, thus it is not shown. Forces in the net elements are considerably lower than those in the cables, thus they will be shown in an independent figure with independent scale later in this section. Overall, the forces are symmetrically distributed around the middle of the barrier. Figure 4.23 also shows the final shape of deformation of the barrier for the two cases. It shows the final height of the barrier at the end of the event (minimum z coordinate of the top cable), which is a crucial design parameter (Bertrand et al., 2008).

For fbNo case (Fig. 4.23a), high tensile forces are observed in the main cables, with significant concentration of these forces on the extremities. These extremities are the last cylinders of the main cables connecting them to the lateral anchors. The highest residual tensile forces are the ones acting on the extremities of cables 4 and 3, in agreement with the findings of Figure 4.22. In addition, the axial forces start reducing as we move to the cylinders in the middle of each cable. For example, for cable 4, the tensile force of cylinders on the edge reaches a value of 475 kN which decreases as we go to the cylinders in the middle where it reaches a value of 260 kN. The same observation could be noted for cable 3 where tensile force decreases from 425 kN to 255 kN as we move along the cable from the edge to the middle respectively. However, for the top cable, the only high concentration of tensile force is observed for the two edge cylinders of the cable (375 kN). The tensile force drops to 215 kN for the other cylinders, once we move away from the two edge cylinders. Concerning the deformation, the final height of the structure is found to be 3.75 m.

For fbEd case(Fig. 4.23b), lower values are observed for the tensile force of the cylinders forming the main cables, in comparison with fbNo case. For example, for cables 3 and 4, the loads on the extremities, are very similar, being 242 and 234 kN respectively. Moreover, the tensile force in cylinders of a given cable is very similar, with no differences along the cable, in contrast to fbNo case. One exception of this observation is the top cable (cable 5) which has a tensile force of 220 kN at the two cylinders on its edge (connected to the anchors). This value drops to 150 kN for the rest of the cylinders of that cable, in similar trend to the top cable of case fbNo. Concerning the deformation, the final height of the structure (minimum z coordinate of the final cable) is found to be 3.2 m, which is 15% lower than the previous case.

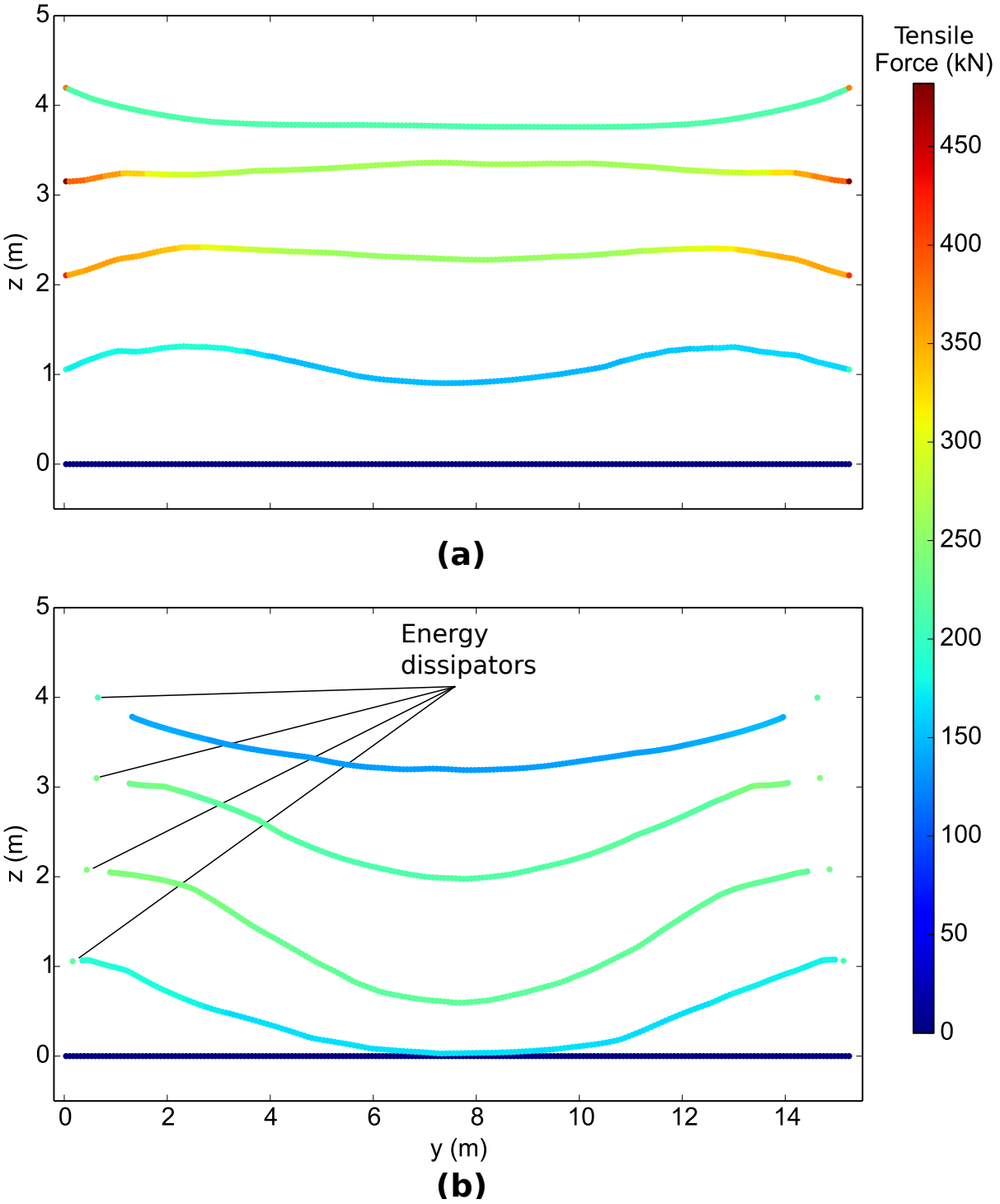

Figure 4.23: *Tensile forces in cylinders forming main cables:* ***(a)*** *flexible barrier without energy dissipators (fbNo),* ***(b)*** *flexible barrier with energy dissipators (fbEd)*

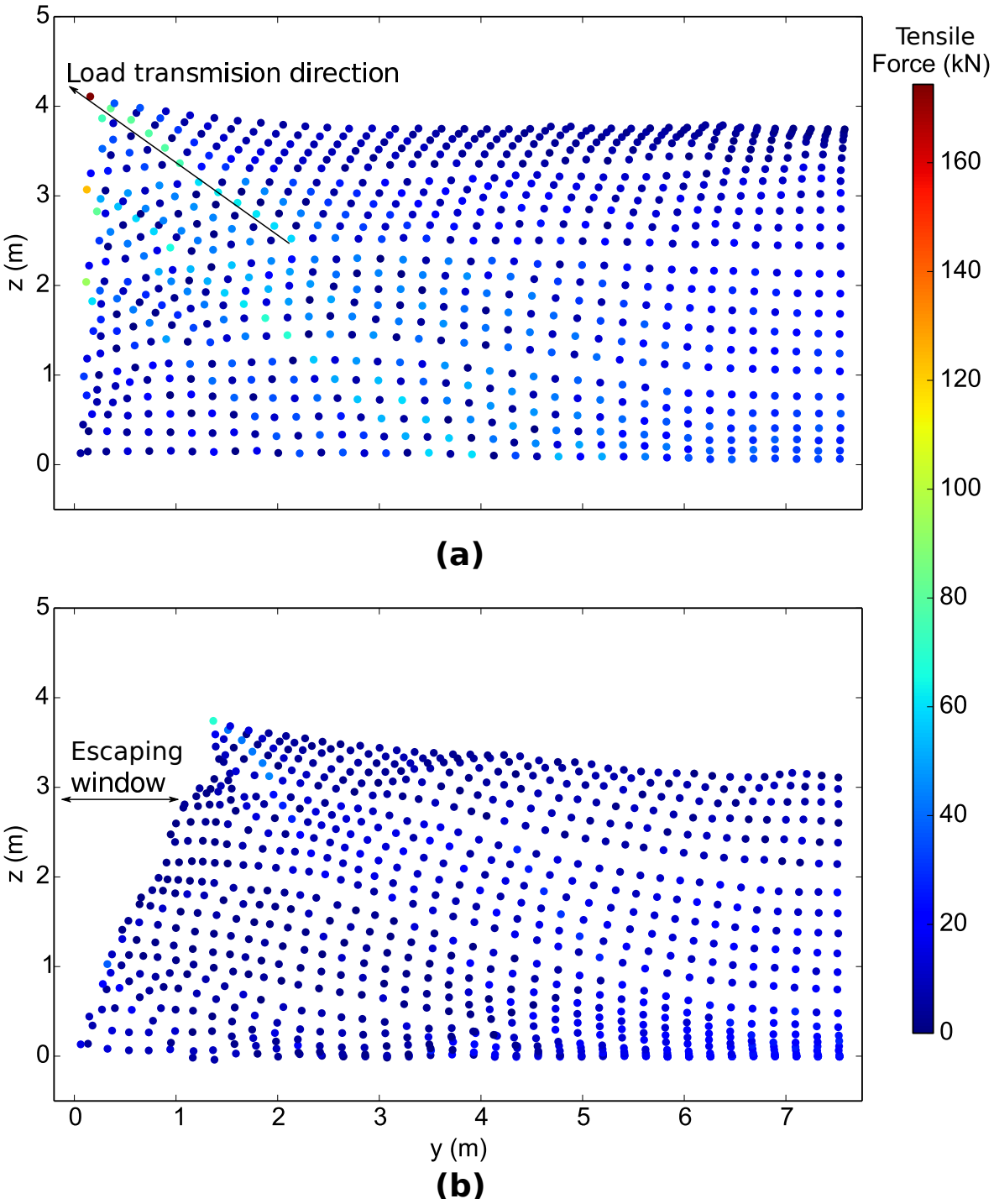

Figure 4.24: *Tensile forces in cylinders forming net elements:* ***(a)*** *flexible barrier without energy dissipators (fbNo),* ***(b)*** *flexible barrier with energy dissipators (fbEd)*

Next, the tensile forces in the net elements are analyzed (Fig. 4.24). For convenience, only the first half of the structure is plotted, since the structure is symmetrical. For fbNo case (Fig. 4.24a), tensile forces in the cylinders of the net elements are higher than the other case. Maximum tensile forces are found to take place in net elements that are close to the edge of the structure. The maximum observed force is the one in the net element that is attached to the top cable, reaching force value of 174 kN. Similar observations are noted for net elements attached to the edge cables 3 and 4, as they are found to be highly loaded, with forces of 93 and 125 kN respectively. In addition, the load transmitted through the net is found to be of a diagonal shape. The force is lower away from the edge of the net and it keeps increasing in the diagonal direction until maximizing at the edge of the barrier. In terms of deformation, no side openings of the net are present, thus no flowing particles were allowed to escape the barrier from the lateral sides.

For fbEd case (Fig. 4.24b), lower tensile forces are present in the cylinders forming net elements, with the maximum being 69 kN which is 60% smaller than the maximum value of fbNo case. However, same observations of load transmissions are present: the load is transmitted diagonally with edge cylinders near the anchors being the highest loaded ones. However, difference between the highest loaded cylinder (69 kN) and the rest of the cylinders of the net is smaller than in the previous case. Concerning the barrier deformation, the extension of the net in the direction of the flow (x-direction) creates the escaping windows on the lateral sides of the barrier (Fig. 4.24b). These windows are responsible for allowing for some part of the granular flow to overflow the barrier from the sides, thus reducing the total residual force applied on the barrier. Moreover, at the middle of the bottom of the barrier, dots representing the cylinders are found to be having very similar z component. This is because they lay on the downstream of the channel base, which is one of the reasons why the total force applied on the barrier for fbEd case is lower than fbNo case.

The load transmission in the barrier can be understood considering the coupling between the forces in both main cables and net elements. Figure 4.25 shows the tensile forces in main cables and net elements for the first half of the barrier. For convenience, only net elements with tensile force larger than 50 kN are shown, to avoid showing the weakly loaded net elements. This is similar, in principle, to force chains were only

strong chains are usually investigated (Azéma and Radjaï, 2012). The highest loaded net cylinders are diagonally connected confirming the diagonal load transmission in the barrier, for both cases.

For fbNo case (Fig. 4.25a), forces are different along the cylinders of the same main cable, with extremities being the highest loaded parts. This difference is seen for each set of cylinders of the main cable (i.e. each set of dots of each main cable in Figure 4.25a). Such a difference in the tensile force in cylinders of the same cable justifies the comparison of the average force (instead of maximum one) that was carried out in Section 4.5.4. This difference is due to the presence of rings, that are spaced by a distance equal to the length of six cylinders of the main cable. Rings connect the net elements from the two sides of the ring. Such configuration means that, at the ring position, part of the load is supported by cylinders of the main cable and the rest is supported by the net cylinders. Figure 4.26 shows a zoomed snapshot from the front view of the barrier, showing the spaced ring and their connection to the rings. The loads are transmitted through the barrier until reaching the anchors via the last cylinders at the extremities of each main cable, referred to as cable-end cylinders (colored in magenta in Figure 4.26a). These cylinders are the highest loaded ones, as they are the connection between the anchors (modeled as fixed points) and the rest of the barrier.

When energy dissipators are used, in fbEd case (Fig. 4.25b), forces in cylinders forming each main cable are very similar, with the exception of the cylinder representing the energy dissipator. This similarity in force could be due to the extra deformation of the barrier provided by the deformation of energy dissipators (Fig. 4.26b). Such an extra deformation could lead to load transmission up to the energy dissipators without highly loading the net elements. The maximum load of the net elements is 60% lower than that of fbNo case. Such reduction in the loading of the net, due to the deformation of energy dissipators, would prevent them from rupture in real barriers.

4.6 Parametric analysis

In this section, different analyses are carried out to see the effect of changing some parameters on the response of the flexible barrier. The first analysis concerns the inclination angle of the channel bed (α) that is varied between 30°, and 40° and its effect on the results. Next, the effect of changing the initial barrier inclination with respect to the gravity

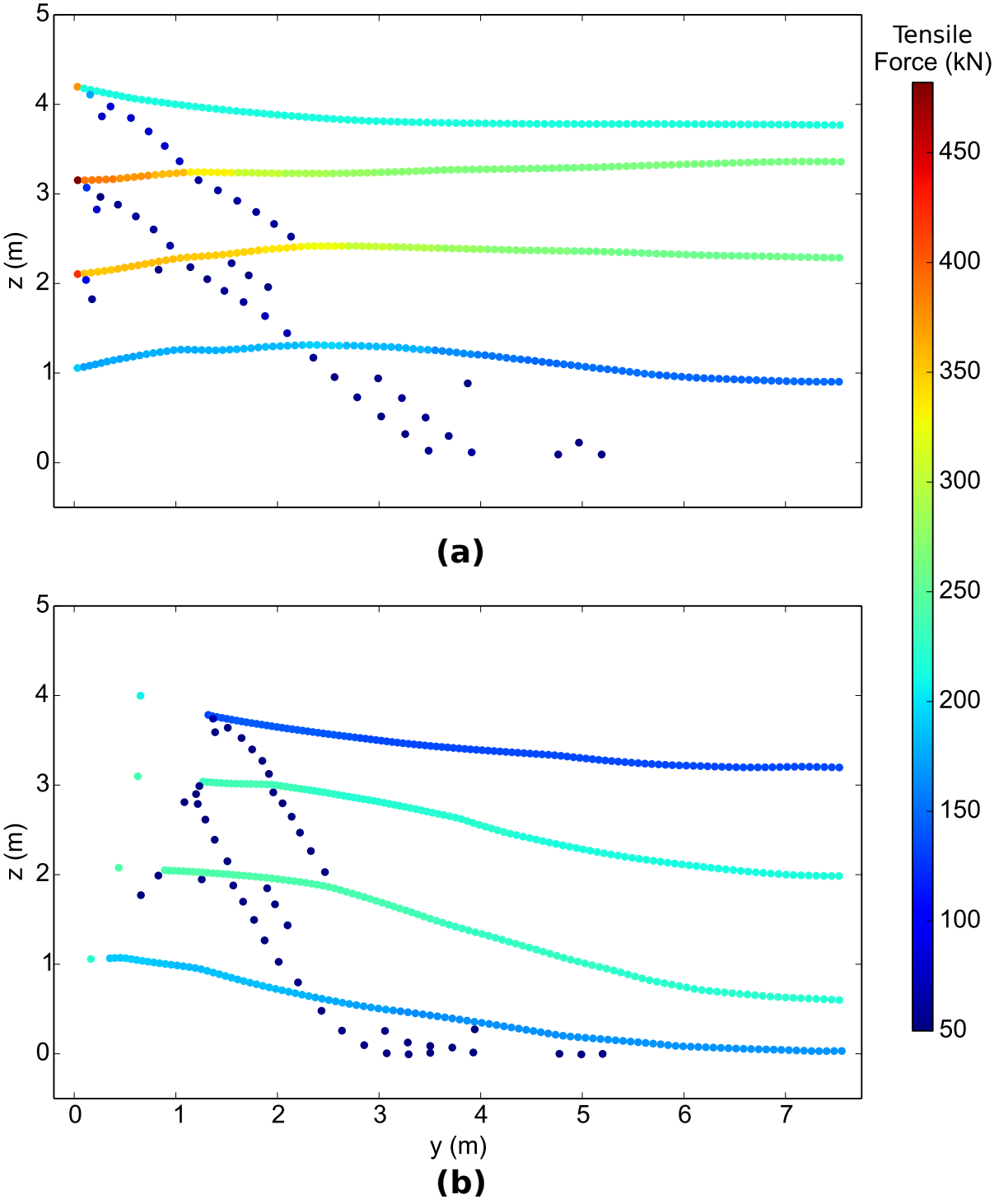

Figure 4.25: *Tensile forces larger than 50 kN in cylinders forming main cables and net elements:* ***(a)*** *flexible barrier without energy dissipators (fbNo),* ***(b)*** *flexible barrier with energy dissipators (fbEd)*

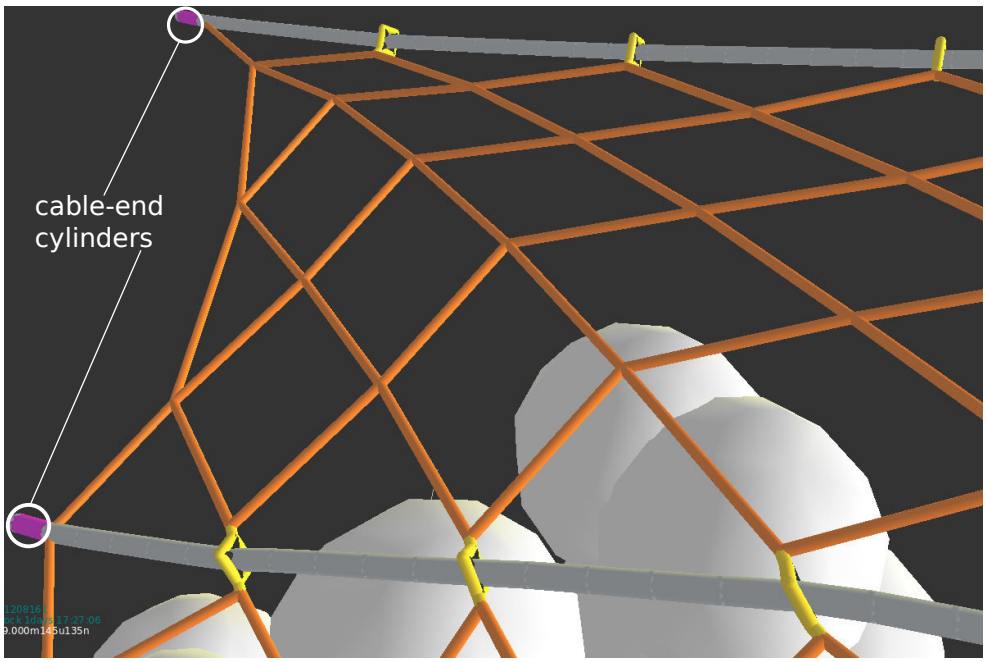

(a)

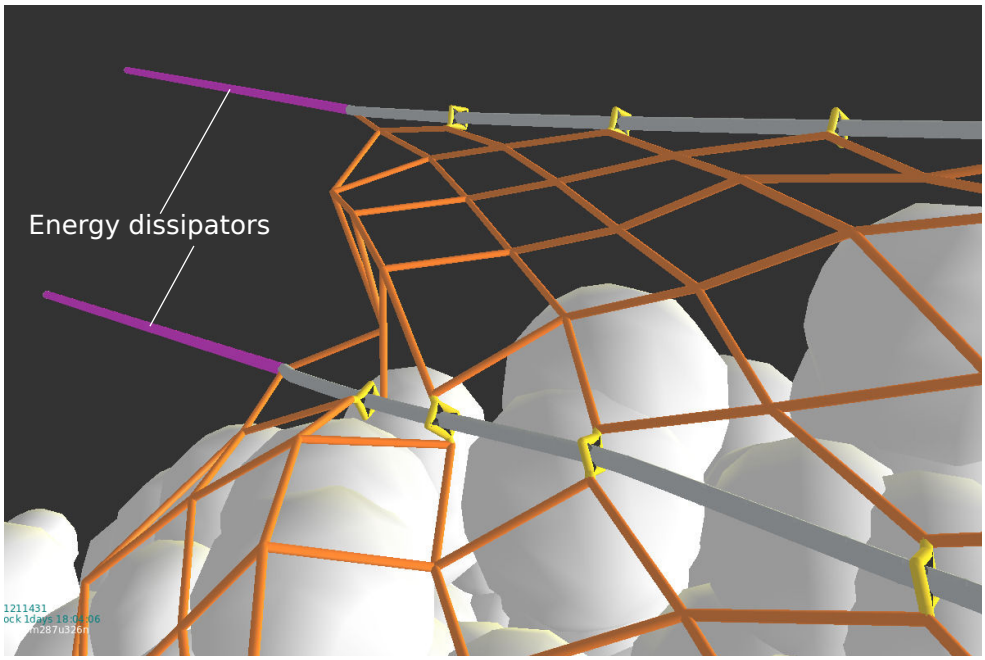

(b)

Figure 4.26: *snapshot of the top left part of the barrier:* ***(a)*** *flexible barrier without energy dissipators (fbNo),* ***(b)*** *flexible barrier with energy dissipators (fbEd)*

vector is investigated. For all the analyses presented here, geometrical configuration, mesh size, number of cables are the same as the ones mentioned in Sections 4.5. For each of the following subsections, the results are first presented for different impact behavior components and then all the results are discussed at the end.

4.6.1 Effect of inclination angle of the channel

In this section, different values of inclination angle of the channel will be tested. This is to investigated the effect of such change on both the flowing velocity (in both x and z directions) and the total force applied on the structure. Inclination angles of 30, 32.5, 35, 37.5 and 40° are tested for a barrier with no energy dissipators (i.e. fbNo case) in order to only see the effect of changing the inclination angle without allowing for particles to escape due to the side openings or the excessive deformation of the structure.

First, the effect of the inclination angle on the average flowing velocity in the direction of the flow (x-direction) is investigated (Fig. 4.27a). For the lowest inclination angle ($\alpha = 30^{\circ}$), a slow evolution of $\overline{U}_x$ is observed, i.e low value of the slope of $\overline{U}_x$: Time curve before the peak. At the peak, $\overline{U}_x$ curve reaches a maximum of 5.4 m/s which is followed by flowing velocity deceleration. In addition, the avalanche event duration is around 8 seconds. By increasing the inclination angle ($\alpha = 32.5^{\circ}$), faster evolution of flowing velocity is observed and higher peaks are reached (6.35 m/s). Furthermore, the duration of the event is decreased in comparison with the previous one, with a total duration of around 7 seconds. The same general observations can be seen for the cases of 35, 37.5 and 40° with peak flow velocity values in the direction of the flow of 7.2, 8.1 and 8.85 m/s respectively and events duration of 6.5, 6 and 5.5 seconds respectively.

The flowing velocity component in the direction perpendicular to the flow channel ($\overline{U}_z$) is also investigated for different values of α (Fig. 4.27b). For $\alpha = 30^{\circ}$, a delayed start of velocity evolution in z-direction (starts at t = 3.9 seconds) is observed with a peak value of 0.21 m/s and a total duration of 3.5 seconds. When increasing the inclination angle ($\alpha = 32.5^{\circ}$), an earlier start of velocity evolution is observed (at t = 3.7 seconds) along with a higher peak value of the average velocity (0.3 m/s) and a shorter duration of the avalanche event (3.2 seconds). With further increase of inclination angle (α values of 35°, 37.5° and 40°) earlier starts of flow evolution are recorded with the flow starting at

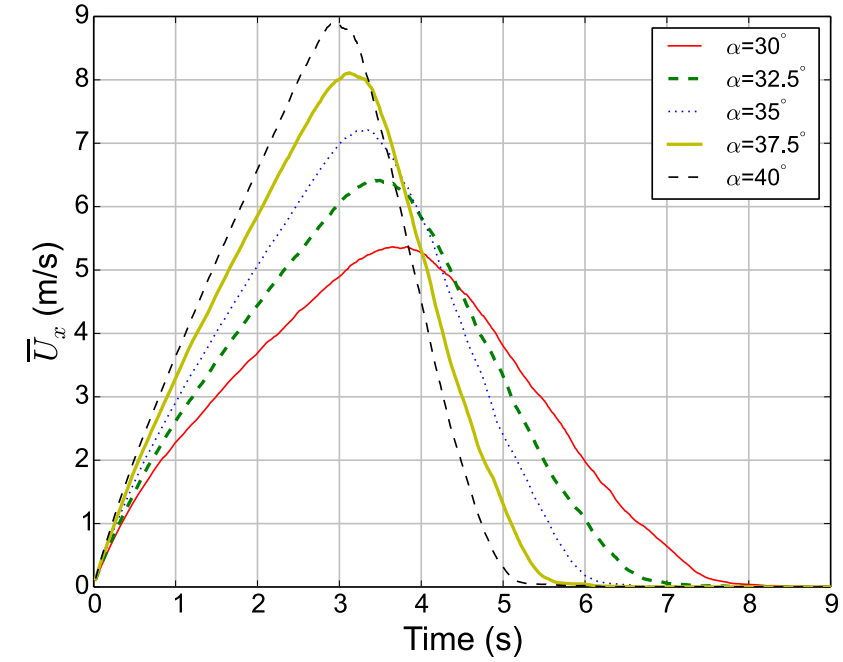

(a)

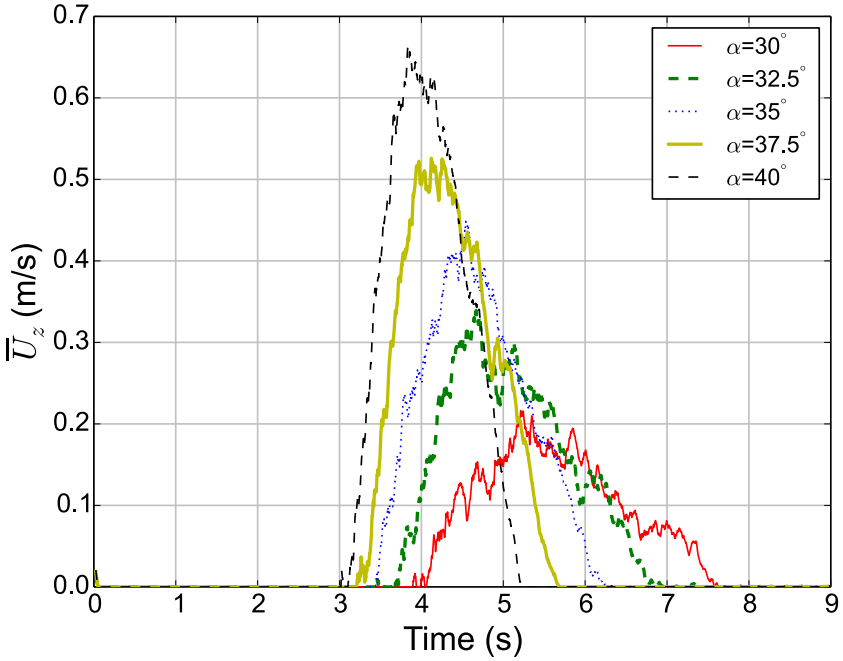

(b)

Figure 4.27: *The evolution with time of the average flow velocity for different values of channel inclination angle:* ***(a)*** *in the direction of the flow,* ***(b)*** *perpendicular to the channel base*

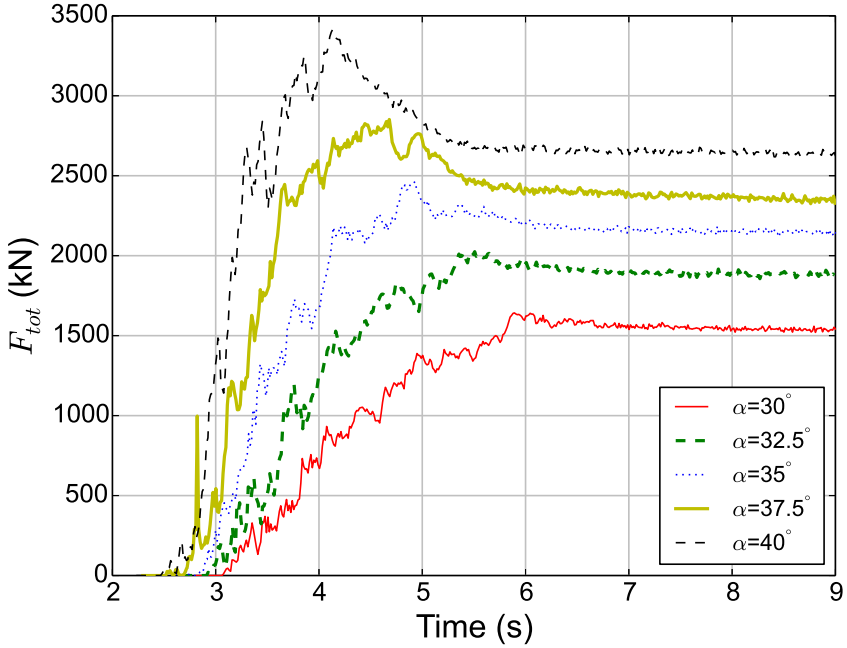

Figure 4.28: *The evolution with time of the total force applied on the barrier, for different values of channel inclination angle*

3.45, 3.20 and 3.10 seconds respectively. Moreover, the durations of the avalanche events are shorter (2.8, 2.45 and 2.15 seconds respectively) and velocities record higher peaks of 0.45, 0.52 and 0.65 m/s respectively.

Next, we investigate the effect of changing α on the total force F_{tot} applied by the flow. F_{tot} was calculated as explained in Section 4.5.2. The total force peak and residual values are found to be strongly dependent on the inclination angle (Fig. 4.28). For the lowest inclination angle investigated $\alpha = 30^{\circ}$, a late evolution of the force is observed which takes place at t = 3.05 seconds. The total force keeps increasing until reaching a peak of 1645 kN which is followed by a slight decrease reaching a constant residual force value at the end of the avalanche event of 1550 kN. For $\alpha = 32.5^{\circ}$, an earlier evolution of the force is observed which takes place at t = 2.95 seconds reaching a peak value of 2035 kN followed by a higher residual force value than that of $\alpha = 30^{\circ}$ (1900 kN). The same trend is observed for higher values of α (35, 37.5 and 40°) which record peak values of 2500, 2950 and 3400 kN respectively and residual force values that are higher than the previous two cases, being 2150, 2400 and 2650 kN respectively.

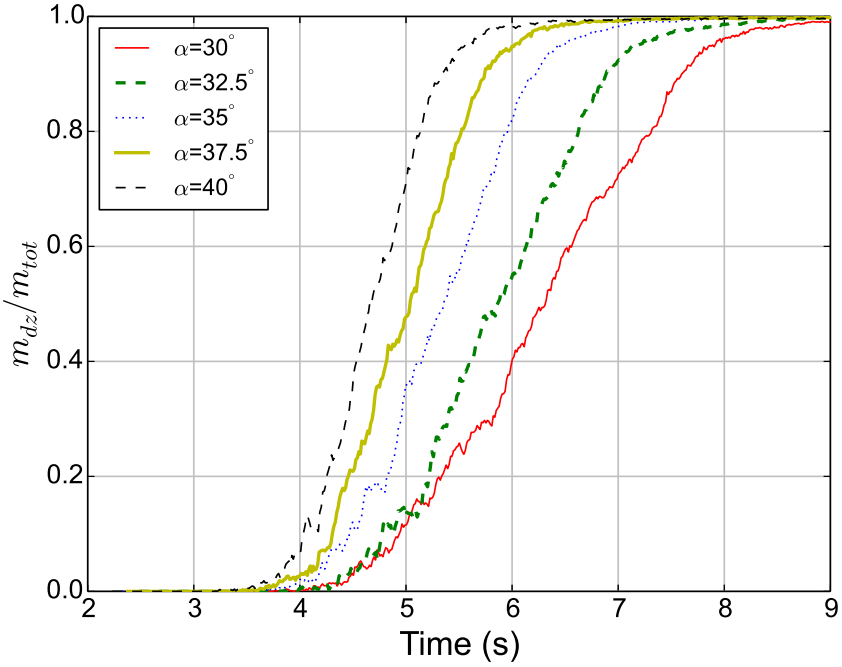

Figure 4.29: *The evolution with time of the dead zone mass, for different values of channel inclination angle*

Finally, the effect of changing α on the evolution of the dead zone mass is considered (Fig. 4.29). Slower evolution of dead zone is observed for low values of inclination angle, like the case for $\alpha = 30^{\circ}$. However, the total duration needed to fully accumulate dead particles (i.e. reaching a ratio of 1 of m_{dz}/m_{tot}) is found to be the longest among the investigated α values. Higher values of inclination angles are found to lead to faster and earlier accumulation of dead particles behind the barrier.

In order to discuss the aforementioned results, the different previous observations need to be linked together in order to understand the effect of inclination angle on the impact behavior. The high peak values of $\overline{U}_x$ linked with high inclination angles led to high peak values of the total force (Fig. 4.30). A strong relationship is observed between the maximum total force $F_{tot_{max}}$ and the maximum flowing velocity in x direction $\overline{U}_{x_{max}}$. This is due to the increase of the kinetic energy of the flow with the increase of α. In other words, increasing the inclination angle of the channel, results in an increase in

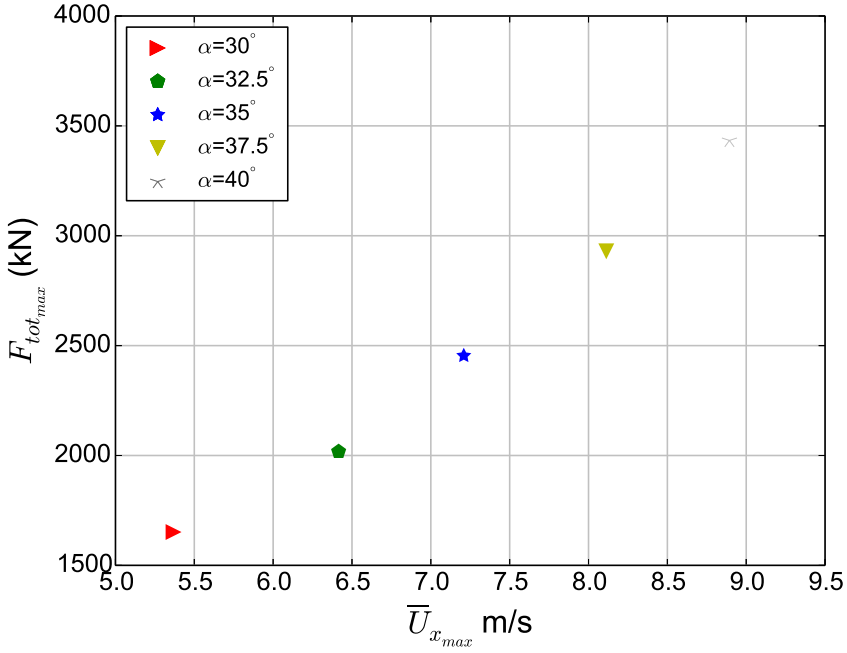

Figure 4.30: *The maximum total force and maximum average flowing velocity in the direction of the flow, for different values of channel inclination angle*

both $F_{tot_{max}}$ and $\overline{U}_{x_{max}}$. The dynamic component of the total force applied on the barrier (due to the kinetic energy of the flow), for high values of α, is one of the most influential components (Faug et al., 2011; Jiang and Towhata, 2013; Albaba et al., 2015).

In terms of the total force evolution, it is observed that the increase of inclination angle is linked to an increase in the ratio of F_{tot}/F_{res}, with F_{res} being the residual force applied on the barrier at the end of the avalanche event (Fig. 4.31). This ratio goes from 1.05 for $\alpha = 30^{\circ}$ to 1.3 for $\alpha = 40^{\circ}$. Similar observations have been reported in the literature for the impact on a rigid wall (Moriguchi et al., 2009; Faug et al., 2011; Jiang and Towhata, 2013) where decreasing the inclination angle was eliminating the distinctive peak force observed before reaching the residual force value (e.g. Fig. 4.32). This is due to the reduction of the kinetic energy of the flow impacting the barrier, since the flowing velocity decreases when decreasing the slope of the channel.

Another aspect of the total force evolution is its relation with the inclination angle and the evolution of the dead zone (Fig. 4.31). For low values of α, such as that of 30°, the residual force value is reached (i.e. $F_{tot}/F_{res} \approx 1$) at the moment where only 65% of the dead zone has accumulated ($m_{dz}/m_{tot} = 0.65$). This means that the remaining 35% of

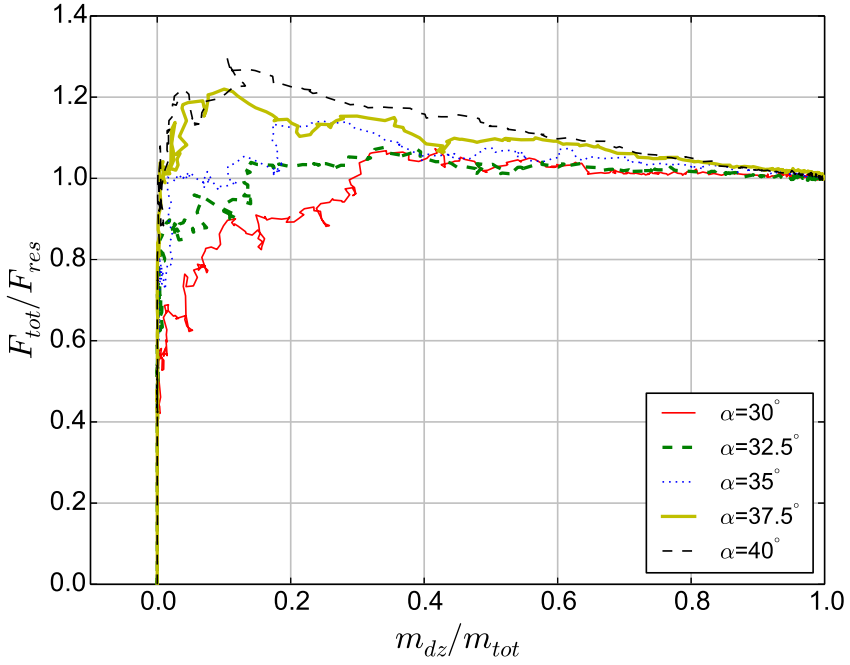

Figure 4.31: *The relation between the evolution of the total force with the evolution of the dead zone mass, for different values of channel inclination angle*

the flow that has not yet been converted into dead particles neither has a contribution to the gravitational nor the dynamic part of the total force. This could be related to the dissipation of kinetic energy within the granular medium behind the barrier when the 35% moving part collide with the dead zone. The contrary is observed for higher values of α, like for example the case with 40° where the residual force value is reached only at the end of the avalanche event where all particles have become dead. In addition, from Figure 4.31, it is worth noting that peak total force values take place when only small proportion of the dead zone has been created ($0.1 < m_{dz}/m_{tot} < 0.2$). This supports the observations in Section 3.7 that at the moment of peak total force, only small portion of that peak is contributed by the gravitational force component (weight of the dead zone). However, detailed comparison between both rigid and flexible structures in terms of impact behavior are needed, which will be presented in Chapter 5.

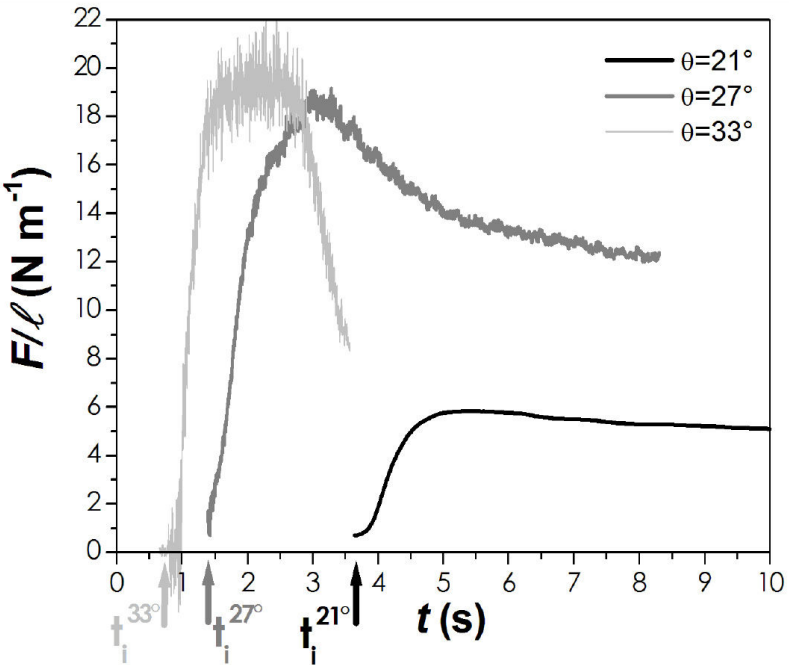

Figure 4.32: *Force per unit width measured on a wall impacted by a granular flow (made of beads) versus time t for three slope inclinations: α =21°, 27° and 33° (after Faug et al., 2011)*

4.6.2 Effect of the initial position of the barrier with respect to the gravity vector

In practice, the flexible barrier is often installed in a vertical direction (parallel to the gravity vector **G**). All previous results were presented for cases with such an arrangement of the barriers. In this section, however, the angle between the barrier and the gravity vector (θ_{fb}) will be tested for different values (Fig. 4.33) for a barrier with energy dissipators (fbEd). This is to investigate whether or not there is an effect of the initial position of the flexible barrier on its impact behavior. Three values of θ_{fb} are compared : 0, 10 and 20°.

First, we investigate the average flowing velocity component in the direction of the flow, which has proven to be the dominant component of flowing velocity (Section 4.5.1). Overall, the trend of the evolution of $\overline{U}_x$ with time is similar for the investigated cases. However, for the time period between 3 seconds and 6 seconds (Fig. 4.34), some differences do appear. The difference indicates that the higher the value of θ_{fb}, the faster the breaking down over time of $\overline{U}_x$ value. For example, at t = 5 seconds, $\overline{U}_x$ values are 0.90,

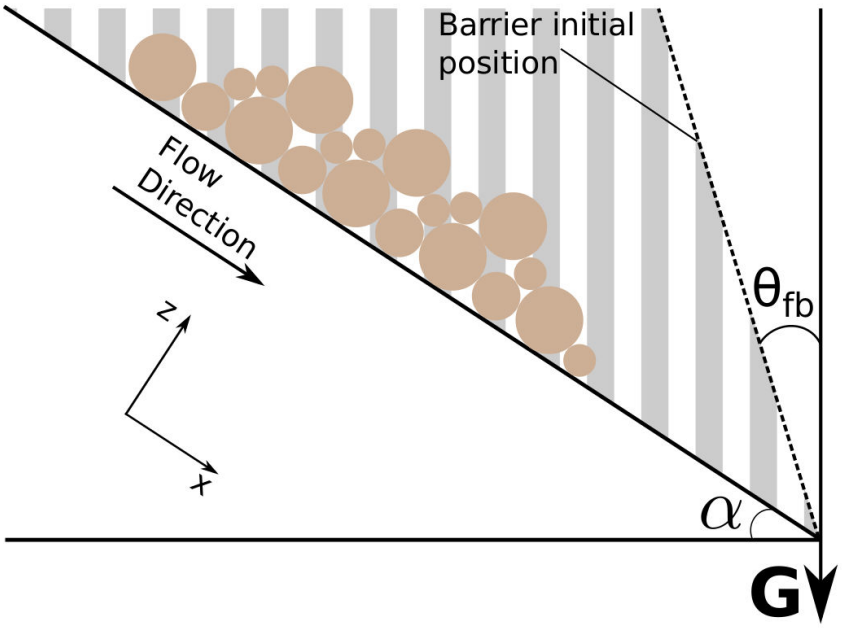

Figure 4.33: *A schematic representation of the inclination of the flexible barrier with respect to the gravity vector*

1.11 and 1.41 m/s for θ_{fb} values of 20, 10 and 0° respectively. Similar little differences can be observed for the evolution of the dead zone mass (Fig. 4.35). For a barrier with initial position in the direction of gravity vector (i.e. $\theta_{fb} = 0$), the rate of evolution of the dead zone mass is found to be slower than the other two cases. Furthermore, at the end of the impact event, 94% of the total mass is retained when $\theta_{fb} = 0$. When increasing the value of θ_{fb}, this percentage is found to slightly increase to 96%.

The difference in results, although very limited, might be due to the change of the volume of the space between the barrier and the channel base, represented by the hashed area in Figure. 4.33. This volume gets smaller when increasing the value of θ_{fb} causing the moving particles to die faster. This might be due to the limited volume available for particles' velocity to evolve. In addition, this could also be linked to the viscous dissipation of energy by collision between particles, as this collision is more possible when the volume is smaller.

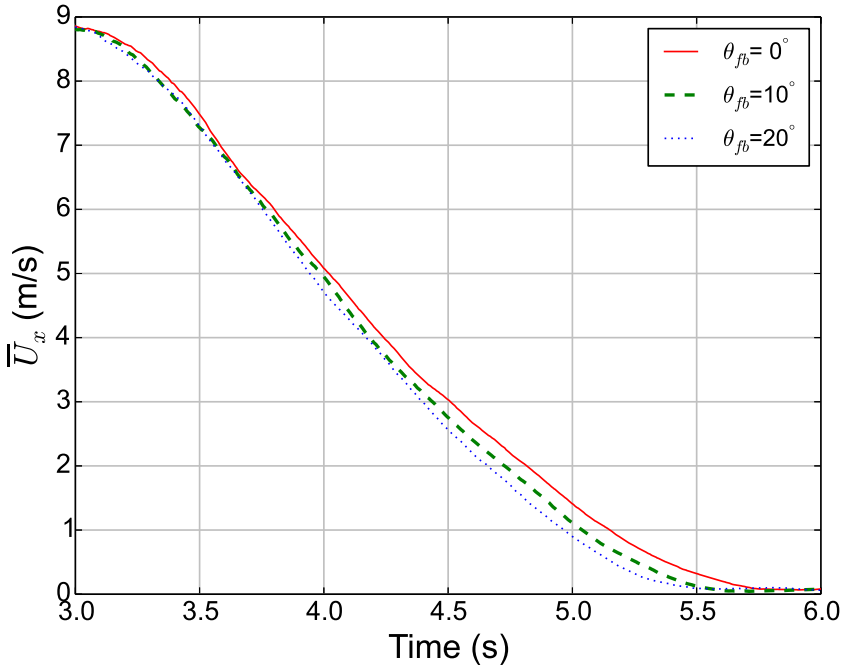

Figure 4.34: *The evolution with time of the average flow velocity component in the direction of the flow for different inclination angle of the barrier with respect to the gravity vector*

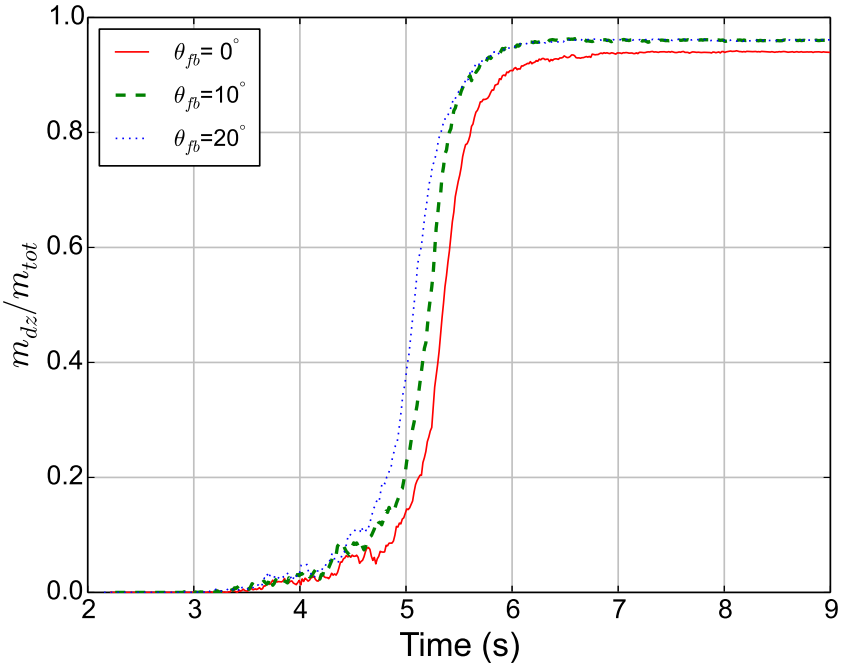

Figure 4.35: *The evolution with time of the dead zone mass for different inclination angle of the barrier with respect to the gravity vector*

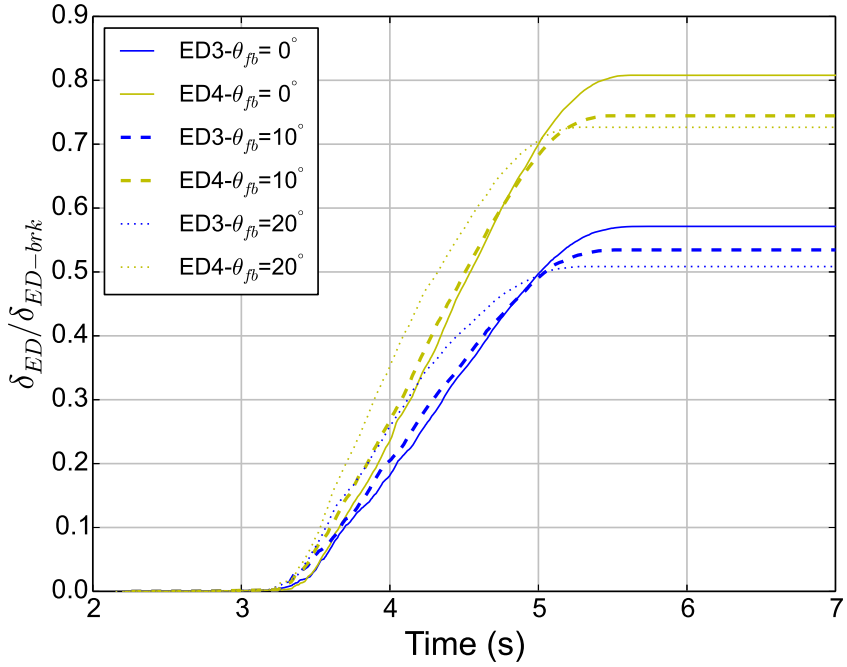

Figure 4.36: *The evolution with time of the average deformation of the two energy dissipators at cables 3 and 4, for different inclination angle of the barrier with respect to the gravity vector*

The retained mass was found to slightly increase when increasing the value of θ_{fb}. This increase is due to the limited opening of the escaping windows from the sides. This could be checked by calculating the deformation of the energy dissipators. The higher the deformation of energy dissipators, the wider the side opening of the escaping windows (Fig 4.18). Figure. 4.36 shows the deformation of the energy dissipators of cables 3 and 4 with time for different values of θ_{fb}. It can be seen that increasing the value of θ_{fb} decreases the final deformation of these dissipators which, in turn, decrease the lateral extension of the escaping windows. Such decrease would limit the amount of particles escaping from the barrier and thus more particles at the end will be retained. However, overall, the difference between results is limited. Moreover, installing a barrier with an angle between it and the gravity vector (i.e. positive values of θ_{fb}) might be a challenge in practice.

4.7 Conclusions

In this chapter, numerical modeling of a flexible barrier impacted by a granular flow has been presented. The considered structure was similar in principle to the ones in practice consisting of net mesh, sliding rings, main cables, lateral cables, energy dissipators and lateral anchors. The granular flow model was the same as the one calibrated and validated in Chapter 3. The cylinder model used as an elementary object for modeling was presented in details. Different types of interaction for this model were explained: sphere-sphere interaction, sphere-cylinder interaction and also cylinder-cylinder interaction.

The different parts of the flexible barrier have been discussed in details showing their validation procedure. A general mesh type has been chosen that is made of 45-degree rotated squares. The net element model was calibrated against experimental net punching data. The sliding rings were modeled as a square made of four cylinders that could slide on the cylinders of the main cables. Different values of friction between the two have been tested. Differences in results of energy dissipators deformation, maximum extension and forces on the anchors were found to be lower than 5%. Energy dissipators were modeled as elastic perfectly-plastic elements with threshold elastic limit and maximum allowable deformation.

After presenting the details of modeling different parts of the barrier, full scale simulations were conducted for two flexible barriers, a flexible barrier with no energy dissipators (fbNo) and a flexible barrier with two energy dissipators installed at the extremities of each main cable (fbEd). The presence of energy dissipators was found to be essential for dissipating the kinetic energy of the flow. They play a role in reducing the total impact force applied on the structure (both peak and residual), by elongating the duration of the impact event. Furthermore, they allow for additional deformation of the structure which reduces the internal force within the main cables. Moreover, they limited the forces transmitted to the lateral anchors. By analyzing the load transmission in the barrier for both cases (fbNo and fbEd), using energy dissipators was found to be advantageous in reducing the tensile force in the net elements by 60% in comparison with fbNo case. In addition, the tensile forces are distributed more evenly between the main cables when energy dissipators were used.

Some parametric analyses were carried out afterwards to investigate the sensitivity of some parameters to the model results. First the effect of changing the inclination angle of the base was studied in terms of forces applied on the structure and its deformation. Using higher inclination angles was found to increase average flowing velocities (in both x and z directions) leading to higher peak forces and lower impact duration. Afterwards, the effect of inclination angle of the flexible barrier with respect to the gravity vector was investigated. It was found that increasing this angle between the two would accelerate the rate of dead zone mass creation which decreases the duration of the impact. Moreover, the deformation of the energy dissipators was found to be lower for higher values of this inclination angle. However, overall, the difference in the results for different barrier inclination angles is very limited. In the next chapter, some design guidelines will be recommended using the numerical model presented in this chapter.

Chapter 5

Best practice and recommendations for the design of debris flow mitigation structures

Contents

5.1 Introduction

This chapter presents some guidelines and recommendations concerning the impact behavior of granular flows. It starts with the comparison with load estimation guidelines that were proposed recently by Volkwein (2014). The differences and similarities between the DEM model and the design guidelines in terms of force estimation on a barrier are highlighted. Next, the effect of the type of the protection structure (rigid or flexible) is investigated in terms of velocity of the flow, total force applied on the structure and the evolution of the dead zone mass. Afterwards, the best practice for dimensioning flexible barriers is analyzed in terms of the bottom opening of the barrier and the size of the mesh. Different values of these two parameters are tested and their effect on the overflowing percentage is highlighted. Then, recommendations are presented concerning the initial geometrical configuration of flexible barriers and the technology of lateral cables connection. Finally, conclusions are drawn out of the discussed results.

5.2 Comparison between the DEM model and load estimation guidelines

In this section, we will compare the DEM model with engineering guidelines for estimating the loads applied on a protection structure by debris flows. The aim is to investigate the differences between using simple design equations and the use of numerical simulations.

5.2.1 Load estimation guidelines for design engineers

Recently, Volkwein proposed design guidelines for the design of flexible debris flow barriers (Volkwein, 2014). These guidelines include load estimation based on forced-based loading approach (Wendeler, 2008). In the guidelines, the hydrostatic p_{stat} and the hydrodynamic p_{dyn} pressures are assumed to act uniformly over the width of the channel. These pressures are calculated as follows:

$$p_{stat} = KH\rho g\ cos(\alpha) \tag{5.1}$$

$$p_{dyn} = \lambda \rho v^2 \tag{5.2}$$

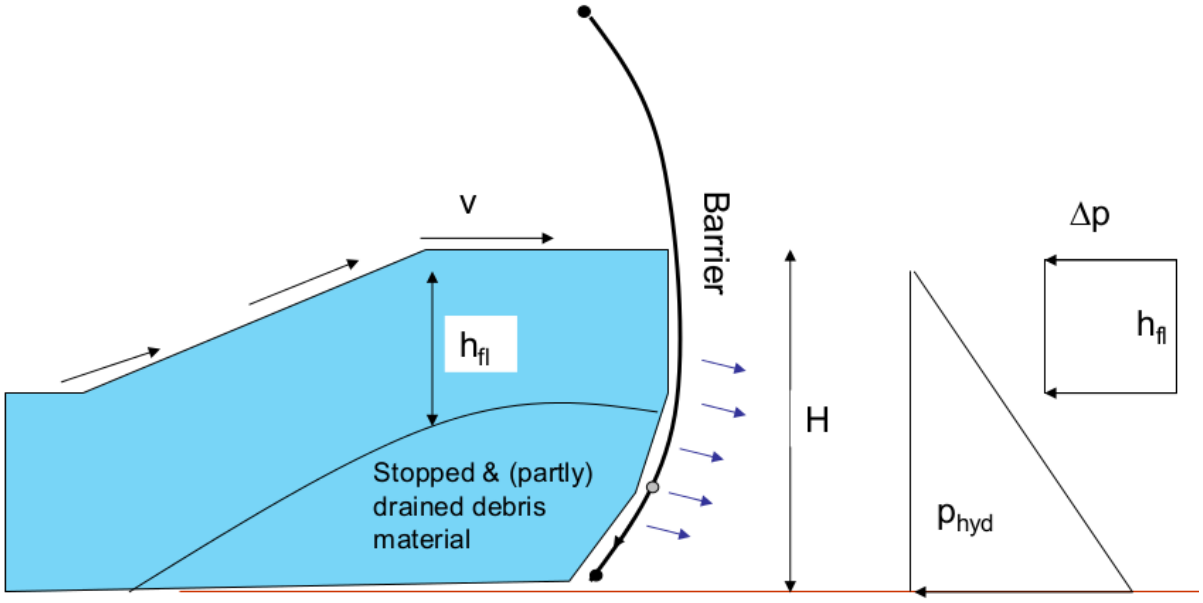

Figure 5.1: *Hydrostatic and hydrodynamic pressures applied on a barrier impacted by debris flow (after Volkwein, 2014)*

where v is the impact speed, H is the filling height, ρ is the flow density (1600 - 2200 kg/m^3), λ is pressure coefficient (2 for high debris density, 0.7-1 for a density of 1900 kg/m^3), K is the earth pressure coefficient (taken as 1) and g is the gravitational vector (9.81 m/s^2). $cos(\alpha)$ accounts for the inclination angle of the channel.

The hydrostatic pressure comprises the pressure applied by the weight of both the dead zone and the flowing particles. On the other hand, the hydrodynamic pressure is related to the kinetic energy of the flowing particle, and thus depends mainly upon their flowing speed.

5.2.2 DEM model considered for comparison with load estimation guidelines

The impact of a granular flow against a rigid wall is simulated for comparison with the guidelines estimation. The wall and the flow characteristics are the same as the ones used in Chapter 3 but with a larger dimensions. The flow has a density ρ = 1350 kg/m^3 and is composed of particles of D_{50} = 112 mm and the number of particles is 13,171 clumps, where each clump is made of two identical spheres. The barrier is 5 m wide and 5.5 m high. No overflowing of the wall took place during the impact event.

At different snap shots of time, two different types of particles are identified: particles forming the dead zone and particles forming the flowing mass (Fig. 5.2a). For each type, the interaction forces between the particles and the wall are summed and then normalized by the width of the wall and thus expressed in kN/m.

In order to be comparative with the two interaction forces calculated in the DEM model, the two equivalent forces from the guidelines would be:

$$F_1 = H_{dead}\, K\, \rho\, g\, cos(\alpha)\, (\frac{H_{dead}}{2} + H_{mov}) \tag{5.3}$$

$$F_2 = \frac{K\, H_{mov}^2\, \rho\, g\, cos(\alpha)}{2} + \lambda\, \rho\, v^2 \tag{5.4}$$

where H_{dead} is the height of the dead zone and H_{mov} is the height of the moving particles that are interacting with the wall. In accordance with the guidelines, K is taken as 1 while λ is taken as 0.7 as the bulk density of the flow is low.

The sum of forces from pressures in Equations 5.1 and 5.2 is equal to that of Equations 5.3 and 5.4, as shown in Figures 5.2b and 5.2c. In fact, Equation 5.3 represents the sum of forces applied at contact points between the dead zone and the wall similar to the way they are calculated in the DEM model. Likewise, Equation 5.4 represents the sum of forces applied at contact points between the moving particles and the wall. As a result, both methods can be compared.

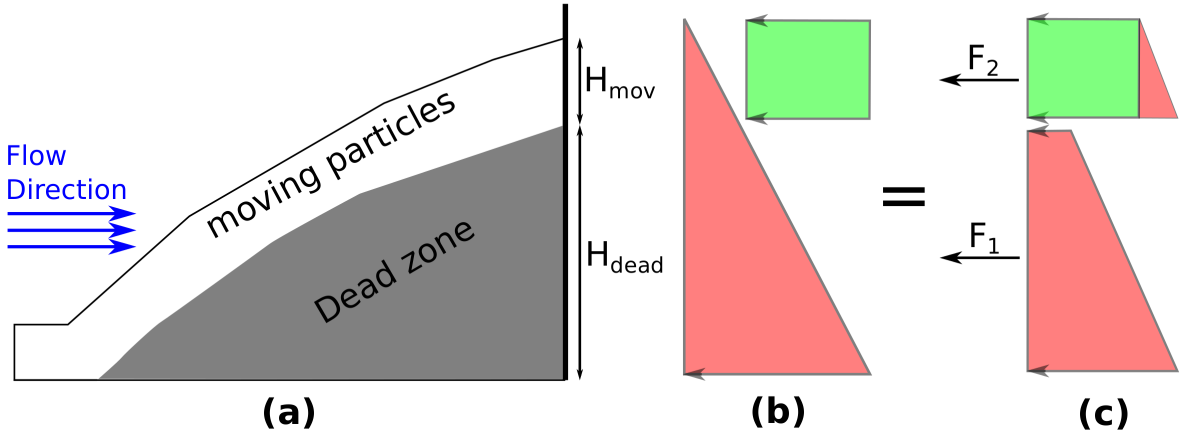

Figure 5.2: *Pressures applied on the wall:* ***(a)*** *Dead and moving parts of the flow,* ***(b)*** *Pressures from Volkwein (2014),* ***(c)*** *The equivalent pressures considered for comparison with DEM results*

5.2.3 Comparison and discussion

Figure 5.3 shows the evolution of forces applied by the dead mass (F_1) and the flowing mass (F_2) on the wall, calculated from both the DEM model and the guidelines. For F_1 (Fig. 5.3a), at the beginning of the formation of dead zone, the DEM model force curve starts increasing earlier than that of the guidelines (at t < 4 seconds). Afterwards, it increases rapidly up to a peak value of 53 kN/m. Such a peak is not predicted by the guidelines curve at the same time (F_1 = 28 kN/m), which keeps increasing progressively. At the end of the impact, when all particles become dead, the DEM curve converges to a value that is 23% higher than that of the guidelines. Overall, the guidelines estimation is found to underestimate the force applied by the dead zone mass on the wall.

On the other hand, for F_2 (Fig. 5.3b), both force curves are similar at the beginning of the impact. However, as the force reaches its peak value, the force calculated according to the guidelines is higher than the one from the DEM model. The guidelines peak force is 2.2 times higher than that of the DEM at the same time. Thus, in contrast to $F1$, the guidelines overestimate the impact force applied by the moving particles on the wall. However, overall, the two curves follow the same trend, but with the guidelines curve being amplified.

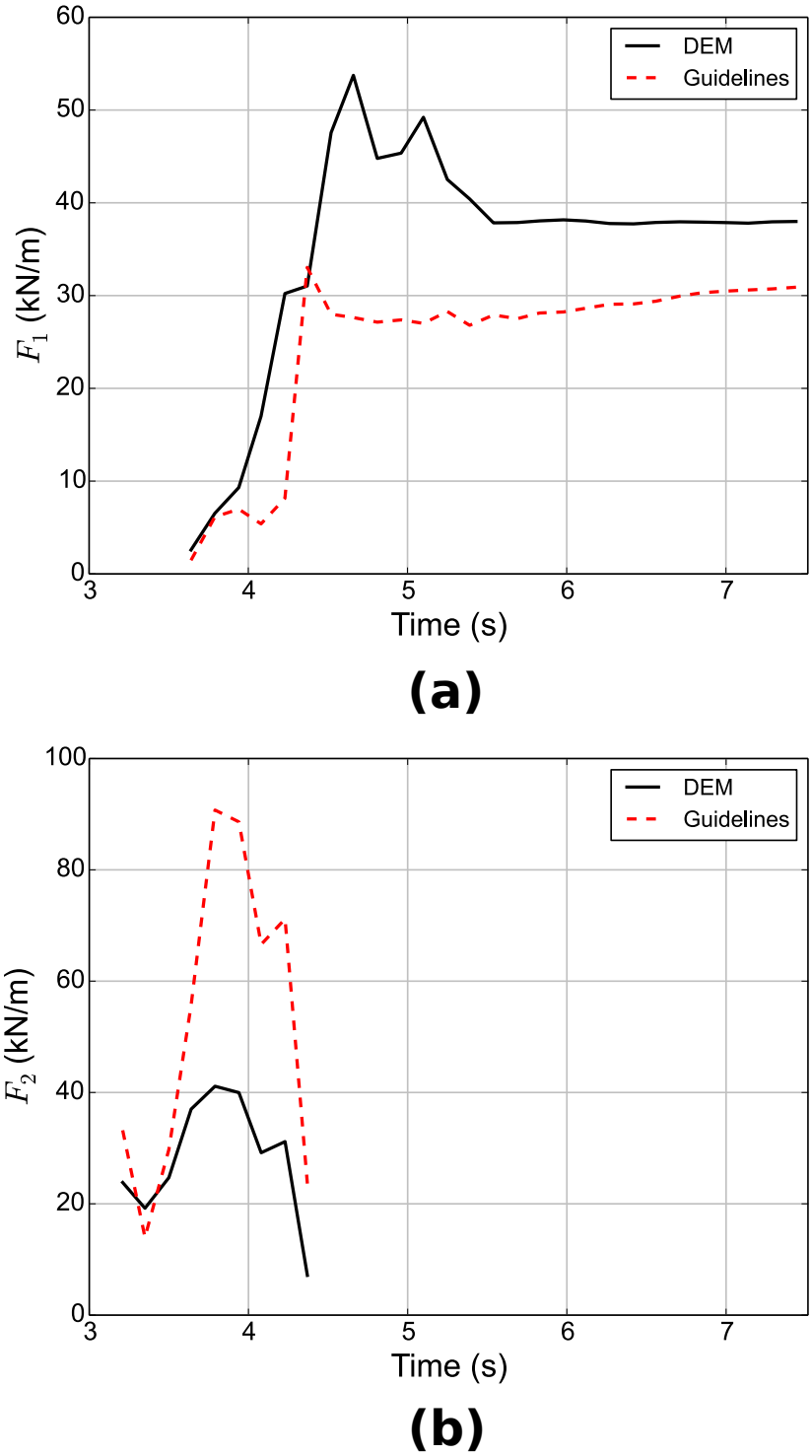

Figure 5.3: *Evolution of forces applied on a barrier by a granular flow calculated by the DEM model and Volkwein load-estimation guidelines:* ***(a)*** *Force transmitted through the dead zone,* ***(b)*** *Force transmitted through the moving particles*

Such discrepancies in the results between the two cases can be understood by going back to Equations 5.3 and 5.4. For F_1, Equation 5.3 uses an earth coefficient that is equal to 1 during the whole period of the impact event. K can be defined as the ratio between horizontal and vertical stresses of the granular medium (Das, 2013). Assuming a constant value of K of behind the wall might not be valid during the impact. At the beginning of the impact, the small dead zone that is formed is subjected to high stresses from the moving particles that collide with that zone. Theses stresses are transferred to the wall through the dead zone. The guidelines curve does not take into account this effect and thus does not predict such stresses. Afterwards, as more dead particles accumulate behind the wall, the dead zone continues to be subjected to high stresses from the flowing particles, indicating the presence of a passive earth pressure (to use the common soil mechanics terminology) (Hutter et al., 1995). Such stresses might result in values of coefficient K higher than 1. At the end of the impact, the difference between the two curves could be again due to the value of K. K at the static state depends on the value of friction between the final mass and the wall and also the final mass and the channel base, as shown earlier in Section 3.7.

For F_2, in Equation 5.4, the flowing velocity of the particles was taken as the average flowing velocity of all particles of the flow. This value might be overestimating the force from the guidelines (compared with DEM-calculated force) because moving particles lose part of their velocity as they collide with the dead zone (Segalini et al., 2013). The moving particles collide with the dead zone and then overflow it up to the point of impact with the wall. Such collision reduces the flowing velocity of the particles and thus the dynamic impact between the moving particles and the wall is minimized. This reduction has been included in hydrodynamic models of granular flows overtopping rigid walls (e.g. Chanut et al., 2010). Moreover, in experiments, a reduction in flowing velocity of moving particles have been observed for flows impacting rigid walls (Faug et al., 2002; Pudasaini et al., 2007; Faug et al., 2011; Caccamo et al., 2012). The same has been observed for non-overtopping cases (Jiang and Towhata, 2013), when comparing two successive snapshots of time for the surface flowing velocity (Fig 5.4) analyzed using Particle Image Velocimetry (PIV) analysis.

To investigate the previous argument, the flowing speed (i.e. the norm of velocity vector) of each particle is plotted at different snapshots of time (Fig. 5.5), for particles that lie in the middle of the channel (within 45% and 55% of the its width). It can be noted that, after the dead zone starts accumulating, the moving particles collide with the

Figure 5.4: *Side view, top view, and velocity map for different time points of a dry granular flow impacting a rigid wall (after Jiang and Towhata, 2013)*

dead zone with a high speed. This collision could be leading to values of K higher than 1. Moreover, the flowing speed of the moving particles is dramatically reduced after the collision. As a result, these moving particles impact the wall with a reduced velocity. Such reduction of velocity is not taken into account by Equation 5.4.

5.3 Effect of the type of protection structure on its impact behaviour against granular flows

In this section, the impact behavior is analyzed for the same granular flow but different protection structure types. This is to investigate the effect of the structure type on the impact behavior. Three different barriers are considered: a flexible barrier without energy dissipators (fbNo), a flexible barrier with energy dissipators (fbEd) and a rigid wall (rigW). The two flexible barriers (fbNo and fbEd) are the same as ones used in Chapter 4. The rigid wall stiffness parameters are the same as the ones used in Chapter 3. The width and height of the wall are the same as the two flexible barriers. The aim is to investigate the effect of the global stiffness of the barrier on the barrier's response to the granular flow impact. Evolution of flowing velocities (in x and z directions), total force and dead zone with time are compared for the three cases. Such comparison is helpful for design engineers as it shows the effect of the choice of a specific structure type on the whole impact process as well as the loading to consider for design purpose.

Figure 5.6a shows the evolution of $\overline{U}_x$ with time for the three structures. For the rigid wall case (rigW), the peak value reached by $\overline{U}_x$ is found to be slightly lower than that of the two flexible barriers. Furthermore, after the peak, the velocity tends to decay faster in the rigid wall case and thus having a total duration of only 5 seconds.

Similar observations are seen for the evolution of $\overline{U}_z$ with time (Fig. 5.6b). For the three structures, the evolution of $\overline{U}_z$ starts just after the values of $\overline{U}_x$ in Figure 5.6 starts decreasing. This indicates a divergence of part of the flow into x-z plane due to the impact on the structures (Faug et al., 2002, 2011; Caccamo et al., 2012). For the rigid wall case (rigW), the peak value reached is 0.58 m/s which is lower than fbNo case (0.72 m/s) and fbEd case (0.64 m/s). Moreover, $\overline{U}_z$ is found to decay faster in the rigW case leading to a lower duration of evolution (2 seconds).

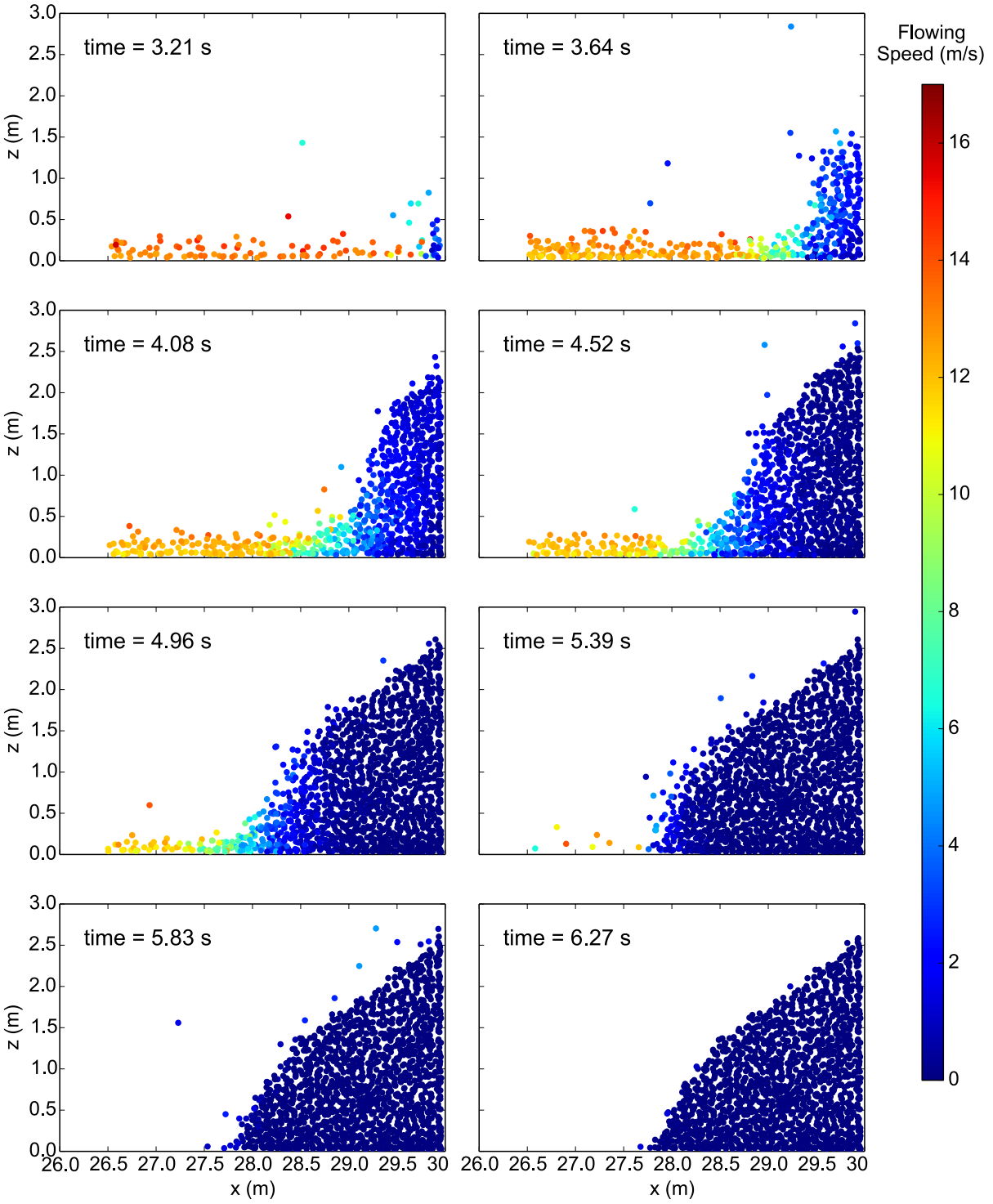

Figure 5.5: *Snapshots at given times of the velocity map of particles that that lie in the middle of the channel*

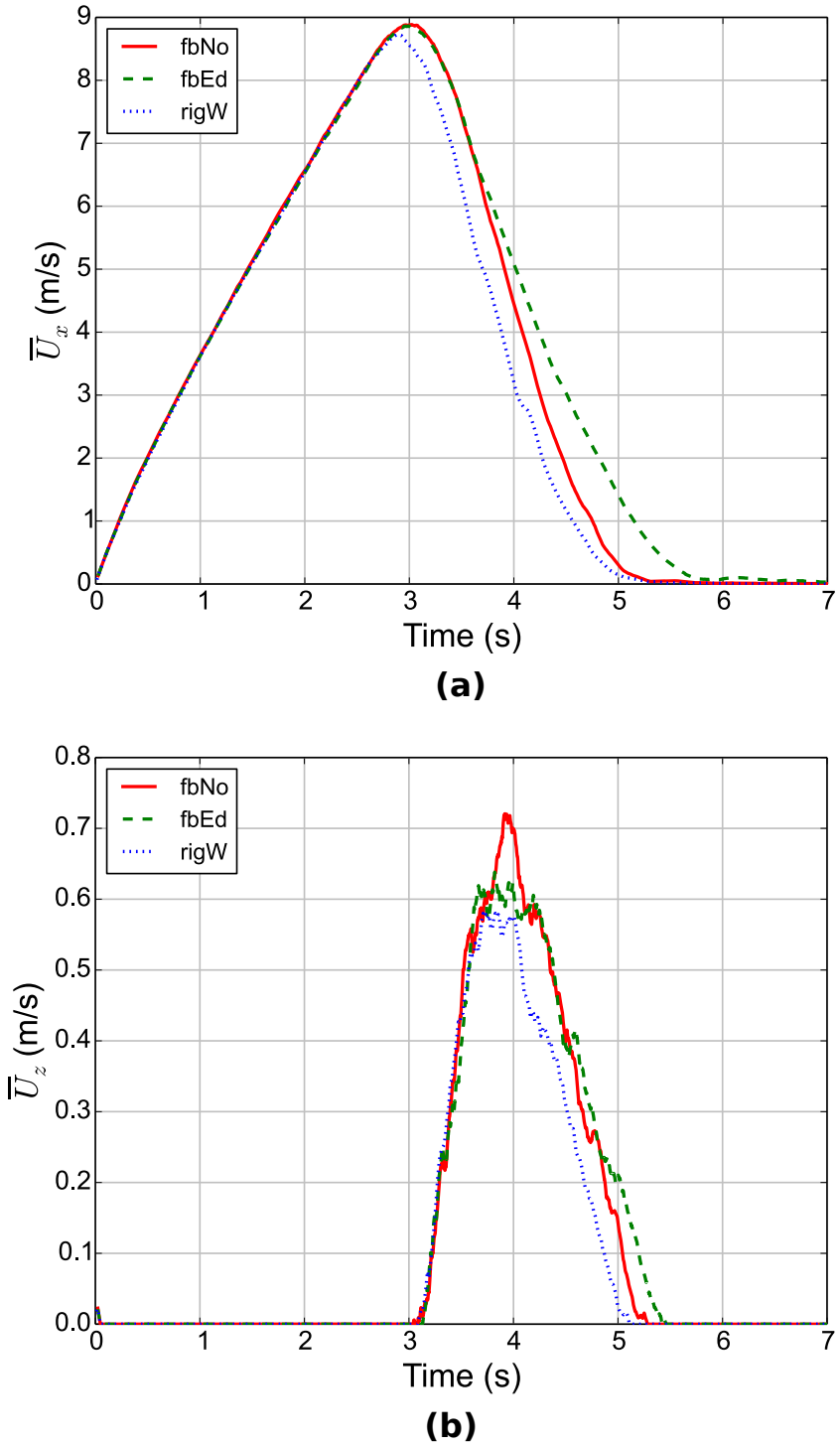

Figure 5.6: *Average flow velocity component for three structures: a flexible barrier without energy dissipators (fbNo) and a flexible barrier with energy dissipators (fbEd) and a rigid wall (rigW):* ***(a)*** *in the direction of the flow,* ***(b)*** *perpendicular to the channel base*

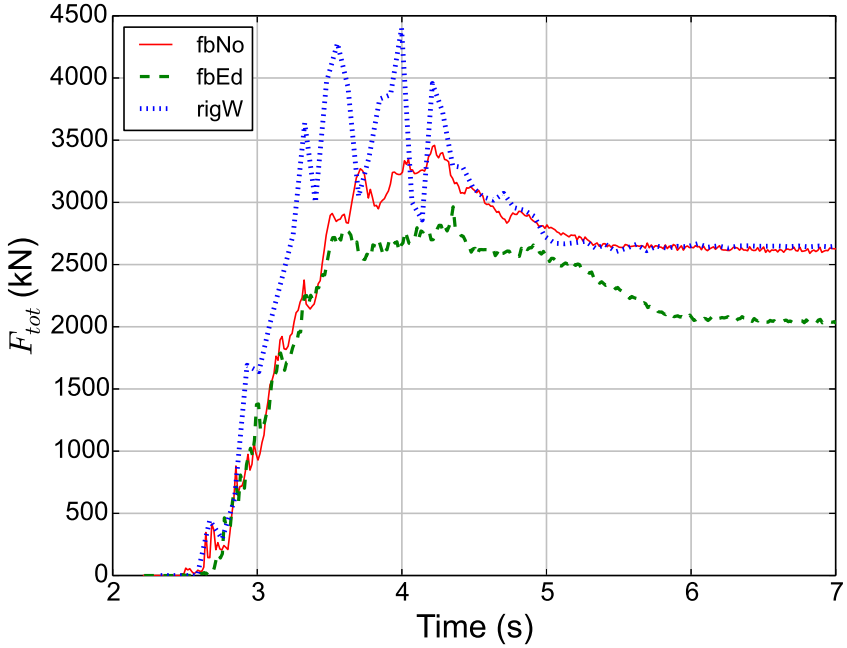

Figure 5.7: *Evolution of the total force applied by the flow, for three structures: a flexible barrier without energy dissipators (fbNo) and a flexible barrier with energy dissipators (fbEd) and a rigid wall (rigW)*

Concerning the evolution of the total force applied on the structures, three phases could be identified: an accumulative phase with the force increasing with time, a phase where the peak value is reached and a third declining phase until reaching the residual force values (Fig. 5.7). For the first phase, the evolution of total force is faster for the rigid wall (rigW) than the flexible barriers. In the seconds phase, the rigW case reaches the peak value of the total force at t = 4 seconds, while it is reached for fbNo and fbEd cases at t = 4.22 and 4.35 seconds respectively. The peak force value is higher for rigW case (4400 kN) than those of fbNo (3460 kN) and fbEd (2950 kN). Finally, the third phase starts after the peak where the rate of decrease of F_{tot} is faster for rigW case than the other two cases. The final force values reached for rigW and fbNo cases are the same (2650 kN) while a lower value is recorded for fbEd case (2050 kN).

The final results compared between the three structures are the evolution of the dead zone mass with time (Fig. 5.8). The dead zone mass accumulation is found to start earlier (at t = 3.15 seconds) when a rigid wall is installed against the flow. Besides, the rate of dead zone accumulation is faster, due to the absence of any deformation of the structure,

in contrast to the flexible barriers. The total final mass of the dead zone is equal to the total mass at the end of the avalanche event of the two cases rigW and fbNo, while it is 5% low for the fbEd.

The previous results can be explained based on the concept of global stiffness of the structure and its capability to deform. When a highly stiff non-deformable structure is installed (rigW), the flowing velocity in both x and z directions were found to record lower peaks and to be broken down much faster than the other two cases. This is due to the non-deformability of the wall which does not allow for further evolution of the flowing velocity, in contrast to fbNo and fbEd cases.

The same concept can be used to explain the difference in F_{tot} with time. The rigid wall has a higher global stiffness than the flexible barriers and thus has higher interaction force with the flowing particles. A strong fluctuation of F_{tot} signal was observed for rigW case which could be due to the development of force chains behind the wall, as previously detailed in Section 3.6.2. However, no such strong fluctuation is seen for the two flexible barriers, which might be due to their ability to deform which prevent the process of successive build-ups and losses of force chains. For the residual value of the total force, both rigW and fbNo where found to converge to the same value since the initial mass of the avalanche is the same. This supports the argument in Section 4.5.3 that the drop of residual force value when energy dissipators are used is mainly caused by a loss of retained material and also the support from the base on the downstream of the channel.

The deformability of the structure is also a key player in the evolution of the dead zone mass. The rigid wall is not deformable and thus does not allow for further evolution of the velocity of the flow. As a result, particles tend to die faster than the other two cases. It is worth noting that, in general, results of rigW and fbNo are close to each other when compared with those of fbEd case. This confirms the importance of using energy dissipators in allowing for barrier to deform which result in lower total force values applied on the barrier, both the peak and the residual.

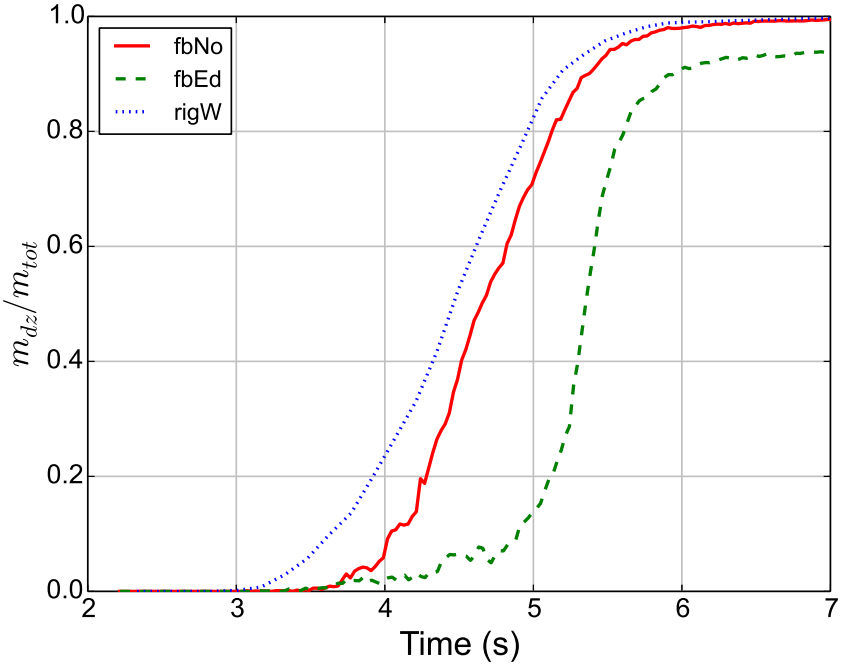

Figure 5.8: *Evolution of dead zone mass, for three structures: a flexible barrier without energy dissipators (fbNo) and a flexible barrier with energy dissipators (fbEd) and a rigid wall (rigW)*

5.4 Recommendations for the dimensioning of flexible barriers

In this section, the dimensioning of flexible barriers will be studied by considering the retaining capacity of the barrier. Two parameters are tested for several values: the first is the bottom opening of the barrier and the second is the mesh size of the net. The aim is to recommend the values of these two parameters with respect to the particle size distribution of the granular flow.

5.4.1 Bottom opening of the barrier

Flexible barriers are sometimes fixed from the bottom, in order not to allow particles to go beneath them. This is especially important in debris flow conditions where excessive overflowing could damage the nearby infrastructure. However, in other cases, a bottom opening is allowed to permit the normal transport of sediments for non-extreme events (Volkwein, 2014; Wendeler and Volkwein, 2015; Iwanaga, 2015). In this section, the effect

of allowing for a bottom opening (b_o) of the barrier will be investigated in terms of the retained mass. This is to see whether or not allowing for some particles to go beneath the barrier will greatly affect the final retained mass.

Four values of b_o are tested for the same barrier. These values are taken as a percentage of the diameter size of the flowing particles in order to keep the results rather general. The four b_o tested values are equal to: D_{90}, D_{70}, D_{50} and D_{30}. The tests were carried out for a flexible barrier that has no energy dissipators. This is to prevent the creation of escaping windows on the sides of the barrier and thus allow for overflowing process only by particles going beneath the barrier.

Figure 5.9 shows time evolution of overflowing percentages for the four tested values of b_o. Little differences can be seen for the rate of evolution of overflowing of the different curves. For example, at t = 5 seconds, 78.5% of particles mass have overflown the barrier when $b_o = D_{30}$. This percentage rises to 83.2% when using $b_o = D_{90}$. This agrees with the assumption that, the larger the bottom opening, the faster the rate of the overflowing percentage. However, at the end of the impact event, all particles have overflown the barrier for the four tests.

Such findings can be explained by the vertical displacement of the bottom cable of the barrier. As the bottom cable gets displaced vertically, the bottom opening increases allowing for more particles to go through (Fig. 5.10). Three stages of the cable's vertical displacement could be identified from the figure. The first stage takes place at the beginning of the impact where a sharp increase of cable's vertical displacement is recorded due to the impact, with no particles overflowing beneath the bottom cable. Afterwards, the second stage starts which is characterized by a continuous overflowing of particles coupled with fluctuative vertical displacement of the bottom cable. These fluctuations might be due to the different surges of the flow that hit the barrier, get the cable displaced vertically and then escape beneath it. This mechanism continues until the final stage which is marked by a sharp decrease in the vertical displacement of the cable as most of the flow has overflown the barrier.

To sum up, allowing for a bottom opening, even as small as D_{30}, would lead the flow to totally overflow the barrier from the bottom. This is consistent with some recommendations in the literature that the bottom cable should be fixed (Brighenti et al., 2013).

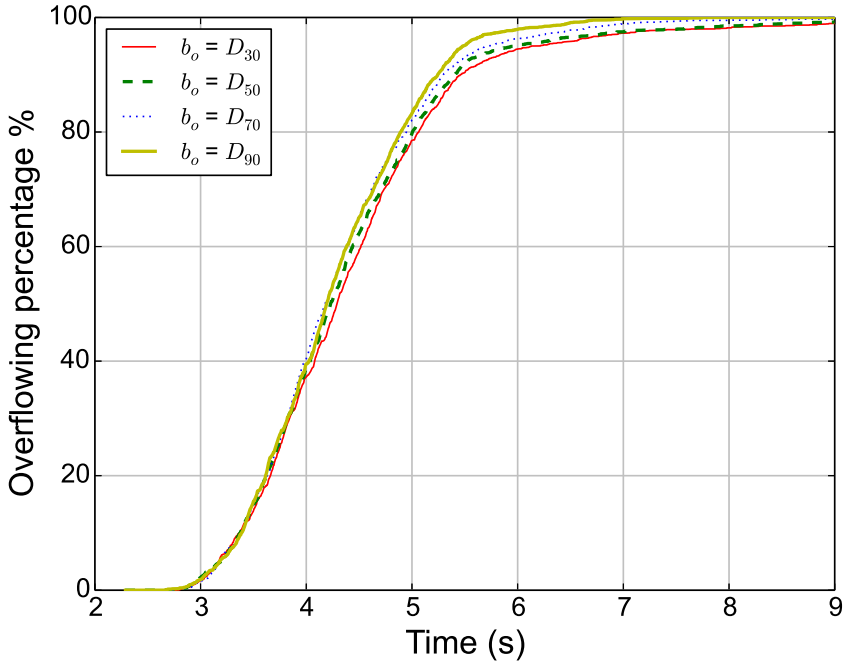

Figure 5.9: *Evolution of overflowing percentage for different values of bottom openings of the barrier*

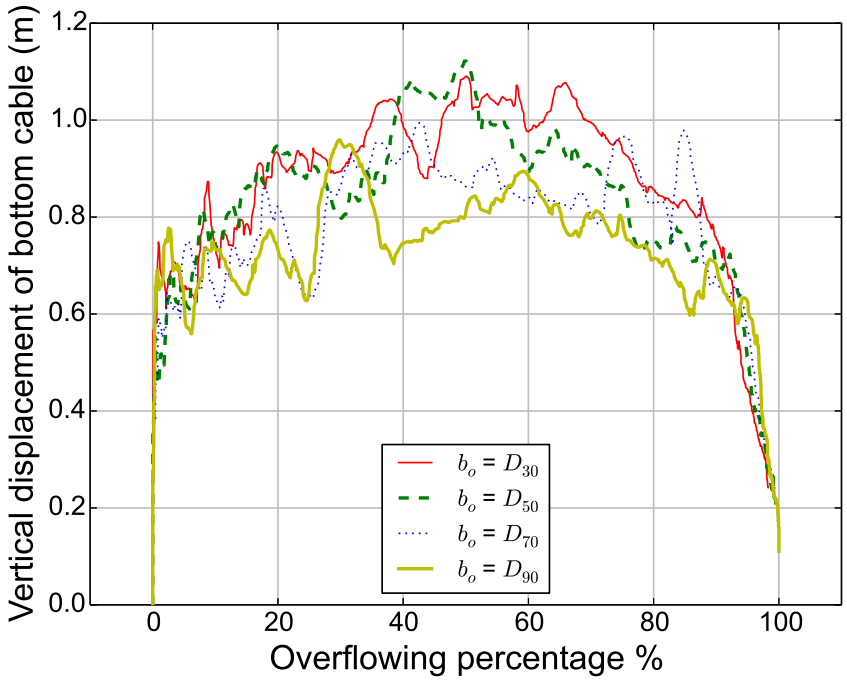

Figure 5.10: *Evolution of maximum vertical displacement of the bottom cable with the overflowing percentage for different values of bottom openings of the barrier*

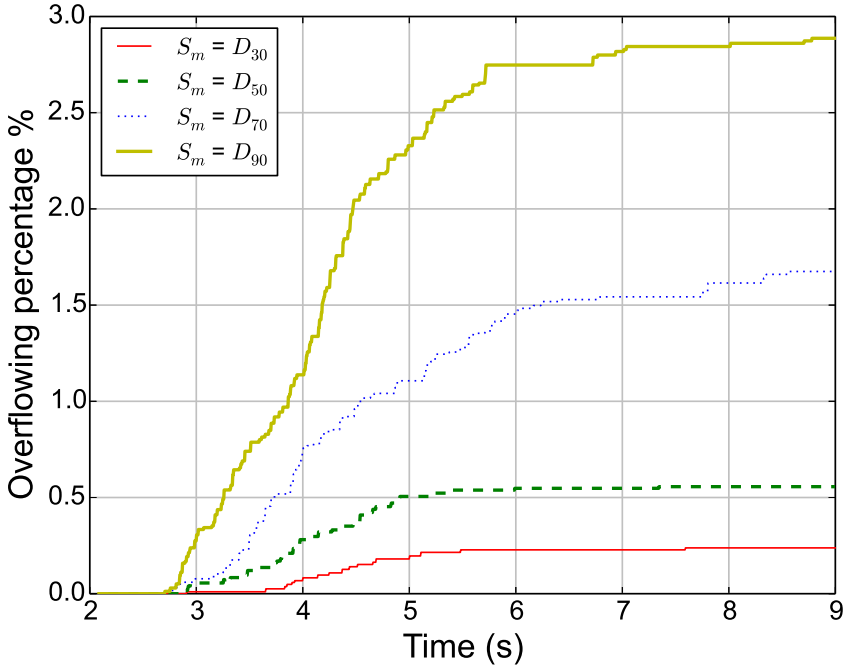

Figure 5.11: *Evolution of overflowing percentage for different values of mesh size of the net*

5.4.2 Mesh size of the net

In this section, different values of mesh size (S_m) of the net are tested to investigate the percentage of particles that would go through the mesh. The four S_m tested values are equal to: D_{30}, D_{50}, D_{70} and D_{90}. The tests were carried out for a barrier with no energy dissipators and twice the height of barriers in Chapter 4. This is to prevent particles from overflowing the barrier from the sides or from the top. Thus, the overflowing results are only for particles going through the net.

The percentage of particles going through the net is found to be dependent on the mesh size (Fig. 5.11). Smaller mesh size ($S_m = D_{30}$) leads to lower percentage of overflowing (0.2%). However, in all cases, most of the mass of the granular flow is retained. For large mesh size as for $S_m = D_{90}$, the final retained mass is 97%. This is consistent with some guidelines in the literature suggesting that a mesh size of up to D_{90} would be convenient for retaining the granular flow mass (Volkwein, 2014; Wendeler and Volkwein, 2015).

5.5 Recommendations for the initial configuration of flexible barriers

5.5.1 Comparison between two barriers with two different inital orientation with respect to the channel base

In the literature, impact tests of granular flows against barriers have been carried out with two different barrier positions. Some are preformed with barriers that are positioned in a direction parallel to gravity vector (referred to later as 'fbG') while others have positioned the barrier normal to the channel base (referred to later as 'fbN'). In this section, a comparison between the two cases will be carried out in order to investigate the effect of this positioning of the barrier on the impact results. Both barriers have energy dissipators installed at the extremities of each main cable, and have the same mechanical and geometrical parameters introduced earlier in Chapter 4. The maximum allowable deformation of energy dissipators (δ_{ED-brk}), is increased to 3.5 meters for both barriers in order to sustain the high deformation of barrier fbN without failure.

The comparison is concerned with the evolution of: average flowing velocity in x-direction, total force applied on the barrier, amount of retained mass and the deformation of the barrier. The barrier parallel to gravity vector (fbG) is the one that has been used in Chapter 4 and was extensively investigated. It would be used here as a reference case.

First, the flowing velocity in x-direction is compared, in order to see the flowing velocity break down and the duration of the impact event (Fig. 5.12). When the barrier is normal to the base (fbN), a longer duration of the impact is observed. The flow is broken down over a period of 8 seconds, which is 30% longer than that of fbG case. This agrees with results of Section 4.6.2 which suggested that decreasing the volume between the barrier and the upstream side of the channel base would decrease the flowing break down time and thus shorten the impact event.

Next, the total force applied on the barrier is compared (Fig. 5.13). At the early stage of the impact, the evolution of total force is lagged by 0.2 seconds for fbN case, which could be due to the lower volume available for the flow to evolve. At the peak, however, similar values of F_{tot} are reached, with fbG case being slightly higher (2990 kN).

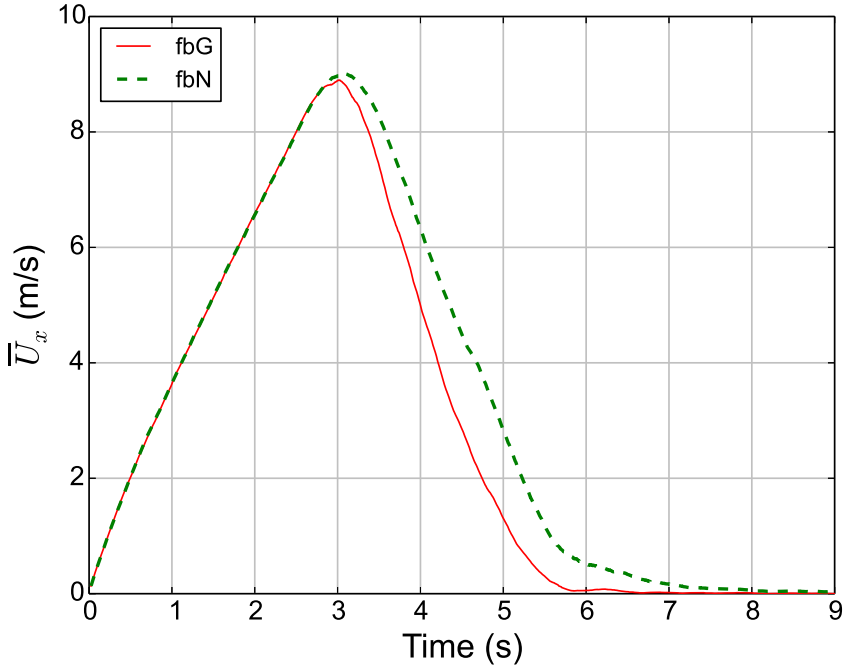

Figure 5.12: *Evolution of average flowing velocity in x-direction for two cases: a flexible barrier parallel to gravity vector (fbG) and a flexible barrier normal to the channel base (fbN)*

Afterwards, the curves converge to the residual values which are 2040 and 1120 kN for fbG and fbN respectively. This difference in residual force, although the initial mass of granular flow is the same, is due to the difference in the amount of retained mass.

Figure 5.14 shows the evolution of the dead zone mass and the final retained mass. For fbN case, the dead zone mass evolution is 1.5 seconds delayed than that of fbG case. Moreover, the final retained mass behind the barrier is significantly lower. Only half of the initial mass of the flow is retained when the barrier is normal to the channel base. The other half is found to overflow the barrier from the sides and also from the top. The top overflowing is controlled by the reduction of the height of the barrier. On the other hand, the side overflowing is due to the opening of 'escaping windows' which are controlled by the deformation of energy dissipators.

The final heights of the barriers measured from the base in the direction of z-axis, are 0.79 and 3 m for fbN and fbG cases respectively. Such reduced height of the barrier, for fbN case, minimizes the barrier's retaining capacity (Fig. 5.15). This reduction of the height is caused by the elongation of energy dissipators installed on the sides of each

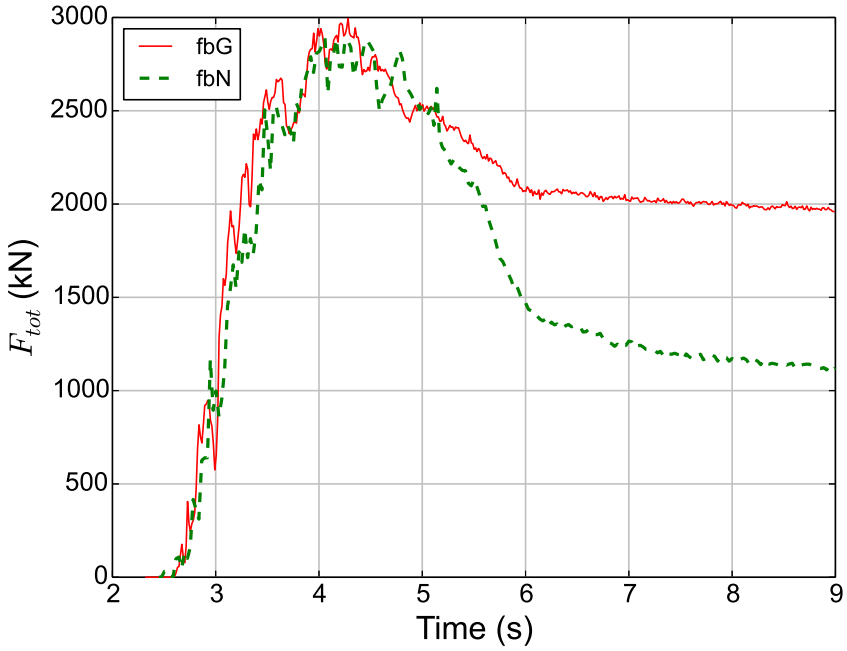

Figure 5.13: *Evolution of total force applied on the barrier for two cases: a flexible barrier parallel to gravity vector (fbG) and a flexible barrier normal to channel base (fbN)*

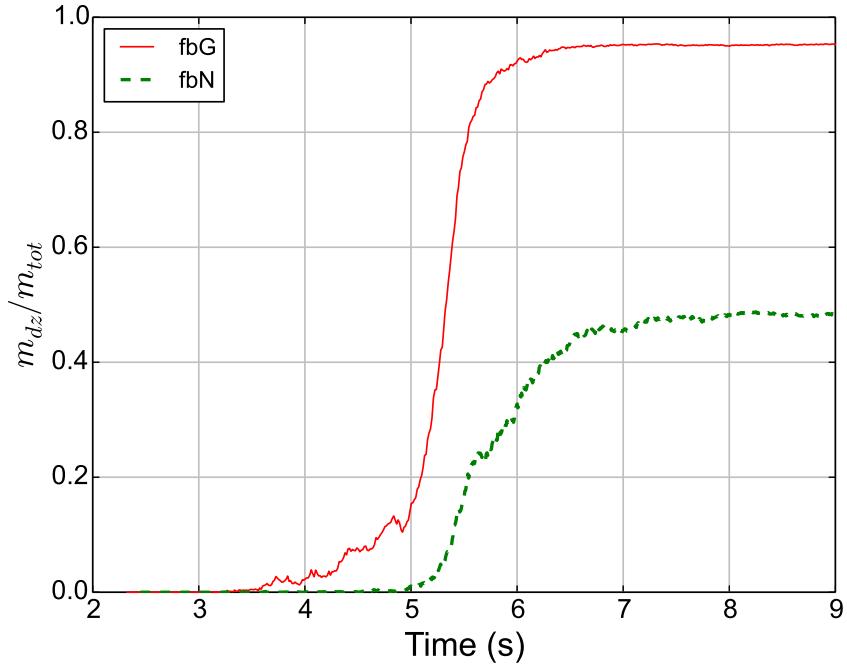

Figure 5.14: *Evolution of dead zone mass behind the barrier for two cases: a flexible barrier parallel to gravity vector (fbG) and a flexible barrier normal to channel base (fbN)*

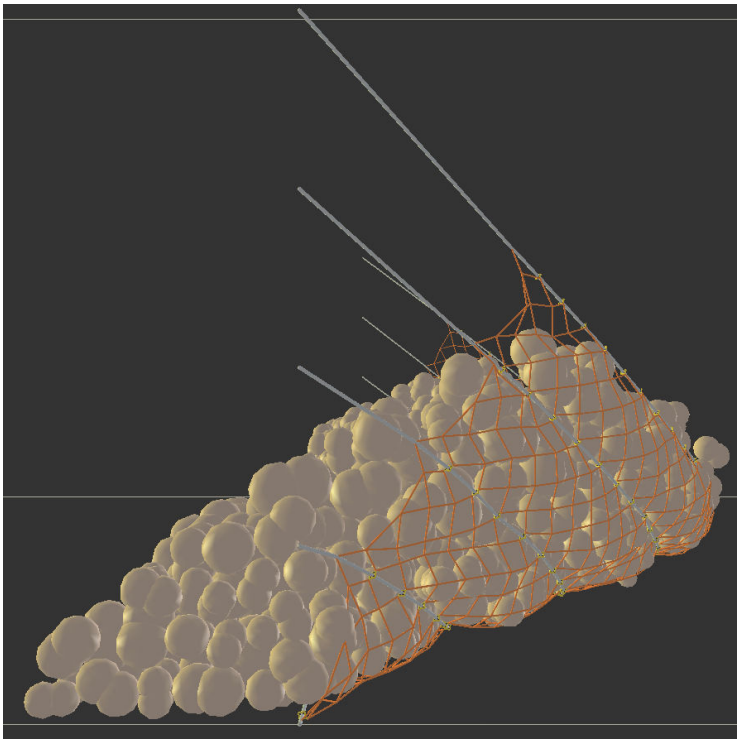

Figure 5.15: *Side view of the final retained mass of a flexible barrier normal to channel base (fbN)*

main cable. The deformation of energy dissipators installed on cables 3,4 and 5 is shown in Figure 5.16. Higher deformations are observed for fbN case, especially cables 4 and 5 which reach deformations of 2.19 and 2.96 meters respectively. Such high deformations lead to the loss of retaining capacity of the barrier.

5.5.2 Effect of lateral cable connection technology on the impact behavior of flexible barriers

In this section, two different approaches of connecting the lateral cables to other components of the flexible barriers are compared. The first approach is connecting the lateral cable to energy dissipators which are then connected to lateral anchors (Fig. 5.17a), similar to the barrier introduced in Chapter 4. The barrier with this lateral cable configuration will be referred to in this section as 'des_1'. The second approach is to connect the lateral cables directly to the anchors (Fig. 5.17b), referred to here as 'des_2'. We will compare the total force applied on each barrier, deformation of energy dissipators and forces on the

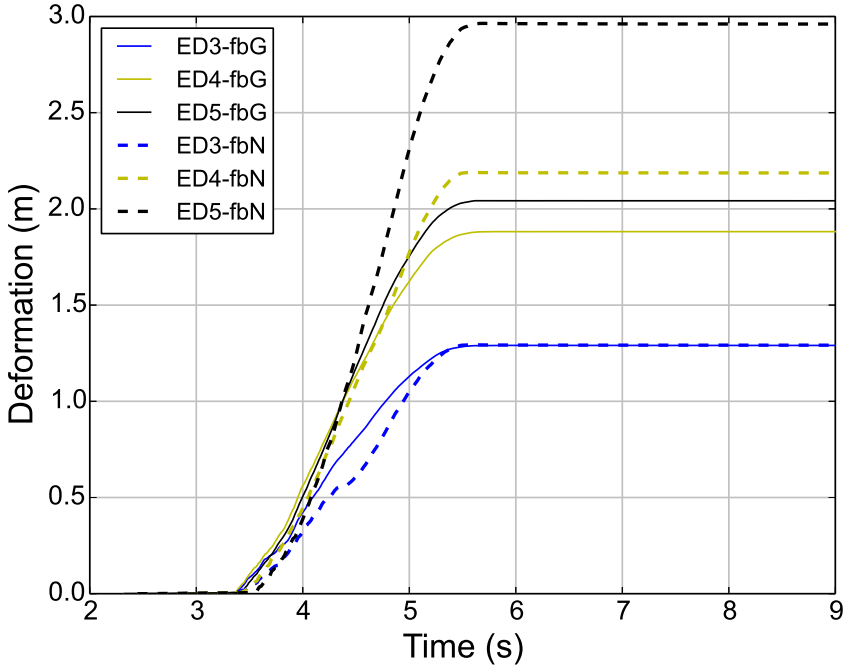

Figure 5.16: *Evolution of deformation of energy dissipators installed on cables 3, 4 and 5 for two cases: a flexible barrier parallel to gravity vector (fbG) and a flexible barrier normal to channel base (fbN)*

anchors. The aim of this comparison is to recommend the best design technology for connecting the lateral cables, which optimizes the performance of energy dissipators and limits the forces transmitted to the anchors.

First, we investigate the total force applied on both barriers (Fig. 5.18). This is to compare the amount of total force and the time required for this force to reach its residual value, indicating the end of the impact event. At the beginning of the impact, both design technologies record similar total force values. Afterwards, des_2 is found to have higher peak total force, which reaches a value of 3300 kN. Afterwards, the total force curves converge to residual values of 2040 and 2650 kN for des_1 and des_2 respectively. The total duration of the impact is shorter for des_2, having a total impact duration of 3 seconds, which is 15% shorter than that of des_1.

The difference in the residual impact force is due to the difference in the retained mass and also the support from the downstream part of the base in des_1 case. Figure 5.19 shows the dead zone accumulation with time and the final retained mass for the two cases under consideration. The accumulation of dead zone mass starts at t = 3.5 seconds

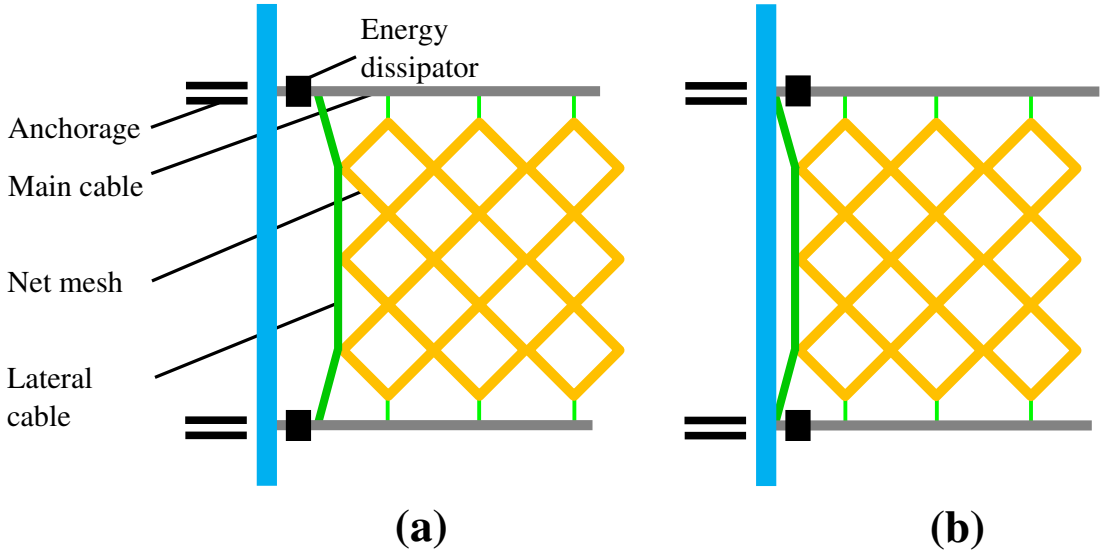

Figure 5.17: *Schematic representation of two technologies for connecting the lateral cables:* ***(a)*** *lateral cables connected to energy dissipators (des_1),* ***(b)*** *lateral cables connected directly to the anchors (des_2)*

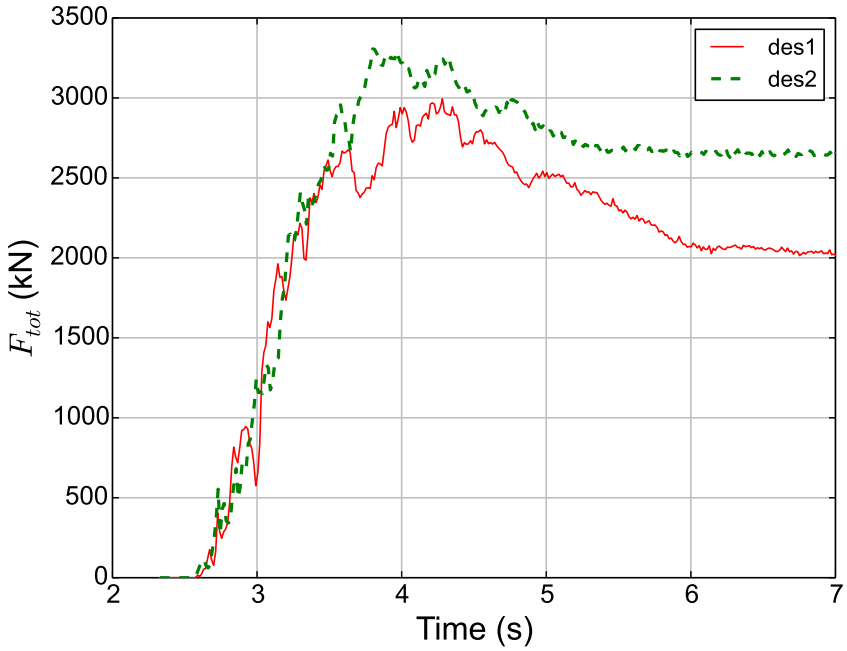

Figure 5.18: *Evolution of total force applied on barriers with two different configurations of the lateral cables: lateral cables connected to energy dissipators (des_1) and lateral cables connected directly to the anchors (des_2)*

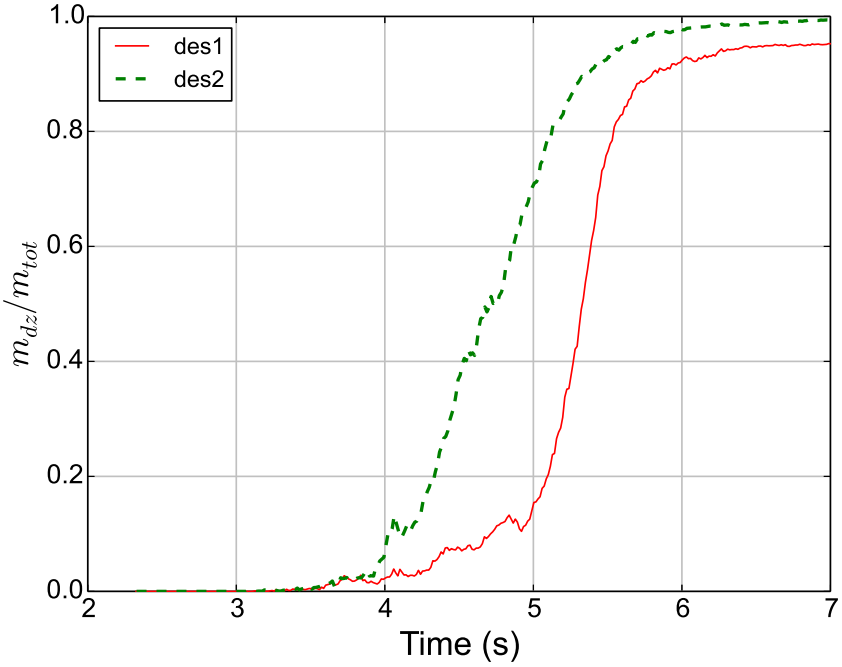

Figure 5.19: *Evolution of the dead zone mass for two different configurations of the lateral cables: lateral cables connected to energy dissipators (des_1) and lateral cables connected directly to the anchors (des_2)*

for both cases. Afterwards, the mass in des_2 case is found to accumulate faster behind the barrier. Finally, at the end of the impact event, all of the initial mass is found to be retained by the barrier in des_2 case while 4.5% percent of the initial mass is lost in des_1 case. This difference in retained mass is due to the lateral escaping windows on the sides of the barriers, which are due to the deformation of energy dissipators as explained earlier in Chapter 4.

The deformation of energy dissipators is investigated for both cases. It is the average deformation of the two energy dissipators installed at the end of each main cable (Fig. 5.20). A big difference is seen for the deformation of energy dissipators between the two cases. Very small amount of energy has been dissipated by energy dissipators for case des_2. The maximum deformation takes place on cable 4 with a deformation of 0.23 m. However, this deformation is 87% lower than that of des_1 case. This indicates that high loads have been transferred via the lateral cables to the anchors in des_2 case without being dissipated through the energy dissipators. Thus, the loads applied on the anchors need to be investigated.

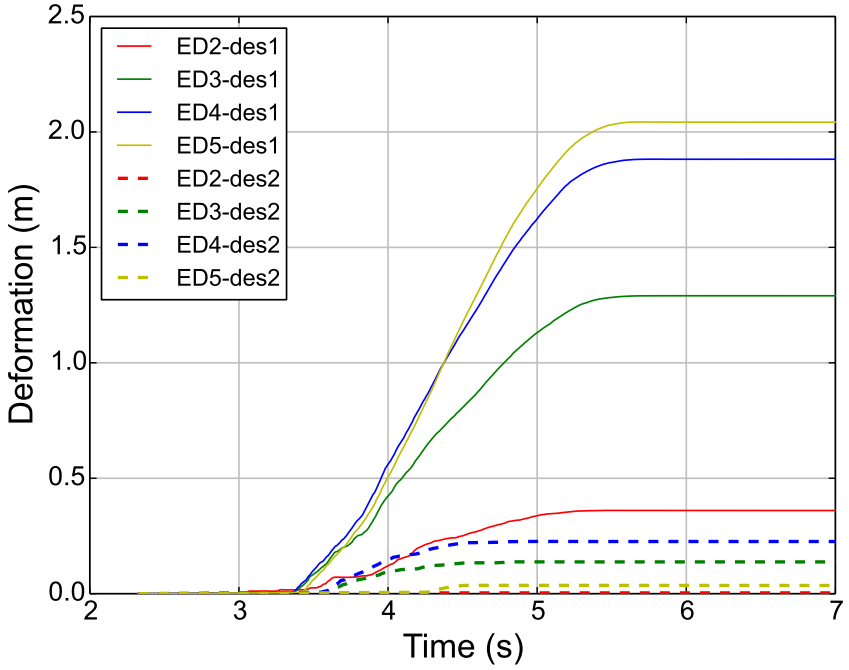

Figure 5.20: *Evolution of the deformation of energy dissipators for two different configurations of the lateral cables: lateral cables connected to energy dissipators (des_1) and lateral cables connected directly to the anchors (des_2)*

Figure 5.21 shows the average force of the two anchors at the extremities of each main cable, for the two cases under consideration. Forces applied on the anchors in des_1 case are limited by the maximum allowable force in the energy dissipators, and thus do not exceed 250 kN. On the other hand, no limit can be seen for the forces applied on the anchors in des_2 case. Forces applied on the anchors are much higher than that in des_1 case, having peak forces of 440 and 540 kN for anchors installed on cables 4 and 5 respectively. Moreover, the residual force values in the anchors are also higher than that of des_1 case. Anchors of cables 4 and 5 have residual force values of 400 and 500 kN respectively.

By analyzing the aforementioned results, des_2 case is advantageous in retaining all the initial mass and preventing lateral overflowing from taking place through lateral escaping windows. However, this takes place at the expense of the barrier's ability to dissipate energy. The energy dissipators were found to have very small deformations indicating that they have not been properly functioning. High loads have been transmitted to the anchors which are likely to cause the anchors to fail. All these differences between des_1 and des_2 are due to the way loads are transmitted. When having the first

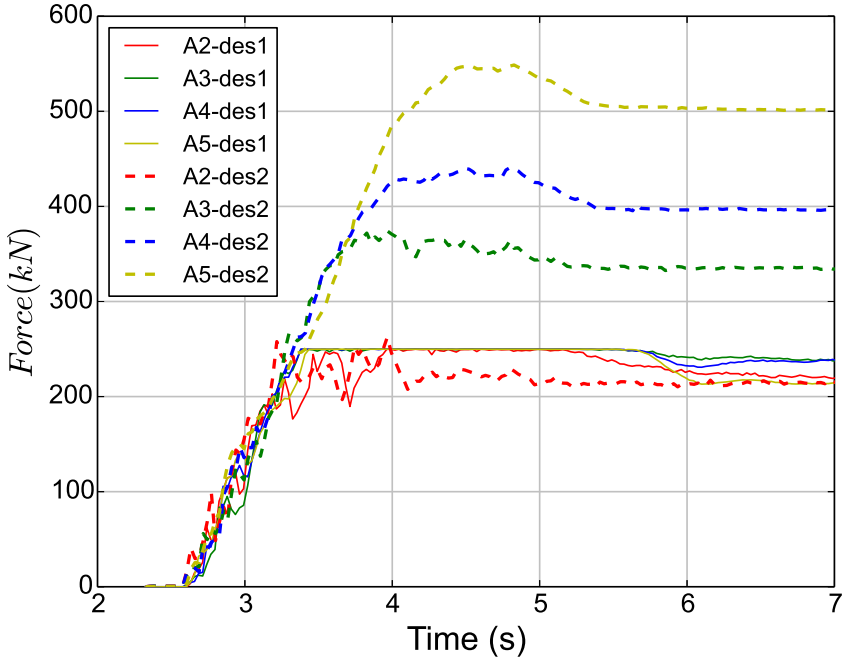

Figure 5.21: *Evolution of forces applied on the anchors for two different configurations of the lateral cables: lateral cables connected to energy dissipators (des_1) and lateral cables connected directly to the anchors (des_2)*

design configuration, all loads in main cables and net elements are transmitted to energy dissipators which are limited by the maximum allowable forces of these dissipators. As a result, the anchors are protected from failure.

On the other hand, in des_2 case, the lateral cables transmit the loads of the net directly to the anchors without passing first through the energy dissipators. Some forces in the anchors are 2.2 times higher than the allowable force in the energy dissipators, thus leading to anchorage failure if a tensile strength is imposed. Moreover, the net elements are highly loaded and thus rupture of net elements would also take place.

Although des_1 design configuration is preferable to des_2, the loss of the retained mass need to be solved. A good design of a flexible barrier should not allow for lateral flowing of the barrier (Volkwein, 2014). This could be solved by having an extra length of the net mesh in a direction parallel to the sides of the channel. Such extra length would function once the energy dissipators start deforming, and thus retaining the mass that would normally escape from the lateral sides. This extra length is approximated in the DEM model by lateral extensions of the net to the sides of the barrier (Fig. 5.22).

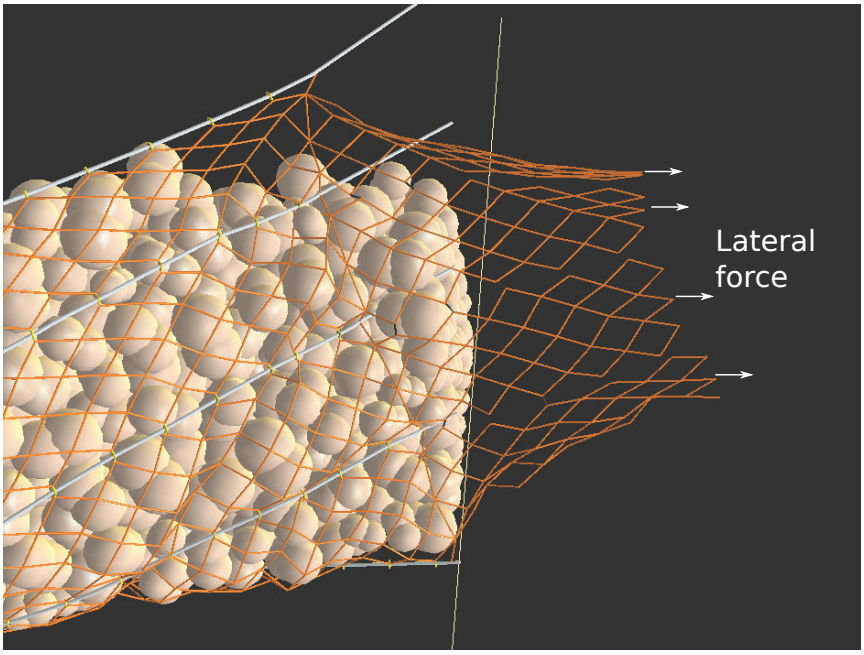

Figure 5.22: *Snapshot at the end of the impact event showing the extra length of the net as a solution to optimize the retaining capacity*

These extensions are supported by small lateral forces in order to prevent any unrealistic deformation. These forces are an approximation of the frictional force that would exist in real barriers between this extra length and the lateral sides of the channel and the dead zone mass.

5.6 Conclusions

This chapter presents different studies of the impact of granular flows on protection structures, with the aim of stating some recommendations and guidelines for the design of these structures. First, results of load estimation guidelines were compared with the results of the DEM model in terms of the impact force on a rigid wall. The guidelines were found to underestimate force transmitted through the dead zone while it overestimates the one applied by the moving particles. The discrepancies of the results of the former were related to the value of earth coefficient (K) which might be changing during the impact event, instead of being constant as stated in the guidelines. For the moving

particles, the differences were thought to be due to the reduction of the flow speed of the flowing part of the flow due to the collision with the dead zone. Such reduction is not taken into account by the guidelines.

Afterwards, the effect of changing the structure type on the impact behavior was investigated. This is to highlight the importance of the choice of the structure type to be used for protection. Three types of protection structures were compared: a rigid wall (rigW), a flexible barrier with no energy dissipators (fbNo) and a flexible barrier with energy dissipators (fbEd). The use of a rigid wall was found to increase the peak force applied by the flow and shorten the impact duration. In contrast, a flexible barrier with energy dissipators, thanks to its excessive deformation, was subjected to lower peak force and longer impact period.

Next, recommendations were drawn concerning the dimensioning of flexible barriers. Two parameters were sensitively tested for different values: the bottom opening of the barrier and the size of the mesh forming the net. The aim was to compare the overflowing percentage of the flow for the different tests. It was found that allowing for a bottom opening of the barrier, even as small as D_{30}, would allow all particles to flow beneath the barrier. This resulted in no mass being retained by the barrier. Concerning the mesh size, it was found that using a mesh size up to D_{90} is convenient as it retains 97% of the flowing mass. This finding is consistent with the recommendations of Volkwein (2014) concerning the mesh size.

Finally, recommendations were drawn concerning the initial geometrical configuration of flexible barriers and the technology of lateral cables connection. For the initial geometrical configuration, two different barriers were tested: a barrier that is parallel to gravity vector (fbG) and a barrier that is normal to the channel bed (fbN). The latter was found to be subjected to higher deformation, with the energy dissipators of the top cable deforming 1.5 times more than that of fbG case. Such deformation led to large reduction in the height of the barrier. As a result, the final retained mass was only 50% of the initial one.

Regarding the side cable connection, two design approaches were compared: the first was connecting the lateral cable to energy dissipators which are then connected to lateral anchors (des_1) while the second was to connect the lateral cable directly to the lateral anchors (des_2). The latter approach was found to be unsuitable because: it has a higher

peak force, almost negligible energy dissipators deformation and higher forces applied to the anchors. All these drawbacks were avoided when des_1 was adopted. The only drawback of des_1 was that lateral escaping windows were opening on the sides of the barrier allowing for some particles to overflow. The solution for this problem is to use additional length of the net in order to close these windows once they are created and thus retain all the initial mass of the flow.

Chapter 6

Conclusions and Perspectives

The increasing urbanization of mountainous areas raised the importance of mitigating geohazards such as landslides and debris flows. Debris flows exert large destructive loading in short period of time which could cause fatalities in the locals of neighboring communities and severe destruction of infrastructures. This thesis presented a DEM model aimed at studying the effect of such loadings on debris flow mitigating structures, being mainly rigid walls and flexible barriers. Three different aspects of such impact have been covered: the impact on rigid walls, the impact on flexible barriers and the guidelines and recommendations concerning the flexible barriers design and best practice. Main conclusions of these aspects and the prospective of the future work are listed in the following sections.

General conclusions

A visco-elastic contact law with Mohr-Coulomb failure criterion was found to be suitable for modeling granular flows in inclined flumes. Real gravel particles in the experiment used to calibrate model required using non-spherical particles in the DEM model. Clumped particles, that are formed by two identical overlapping spheres with an aspect ratio of 3/2, were found to reproduce the flow behavior of the gravel particles. Results indirectly related to the final shape of the deposit behind the wall were compared with the experiment. Better agreements with the experiment was achieved when such clumps

are used, compared with simple spherical particles. This was attributed to the decrease in the rotational kinetic energy (reduced by 70%) and the possible increase in the interlocking between particles.

The normal viscous damping coefficient γ_n, representing the energy dissipated by collision was found to be affecting the flow thickness. Using low values of γ_n leads to very dilute dispersive flow behavior, in contrast to the experimental flow behavior. However, for different values of γ_n, no significant difference was observed for the average flowing velocity in the direction of the flow when measured in a volumetric boundary 40 cm away from the rigid wall.

The total force impacting the rigid wall can be divided into a dynamic force and a gravitational one. Accurate calculation of the gravitational part, which is due to the weight of the dead zone accumulating behind the wall, requires using the instantaneous values of the friction angle between the dead zone and the base (δ_1) and also the friction angle between the dead zone and the wall (δ_2). The dynamic part of the force, which is mainly related to the dynamic energy of the flow, was found to contribute to 85% of the peak total normal force applied on the wall, with the weight of the dead zone contributing to 15% of that peak, for high values of the inclination angle. This highlights the importance of properly modeling the granular flow, in order to accurately estimate the total impact force.

Impact results on each part of the wall show some heterogeneities, during both the impacting and depositing stages. These observations were found to be present for both the experiment and the numerical models. Numerical tests of samples with same volume and testing geometry but different initial arrangements of particles led to different final normal force values on each part of the wall. Such differences, although the mass is the same, are attributed to the development of different force chains at the micro-scale. Forces are concentrated on some parts of the wall due to the possible creation of long force chains. Such discrepancies, does not affect the total normal force applied on the wall which is found to be very similar between the different tests.

The size of particles composing the flow has an effect on the amplitude of fluctuations observed for the signal of total normal force applied on the wall. For samples of same volume but different D_{50}, the amplitude of fluctuations increases when increasing D_{50}. This could be related to successive build ups and losses of force chains in the granular

medium. However, if averaged over a time window, the average total force is similar. Such findings can justify using bigger particles in DEM to simulate the impact of a flow made of smaller particles, to reduce computation cost.

For impacts on flexible barriers, the DEM model was easy to calibrate against experimental data (e.g. net punching test), as it only requires tuning the stiffness and the tensile strength (if imposed). The value of the friction angle between sliding rings and main cables (δ_{rc}) was not of a great influence on the macroscopic behavior of the barrier. For different values of δ_{rc}, the differences in energy dissipators deformation, maximum extension of the cables and forces on the anchors are less than 5%.

The role of energy dissipators, which are modeled as elasto-plastic material in the model, is essential for dissipating the kinetic energy of the flow. When used, energy dissipators reduce the total impact force applied on the barrier. The peak force is reduced by elongating the impact time, while the residual force is reduced due to the deformation of the barrier causing interactions between the retained mass and the downstream part of the channel base. As a result, internal forces in main cables and forces applied on the anchors are minimized, which would prevent the structural failure of the barrier.

The inclination angle of the base (α) affects the impact behavior on debris flow barriers. Higher inclination angles led to higher flowing velocities due to the increase in the kinetic energy. This led to higher peak total force on the barrier. On the other hand, low values of α eliminated the peak part of the total force, and the flow gradually accumulated behind the barrier.

For design engineers, it is important to understand the difference in the impact mechanism between rigid walls and flexible barriers. For the same impacting flow, rigid walls are exposed to higher impact force due to short impact period. Moreover, due to the lack of deformability, particles impacting the wall tend to die (stop moving) faster which leads to higher rate of accumulation of dead zone mass. On the contrary, flexible barriers with energy dissipators are exposed to lower peak force due to the long impact duration.

Debris flow impact is usually estimated for design purposes using hydraulic models. The DEM model hydrostatic and hydrodynamic impact forces were compared with guidelines for estimating these forces. Discrepancies between the two are caused by the coefficients used to estimate the two types of forces. The value of the earth coefficient

(K) used to estimate the hydrostatic force could vary during the impact process due to the stresses caused by the dynamic part of the flow. Similarly, hydrodynamic force coefficient (λ) varies with time due to the reduction in velocity because of the impact between the dynamic part and the dead zone. As a result, assuming fixed values of K and λ might be oversimplifying the impact estimation of debris flows.

Concerning the dimensioning of flexible barriers, using mesh size up to D_{90} is adequate in terms of the retained mass, as only 3% of the initial mass would go through the net. Moreover, if the bottom cable is not fixed as to allow for sediment transport during non-extreme debris events, all particles forming the flow would overflow the barrier from the bottom in the case of an extreme event. The result is the same what ever the value of the bottom opening is. This is because of the deformation of the barrier which causes an excessive vertical displacement of the bottom cable, increasing the bottom opening. Thus, if such bottom opening is to be allowed, it is important to make sure that the flow mass will be retained during extreme debris flow events.

The initial configuration of flexible barriers has an effect on their impact behavior. A barrier that is normal to the channel bed (fbN), although subjected to same forces as a barrier that is parallel to gravity vector (fbG), is found to record higher deformation. For example, top cable deformation is 1.5 times more than that of fbG case. This leads fbN barrier to lose 50% of the initial mass due to severe reduction of its height. Lastly, if supporting cables are connected directly to the anchors, high forces would be directly transferred to the anchors without being dissipated in energy dissipators. To avoid this, lateral cables should be first connected to energy dissipators which are then connected to the anchors. However, in such a case, lateral windows would open from the sides allowing for some particles to overflow the barrier from the sides. Thus, the length of the net should be long enough so that when the barrier deform its retaining capacity is not affected.

Perspectives

The granular flow studied in the frame of this thesis was a dry granular flow, with no consideration of a fluid phase. The presence of the fluid would help in a better representation of debris flows, especially the viscous behavior due to the mixture of water and fine particles. Water-saturated debris flows could thus be modeled as a mixture of solid

particles (with DEM) and a viscous fluid made of water-fine grains mixture. Several methods of Computational Fluid Dynamics (CFD) could be used for modeling the fluid. For example, the fluid code be modeled using Lattice Boltzmann Method (LBM) that could be coupled with DEM (e.g. Leonardi et al., 2015). However, coupling DEM with LBM in 3D is computationally very expensive. An alternative could be representing the fluid using Pore Finite Volume (PFV) and then coupling it with DEM (e.g. Marzougui et al., 2015). A third possibility could be representing the fluid using Smoothed-Particle Hydrodynamics (SPH) and then coupling it with DEM (e.g. Cleary, 2015). The choice of the CFD method to use should balance between the precision of representing the fluid and the computational cost.

On the micro-scale, the development of force chains in the granular medium behind the wall, in both impacting the depositing stages, could be studied in more details (2D e.g. Peters et al., 2005). These chains could be quantified in 3D by calculating the length and number of force chains and link them to the total force signal. Moreover, force chains buckling can be quantified and be related to the reduction in the impact force.

One geometry of the net (45-degrees rotated mesh) has been tested and the internal distribution of tensile forces has been analyzed. Other more complex geometries could be tested in order to see whether or not this would affect the force transmission from the net to other components of the barrier. In addition, the flexible barrier model could be compared with full-scale tests on flexible barriers for macro-scale validation.

Bibliography

Agostini, R., Mazzalai, P., and Papetti, A. (1988). *Le reti metalliche a maglia esagonale nella difesa dei versanti*. Officine Maccaferri.

Albaba, A., Lambert, S., Nicot, F., and Chareyre, B. (2015). Relation between microstructure and loading applied by a granular flow to a rigid wall using dem modeling. *Granular Matter*, 17(5):603–616.

Armanini, A. (1997). On the dynamic impact of debris flows. In *Recent developments on debris flows*, pages 208–226. Springer.

Armanini, A., Dellagiacoma, F., and Ferrari, L. (1991). From the check dam to the development of functional check dams. In *Fluvial hydraulics of mountain regions*, pages 331–344. Springer.

Azanza, E., Chevoir, F., and Moucheront, P. (1999). Experimental study of collisional granular flows down an inclined plane. *J. Fluid Mech.*, 400:199–227.

Azéma, E. and Radjaï, F. (2012). Force chains and contact network topology in sheared packings of elongated particles. *Phys. Rev. E*, 85(3):031303.

Bertolo, P., Oggeri, C., and Peila, D. (2009). Full-scale testing of draped nets for rock fall protection. *Canadian Geotechnical Journal*, 46(3):306–317.

Bertrand, D., Nicot, F., Gotteland, P., and Lambert, S. (2008). Discrete element method (dem) numerical modeling of double-twisted hexagonal mesh. *Can. Geotech. J.*, 45(8):1104–1117.

Bertrand, D., Trad, A., Limam, A., and Silvani, C. (2012). Full-scale dynamic analysis of an innovative rockfall fence under impact using the discrete element method: from the local scale to the structure scale. *Rock mechanics and rock engineering*, 45(5):885–900.

Boetticher, A., Hübl, J., Wendeler, C., and Volkwein, A. (2011). Modeling the impact of shallow landslides on flexible protection barriers. *Math. Geosci. Crossroads Theory Pract. Marschallinger, R. & Zobl, F., Salzburg, Austria*, pages 659–670.

Bonati, A. and Galimberti, V. (2004). La valutazione sperimentale di sistemi di difesa attiva dalla caduta massi. In *Proceedings of the Conference on Bonifica dei versanti rocciosi per la protezione del territorio, Trento, Italy*, pages 11–15.

Bourrier, F., Kneib, F., Chareyre, B., and Fourcaud, T. (2013). Discrete modeling of granular soils reinforcement by plant roots. *Ecological Engineering*, 61:646–657.

Bourrier, F., Lambert, S., and Baroth, J. (2015). A reliability-based approach for the design of rockfall protection fences. *Rock Mechanics and Rock Engineering*, 48(1):247–259.

Boutillier, B. and Marzouk, A. (2010). Dissipating devices for rockfall protection kits. In *Proc. of 3rd Euromediterranean Symposium on Advances in Geomaterials and Structures, AGS10, Djerba, Tunisie, 10-12 mai, 2010*.

Brighenti, R., Segalini, A., and Ferrero, A. M. (2013). Debris flow hazard mitigation: a simplified analytical model for the design of flexible barriers. *Computers and Geotechnics*, 54:1–15.

Buchholtz, V. and Pöschel, T. (1998). Interaction of a granular stream with an obstacle. *Granular Matter*, 1(1):33–41.

Caccamo, P., Chanut, B., Faug, T., Bellot, H., and Naaim-Bouvet, F. (2012). Small-scale tests to investigate the dynamics of finite-sized dry granular avalanches and forces on a wall-like obstacle. *Granular Matter*, 14(5):577–587.

Calvetti, F., Crosta, G., and Tatarella, M. (2000). Numerical simulation of dry granular flows: from the reproduction of small-scale experiments to the prediction of rock avalanches. *Rivista Italiana di Geotecnica*, 34(2):21–38.

Campbell, C. S. (1990). Rapid granular flows. *Annual Review of Fluid Mechanics*, 22(1):57–90.

Campbell, C. S. (2002). Granular shear flows at the elastic limit. *Journal of fluid mechanics*, 465:261–291.

Campbell, C. S., Cleary, P. W., and Hopkins, M. (1995). Large-scale landslide simulations: Global deformation, velocities and basal friction. *J. Geophys. Res. B: Solid Earth (1978–2012)*, 100(B5):8267–8283.

Castro-Fresno, D., del Coz Diaz, J., López, L., and Nieto, P. G. (2008). Evaluation of the resistant capacity of cable nets using the finite element method and experimental validation. *Engineering Geology*, 100(1):1–10.

Catalano, E., Chareyre, B., and Barthélémy, E. (2014). Pore-scale modeling of fluid-particles interaction and emerging poromechanical effects. *International Journal for Numerical and Analytical Methods in Geomechanics*, 38(1):51–71.

Cazzani, A., Mongiovı, L., and Frenez, T. (2002). Dynamic finite element analysis of interceptive devices for falling rocks. *International Journal of Rock Mechanics and Mining Sciences*, 39(3):303–321.

Chambers, J. M. and Hastie, T. J. (1991). *Statistical models in S*. CRC Press, Inc.

Chanut, B., Faug, T., and Naaim, M. (2010). Time-varying force from dense granular avalanches on a wall. *Physical review E*, 82(4):041302.

Chu, T., Hill, G., McClung, D., Ngun, R., and Sherkat, R. (1995). Experiments on granular flows to predict avalanche runup. *Can. Geotech. J.*, 32(2):285–295.

Cleary, P. W. (2015). Prediction of coupled particle and fluid flows using dem and sph. *Minerals Engineering*, 73:85–99.

Cundall, P. A. (1971). A computer model for simulating progressive large scale movements in blocky rock systems. In *Proc. Symp. Rock Fracture (ISRM), Nancy*, volume 1.

Cundall, P. A. and Strack, O. D. (1979). A discrete numerical model for granular assemblies. *Geotechnique*, 29(1):47–65.

da Cruz, F., Emam, S., Prochnow, M., Roux, J.-N., and Chevoir, F. (2005). Rheophysics of dense granular materials: Discrete simulation of plane shear flows. *Physical Review E*, 72(2):021309.

Das, B. M. (2013). *Advanced soil mechanics*. CRC Press.

Davies, T. and McSaveney, M. (1999). Runout of dry granular avalanches. *Canadian Geotechnical Journal*, 36(2):313–320.

Domnik, B. and Pudasaini, S. P. (2012). Full two-dimensional rapid chute flows of simple viscoplastic granular materials with a pressure-dependent dynamic slip-velocity and their numerical simulations. *Journal of Non-Newtonian Fluid Mechanics*, 173:72–86.

Effeindzourou, A., Chareyre, B., Thoeni, K., Giacomini, A., and Kneib, F. (2016). Modelling of deformable structures in the general framework of the discrete element method. *Geotextiles and Geomembranes*, 44(2):143–156.

ESPON (2005). Landslide hazard map of europe, european spatial planning observation network (espon). http://www.espon.eu/export/sites/default/Documents/Events/ESPON2006Seminars/Seminars/2003/october_matera/1.3.1.ppt.

Faug, T., Beguin, R., and Chanut, B. (2009). Mean steady granular force on a wall overflowed by free-surface gravity-driven dense flows. *Phys. Rev. E*, 80(2):021305.

Faug, T., Caccamo, P., and Chanut, B. (2011). Equation for the force experienced by a wall overflowed by a granular avalanche: experimental verification. *Physical Review E*, 84(5):051301.

Faug, T., Caccamo, P., and Chanut, B. (2012). A scaling law for impact force of a granular avalanche flowing past a wall. *Geophysical Research Letters*, 39(23).

Faug, T., Lachamp, P., and Naaim, M. (2002). Experimental investigation on steady granular flows interacting with an obstacle down an inclined channel: study of the dead zone upstream from the obstacle. application to interaction between dense snow avalanches and defence structures. *Nat. Hazards Earth Syst. Sci.*, 2(3/4):187–191.

Friedmann, S. J., Taberlet, N., and Losert, W. (2006). Rock-avalanche dynamics: insights from granular physics experiments. *International Journal of Earth Sciences*, 95(5):911–919.

Gentilini, C., Govoni, L., de Miranda, S., Gottardi, G., and Ubertini, F. (2012). Three-dimensional numerical modelling of falling rock protection barriers. *Computers and Geotechnics*, 44:58–72.

Ghaisas, N., Wassgren, C. R., and Sadeghi, F. (2004). Cage instabilities in cylindrical roller bearings. *Journal of tribology*, 126(4):681–689.

Gottardi, G. and Govoni, L. (2010). Full-scale modelling of falling rock protection barriers. *Rock mechanics and rock engineering*, 43(3):261–274.

Goujon, C., Dalloz-Dubrujeaud, B., and Thomas, N. (2007). Bidisperse granular avalanches on inclined planes: A rich variety of behaviors. *The European Physical Journal E*, 23(2):199–215.

Grassl, H. (2002). *Experimentelle und numerische Modellierung des dynamischen Trag-und Verformungsverhaltens von hochflexiblen Schutzsystemen gegen Steinschlag*. PhD thesis, Diss., Technische Wissenschaften ETH Zürich, Nr. 14817, 2002.

Gray, J., Wieland, M., and Hutter, K. (1999). Gravity-driven free surface flow of granular avalanches over complex basal topography. In *Proceedings of the Royal Society of London A: Mathematical, Physical and Engineering Sciences*, volume 455, pages 1841–1874. The Royal Society.

Guasti, G., Volkwein, A., and Wendeler, C. (2011). Design of flexible debris flow barriers. In *5th International Conference on Debris-Flow Hazard âĂIJMitigation, Mechanics, Prediction and AssessmentâĂİ, Padua, Italy, June*, pages 14–17.

Handy, R. L. (1985). The arch in soil arching. *J. Geotech. Eng. ASCE*, 111(3):302–318.

Hearn, G., Barrett, R. K., and Henson, H. H. (1995). Development of effective rockfall barriers. *J. Transp. Eng.*, 121(6):507–516.

Hervás, J. (2003). *Lessons learnt from landslide disasters in Europe*. European Commission, Joint Research Centre, Institute for the Protection and the Security of the Citizen, Technological and Economic Risk Management Unit.

Hu, K., Wei, F., and Li, Y. (2011). Real-time measurement and preliminary analysis of debris-flow impact force at jiangjia ravine, china. *Earth Surface Processes and Landforms*, 36(9):1268–1278.

Hubert, J. F. and Filipov, A. J. (1989). Debris-flow deposits in alluvial fans on the west flank of the white mountains, owens valley, california, usa. *Sedimentary Geology*, 61(3):177–205.

Hübl, J., Suda, J., Proske, D., Kaitna, R., and Scheidl, C. (2009). Debris flow impact estimation. In *Proceedings of the 11th International Symposium on Water Management and Hydraulic Engineering, Ohrid, Macedonia*, pages 1–5.

Hungr, O. (1995). A model for the runout analysis of rapid flow slides, debris flows, and avalanches. *Canadian Geotechnical Journal*, 32(4):610–623.

Hutter, K., Koch, T., Pluüss, C., and Savage, S. (1995). The dynamics of avalanches of granular materials from initiation to runout. part ii. experiments. *Acta Mech.*, 109(1-4):127–165.

Iverson, R. and Denlinger, R. (1987). The physics of debris flowsâĂŢa conceptual assessment. *IAHS-AISH publication*, (165):155–165.

Iverson, R. M. (2003). The debris-flow rheology myth. *Debris-flow hazards mitigation: mechanics, prediction, and assessment*, 1:303–314.

Iverson, R. M., Logan, M., and Denlinger, R. P. (2004). Granular avalanches across irregular three-dimensional terrain: 2. experimental tests. *Journal of Geophysical Research: Earth Surface (2003–2012)*, 109(F1).

Iwanaga, J. O. (2015). Application of flexible ring net barriers technology for debris flow control in san martin torrent âĂŞ ayacucho - peru. In *E-proceedings of the 36th IAHR World Congress 28 June - 3 July, 2015, The Hague, the Netherlands*, pages 9–p.

Jakob, M. and Oldrich, H. (2005). *Debris-flow hazards and related phenomena*. Springer.

Jiang, Y.-J. and Towhata, I. (2013). Experimental study of dry granular flow and impact behavior against a rigid retaining wall. *Rock Mech. Rock Eng.*, 46(4):713–729.

Keller, S., Ito, Y., and Nishimura, K. (1998). Measurements of the velocity distribution in ping-pong-ball avalanches. *Ann. Glaciol.*, 26:259–264.

Lemieux, P.-A. and Durian, D. (2000). From avalanches to fluid flow: a continuous picture of grain dynamics down a heap. *Phys. Rev. Lett.*, 85(20):4273.

Leonardi, A., Wittel, F. K., Mendoza, M., Vetter, R., and Herrmann, H. J. (2015). Particle-fluid-structure interaction for debris flow impact on flexible barriers. *Computer-Aided Civil and Infrastructure Engineering*.

Lo, D. (2000). *Review of natural terrain landslide debris-resisting barrier design*. Geotechnical Engineering Office, Civil Engineering Department.

Majoral, R., Bertolo, P., and Giachetti, G. (2008). Las mallas en la estabilizacion de taludes, ii curso sobre proteccion contra caida de rocas. *Colegio de Ingegneros de Caminos, Canales y puertos, Madrid, Spain*, 26.

Mancarella, D. and Hungr, O. (2010). Analysis of run-up of granular avalanches against steep, adverse slopes and protective barriers. *Canadian Geotechnical Journal*, 47(8):827–841.

Manzella, I. and Labiouse, V. (2009). Flow experiments with gravel and blocks at small scale to investigate parameters and mechanisms involved in rock avalanches. *Engineering Geology*, 109(1):146–158.

Marzougui, D., Chareyre, B., and Chauchat, J. (2015). Microscopic origins of shear stress in dense fluid–grain mixtures. *Granular Matter*, 17(3):297–309.

MiDi, G. (2004). On dense granular flows. *The European Physical Journal E*, 14(4):341–365.

Mollon, G., Richefeu, V., Villard, P., and Daudon, D. (2012). Numerical simulation of rock avalanches: influence of a local dissipative contact model on the collective behavior of granular flows. *Journal of Geophysical Research: Earth Surface (2003–2012)*, 117(F2).

Moriguchi, S., Borja, R. I., Yashima, A., and Sawada, K. (2009). Estimating the impact force generated by granular flow on a rigid obstruction. *Acta Geotechnica*, 4(1):57–71.

Mustoe, G. and Huttelmaier, H. (1993). Dynamic simulation of a rockfall fence by the discrete element method. *Computer-Aided Civil and Infrastructure Engineering*, 8(6):423–437.

Nicot, F., Cambou, B., and Mazzoleni, G. (2001). From a constitutive modelling of metallic rings to the design of rockfall restraining nets. *International journal for numerical and analytical methods in geomechanics*, 25(1):49–70.

Nicot, F., Nouvel, P., Cambou, B., Rochet, L., and Mazzoléni, G. (1999). Etude du comportement mecanique des ouvrages souples de protection contre les eboulements rocheux. *Revue française de génie civil*, 3(5):295–319.

Okura, Y., Kitahara, H., and Sammori, T. (2000). Fluidization in dry landslides. *Engineering Geology*, 56(3):347–360.

Pastor, M., Blanc, T., Haddad, B., Petrone, S., Morles, M. S., Drempetic, V., Issler, D., Crosta, G., Cascini, L., Sorbino, G., et al. (2014). Application of a sph depth-integrated model to landslide run-out analysis. *Landslides*, 11(5):793–812.

Peters, J., Muthuswamy, M., Wibowo, J., and Tordesillas, A. (2005). Characterization of force chains in granular material. *Physical review E*, 72(4):041307.

Pitman, E., Nichita, C., Patra, A., Bauer, A., Bursik, M., and Weber, A. (2003). A model of granular flows over an erodible surface. *Discrete and Continuous Dynamical Systems Series B*, 3(4):589–600.

Pitman, E. B. and Le, L. (2005). A two-fluid model for avalanche and debris flows. *Philosophical Transactions of the Royal Society of London A: Mathematical, Physical and Engineering Sciences*, 363(1832):1573–1601.

Pouliquen, O. and Renaut, N. (1996). Onset of granular flows on an inclined rough surface: dilatancy effects. *Journal de Physique II*, 6(6):923–935.

Pudasaini, S. and Domnik, B. (2009). Energy considerations in accelerating rapid shear granular flows. *Nonlinear Processes in Geophysics*, 16(3):399–407.

Pudasaini, S., Wang, Y., and Hutter, K. (2005a). Modelling debris flows down general channels. *Natural Hazards and Earth System Science*, 5(6):799–819.

Pudasaini, S. P., Hsiau, S.-S., Wang, Y., and Hutter, K. (2005b). Velocity measurements in dry granular avalanches using particle image velocimetry technique and comparison with theoretical predictions. *Physics of Fluids*, 17(9):093301.

Pudasaini, S. P. and Hutter, K. (2003). Rapid shear flows of dry granular masses down curved and twisted channels. *J. Fluid Mech.*, 495:193–208.

Pudasaini, S. P. and Hutter, K. (2007). *Avalanche dynamics: dynamics of rapid flows of dense granular avalanches*. Springer Science & Business Media.

Pudasaini, S. P., Hutter, K., Hsiau, S.-S., Tai, S.-C., Wang, Y., and Katzenbach, R. (2007). Rapid flow of dry granular materials down inclined chutes impinging on rigid walls. *Physics of Fluids (1994-present)*, 19(5):053302.

Pudasaini, S. P. and Kröner, C. (2008). Shock waves in rapid flows of dense granular materials: Theoretical predictions and experimental results. *Physical Review E*, 78(4):041308.

Remaitre, A. and Malet, J. (2010). The effectiveness of torrent check dams to control channel instability: example of debris-flow events in clay shales. *Check dams, morphological adjustments and erosion control in torrential streams. Nova Science Publishers Inc., New York*, pages 211–237.

Savage, S. and Hutter, K. (1991). The dynamics of avalanches of granular materials from initiation to runout. part i: Analysis. *Acta Mechanica*, 86(1-4):201–223.

Savage, S. B. (1984). The mechanics of rapid granular flows. *Adv. Appl. Mech.*, 24:289–366.

Savage, S. B. and Hutter, K. (1989). The motion of a finite mass of granular material down a rough incline. *Journal of fluid mechanics*, 199:177–215.

Scheidl, C., Chiari, M., Kaitna, R., Müllegger, M., Krawtschuk, A., Zimmermann, T., and Proske, D. (2013). Analysing debris-flow impact models, based on a small scale modelling approach. *Surveys in Geophysics*, 34(1):121–140.

Schwager, T. and Pöschel, T. (2007). Coefficient of restitution and linear–dashpot model revisited. *Granular Matter*, 9(6):465–469.

Segalini, A., Brighenti, R., Ferrero, A., and Umili, G. (2013). Comparison between the mechanical behavior of barriers against rock fall vs debris flows. In Kwasniewski, M. and Lydzba, D., editors, *Rock Mechanics for Resources, Energy and Environment*. CRC Press.

Silbert, L. E., Ertaş, D., Grest, G. S., Halsey, T. C., Levine, D., and Plimpton, S. J. (2001). Granular flow down an inclined plane: Bagnold scaling and rheology. *Phys. Rev. E*, 64(5):051302.

Šmilauer, V., Catalano, E., Chareyre, B., Dorofeenko, S., Duriez, J., Gladky, A., Kozicki, J., Modenese, C., Scholtès, L., Sibille, L., StránskÃ¡, J., and Thoeni, K. (2010). *Yade Documentation*. Http://yade-dem.org/doc/.

Taboada, A. and Estrada, N. (2009). Rock-and-soil avalanches: Theory and simulation. *Journal of Geophysical Research: Earth Surface (2003–2012)*, 114(F3).

Takahashi, T. (1991). *Debris flow*. Balkema.

Takahashi, T. (2007). *Debris flow: mechanics, prediction and countermeasures*. CRC Press.

Teufelsbauer, H., Wang, Y., Chiou, M.-C., and Wu, W. (2009). Flow–obstacle interaction in rapid granular avalanches: Dem simulation and comparison with experiment. *Granular Matter*, 11(4):209–220.

Thoeni, K., Lambert, C., Giacomini, A., and Sloan, S. (2011). Discrete modelling of a rockfall protective system. In *Particle-based methods II: Fundamentals and applications. II International conference on particle-based methods. CIMNE International Center for Numerical Methods in Enginering*, pages 24–32.

Valentino, R., Barla, G., and Montrasio, L. (2008). Experimental analysis and micromechanical modelling of dry granular flow and impacts in laboratory flume tests. *Rock Mech. Rock Eng.*, 41(1):153–177.

Volkwein, A. (2005). Numerical simulation of flexible rockfall protection systems. *Proc. Computing in civil engineering*.

Volkwein, A. (2014). Flexible debris flow barriers - design and application. Technical report, WSL Ber. 18.

Watanabe, M. and Ikeya, H. (1981). Investigation and analysis of volcanic mudflows on mt. sakurajima, japan. In *Erosion and Sediment Transport Measurement*, volume 133, pages 245–256.

Wendeler, C. and Volkwein, A. (2015). Laboratory tests for the optimization of mesh size for flexible debris-flow barriers. *Natural Hazards and Earth System Sciences Discussions*, 3:2099–2118.

Wendeler, C., Volkwein, A., Roth, A., Herzog, B., Hahlen, N., and Wenger, M. (2008). Hazard prevention using flexible multi-level debris flow barrier. In *Interpraevent*, volume 1, pages 547–554.

Wendeler, C. S. I. (2008). *Murgangrückhalt in Wildbächen: Grundlagen zu Planung und Berechnung von flexiblen Barrieren*. PhD thesis, Eidgenössische Technische Hochschule Zürich.

Zhang, S. (1993). A comprehensive approach to the observation and prevention of debris flows in china. *Natural Hazards*, 7(1):1–23.

Zhou, Y., Wright, B., Yang, R., Xu, B., and Yu, A. (1999). Rolling friction in the dynamic simulation of sandpile formation. *Physica A: Statistical Mechanics and its Applications*, 269(2):536–553.

Zienkiewicz, O. C. and Taylor, R. L. (2005). *The finite element method for solid and structural mechanics*. Butterworth-heinemann.

Appendices

Appendix A. Original article: Relation between microstructure and loading applied by a granular flow to a rigid wall using DEM modeling

Granular Matter (2015) 17:603–616
DOI 10.1007/s10035-015-0579-8

ORIGINAL PAPER

Relation between microstructure and loading applied by a granular flow to a rigid wall using DEM modeling

Adel Albaba[1,3] · **Stéphane Lambert**[1,3] · **François Nicot**[1,3] · **Bruno Chareyre**[2,3]

Received: 15 January 2015 / Published online: 25 August 2015

Abstract This paper presents a numerical model based on Discrete Element Method used to reproduce a series of tests of dry granular flow impacting a rigid wall. The flow was composed of poly-dispersed non-spherical particles flowing in an inclined chute with different inclination angles. The model has been calibrated based on the flow thickness measurements and the shape of the flowing particles (a single sphere and a clump). Quantitative comparison with experimental data showed good agreement in terms of peak impact force on the wall, the time of the peak and also the residual force values at the end of the tests. After validating the model, relation between microstructure and the normal impact force against the wall was investigated, by comparing the variation of impact force values along the height of the wall for different tests. Microstructural heterogeneities were observed in the impacting and depositing stages of the flow, indicating the presence of arching effect in the granular medium behind the wall.

Keywords DEM · Granular flow · Rigid wall · Numerical modeling

✉ Adel Albaba
adel.albaba@irstea.fr

Stéphane Lambert
stephane.lambert@irstea.fr

François Nicot
francois.nicot@irstea.fr

Bruno Chareyre
bruno.chareyre@3sr-grenoble.fr

[1] Irstea, UR ETGR, 2 rue de la papeterie, 38402 St-Martin d'Hères, France

[2] 3SR, CNRS, 38000 Grenoble, France

[3] Université Grenoble Alpes, 38000 Grenoble, France

1 Introduction

The urbanization of mountainous areas raised the importance of mitigating the threats to people and infrastructures linked to natural hazards such as rockfalls and shallow slope failures. Several shallow slope failures happened in the past (following a rainfall or an earthquake) resulting in granular flows, loss of lives and damage to the infrastructures.

Granular flows have been classified as one of the most hazardous landslides due to their high flow velocity and impact forces, long runout distance and poor temporal predictability [1]. More specifically, dry granular flows produced by shallow slope failures were found to travel long distances destroying infrastructures and blocking vital roads. In terms of formation, they contain large blocks of gravel and rock fragments.

Granular flows exert large forces within a short period of time. Such a force generally varies with slope angle, thickness of the flowing material and velocity at the moment of the impact. This hazard can be limited using retention systems similar in principle to rockfall barriers. Different protection structures have been proposed in the literature for the mitigation of natural hazards; they are mainly retaining walls or flexible structures. Retaining walls have been widely used in China and also in Japan [2] for the prevention of rockfalls and granular flows. For the same reason, different types of flexible structures using net fences have been developed over the last decades [3–6]. Several researches have been carried out in order to model granular flows. On one hand, continuum treatment has often been adopted where flows characteristics are analyzed by the Eulerian forms of continuity and momentum equation [7–10].

On the other hand Discrete Element Method (DEM) has also been an active tool for modeling granular flows [11,12]. Silbert et al. [13] carried out 2D and 3D simulations of mono-

dispersed particles flowing in a steady-state condition where observations were taken regarding structure and rheology of the flow. DEM was also used to simulate a rock avalanche event that took place in Italy [14]. Faug et al. [15] proposed a hydrodynamic model based on depth-averaged momentum conservation which was used to predict DEM numerical results of a free-surface gravity-driven dense flow overflowing a wall. Using angular shaped elements, Mollon et al. [16] numerically investigated the propagation of granular masses down a slope where energy evolution was studied along with run-out mechanism.

On the experimental side, various experiments have been conducted ranging from studies on geological debris flows to well characterized laboratorial granular flows down an inclined plane [8,17,18]. Several materials have been used varying from sand [19] to ping-pong balls [20]. Moreover, with the use of video-filming and different granular media and chute geometries, Hutter et al. [7] carried out well-defined laboratory experiments and compared them with their mathematical models. Furthermore, Faug et al. [21] experimentally investigated the dead zone formation of glass beads behind an obstacle down an inclined channel. In addition, other DEM models were validated against small tests experiments in different slopes for better prediction of runout distances and impact force against obstacles [22]. However, none of these experiments considered coarse-grained flow of angular particles impacting an obstacle, which is typical in natural granular flows.

The aim of this paper is to investigate the relation between microstructure and loading applied by granular flow to a rigid wall. This is done by developing a numerical model capable of simulating the impact of dry coarse-grained flow against a rigid wall taking into account the shape effect of the angular particles. First, we will introduce the experimental data used for calibration and validation. Afterwards, we will describe the model in terms of contact law, particles shape and chute characteristics. The model calibration is presented where comparison is made between sphere and clump shapes. Next, the validation of the model is introduced in which values of normal impact force on a rigid obstacle are compared with the experimental data. Finally, the obtained results are discussed followed by conclusions of the presented work.

2 Experimental data

Jiang and Towhata [23] recently studied the impact behavior of dry granular flow against a rigid retaining wall using poly-dispersed mixture of limestone gravel which has a measured angle of repose of 53°. The gravel flow mixture had particles ranging from 10 to 20 mm in diameter. The samples were prepared with a specific weight of 13.5 kN/m^3 in a box with varying lengths (from 14 to 44 cm with a 5 cm step)

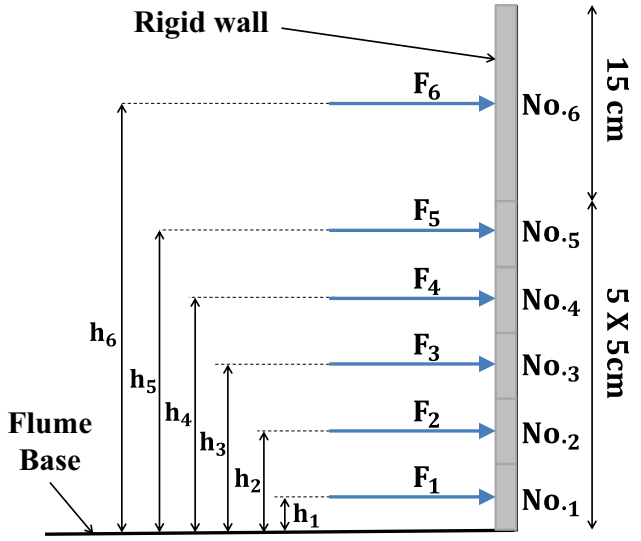

Fig. 1 Rigid wall division from the bottom to the top (adapted from [23])

and heights (from 5 to 20 cm with a 5 cm step) but with a 30 cm fixed width. The samples were released in a dam-break manner in which the gate was pulled instantaneously [24].

The chute was rectangular in cross section with 219 cm length, 30 cm width and 35 cm height. Different inclination angles α were tested ranging from 30° to 45°. The friction angle of the chute base, chute sides and the rigid wall were 25°, 15° and 21° respectively. The base of the chute was a planar surface without any fixation of particles. The chute ended with a rigid wall perpendicular to the chute base and divided into six horizontal segments, marked from 1 to 6 starting from the bottom (Fig. 1).

Measurements of normal impact force vs. time were recorded for different heights of the wall. In addition, observations of flow thickness and flow velocity were taken at the time where the total normal force on the wall reached its maximum value. These experimental data were selected for our model calibration and validation. This is because it considers elongated coarse-grained flow of angular particles which is the main case for natural granular flow. In addition, the study provided detailed measurements of normal impact force for different heights (different segments of the rigid wall). Three different tests have been presented in the paper: Test L34-H15-α45°, Test L44-H15-α40° and Test L44-H20-α40°. A test marked by L44-H15-α40° represents a sample having 44 cm in length, 15 cm in height and 40° inclination angle.

3 Numerical modeling

The numerical simulation of the dry granular flow was carried out using Discrete Element Method. Nowadays DEM is widely used for modeling granular media. It is particu-

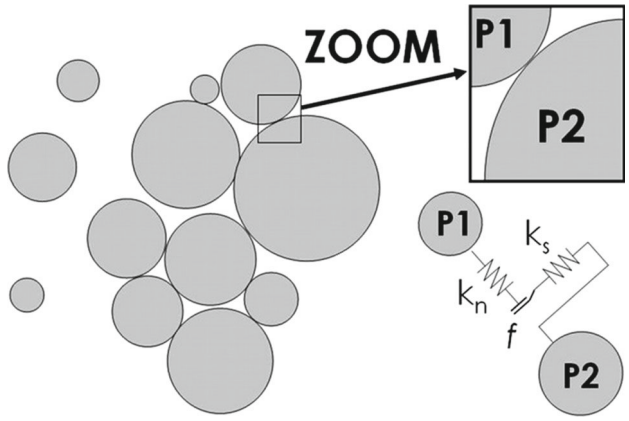

Fig. 2 Assembly of discrete elements illustrating different contact types [27]

larly efficient for static and dynamic simulation of granular assemblies where medium can be described at a microscopic scale. The method is based on an explicit finite difference scheme proposed by Cundall and Strack [25]. It applies for collection of discrete bodies interacting with each other by a contact law. Different contact forces can be considered in different directions; the normal direction and also the tangential direction (Fig. 2). Calculations alternate between the application of Newtons second law to particles motion and a force-displacement law resulting from the interaction models. In comparison with Finite Element Method (FEM), DEM makes large displacements between elements easy to simulate and computationally inexpensive, which is useful when dealing with discontinuous problems in granular medium.

YADE software has been used as a modeling tool which is an extensible open-source framework for discrete numerical models, focused on DEM [26]. The simulation loop in YADE starts with detecting the contact between particles. Next, the chosen contact law is applied in which results in new position and velocity of the particles. YADE contains the main components for the application of DEM which include Newtons law, time integration algorithms, damping methods, collision detection, data classes (storing information about bodies and interactions) and command OpenGL methods for drawing popular geometries.

3.1 Contact law

A visco-elastic contact law with Mohr-coulomb failure criterion (Fig. 3) has been adopted where normal and tangential contact forces F_n, F_t between particles were calculated as follows:

$$\mathbf{F_n} = (k_n u_n - \gamma \dot{u}_n)\mathbf{n} \tag{1}$$

$$\mathbf{F_t} = \begin{cases} \frac{k_t \mathbf{u_t}}{|k_t \mathbf{u_t}|} |\mathbf{F_n}| tan\phi & if\, |k_t \mathbf{u_t}| > |\mathbf{F_n}| tan\phi \\ k_t \mathbf{u_t} & otherwise \end{cases} \tag{2}$$

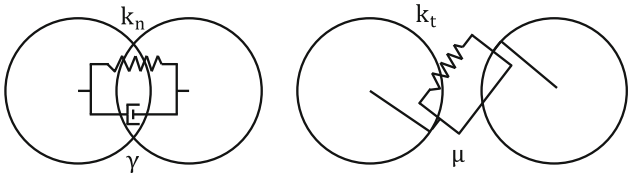

Fig. 3 Normal and tangential interaction forces of the contact law used in the model

where k_n and k_t are the normal and tangential stiffness parameters, u_n and u_t are the normal and shear displacements, ϕ is the friction angle and γ is the normal visco-elastic coefficient.

The normal stiffness of the contact between two particles (k_n) was calculated as [30]:

$$k_n = \frac{2E_1 r_1 E_2 r_2}{E_1 r_1 + E_2 r_2} \tag{3}$$

where E_1 and E_2 are the elastic moduli of the first and second particles respectively (both taken as 10^8 Pa) and r_1 and r_2 are the radii of the first and second particles respectively.

The shear stiffness of the contact (k_t) was taken as $(2/7)k_n$ according to what was previously suggested by Silbert et al. [13]. Based on Schwager and Pöschel [28], with the restitution coefficient (ε) being the ratio between velocities after and before the impact, $\varepsilon_{n,t}$ (normal and tangential restitution coefficient) can be calculated as follows:

$$\beta_{n,t} = \frac{\gamma_{n,t}}{m_{eff}} \tag{4}$$

$$\omega_{n,t} = \sqrt{\left(\frac{2k_{n,t}}{m_{eff}}\right)^2 - \beta_{n,t}^2} \tag{5}$$

$$\varepsilon_{n,t} = \frac{\dot{u}(t_c^0)}{\dot{u}(0)} = e^{-\beta_{n,t}\pi/\omega_{n,t}} \tag{6}$$

where $m_{eff} = (1/m_1 + 1/m_2)$, m_1 and m_2 are the masses of two interacting particles and $\dot{u}(t_c^0)$, $\dot{u}(0)$ are velocities after and before the collision respectively.

The value of $\varepsilon_{n,t}$ was calibrated in Sect. 4.2 considering the flow thickness measurements. The time step value Δt_c has been set which guarantees the numerical stability of our calculation. It is calculated as follows:

$$\Delta t_c = \frac{r_{min}}{\sqrt{E/\rho}} \tag{7}$$

where (r_{min}) is the smallest value of particles radius, E is the elastic modulus and ρ is the density of the solid particle.

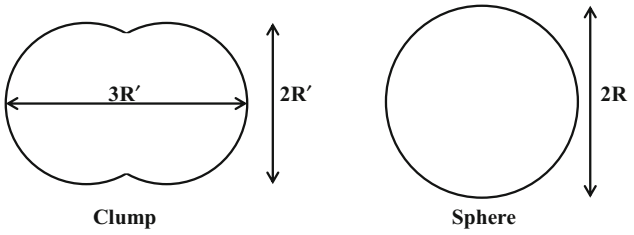

Fig. 4 Particle shapes tested in the simulation: a clump and a simple sphere

3.2 Flowing particles: shape and number

Particles used in the experiment were of limestone gravel ranging from 10 to 20 mm in diameter and had sharp angles and elongated shapes. To account for these effects in our model, two granular samples of same volume and mass were comparatively studied: a sample made of simple spheres and a second sample made of clumps (Fig. 4). The second sample is made of clumps where each clump consists of two identical spheres with radius $R_i^{'}$ and overlapping over a distance $R_i^{'}$ thus having an aspect ratio of 3/2. Since volumes are equal for the two samples, the relationship between R_i and $R_i^{'}$ is:

$$\frac{4}{3}\pi R_i^3 = 2\frac{4}{3}\pi R_i^{'3} - \frac{5}{12}\pi R_i^{'3} \tag{8}$$

Thus, by arranging Eq. 8, we find that $R_i^{'} = \sqrt[3]{\frac{16}{27}}R_i$. It is worth noting that, when using clumps, contact law Eqs. 1 and 2 are applied at the contact between the members that form the clumps (deformation between spherical particles). Afterwards, contact forces are summed on clumps and then the rigid body equations of motion are applied to the clumps [26] . After calibration, clumps were used henceforth as they proved advantageous over spherical shapes (Sect. 4.1).

Concerning the number of particles (n_p) in each simulation, samples were generated with a number of particles similar to that of the experiment (using the same particle size distribution and maintaining the same porosity). This number was calculated using the total weight of the sample and the weight of a single D_{50}-sphere as follows:

$$n_p = \frac{V_t \gamma_t}{V_s \gamma_s} \tag{9}$$

where V_t is the total volume of the sample, γ_t is the specific weight of the sample (13.5 kN/m^3), V_s is the volume of a single D_{50}-sphere and γ_s is the specific weight of gravel particles (taken as 26.5 kN/m^3 for the limestone gravel considered). For instance, the number of particles (clumps) used to generate the sample used in test L44-H15-α40° was 5406 clumps. Since each clump is made of two overlapping spheres, thus, the number of spheres was 10812 spheres.

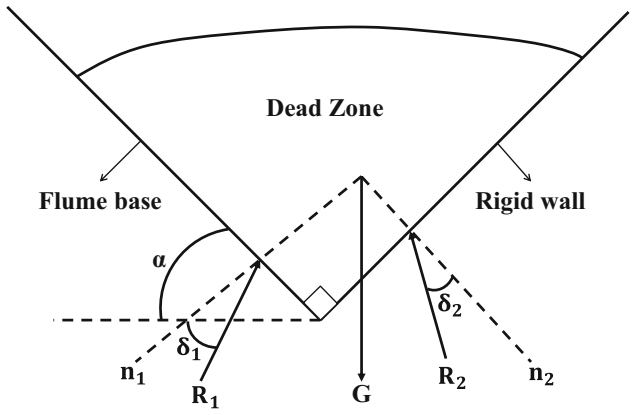

Fig. 5 Static equilibrium of the dead zone accumulation behind the wall

3.3 Dead zone mass

The total force applied on the wall has mainly two components: gravitational component and a dynamic one. The gravitational component (F_g) is due to the weight of the dead zone mass. On the other hand, the dynamic component (F_d) is due to the kinetic energy of the flow [11]. In order to calculate gravitational component of the total force, the dead zone mass needs to be identified. A criterion has been selected defining dead particles as the ones having a translational velocity component in the flow direction smaller than or equal to five percent of a fixed value of flow velocity. This fixed value is the velocity of the flow at the time of the maximum total impact force on the wall (V_{max}), measured for particles lying in distances from 40 to 50 cm away from the wall. Thus, a particle is considered dead if $V_{particle} \leq 5\%\, V_{max}$. In order to calculate the weight of the dead zone (G), we should consider the static equilibrium of this zone (Fig. 5). The base reaction $\mathbf{R_1}$ is the sum of interaction forces between dead particles and the base ($\mathbf{F_{int}}$):

$$\mathbf{R_1} = \sum_{i=1}^{n} \mathbf{F_{int}} \tag{10}$$

Similarly, the walls reaction $\mathbf{R_2}$ is the sum of interaction forces between dead particles and the wall. However, $\mathbf{R_1}$ and $\mathbf{R_2}$ can be related to each other as follows:

$$\mathbf{R_2} = \mathbf{R_1}\frac{sin(\alpha - \delta_1)}{cos(\alpha + \delta_2)} \tag{11}$$

where α is the chute inclination angle, δ_1 is the angle of friction between the base and the dead mass and δ_2 is the angle of friction between the wall and the dead mass. The gravitational force (F_g) is equal to the normal component of the reaction on the wall:

$$F_g = \mathbf{R_2} \cdot \mathbf{n_2} \tag{12}$$

Finally, by considering the static equilibrium of dead zone mass and using Eqs. 11 and 12, we find:

$$F_g = G\frac{sin(\alpha - \delta_1)}{cos(\alpha + \delta_2)}cos\delta_2 \tag{13}$$

It should be noted that values of δ_1 and δ_2 are varying with time during the impact. Thus, the instant values were calculated as follows:

$$\delta_1 = \frac{R_{1t}}{R_{1n}} \tag{14}$$

$$\delta_2 = \frac{R_{2t}}{R_{2n}} \tag{15}$$

where R_{1t}, R_{1n} are the sum of tangential and normal contact forces of the chute base respectively, and R_{2t}, R_{2n} are the sum of tangential and normal contact forces of the wall respectively. Thus, using Eq. 13 with instantaneous values of δ_1 and δ_2, we can get the time evolution of the gravitational force (F_g) applied on the wall. Discussion of results of total force components (gravitational and dynamic) are presented in Sect. 6.3.

4 Model calibration

The model calibration has been carried out considering the shape of the particles and the value of $\varepsilon_{n,t}$ based on the flow thickness measurements and the final shape of the deposit behind the wall. The aim of this calibration is to reach a suitable value for the normal restitution coefficient (ε_n) that lead to a closer behavior to the experimental flow. In addition, good calibration is needed to avoid a very dilute flow which would overflow the obstacle, in contrast to the gravel flow interaction with the rigid wall obtained in the experimental data (Sect. 2). Due to the absence of lubricated contacts, the tangential viscous damping coefficient has been set to zero (i.e. $\varepsilon_t = 1.0$) as suggested by Ghaisas et al. [29].

Friction angles of chute base, side walls and rigid wall were taken similar to values provided by the experimental data (Sect. 2). The model has been calibrated and validated for test L34-H15-α45°, test L44-H15-α40° and test L44-H20-α40°. Results shown in the calibration section are for test L44-H15-α40°.

4.1 Clumps versus spherical particles

The calibration mentioned here for the shape was carried out in parallel with the calibration of normal restitution coefficient (ε_n) mentioned in the following section. For selecting the most representative shape of the angular particles, a comparative study was conducted between clumps and spheres.

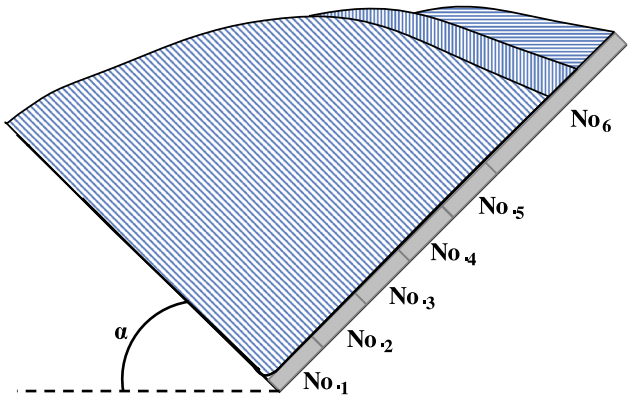

Fig. 6 Schematic representation of three different granular deposits (of same volume) showing the indirect relation between the final shape of the deposit and the residual force applied on the 6th segment of the wall

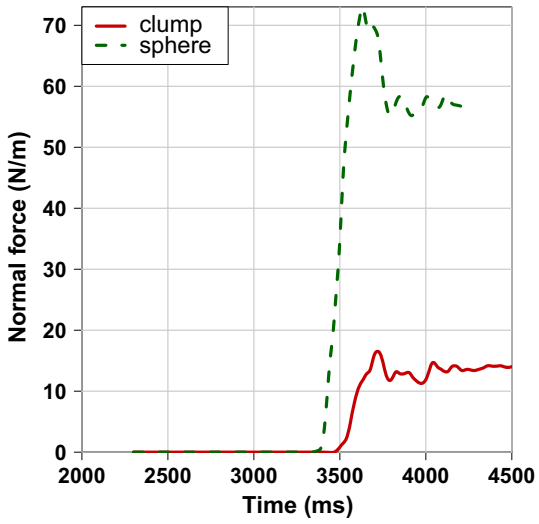

Fig. 7 Variation of normal force on part 6 of the wall with time for spherical and clumped shapes (test L44-H15-α40°)

By using the residual force values on the final segment at the top of the wall (F_6), we can get an indirect indication of how the deposit shape changes i.e. how far the deposit will vertically extend on that segment (Fig. 6). Thus, we compare the residual values of F_6 for each particle type (clump and sphere).

From Fig. 7, when compared to spheres, we see that using clumped particles give final force value closer to the experimental one ($F_{6exp} \approx 14$ N/m), which might indicate a better final shape representation. This might be due to the natural rotational resistance delivered by the clumped shape and also the interlocking between particles which prevent them from rolling over the dead zone. To verify this, we compared the ratio of rotational energy to total kinetic energy (E_{rot}/E_{kin}) for both cases. From Fig. 8, a reduction of this ratio by 70 % can be noticed once clumped particles are used. This way

of reducing rotational energy by shape configuration is preferred over blocking the rotation of any axis as it does not violate the physical laws of motion.

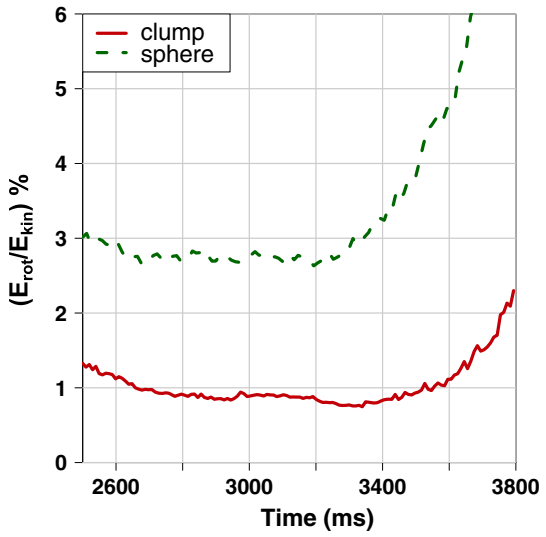

Fig. 8 Ratio of rotational energy to total kinetic energy for clumps and spheres (test L44-H15-α40°)

4.2 Flow thickness and deposit shape

The considered granular flow in the chute has two regimes along the flow thickness (Fig. 9); collisional and frictional regimes [31]. The frictional regime is mainly controlled by the friction angle of the chute base which is clearly stated in the experimental data.

On the other hand, ε_n values affect the collisional part of the flow thickness where dissipation of energy is thought to be caused by particles collision. For this reason, different values of normal restitution coefficient (from 0.1 to 0.9, with 0.1 step) were tested and compared with the experiment for the purpose of model calibration. For convenience, only curves of ε_n of 0.1, 0.3, 0.5, 0.7 and 0.9 are present in the following figures. The targeted part of the flow for calculating flow characteristics were particles within a distance ranging from 40 to 50 cm away from the wall. The flow centerline (h_{cl}) was calculated as follows:

$$h_{cl} = \frac{\sum_{i=1}^{n} h_{particle}}{n} \tag{16}$$

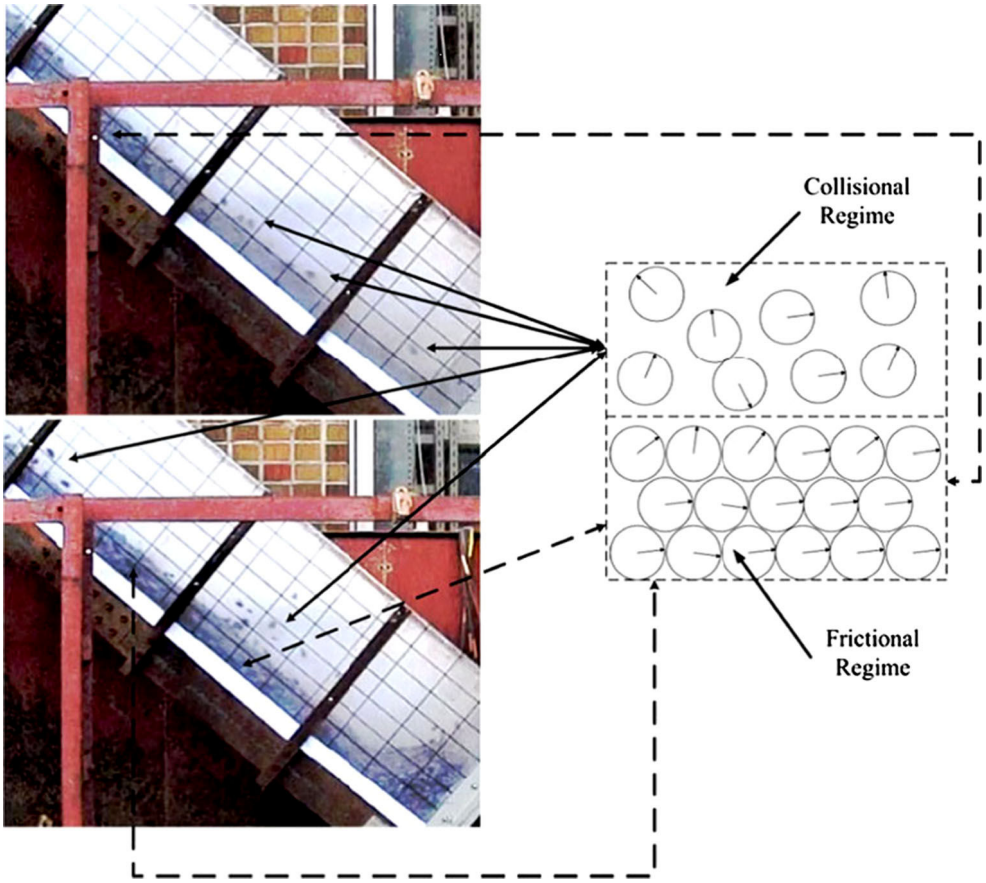

Fig. 9 Snapshots of the experiment showing frictional and collisional regimes of the flow, *top*: before the impact, *bottom*: after the impact [23] (with permission of Springer Science+Business Media)

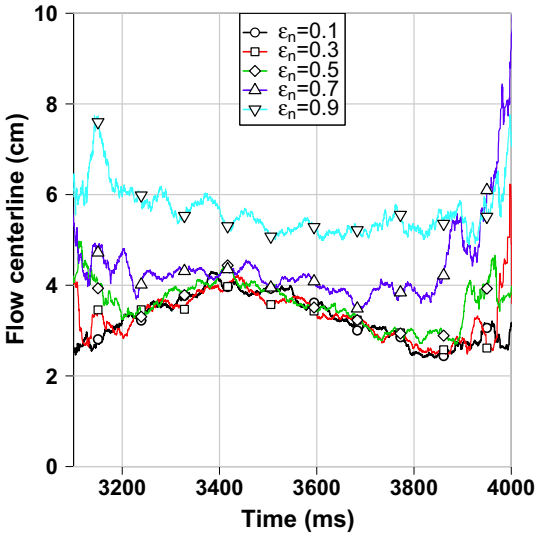

Fig. 10 Variation of average flow thickness (flow centerline) with time using different normal restitution coefficient values (test L44-H15-α40°)

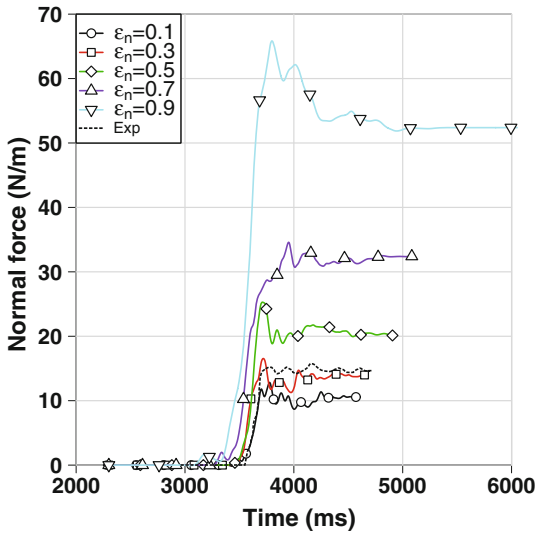

Fig. 11 Variation of normal force on the sixth segment of the wall with time using different normal restitution coefficient values (test L44-H15-α40°)

where $h_{particle}$ is the particle height (measured from its center in a perpendicular direction to the chute base) and n is the number of particles in the targeted volume.

Figure 10 shows the evolution of flow *centerline* for different values of ε_n. The time range where the body of the flow was passing through the measuring window (window from 40 to 50 cm away from the wall) was from 3200 to 3800 ms. Comparison of different values of ε_n is mainly done within this time range to exclude the highly dispersive front and tail parts of the flow.

As shown in Fig. 10, values of ε_n higher than 0.5 lead to a very dilute flow with high flow centerline values. These dispersive flows overflow the wall in contradiction to the observed behavior of the experimental data where no wall overtopping took place. In contrast, denser flows are observed for values of ε_n lower than or equal to 0.5 in accordance with observations of Faug et al. [15].

Likewise, the final deposit shape needs to be verified for different ε_n values. We use again the indirect relation between the final shape and the residual force value F_6 illustrated earlier in Fig. 6. Different values of ε_n are tested and results of force variation on the final segment of the wall are recorded (Fig. 11). Values of ε_n between 0.2 and 0.4 were found to be the most suitable for the coarse-grained gravel flow that we have, as they give the closest values to the experiment in terms of residual force on the 6th segment of the wall ($F_{6exp} \approx$ 14 N/m). As a result, a value of ε_n equal to 0.3 is chosen for our visco-elastic model. Next, we investigate the effect of ε_n values on the flow velocity. As flow velocity mainly depends on the inclination angle and the basal friction of the chute, little effect is noticed for the flow velocity with the change of restitution coefficient (Fig. 12). The considered flow velocity values are the average velocities in the direction of the flow

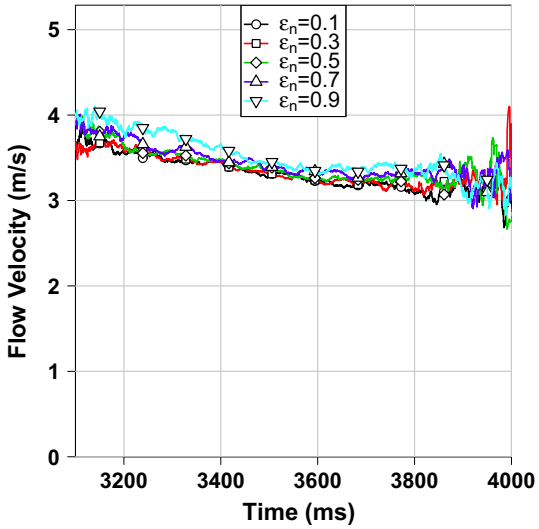

Fig. 12 Variation of average particles velocity with time, for particles on the upper half of the flow (test L44-H15-α40°)

for particles that have positions (measured from their center) in the upper half of the flow, in order to see the variation of particles velocities in the collisional regime of the flow.

The experimental result of flow thickness was calculated at the flow surface excluding particles that are detached from the flow. In order to be comparative with the experiment, the value of the flow thickness for $\varepsilon_n = 0.3$ needs to be verified at the same height. For this aim, we calculated the cumulative frequency of particles heights in which thickness and velocity values were taken at 90 % of total frequency of particle center (Fig. 13). A value of $D_{50}/2$ was added to 90 % cumulative frequency of the flow thickness to account for the free surface of the flow. The calculated thickness in the model (Fig. 13) has a value of 3.9 cm which matches the

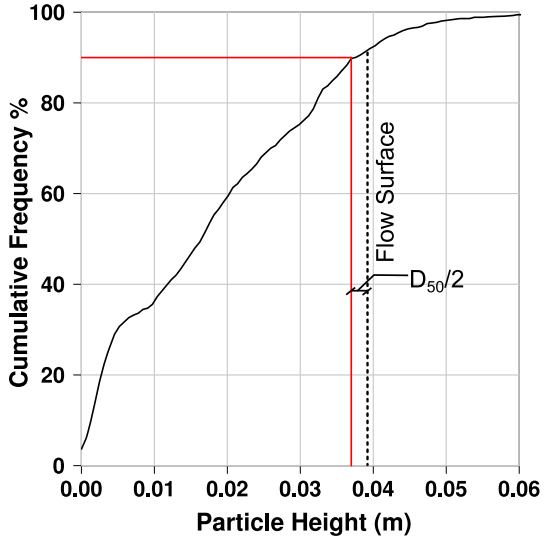

Fig. 13 Cumulative frequency of particles height measured from the center (test L44-H15-α40°)

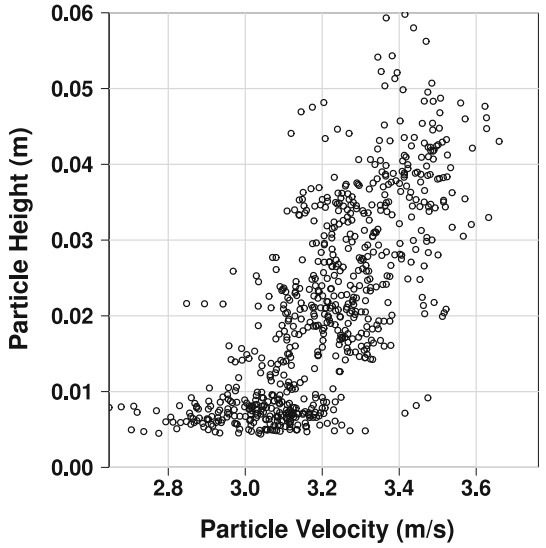

Fig. 14 Variation of particles velocity with heights (test L44-H15-α40°)

experimental value of 3.9 cm taken at the time of maximum impact force on the wall. The flow velocity profile (Fig. 14) suggests a plug flow taking place, which might be due to the high inclination angle of the chute. In addition, comparing the arrival time between the model and the experiment (Fig. 16), we see good match between the two which suggests similar flow velocities. Above all, features of dry granular flows have been observed by the model showing a dilute front followed by a denser part (Fig. 15).

5 Model validation

The rigid wall response against the granular flow impact has been investigated in details, giving special attention to the normal force applied on each part of the rigid wall where curves of normal impact force vs. time were analyzed. Due to the tendency of DEM results showing large fluctuation, a data treatment was needed in order to have results that are quantitatively comparable to the experimental data. Data treatment was carried out using smooth spline method where a smooth curve is fitted to a set of noisy data using spline function. The advantages of using splines are their computational speed and simplicity, as well as the clarity of controlling curvature directly [32]. The following validation sections show results of impacts on the segmented wall for test L34-H15-α45°, test L44-H15-α40° and test L44-H20-α40°. Afterwards, numerical results of total normal force and bending moments are compared with the experiment.

5.1 Test L34-H15-α45°

In this test (Fig. 16a), for the first element of the wall (F_1), the peak force was found to be 396 N/wall width which is fairly close to the experimental value (around 350 N/m). Moreover, the time of the peak force F_1 is relatively similar to the experiment with a value around 3676 ms but with a lower residual force in the model (145 N/m) compared with the experiment (175 N/m). Likewise, in contrast to F_1, the peak value of F_2 in the model (256 N/m) was lower than the experimental value (300 N/m). For F_3 and F_4, the model captured the peak time of forces fairly well (being 3883 and 3994 ms for F_3 and F_4 respectively) but with a lower peak value. The peak force and timing of the peak on F_5 and F_6 were fairly captured by the model along with their residual force values.

5.2 Test L44-H15-α40°

For this test, the peak impact force values were 341 and 232 N/m for F_1 and F_2 respectively (Fig. 16b). Compared to the experiment, similar values were observed but with a reversed order ($F_2 > F_1$). Such discrepancy of the force evolution will be discussed in details in Sect. 6.2. Concerning the rest of the wall, the model managed to capture the peak forces of F_3, F_4, F_5 and F_6 (with a small exception for F_3) with values of 154, 120, 66 and 15 N/m respectively along with peak times 3619, 3808, 3733 and 3761 ms respectively. Residual forces on these parts were found to be 112, 82, 40 and 12 N/m respectively which are close to the experimental observations.

5.3 Test L44-H20-α40°

With the use of higher volume of the sample, the trend of the impact force curves was better captured with the model along with the time lag between each force curve. For instance, F_1 peaks at 2523 ms with a value of 387 N/m (450 N/m in the experiment) which is followed by a peak of F_2 with 288 N/m

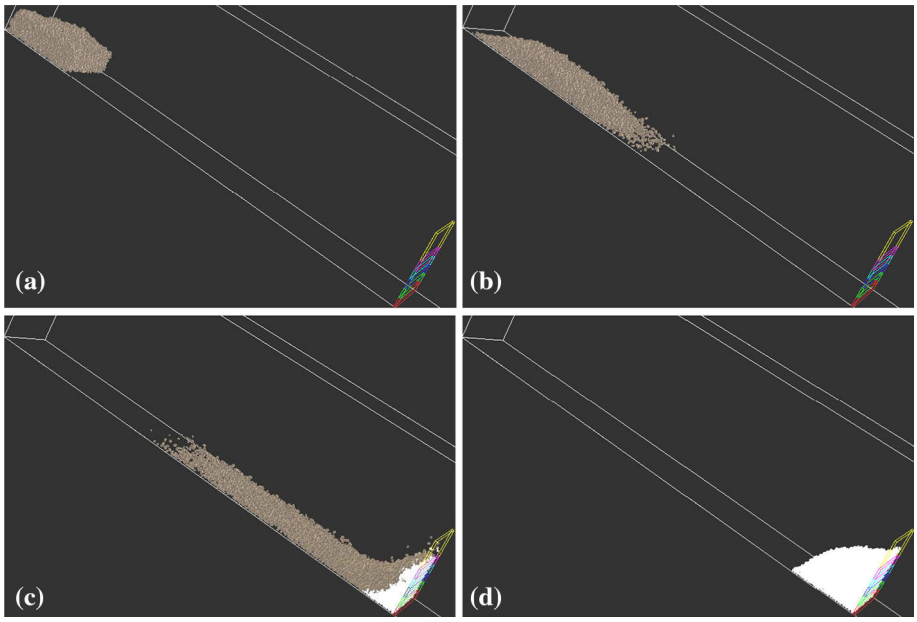

Fig. 15 Snapshots of the 3D view of the evolution of simulated flow through time (test L44-H15-α40°), along with the evolution of dead particles (colored in white): **a** at time = 2300 ms, **b** at time = 2793 ms, **c** at time = 3583, **d** at time = 4400 ms

(340 N/m in the experiment) at 2737 ms (Fig. 16c). Residual forces of F_1 and F_2 were found to be similar to the experiment with values of 227 and 226 N/m respectively. Very good agreement has also been observed for F_3, F_4, F_5 and F_6 in terms of peak forces (172, 172, 108 and 51 N/m) the time of the peak (2864, 3070, 2912 and 3043 ms) and residual force values (116, 134, 65 and 43 N/m).

5.4 Total normal force and bending moment

The total force and bending moment acting on the wall were calculated as follows:

$$F = \sum_{i=1}^{6} F_i \tag{17}$$

$$M = \sum_{i=1}^{6} F_i h_i \tag{18}$$

where F_i is the normal force on each part of the wall and h_i is the distance between the centroid of the walls parts and bottom of the retaining wall (Fig. 1). For the total normal force (Fig. 17), the model fairly agrees with the experiment in terms of the peak force (735 N/m), peak time (3733 ms) and residual total force (576 N/m). The bending moment results (Fig. 17) from the model also agrees with the experiment having a maximum bending moment of 80 N*m/m and peaking at the same time of the total force peak (3733 ms). This agreement in total force between the model and the experiment, although some discrepancies appear in the force distribution on each part of the wall (Fig. 16b), suggests the presence of microstructural heterogeneities (arching effects) in the granular deposit behind the wall [33]. Such heterogeneities are very unstable, and difficult to be well-captured by the numerical modeling spatially and temporally.

6 Discussion

6.1 Forces and bending moment on the wall

By quantitative comparison with experimental results, good agreement has been observed in terms of the peak force on each part of the wall, the time of the peak and the residual force at the end of the test. The time of the first impact has also been found to be similar. Such an agreement suggests the ability of the model to account for the pressure variation with the height of the obstacle. Good agreement has also been observed for total normal force impacting the wall. The maximum total impact force was found to be around 1.25 times the hydrostatic force at the end of the test. In addition, the total bending moment at the toe of the wall predicted with the model was found to be similar when compared to the experimental data. Although out of the scope of this study, it is worth noting that the tangential force (F_t) on the wall was found to be negligible in accordance with Faug et al. [15], whatever the slope inclination is. This might need further experimental studies with sensors measuring the variation of tangential force on the wall.

6.2 Arching effect within the granular medium

Results from Fig. 16 suggest a non-linear distribution of forces on different parts of the wall. In particular, the force at the toe of the wall is sometimes smaller than the one on

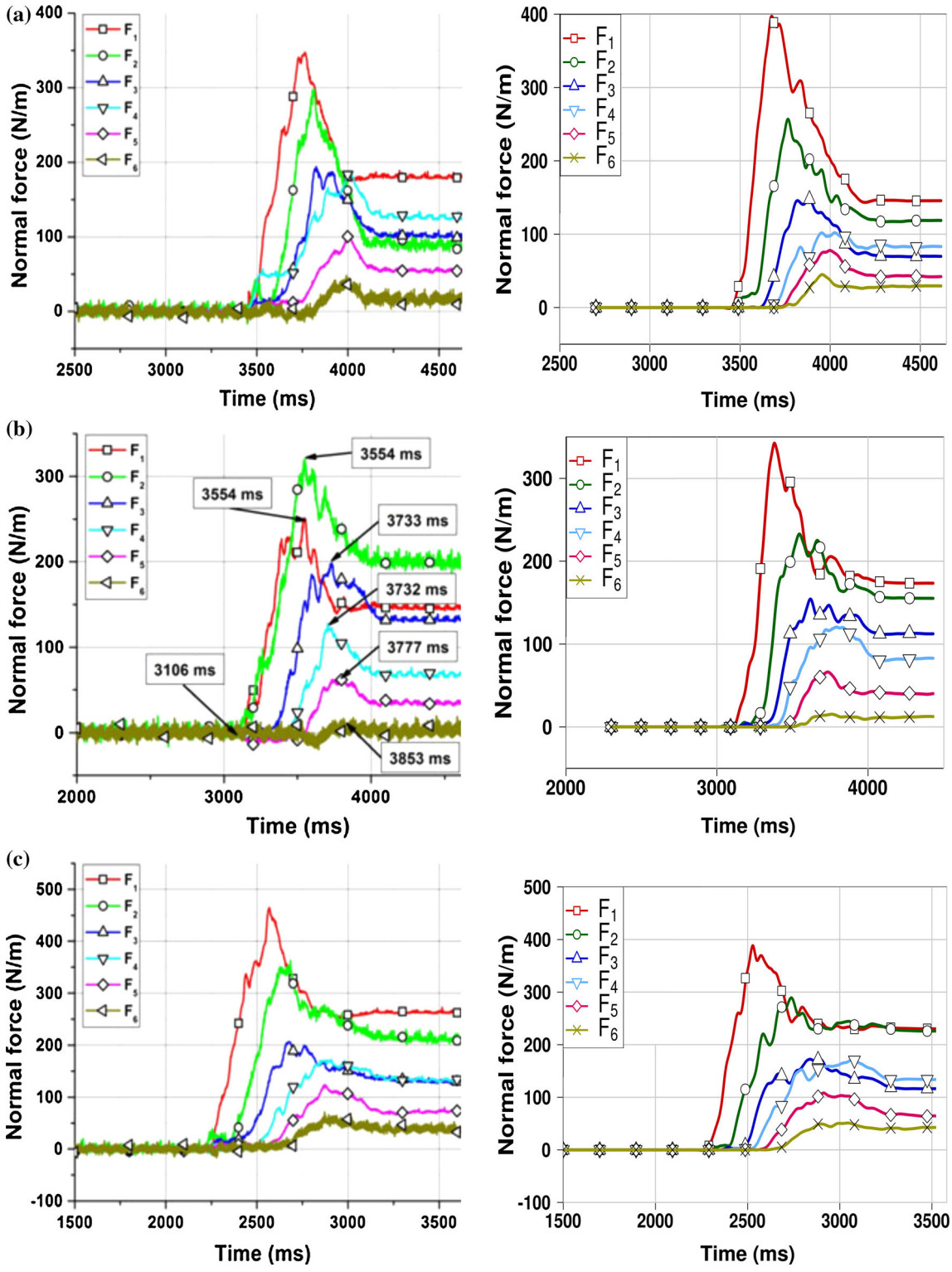

Fig. 16 Time history of normal force variation: model (*right*) and experiment [23] (*left*): **a** test L34-H15-α45° **b** test L44-H15-α40° **c** test L44-H20-α40°

the segment above. These discrepancies indicate the possible presence of arching effects in the impacting and depositing stages of the flow. According to Jiang and Towhata [23], this might be due to a formation of an arch-like protective layer on segment 1 of the wall resulting in a non-linear distribution of forces with depth. Such a layer is also thought to affect

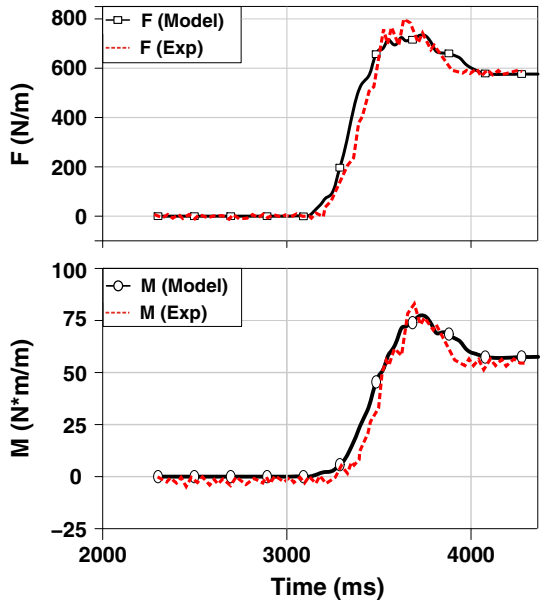

Fig. 17 Time history of total normal force and bending moment, test L44-H15-α40°: numerical model and experiment (data from [23])

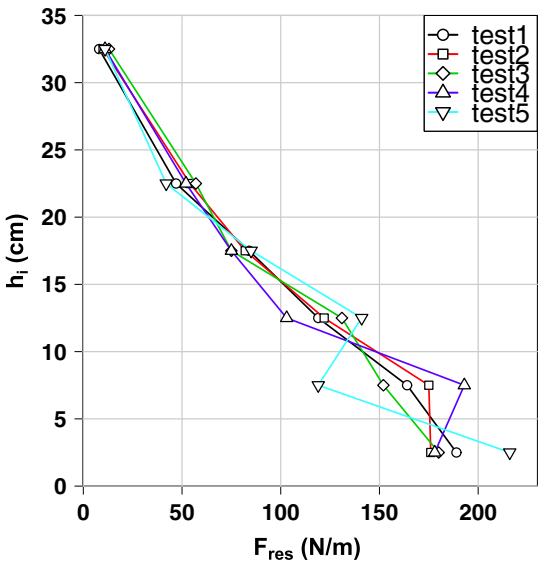

Fig. 18 Variation of normal residual force with walls height for five tests carried out under the same initial conditions (test L44-H15-α40°)

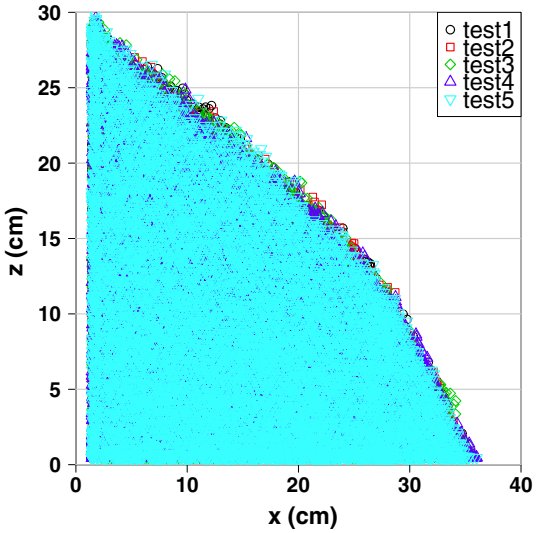

Fig. 19 The final deposit shape for five tests that have the same initial conditions (test L44-H15-α40°)

the residual force values. To some extent, non-linearity was observed to be present in the model, especially for residual forces of F_1–F_2 and F_3–F_4. This might be due to the force chain distribution behind the wall. Force chains are strongly depending on the particles position and orientation with respect to the wall [34]. The distribution of contact forces on the wall is expected to be different from one test to another, especially at the toe of the wall, even if conducted in the same initial conditions (same volume of the sample and inclination angle). Figure 18 represents the variation of residual forces with the height of the wall for simulations performed for the same initial testing conditions; 44 cm length, 30 cm width and 15 cm height and 40° inclination angle (16 simulations were performed but only five are presented for convenience). However, each test has different initial spatial distribution of particles.

Differences between the five tests can be seen for the value of the residual force at each wall segment. These differences are found to increase with depth. For instance, the forces on the 6th segment of the wall (F_6) are very similar for the considered tests. Less agreement is seen for values of F_5 and beyond. The most significant difference can be seen in the segments number 1 and 2 (F_1 and F_2) at the bottom of the wall. For example, the difference between tests 4 and 5 for the value of F_2 is around 35%, although the shape of the granular deposits is the same at the end of the different simulations (Fig. 19). As a result, such discrepancy in residual force values can not be explained by a difference in granular shape deposit.

Since these discrepancies are the highest for segments 1 and 2 of the wall (i.e. F_1 and F_2), the spatial distribution of contact force values on these segments was investigated. Fig. 20 shows the distribution of contact forces for tests 4 and 5 over segments 1 and 2 of the wall. For test 4 (Fig. 20, top), there are two zones of high concentration of contact force in segment number 2 of the wall. Less force concentration is seen for segment number 1 of the wall. As a result, F_2 value is higher than F_1 in Fig. 19 for test 4. In contrast, for test 5 (Fig. 20, bottom), several zones of high concentration of contact forces are present in segment number 1 of the wall. Much lower concentration of contact force is present for segment number 2. Consequently, F_1 value is much higher than that of F_2 in Fig. 19 for test 5. Thus, it is more likely that the discrepancies seen in Fig. 19 for the different tests are

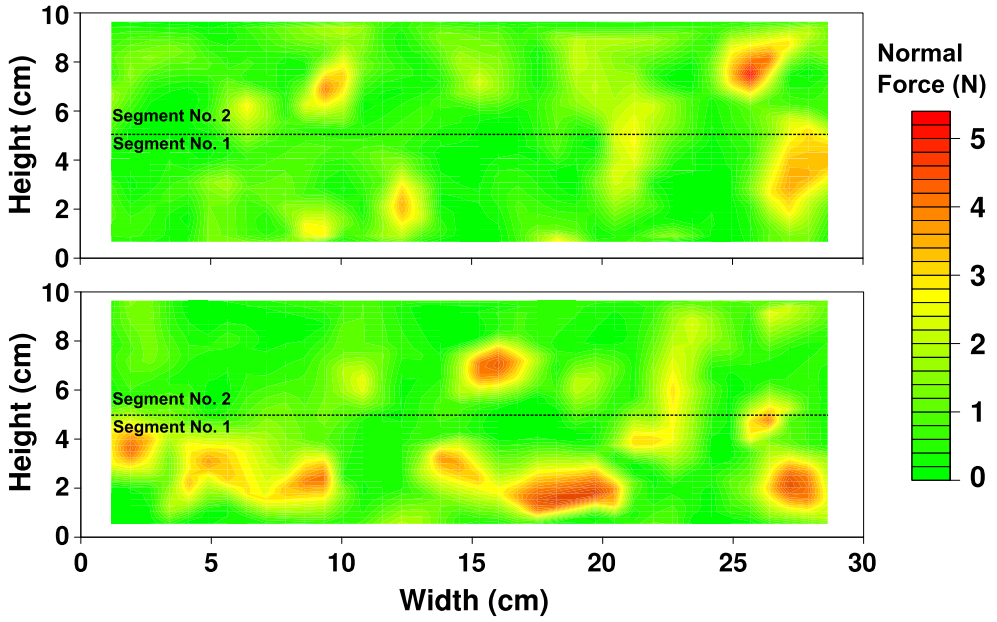

Fig. 20 Residual normal contact forces between segments 1 and 2 of the wall and particles deposited on them, *top*: test 4, *bottom*: test 5

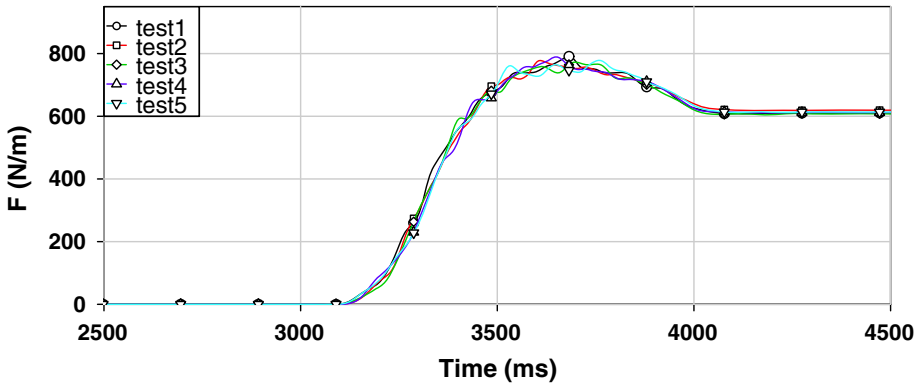

Fig. 21 Time history of the evolution of total normal force with time for five tests that have the same initial conditions (test L44-H15-α40°)

caused by microstructural heterogeneities, like for example arching effects. However, when the total normal impact force on the wall is considered (Fig. 21), little difference is seen between the 5 tests. Total normal impact force values are very similar in the impacting and depositing stages of the granular flow impact on the rigid wall. As a result, for engineering applications such as the design of rigid barriers where the driving factor is the total normal force on the barrier, there might be no need to consider the discrepancies seen on the segment-scale of the wall.

It is worth noting that it is numerically possible for the model (example: test 4 in Fig. 18) to capture what might be a strong arching in the experiment (Fig. 16b) in which we have $F_1 \leq F_2$. Nevertheless, quantifying the force chains in the 3D environment is out of the scope of this paper. Above all, matching between numerical simulations and experiments should mainly concern the total normal force and bending moment on the wall rather than on each segment.

6.3 Evolution of total force components

The variation of total normal impact force with time was studied considering two components: gravitational and dynamic (Fig. 22). The calculation method has been presented earlier in Sect. 3.3. Instant values of δ_1 and δ_2 were calculated in the numerical simulation at each time step and then used in Eq. 13 to calculate the gravitational force. We can see that the final value of gravitational force (F_g) corresponds well to that of total force (F_{tot}) while the dynamic force (F_d) converges to zero agreeing with the absence of any movement of the particles.

We can also notice that at the beginning of the impact, small contribution of gravitational force is observed (Fig. 22). As time passes, more particles accumulate behind the wall and the gravitational force contribution becomes more significant. In addition, at the critical time where the total force reaches its maximum value, the dynamic component of the force is around 85 % of the total while the gravitational one

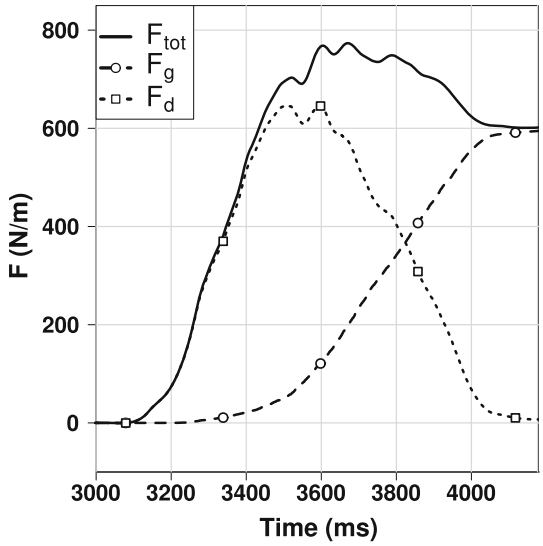

Fig. 22 Variation of total force components with time (test L44-H15-α40°)

is only 15%. This indicates the importance of having a good model for the flow with its flow thickness and velocity measurements. Predicting the components of the total force might be needed for the next step when the flexible structure is introduced. The gravitational force variation with time will help in designing the different parts of the flexible structures according to the type of forces they are subjected to. Furthermore, good prediction of gravitational force could help in accounting for different scenarios of failure that might take place.

7 Conclusions

Dry granular flows can occur following earthquakes, which can exert large destructive forces on neighboring urban areas. The evaluation of such forces is essential for protective structures design. In this paper, we have developed a numerical model for the impact of dry granular flow against a rigid wall using clumped particles. With the use of experimental data of dry gravel flow, we calibrated our model considering the shape of the particle, the flow thickness and the final shape of the deposit on the wall. Concerning the shape, the use of clumps was found to be beneficial for accounting for the shape effects caused by the sharp angles of coarse-grained particles. It was shown that the use of clumped particles is preferred over spherical ones in controlling rotational velocity which was reduced by 70 %. Indeed, the shape of the deposition behind the wall was improved by the clumped particles leading to a force distribution which is closer to the experimental values. Good agreement has been observed in terms of flow thickness and flow arrival times between the model and the experiment.

The proposed model has shown capabilities of capturing the main features of normal impact force against a rigid wall. These features are the peak force on each part of the wall, the time of the peak and the residual force at the end of the test. Moreover, total normal force and bending moment at the toe of the wall were closely captured by the model.

On the microscopic scale, microstructural heterogeneities (arching effect) were present in the experimental data and also, to some extent, in the numerical model. They were found to take place in the granular medium behind the rigid wall in both impacting and depositing stages. These heterogeneities were present even for samples with the same size and chute inclination angle, but different initial arrangement of particles. Such heterogeneities are unstable, and difficult to be precisely captured spatially and temporally.

In terms of total force components, it has been shown that accounting for the instant values of the ratio F_t/F_n for the interaction between the flow and both the wall and the base leads to better prediction of the accumulation process of this gravitational force on the wall. The dynamic component was found to contribute to 85% of the maximum total impact force on the wall. The next step would be to replace the rigid wall in the model with a flexible structure (net elements) in which the impact behavior will be studied in details.

Acknowledgments The research leading to these results has received funding from the People Programme (Marie Curie Actions) of the European Union's Seventh Framework Programme FP7/2007-2013/ under REA grant agreement number 289911. The authors would also like to acknowledge the many valuable suggestions made by Thierry Faug, a researcher in Irstea research institute in Grenoble.

References

1. Jakob, M., Oldrich, H.: Debris-flow hazards and related phenomena. Springer, Newyork (2005)
2. Kishi, N., Ikeda, K., Konno, H., Kawase, R.: In: Proceedings of Structures under Shock and Impact IV, pp. 351–360 (2000)
3. Nicot, F., Cambou, B., Mazzoleni, G.: From a constitutive modelling of metallic rings to the design of rockfall restraining nets. Int. J. Numer. Anal. Methods Geomech. **25**(1), 49–70 (2001)
4. Volkwein, A.: Proceedings of Computing in Civil Engineering. ASCE, Cancun (2005)
5. Hearn, G., Barrett, R.K., Henson, H.H.: Development of effective rockfall barriers. J. Transp. Eng. **121**(6), 507–516 (1995)
6. Peila, D., Pelizza, S., Sassudelli, F.: Evaluation of behaviour of rockfall restraining nets by full scale tests. Rock Mech. Rock Eng. **31**(1), 1–24 (1998)
7. Hutter, K., Koch, T., Pluüss, C., Savage, S.: The dynamics of avalanches of granular materials from initiation to runout. Part II experiments. Acta Mech. **109**(1–4), 127–165 (1995)
8. Azanza, E., Chevoir, F., Moucheront, P.: Experimental study of collisional granular flows down an inclined plane. J. Fluid Mech. **400**, 199–227 (1999)
9. Pudasaini, S.P., Hutter, K.: Rapid shear flows of dry granular masses down curved and twisted channels. J. Fluid Mech. **495**, 193–208 (2003)

10. Moriguchi, S., Borja, R.I., Yashima, A., Sawada, K.: Estimating the impact force generated by granular flow on a rigid obstruction. Acta Geotech. **4**(1), 57–71 (2009)
11. Buchholtz, V., Pöschel, T.: Interaction of a granular stream with an obstacle. Granul. Matter **1**(1), 33–41 (1998)
12. Teufelsbauer, H., Wang, Y., Chiou, M.C., Wu, W.: Flow-obstacle interaction in rapid granular avalanches: DEM simulation and comparison with experiment. Granul. Matter **11**(4), 209–220 (2009)
13. Silbert, L.E., Ertaş, D., Grest, G.S., Halsey, T.C., Levine, D., Plimpton, S.J.: Granular flow down an inclined plane: bagnold scaling and rheology. Phys. Rev. E **64**(5), 051302 (2001)
14. Calvetti, F., Crosta, G., Tatarella, M.: Numerical simulation of dry granular flows: from the reproduction of small-scale experiments to the prediction of rock avalanches. Rivista Italiana di Geotecnica **34**(2), 21–38 (2000)
15. Faug, T., Beguin, R., Chanut, B.: Mean steady granular force on a wall overflowed by free-surface gravity-driven dense flows. Phys. Rev. E **80**(2), 021305 (2009)
16. Mollon, G., Richefeu, V., Villard, P., Daudon, D.: Numerical simulation of rock avalanches: influence of a local dissipative contact model on the collective behavior of granular flows. J. Geophys. Res. Earth Surf. (2003–2012) **117**(F2), F02036 (2012)
17. Campbell, C.S., Cleary, P.W., Hopkins, M.: Large-scale landslide simulations: global deformation, velocities and basal friction. J. Geophys. Res. B Solid Earth (1978–2012) **100**(B5), 8267–8283 (1995)
18. Lemieux, P.A., Durian, D.: From avalanches to fluid flow: a continuous picture of grain dynamics down a heap. Phys. Rev. Lett. **85**(20), 4273 (2000)
19. Chu, T., Hill, G., McClung, D., Ngun, R., Sherkat, R.: Experiments on granular flows to predict avalanche runup. Can. Geotech. J. **32**(2), 285–295 (1995)
20. Keller, S., Ito, Y., Nishimura, K.: Measurements of the velocity distribution in ping-pong-ball avalanches. Ann. Glaciol. **26**, 259–264 (1998)
21. Faug, T., Lachamp, P., Naaim, M.: Experimental investigation on steady granular flows interacting with an obstacle down an inclined channel: study of the dead zone upstream from the obstacle. Application to interaction between dense snow avalanches and defence structures. Nat. Hazards Earth Syst. Sci. **2**(3/4), 187–191 (2002)
22. Valentino, R., Barla, G., Montrasio, L.: Experimental analysis and micromechanical modelling of dry granular flow and impacts in laboratory flume tests. Rock Mech. Rock Eng. **41**(1), 153–177 (2008)
23. Jiang, Y.J., Towhata, I.: Experimental study of dry granular flow and impact behavior against a rigid retaining wall. Rock Mech. Rock Eng. **46**(4), 713–729 (2013)
24. Pudasaini, S.P., Hsiau, S.S., Wang, Y., Hutter, K.: Velocity measurements in dry granular avalanches using particle image velocimetry technique and comparison with theoretical predictions. Phys. Fluids **17**(9), 093301 (2005)
25. Cundall, P.A., Strack, O.D.: A discrete numerical model for granular assemblies. Geotechnique **29**(1), 47–65 (1979)
26. Šmilauer, V., Catalano, E., Chareyre, B., Dorofeenko, S., Duriez, J., Gladky, A., Kozicki, J., Modenese, C., Scholtès, L., Sibille, L., Stránsk, J., Thoeni, K.: Yade Documentation. http://yade-dem.org/doc/ (2010)
27. Bertrand, D., Nicot, F., Gotteland, P., Lambert, S.: Discrete element method (DEM) numerical modeling of double-twisted hexagonal mesh. Can. Geotech. J. **45**(8), 1104–1117 (2008)
28. Schwager, T., Pöschel, T.: Coefficient of restitution and linear-dashpot model revisited. Granul. Matter **9**(6), 465–469 (2007)
29. Ghaisas, N., Wassgren, C.R., Sadeghi, F.: Cage instabilities in cylindrical roller bearings. J. Tribol. **126**(4), 681–689 (2004)
30. Catalano, E., Chareyre, B., Barthélémy, E.: Pore-scale modeling of fluid-particles interaction and emerging poromechanical effects. Int. J. Numer. Anal. Meth. Geomech. **38**(1), 51–71 (2014)
31. Savage, S.B.: The mechanics of rapid granular flows. Adv. Appl. Mech. **24**, 289–366 (1984)
32. Chambers, J.M., Hastie, T.J.: Statistical Models in S. CRC Press, Inc., Boca Raton (1991)
33. Handy, R.L.: The arch in soil arching. J. Geotech. Eng. ASCE **111**(3), 302–318 (1985)
34. Azéma, E., Radjaï, F.: Force chains and contact network topology in sheared packings of elongated particles. Phys. Rev. E **85**(3), 031303 (2012)

Abstract

This thesis presents a discrete element model of granular debris flow interaction with both rigid and flexible structures. The flow was modeled using non-spherical particles and a visco-elastic contact law. Available experimental data from the literature were used to calibrate and validate the impact model against a rigid wall. On the micro-scale, development of force chains caused heterogeneous distribution of normal force on each part of the wall, for multiple same-test conditions. The flexible barrier components were modeled using cylindrical elements. The use of energy dissipators was found to be essential in dissipating the kinetic energy of the flow and thus control the forces applied on the lateral anchors. In terms of impact force, the flexible barrier is subjected to 50% lower impact force than that of the rigid wall, for the same impacting flow. The model was used to recommend some dimensioning values of flexible barriers. For instance, using a mesh size up to D_{90} of the incoming flow is suitable for retaining the flowing material. In addition, if the bottom cable is not fixed, the flexible barrier would lose its retaining capacity in extreme debris flow events.

Keywords:
Discrete Element Method, Granular debris flows, Protection Structures, Rigid Walls, Flexible Barriers, Force Chains

Résumé

Cette thèse présente un modèle aux éléments discrets de l'impact des laves torrentielles sur des structures rigides et flexibles. L'écoulement est modélisé en utilisant des particules non sphériques et une loi de contact viscoélastique. Des données expérimentales de la littérature sont utilisées pour calibrer et valider le modèle d'impact sur un mur rigide. À l'échelle microscopique, la distribution hétérogène de la force normale sur chaque partie du mur est due au développement des chaînes de force, qui est différent pour chaque arrangement de particules. Les composants flexibles du filet sont modélisés en utilisant des éléments cylindriques. Le rôle des dissipateurs d'énergie apparaît essentiel pour réduire la force d'impact sur le filet et limiter la force appliquée sur les points d'ancrage latéraux. En termes de force d'impact, le filet est soumis à une force d'impact 50% inférieure à celle du mur rigide, pour un même écoulement granulaire. Les simulations permettent de définir des recommandations pour le dimensionnement des filets. Il est constaté que l'utilisation d'un maillage de filet plus petit que D_{90} de l'écoulement est acceptable en termes de capacité à retenir les matériaux en écoulement. De plus, Il est montré que, lors d'événement extrême, si le câble en bas du filet n'est pas fixé le filet pourrait perdre totalement sa capacité de retenue.

Mots clés:
Méthode des éléments discrets, Laves torrentielles granulaires, Structures de protection, Mur rigide, filet de protection, Chaînes de forces